

A numerical investigation of the effect of crosswinds on  
the slipstream of a model-scale freight train and  
associated effects

By

Dominic Christopher Flynn

A thesis submitted to the University of Birmingham for the degree of  
DOCTOR OF PHILOSOPHY

Birmingham Centre for Railway Research and Education

School of Civil Engineering

University of Birmingham

May 2015

UNIVERSITY OF  
BIRMINGHAM

**University of Birmingham Research Archive**

**e-theses repository**

This unpublished thesis/dissertation is copyright of the author and/or third parties. The intellectual property rights of the author or third parties in respect of this work are as defined by The Copyright Designs and Patents Act 1988 or as modified by any successor legislation.

Any use made of information contained in this thesis/dissertation must be in accordance with that legislation and must be properly acknowledged. Further distribution or reproduction in any format is prohibited without the permission of the copyright holder.

# Abstract

A numerical investigation is presented in which the effect of crosswinds on the slipstream of a fully-loaded model-scale freight train is studied. The work used delayed detached-eddy simulation in order to produce accurate time-averaged data and also allowed for the instantaneous flow to be analysed.

Significant slipstream amplification is shown for both pressure and velocity transients on the leeward side of the train. The most significant slipstream amplification is observed at the 30° yaw angle case where high velocities remain almost constant at the furthest measurement position from train side.

Instantaneous slipstream velocities on the leeward side of the train were inputted into a mathematical model which was used to predict the effect of wind gusts on a representative sample of the population. It was found that at 4 m from train side the person instability due to slipstream amplification for the 30° case is nearly double that from the 10° case.

The results presented highlight the potential risk associated with slipstream amplification around freight trains, although due to the immaturity of the field, no amendments are made to the codes of practice.

## **Acknowledgements**

I would firstly like to thank my supervisors Dr Hassan Hemida and Prof Chris Baker for sharing their expertise and insights during this research.

Thanks also go to

- Dr Sarah Jordan for providing the spring-mass-damper-model which has given an extra dimension to this research.
- Dr David Soper who contributed to numerous discussions about train aerodynamics, provided validation data and produced the finest CAD modelling known to man or beast.
- Dr Matthew ‘Verbose’ Haines for participating in hours of discussions about CFD in wind engineering.
- Dr Andrew Quinn and Prof Mark Sterling for providing strong motivation to improve this research perspective and my writing style.
- Paul Hatton & IT Services for helping with all manner of technical issues with BlueBEAR.
- Tony Rogers for demystifying the world of purchasing and finance and finally, Aslam Ghumra for his support during BEAR-related activities.

# Contents

Chapter 1 Introduction .....	1
1.1 Outline of studies .....	1
1.2 Research background .....	1
1.3 Aims and objectives .....	4
1.4 Structure of thesis.....	5
Chapter 2 Literature Review .....	8
2.1 Introduction .....	8
2.2 The application of computational fluid dynamics modeling to train aerodynamics ...	8
2.3 Slipstreams .....	10
2.3.1 Preliminaries .....	10
2.4 Slipstream-induced accidents.....	11
2.5 Characteristic features of train slipstreams .....	12
2.5.2 Train slipstreams and experimental methodologies.....	24
2.5.3 CFD slipstream investigations .....	35
2.5.4 Data analysis methods for slipstream measurements.....	37
2.6 Crosswind effects on train slipstreams.....	39
2.6.1 Relative crosswind profile .....	40
2.6.2 Crosswind-affected slipstreams .....	42
2.6.3 Crosswinds, slipstreams and TSI.....	55
2.7 The effect of slipstreams on persons and objects at trackside.....	56
2.7.1 Objects and persons on platforms .....	57
2.7.2 Human stability in windy conditions .....	58
2.7.3 Risk .....	59
2.8 Aerodynamic loading of container freight trains .....	59
2.8.1 Aerodynamic drag of vehicles/trains .....	60
2.8.2 Crosswind loading on trains.....	61
2.8.3 CFD for crosswind assessment of trains.....	66
Chapter 3 Methodology .....	69
3.1 Introduction .....	69
3.2 Computational fluid dynamics .....	69
3.2.1 OpenFOAM .....	70
3.3 Slipstream Simulation setup.....	71
3.3.1 Geometry.....	71
3.3.2 No-crosswind case .....	75
3.3.3 Crosswind cases .....	82
3.4 Numerical method .....	86

3.4.1	Discretisation .....	86
3.4.2	Pressure/velocity decoupling .....	92
3.4.3	Matrix Solution Algorithms .....	92
3.4.4	Large-eddy simulation .....	93
3.4.5	Delayed Detached-Eddy Simulation.....	97
Chapter 4	The slipstream flow around a freight train in no wind conditions .....	104
4.1	Introduction .....	104
4.2	Solution verification and validation .....	104
4.2.1	Mesh sensitivity .....	105
4.2.2	Validation.....	106
4.2.3	Ensemble-averaging vs. time-averaging.....	109
4.3	Time-averaged flow .....	111
4.3.1	Slipstream measurement positions.....	111
4.3.2	Velocity magnitude at train side .....	113
4.3.3	Velocity magnitude above train roof .....	117
4.3.4	Velocity components at train side.....	118
4.3.5	Boundary layer profiles.....	127
4.3.6	Inter-wagon spacings .....	130
4.3.7	Displacement thickness.....	134
4.3.8	Pressure coefficients at train side.....	136
4.3.9	Nose region visualisation.....	140
4.4	Instantaneous flow.....	143
4.4.1	Vortex generation.....	143
4.4.2	Turbulence intensity at train side.....	145
4.4.3	Integral length scale .....	147
4.4.4	Force coefficients.....	150
4.5	Technical standards for interoperability.....	157
4.6	Summary .....	159
Chapter 5	Freight train subjected to a 30° crosswind .....	161
5.1	Introduction .....	161
5.2	Solution verification and validation .....	161
5.2.1	Mesh Sensitivity.....	161
5.2.2	Verification of sub-grid viscosity levels .....	162
5.2.3	Validation.....	163
5.3	Time-averaged flow .....	165
5.3.1	Boundary layer development in the computational domain .....	165
5.3.2	Velocity magnitude on the windward side of the train .....	167

5.3.3	Velocity magnitude on the leeward side of the train .....	169
5.3.4	Velocity components on the windward side of the train.....	172
5.3.5	Velocity components on the leeward side of the train.....	178
5.3.6	Pressure on the windward side of the train .....	186
5.3.7	Pressure on the leeward side of the train .....	188
5.3.8	Flow structures.....	190
5.3.9	Surface pressure coefficients .....	192
5.3.10	Flow structures in the inter-wagon spacings.....	193
5.3.11	Forces experienced by locomotive and containers .....	195
5.4	Instantaneous flow.....	202
5.4.1	Vortex generation.....	202
5.4.2	Time-varying force coefficients.....	203
5.4.3	Turbulence intensity on the windward side of the train.....	205
5.4.4	Integral length-scale.....	207
5.5	Concluding remarks .....	207
Chapter 6 Freight train subjected to a 10° Crosswind .....		210
6.1	Introduction .....	210
6.2	Solution verification.....	210
6.2.1	Mesh sensitivity .....	210
6.2.2	Verification of sub-grid viscosity levels .....	211
6.3	Time-averaged flow .....	212
6.3.1	Velocity magnitude on the windward side of the train .....	212
6.3.2	Velocity magnitude on the leeward side of the train .....	215
6.3.3	Velocity components on the windward side of the train.....	218
6.3.4	Velocity components – leeward.....	224
6.3.5	Pressure on the windward side of the train .....	230
6.3.6	Pressure on the leeward side of the train .....	232
6.3.7	Flow visualisation .....	234
6.3.8	Surface pressure coefficients .....	236
6.3.9	Flow structures in the inter-wagon spacings.....	237
6.3.10	Slipstream comparison to ICE 2 .....	239
6.3.11	Forces experienced by locomotive and containers .....	241
6.4	Instantaneous flow.....	246
6.4.1	Vortex generation.....	246
6.4.1	Turbulence intensity on the windward side of the train.....	247
6.4.2	Integral length scale .....	250
6.4.3	Force coefficients.....	250

6.4.4	TSI velocities .....	253
6.4.5	TSI pressures.....	254
6.5	Concluding remarks .....	255
Chapter 7	A comparative analysis of the slipstream around the freight train from all crosswind conditions.....	257
7.1	Introduction .....	257
7.2	Time-averaged velocity magnitudes .....	257
7.3	Instantaneous peak velocity magnitudes .....	268
7.4	Time-averaged pressure .....	272
7.5	Instantaneous peak-to-peak pressure transients .....	282
7.6	Force coefficients .....	285
7.7	Concluding remarks .....	288
Chapter 8	Human stability of a person subjected to a slipstream-generated wind gust .....	290
8.1	Introduction .....	290
8.2	Stability of people subjected to winds.....	291
8.2.1	Cuboid model.....	292
8.2.2	Three-mass system.....	293
8.2.3	Wind tunnel tests and model calibration.....	294
8.2.4	Pushchairs .....	297
8.3	Velocity inputs for person and pushchair models .....	297
8.4	Randomly-generated people.....	299
8.5	Results .....	301
8.6	Discussion .....	305
8.7	Conclusions .....	307
Chapter 9	Conclusions and recommendations for future work .....	309
9.1	Conclusions .....	309
9.2	Recommendations for future work.....	314
Appendix A	Author's publications .....	323
Introduction.....		323

## List of Figures

Figure 1 Schematic of slipstream measurement coordinate systems for trackside and platform measurements.....	11
Figure 2 Sign on a station platform warning passengers to keep clear of the platform edge because of possible train slipstream effects (© www.geograph.org.uk) .....	11
Figure 3 Schematic of the flow regions in a train's slipstream .....	13
Figure 4 Idealised nose pressure coefficients obtained from potential flow calculations (Sanz-Andrés and Santiago-Prowald, 2002).....	14
Figure 5 Operational Class 66 locomotive hauling FEA-B container wagons through Virginia Water station (Tagishsimon, 2004).....	15
Figure 6 Schematic of the velocity profile from the flow over a slip wall and in a 2-dimensional boundary layer. Free-stream velocity, longitudinal velocity and height position from wall are given as $u_\infty$ , $u$ and $dy$ , respectively. Hashed area indicates missing mass and momentum flux from the presence of the boundary layer. ....	17
Figure 7 A comparison between displacement thicknesses of model-scale and full-scale ICE2 slipstreams (Sterling et al., 2008) (modified) .....	19
Figure 8 Displacement thickness, $\delta^*$ , (m) along the train length for freight consists 1(red), 2 (green), 3 (blue), 4 (black), 5 (cyan) (Soper, 2014). Loading configurations are shown in Figure 9. ....	20
Figure 9 Loading configurations used by Soper (2014) .....	20
Figure 10 Form parameter over the roof and around the side of a 1/25 <sup>th</sup> scale ICE2 (Baker et al., 2001) .....	22
Figure 11 Flow structures obtained using CFD in near wake of the a) CRH2 Chinese passenger train (Huang et al., 2014) and b) the near wake of a simplified ICE2 (Hemida et al., 2012a) .....	23
Figure 12 Normalised longitudinal slipstream velocities for a) two freight consists $y''=1.5$ m and $z'=1$ m (Sterling et al., 2008) .....	26
Figure 13 Peak one second moving averages $y''=1.5$ m ( $z'$ unknown) (Figura-Hardy, 2005)	

Figure 14 Flow regimes around representative street canyons for differing H/W ratios (Oke, 1988) .....	28
Figure 15 Turbulence intensities in the slipstreams of ICE2 and a freight consist on platforms and at trackside (Sterling et al., 2008) (Modified).....	29
Figure 16 Skewed velocity profile relative to a moving vehicle (Dorigatti, 2013) .....	41
Figure 17 Relative yaw angle of crosswind experienced by train for differing train speeds (Baker, 2010) .....	41
Figure 18 Turbulence intensity profile relative to a vehicle moving at differing speeds (Baker, 2010) .....	42
Figure 19 Maximum one second moving average velocities from freight trains 1.5 m from the platform edge (Figura-Hardy, 2005).....	44
Figure 20 Maximum normalised slipstream velocities on the leeward side of a) passenger trains and b) freight trains (Baker et al., 2007) .....	45
Figure 21 Normalised ensemble-averaged slipstream velocities of the S-103 at a) $z=0.2$ m and b) $z=1.2$ m (Baker et al., 2013b) .....	47
Figure 22 Normalised MOSMA velocities from the slipstream of the Velaro S-103 ET (Baker et al., 2013a).....	48
Figure 23 ICE2 model and crosswind generator used in (Baker et al., 2001) .....	49
Figure 24 Horizontal velocities on the leeward side of a model-scale ICE 2 for a) no-crosswind and b) an $11^\circ$ crosswind (Baker et al., 2007) (modified) .....	50
Figure 25 Crosswind $U_h$ – no-crosswind $U_h$ on the leeward side of model-scale ICE2 with crosswind at distances from train side and $z=2.25$ m (Sterling et al. 2008) .....	51
Figure 26 Leeward vortex along the length of an ICE 2 passenger train with a crosswind at $30^\circ$ yaw (Diedrichs, 2003) .....	52
Figure 27 Rolling moments about the leeward rail (Johnson, 2012).....	63
Figure 28 Freight wagon used by Hemida and Baker (2010) and flatliner .....	68
Figure 29 Dimensions of the CAD model of the Class 66 locomotive. ....	72
Figure 30 Numerical (left) and experimental (Soper, 2014) (right) Class 66 locomotive models with four fully-loaded FEA-type B container wagons. ....	73

Figure 31 Dimensions of ISO container model. ....	74
Figure 32 Dimensions of the flatbed wagon. ....	74
Figure 33 Distances of front faces of locomotive and containers from the origin and size of inter-wagon spacings .....	75
Figure 34 Computational domain used for no-crosswind simulations .....	76
Figure 35 Surface mesh on the complex geometry of the Class 66 locomotive and first container wagon. ....	79
Figure 36 Mesh resolution around the Class 66 locomotive on a cut plane at $y=0$ m. ....	80
Figure 37 Time-averaged velocity profile of an idealised 2-D boundary layer: expected profile (black line) and simulated velocity profile in CFD (red line) using coarse mesh (dashed line). ....	81
Figure 38 Computational domain for the crosswind simulations, missing walls are inlets and roof. ....	82
Figure 39 Mesh regions used in the crosswind cases .....	85
Figure 40 One-dimensional control volume .....	87
Figure 41 Schematic diagram of a particle travelling through a one-dimensional mesh over three time-steps and conforming to the CFL condition .....	91
Figure 43 Longitudinal velocity component for the coarse (25 million cells) and fine (34 million cells) meshes. ....	105
Figure 42 Percentage of resolved turbulence kinetic energy around the Freight train at $y=2.34$ m and $z=2$ m. ....	106
Figure 3 Time and ensemble-averaged $C_p$ at $y=1.75$ m and $z=2.25$ m, for the numerical (dashed line) time-average and experimental ensemble average (solid black line) with $\pm 1$ standard deviation of the ensemble in red. ....	107
Figure 4 Time and ensemble-averaged longitudinal components of velocity at $y=1.75$ m and $z=2.25$ m, for the numerical (dashed line) time-average and experimental ensemble average (solid black line) with $\pm 1$ standard deviation of the ensemble in red. ....	107
Figure 46 Instantaneous $U_h$ at the validation at $y=1.75$ and $z=2.25$ m .....	110
Figure 47 $U_h$ at probe position 2 for time-averaged, ensemble-averaged and $\pm 1$ standard deviation from the ensemble-average .....	111

Figure 7 Locations of slipstream measurement at train side relative to COT and TOR.....	112
Figure 8 Locations of slipstream measurement above the roof of the train relative to COT and TOR.....	113
Figure 9 Normalised velocity magnitude, U, at varying distances from COT at a) z=0.25 m, b) z=0.5 m, c) z=1 m, d) z=2 m, e) z=3 m and f) z=4 m.....	114
Figure 10 Time-averaged velocity streamlines projected onto a horizontal cut-plane at z=1 m, coloured by velocity magnitude.....	115
Figure 11 Normalised velocity magnitude, U, at varying distances above TOR at a) y=1.59 m, b) y=1.84 m, c) y=2.34 m and d) y=3.34 m.....	116
Figure 12 Normalised velocity magnitude, U, above the train roof at varying distances from COT at (a) z=4.5 m, (b) z=4.75 m and (c) z=5.0 m.....	117
Figure 54 Upstream and nose region velocity components at y=1.59 m and z=0.25 m.....	119
Figure 14 Velocity components at z=0.25 m above TOR and at a) y=1.59 m, b) y=1.84 m, c) 2.34 m and d) y=3.34 m.....	120
Figure 15 Velocity components at z=0.5 m above TOR and at a) y=1.59 m, b) y=1.84 m, c) 2.34 m and d) y=3.34 m.....	121
Figure 57 Mean velocity magnitude showing locations of sharp double peak at z=0.5 m where black line is sampling location at y=1.59 m (train travelling from right to left).....	122
Figure 58 Longitudinal velocity components on a plane at a) z=0.25 m and b) z=0.5 m.....	122
Figure 18 Velocity components at z=1.0 m above TOR and at a) y=1.59 m, b) y=1.84 m, c) 2.34 m and d) y=3.34 m.....	123
Figure 19 Velocity components at z=2.0 m above TOR and at a) y=1.59 m, b) y=1.84 m, c) 2.34 m and d) y=3.34 m.....	124
Figure 20 Velocity components at z=3.0 m above TOR and at a) y=1.59 m, b) y=1.84 m, c) 2.34 m and d) y=3.34 m.....	125
Figure 21 Velocity components at z=4.0 m above TOR and at a) y=1.59 m, b) y=1.84 m, c) 2.34 m and d) y=3.34 m.....	126
Figure 22 Longitudinal velocity profiles with distance from the side of each container (1, 2, 3 or 4) at a) z=1 m, b) z=2 m and c) z=3 m.....	128

Figure 64 Colour plot of velocity magnitude showing ejections from largest inter-wagon spacing at $z=2$ m for a) $t_1$ and b) $t_2$ .	129
Figure 24 Longitudinal velocity profiles normal to train side at the centre of a) container 1, b) container 2, c) container 3 and d) container 4 at 3 heights above TOR.	130
Figure 66 Designation of inter-wagon spacings	130
Figure 67 Time-averaged streamlines projected on a plane at $y=0$ m coloured by $U$	131
Figure 68 Time-averaged streamlines projected on a plane at half train height coloured by $U$	133
Figure 69 The behaviour of flow in street canyons as functions of $H/W$ and $L/H$ ratios (Oke, 1988)	134
Figure 29 Displacement thickness of the slipstream at mid-height	135
Figure 30 Pressure coefficients at distances from COT and at varying distances above TOR a) $z=0.25$ m, b) $z=0.5$ m, c) $z=1.0$ m, d) $z=2.0$ m, e) $z=3.0$ m and f) $z=4.0$ m	136
Figure 72 Colour contour plot of pressure coefficient on planes at a) $z=1$ m b) $z=2$ m and c) $z=3$ m	138
Figure 32 Mean pressure isosurfaces around the front of the locomotive for $C_p=0.2$ (left) and $C_p=-0.2$ (right), coloured by velocity magnitude	139
Figure 33 Pressure coefficients at distances above TOR and at varying distances from COT (a) $y=1.59$ m, (b) $y=1.84$ m, (c) $y=2.34$ m and (d) $y=3.34$ m	140
Figure 34 Time-averaged velocity vectors on cut planes (coloured by velocity magnitude) at distances above TOR a) $z=0.25$ m, b) $z=0.5$ m, c) $z=1.0$ m, d) $z=2.0$ m, e) $z=3.0$ m and f) $z=4.0$ m	142
Figure 35 Time-averaged velocity vectors on cut planes (coloured by velocity magnitude) at distances from COT, a) $y=0$ m and b) $y=1$ m	143
Figure 36 Isosurfaces of second invariant of the velocity gradient tensor, $Q=50,000$ , coloured by velocity magnitude.	145
Figure 37 Turbulence intensity at distances from the COT and at varying distances above TOR a) $z=0.25$ m, b) $z=0.5$ m, c) $z=1.0$ m, d) $z=2.0$ m, e) $z=3.0$ m and f) $z=4.0$ m	146
Figure 79 Correlation against lag-time for the probe at $y=1.84$ m and $z=2.1$ m for a) $x=21$ m, b) $x=40$ m, c) $x=60$ m and d) $x=80$ m.	149

Figure 80 Force coefficients experienced by the locomotive and each container against loading position.....	154
Figure 81 Force coefficients on a) Class 66 locomotive, b) container 1, c) container 2, d) container 3 and e) container 4.....	155
Figure 82 Horizontal velocity magnitudes at the TSI velocity measurement position (y=3 m, z=0.2 m) with time-averaged velocity (thick black line).....	159
Figure 83 Horizontal velocities with one second moving averages applied at TSI measurement position (y=3 m, z=0.2 m) .....	159
Figure 84 Pressure coefficients on each a) container 1, b) container 2, c) container 3 and d) container 4 at mid-length for fine and coarse meshes.....	162
Figure 85 Sub-grid viscosity ratio, $v_{sgs}/v$ , along train length at half-height at y=2.35 m z=2 m	163
Figure 86 Tap and loop positions a) on the roof of container 3 and b) around the outside ...	164
Figure 87 Pressure coefficients on the third container from numerical and experimental cases (Soper, 2014).....	165
Figure 88 Crosswind component and resultant yaw angle with height above TOR.....	166
Figure 89 Slipstream velocity magnitudes relative to a static observer at a) z=0.25 m, b) z=0.5 m, c) z=1.0 m, d) z=2.0 m, e) z=3.0 m and f) z=4.0 m.....	167
Figure 90 Slipstream velocity magnitudes relative to a static observer varying with height at a) y=1.59 m, b) y=1.84 m, c) y=2.34 m and d) y=3.34 m .....	168
Figure 91 Slipstream velocity magnitudes relative to a static observer at a) z=0.25 m, b) z=0.5 m, c) z=1.0 m, d) z=2.0 m, e) z=3.0 m and f) z=4.0 m.....	169
Figure 92 Velocity magnitude on the leeward side of the passenger train at mid-height (Bowman, 2005) .....	170
Figure 93 Slipstream velocity magnitudes relative to a static observer varying with height at a) y=1.59 m, b) y=1.84 m, c) y=2.34 m and d) y=3.34 m .....	171
Figure 94 Slipstream velocity components at a) =1.59 m, b) y=1.84 m, c) y=2.34 m and d) y=3.34 m .....	172
Figure 95 Slipstream velocity components at a) =1.59 m, b) y=1.84 m, c) y=2.34 m and d) y=3.34 m .....	173

Figure 96 Slipstream velocity components at a) $x=1.59$ m, b) $y=1.84$ m, c) $y=2.34$ m and d) $y=3.34$ m .....	174
Figure 97 Slipstream velocity components at a) $x=1.59$ m, b) $y=1.84$ m, c) $y=2.34$ m and d) $y=3.34$ m .....	175
Figure 98 Slipstream velocity components at a) $x=1.59$ m, b) $y=1.84$ m, c) $y=2.34$ m and d) $y=3.34$ m .....	176
Figure 99 Slipstream velocity components at a) $x=1.59$ m, b) $y=1.84$ m, c) $y=2.34$ m and d) $y=3.34$ m .....	177
Figure 100 Slipstream velocity components at a) $x=1.59$ m, b) $y=1.84$ m, c) $y=2.34$ m and d) $y=3.34$ m .....	179
Figure 101 Colour plots of mean a) longitudinal and b) lateral velocity components on a plane at $z=0.25$ m .....	180
Figure 102 Slipstream velocity components at a) $x=1.59$ m, b) $y=1.84$ m, c) $y=2.34$ m and d) $y=3.34$ m .....	181
Figure 103 Slipstream velocity components at a) $x=1.59$ m, b) $y=1.84$ m, c) $y=2.34$ m and d) $y=3.34$ m .....	182
Figure 104 Slipstream velocity components at a) $x=1.59$ m, b) $y=1.84$ m, c) $y=2.34$ m and d) $y=3.34$ m .....	183
Figure 105 Slipstream velocity components at a) $x=1.59$ m, b) $y=1.84$ m, c) $y=2.34$ m and d) $y=3.34$ m .....	184
Figure 106 Slipstream velocity components at a) $x=1.59$ m, b) $y=1.84$ m, c) $y=2.34$ m and d) $y=3.34$ m .....	185
Figure 107 Pressure coefficients, $C_p$ , on the windward side of the freight train at a) $z=0.25$ m, b) $z=0.5$ m, c) $z=1.0$ m, d) $z=2.0$ m, e) $z=3.0$ m and f) $z=4.0$ m .....	186
Figure 108 Pressure coefficient, $C_p$ , windward varying with height at a) $y=1.59$ m, b) $y=1.84$ m, c) $y=2.34$ m and d) $y=3.34$ m .....	187
Figure 109 Pressure coefficient, $C_p$ , downwind of the freight train at a) $z=0.25$ m, b) $z=0.5$ m, c) $z=1.0$ m, d) $z=2.0$ m, e) $z=3.0$ m and f) $z=4.0$ m .....	188
Figure 110 Pressure coefficient, $C_p$ , downwind varying with height at a) $y=1.59$ m, b) $y=1.84$ m, c) $y=2.34$ m and d) $y=3.34$ m .....	189

Figure 111 Surface streamlines on the roof of containers, coloured by $C_p$ .....	190
Figure 112 Isosurfaces of pressure ( $C_p = -0.6$ ), coloured by velocity magnitude .....	191
Figure 113 Pressure isosurface ( $C_p = -0.6$ ) coloured by velocity magnitude .....	191
Figure 114 Time-averaged velocity streamlines showing leeward vortices for present case (left) and ICE2 at $30^\circ$ (right) (Diedrichs, 2003) .....	192
Figure 115 Surface-pressure coefficients on windward, roof and lee-sides for containers a) 1, b) 2, c) 3 and d) 4 at 25% (green), 50% (purple) and 75% (blue) along each container .....	193
Figure 116 Time-averaged streamlines projected on a plane at half train height coloured by velocity magnitude .....	194
Figure 117 Time-averaged streamlines projected on a plane at $y=0$ m coloured by velocity magnitude .....	195
Figure 118 Plane at $z=2$ m coloured by pressure coefficient showing the pressure around the second container .....	196
Figure 119 Force coefficients experienced by each container and rolling moment experienced by each entire wagon against loading position .....	201
Figure 120 Isosurfaces of the second invariant of the velocity gradient tensor, $Q=50,000$ , coloured by velocity magnitude .....	203
Figure 121 Force coefficients on a) class 66 locomotive, b) container 1, c) container 2, d) container 3 and e) container 4 .....	205
Figure 122 Turbulence intensity on the windward side of the freight train at a) $z=0.25$ m, b) $z=0.5$ m, c) $z=1.0$ m, d) $z=2.0$ m, e) $z=3.0$ m and f) $z=4.0$ m .....	206
Figure 123 Pressure coefficients on each a) container 1, b) container 2, c) container 3 and d) container 4 at mid-length for fine and coarse meshes .....	211
Figure 124 Ratio of sub-grid to kinematic viscosity on the leeward side of the train at $y=2.35$ m and $z=2$ m .....	212
Figure 125 Normalised velocity magnitude relative to a static observer at a) $z=0.25$ m, b) $z=0.5$ m, c) $z=1.0$ m, d) $z=2.0$ m, e) $z=3.0$ m and f) $z=4.0$ m .....	213
Figure 126 Normalised velocity magnitude relative to a static observer varying with height at a) $y=1.59$ m, b) $y=1.84$ m, c) $y=2.34$ m and d) $y=3.34$ m .....	214

Figure 127 Colour plot of normalised velocity magnitude around the train at $z=2$ m. The black line represents the $y=3.34$ m sampling location.....	214
Figure 128 Normalised velocity magnitude relative to a static observer at a) $z=0.25$ m, b) $z=0.5$ m, c) $z=1.0$ m, d) $z=2.0$ m, e) $z=3.0$ m and f) $z=4.0$ m.....	215
Figure 129 Colour plots of normalised velocity magnitude at a) $z=0.25$ m and b) $z=0.5$ m. The black line is $y=1.59$ m from COT.....	217
Figure 130 Normalised velocity magnitude relative to a static observer varying with height at a) $y=1.59$ m, b) $y=1.84$ m, c) $y=2.34$ m and d) $y=3.34$ m .....	217
Figure 131 Normalised velocity components at a) $y=1.59$ m, b) $y=1.84$ m, c) $y=2.34$ m and d) $y=3.34$ m.....	218
Figure 132 Normalised velocity components at a) $y=1.59$ m, b) $y=1.84$ m, c) $y=2.34$ m and d) $y=3.34$ m.....	219
Figure 133 Normalised velocity components at a) $y=1.59$ m, b) $y=1.84$ m, c) $y=2.34$ m and d) $y=3.34$ m.....	220
Figure 134 Normalised velocity components at a) $y=1.59$ m, b) $y=1.84$ m, c) $y=2.34$ m and d) $y=3.34$ m.....	221
Figure 135 Colour plot of longitudinal velocity component around first container wagon on a plane at $z=2$ m.....	222
Figure 136 Normalised velocity components at a) $y=1.59$ m, b) $y=1.84$ m, c) $y=2.34$ m and d) $y=3.34$ m.....	222
Figure 137 Normalised velocity components at a) $y=1.59$ m, b) $y=1.84$ m, c) $y=2.34$ m and d) $y=3.34$ m.....	223
Figure 138 Normalised velocity components at a) $y=1.59$ m, b) $y=1.84$ m, c) $y=2.34$ m and d) $y=3.34$ m.....	224
Figure 139 Normalised velocity components at a) $y=1.59$ m, b) $y=1.84$ m, c) $y=2.34$ m and d) $y=3.34$ m.....	225
Figure 140 Mean velocity streamlines projected onto a colour plot of pressure coefficient, $C_p$ , at $x=12$ m .....	226
Figure 141 Normalised velocity components at a) $y=1.59$ m, b) $y=1.84$ m, c) $y=2.34$ m and d) $y=3.34$ m.....	226

Figure 142 Normalised velocity components at a) $y=1.59$ m, b) $y=1.84$ m, c) $y=2.34$ m and d) $y=3.34$ m .....	227
Figure 143 Normalised velocity components at a) $y=1.59$ m, b) $y=1.84$ m, c) $y=2.34$ m and d) $y=3.34$ m .....	228
Figure 144 Normalised velocity components at a) $y=1.59$ m, b) $y=1.84$ m, c) $y=2.34$ m and d) $y=3.34$ m .....	229
Figure 145 Pressure coefficients relative to a static observer at a) $z=0.25$ m, b) $z=0.5$ m, c) $z=1.0$ m, d) $z=2.0$ m, e) $z=3.0$ m and f) $z=4.0$ m .....	230
Figure 146 Pressure coefficients relative to a static observer varying with height at a) $y=1.59$ m, b) $y=1.84$ m, c) $y=2.34$ m and d) $y=3.34$ m .....	231
Figure 147 Pressure coefficients relative to a static observer at a) $z=0.25$ m, b) $z=0.5$ m, c) $z=1.0$ m, d) $z=2.0$ m, e) $z=3.0$ m and f) $z=4.0$ m .....	232
Figure 148 Pressure isosurface ( $C_p=-0.7$ ) coloured by mean velocity magnitude.....	233
Figure 149 Pressure coefficients relative to a static observer varying with height at a) $y=1.59$ m, b) $y=1.84$ m, c) $y=2.34$ m and d) $y=3.34$ m .....	233
Figure 150 Isosurface of pressure coefficient ( $C_p=-0.3$ ) around the locomotive, coloured by velocity magnitude.....	234
Figure 151 Longitudinal vortices on the leeward side of the train .....	235
Figure 152 Streamlines projected onto a plane at mid-height showing regions of flow reattachment, coloured by velocity magnitude .....	235
Figure 153 Surface-pressure coefficients on windward, roof and lee-sides for containers a) 1, b) 2, c) 3 and d) 4 at 25% (green), 50% (purple) and 75% (blue) along each container .....	236
Figure 154 Pressure isosurfaces ( $C_p=-0.15$ ) showing roll vortices on the roofs of containers 1 and 2.....	237
Figure 155 Mean streamlines projected on colour plot of velocity magnitude at mid-height for inter-wagon spacings a) 1, b) 2, c) 3 and d) 4.....	238
Figure 156 Mean streamlines projected on colour plot of velocity magnitude at COT for inter-wagon spacings a) 1, b) 2, c) 3 and d) 4 .....	239

Figure 157 Time-averaged and ensemble-mean normalised horizontal slipstream velocities, $U_h$ , on the leeward side of the freight train in the present work and the ICE2 (Baker et al., 2001) at a) 1 m and b) 2m from train side at $z=2.25$ m .....	240
Figure 158 Time-averaged and ensemble-mean horizontal velocities, $U_h$ , on the leeward side of the freight train in the present work and the ICE2 (Baker et al., 2001) at a) 1 m and b) 2m from train side at $z=2.25$ m .....	241
Figure 159 Force and moment coefficients experienced by the locomotive, containers and wagons against loading position .....	245
Figure 160 Isosurfaces of the second invariant of the velocity gradient tensor, $Q=50,000$ , coloured by velocity magnitude.....	247
Figure 161 Turbulence intensity on the windward side of the freight train at a) $z=0.25$ m, b) $z=0.5$ m, c) $z=1.0$ m, d) $z=2.0$ m, e) $z=3.0$ m and f) $z=4.0$ m.....	249
Figure 162 Vortices generated around the rear windward side of the last container wagon. Isosurfaces of $Q=50,000$ , coloured by velocity magnitude. ....	249
Figure 163 Instantaneous force coefficients for a) class 66 locomotive, b) container 1, c) container 2, d) container 3 and e) container 4.....	252
Figure 164 Horizontal velocity magnitudes at the TSI velocity measurement position ( $y=3$ m, $z=0.2$ m) with time-averaged velocity (thick black line).....	253
Figure 165 Maximum (purple), minimum (green) and the difference (blue) instantaneous horizontal velocities .....	254
Figure 166 Instantaneous pressures at $y=2.5$ m and $z=3.3$ m .....	255
Figure 167 Slipstream velocity magnitudes relative to a static observer at $z=0.5$ m at a) $y=1.59$ m, b) $y=1.84$ m, c) $y=2.34$ m and d) $y=3.34$ m for the no-crosswind, $10^\circ$ and $30^\circ$ crosswind cases on the windward side of the train .....	259
Figure 168 Slipstream velocity magnitudes relative to a static observer at $z=2$ m at a) $y=1.59$ m, b) $y=1.84$ m, c) $y=2.34$ m and d) $y=3.34$ m for the no-crosswind, $10^\circ$ and $30^\circ$ crosswind cases on the windward side of the train .....	260
Figure 169 Slipstream velocity magnitudes relative to a static observer at $z=4$ m at a) $y=1.59$ m, b) $y=1.84$ m, c) $y=2.34$ m and d) $y=3.34$ m for the no-crosswind, $10^\circ$ and $30^\circ$ crosswind cases on the windward side of the train .....	261

Figure 170 Slipstream velocity magnitudes relative to a static observer at $z=0.5$ m at a) $y=1.59$ m, b) $y=1.84$ m, c) $y=2.34$ m and d) $y=3.34$ m for the no-crosswind, $10^\circ$ and $30^\circ$ crosswind cases on the leeward side of the train .....	262
Figure 171 Slipstream velocity magnitudes relative to a static observer at $z=2$ m at a) $y=1.59$ m, b) $y=1.84$ m, c) $y=2.34$ m and d) $y=3.34$ m for the no-crosswind, $10^\circ$ and $30^\circ$ crosswind cases on the leeward side of the train.....	263
Figure 172 Slipstream velocity magnitudes relative to a static observer at $z=4$ m at a) $y=1.59$ m, b) $y=1.84$ m, c) $y=2.34$ m and d) $y=3.34$ m for the no-crosswind, $10^\circ$ and $30^\circ$ crosswind cases on the leeward side of the train.....	265
Figure 173 Time-averaged velocity magnitude at $z=0.5$ m .....	266
Figure 174 Time-averaged velocity profiles at $z=2$ m.....	267
Figure 175 Time-averaged velocity profiles at $z=4$ m.....	268
Figure 176 Instantaneous velocity magnitudes relative to a static observer at $z=2$ m and $y=1.59$ m for the no-crosswind, $10^\circ$ and $30^\circ$ crosswind cases on the leeward side of the train 269	
Figure 177 Instantaneous velocity magnitudes relative to a static observer at $z=2$ m and $y=1.84$ m for the no-crosswind, $10^\circ$ and $30^\circ$ crosswind cases on the leeward side of the train 270	
Figure 178 Instantaneous velocity magnitudes relative to a static observer at $z=2$ m and $y=2.34$ m for the no-crosswind, $10^\circ$ and $30^\circ$ crosswind cases on the leeward side of the train 271	
Figure 179 Instantaneous velocity magnitudes relative to a static observer at $z=2$ m and $y=3.34$ m for the no-crosswind, $10^\circ$ and $30^\circ$ crosswind cases on the leeward side of the train 272	
Figure 180 Slipstream pressure coefficients relative to a static observer at $z=0.5$ m at a) $y=1.59$ m, b) $y=1.84$ m, c) $y=2.34$ m and d) $y=3.34$ m for the no-crosswind, $10^\circ$ and $30^\circ$ crosswind cases on the windward side of the train .....	273
Figure 181 Slipstream pressure coefficients relative to a static observer at $z=2$ m at a) $y=1.59$ m, b) $y=1.84$ m, c) $y=2.34$ m and d) $y=3.34$ m for the no-crosswind, $10^\circ$ and $30^\circ$ crosswind cases on the windward side of the train .....	274

Figure 182 Slipstream pressure coefficients relative to a static observer at $z=4$ m at a) $y=1.59$ m, b) $y=1.84$ m, c) $y=2.34$ m and d) $y=3.34$ m for the no-crosswind, $10^\circ$ and $30^\circ$ crosswind cases on the windward side of the train .....	275
Figure 183 Slipstream pressure coefficients relative to a static observer at $z=0.5$ m at a) $y=1.59$ m, b) $y=1.84$ m, c) $y=2.34$ m and d) $y=3.34$ m for the no-crosswind, $10^\circ$ and $30^\circ$ crosswind cases on the leeward side of the train .....	276
Figure 184 Time-averaged pressure isosurfaces ( $C_p=-0.3$ ) around the locomotive, coloured by velocity magnitude for the a) no-crosswind, b) $10^\circ$ crosswind and c) $30^\circ$ crosswind cases ..	277
Figure 185 Slipstream pressure coefficients relative to a static observer at $z=2$ m at a) $y=1.59$ m, b) $y=1.84$ m, c) $y=2.34$ m and d) $y=3.34$ m for the no-crosswind, $10^\circ$ and $30^\circ$ crosswind cases on the leeward side of the train.....	278
Figure 186 Slipstream pressure coefficients relative to a static observer at $z=4$ m at a) $y=1.59$ m, b) $y=1.84$ m, c) $y=2.34$ m and d) $y=3.34$ m for the no-crosswind, $10^\circ$ and $30^\circ$ crosswind cases on the leeward side of the train.....	279
Figure 187 Colour plot of time-averaged pressure at $z=0.5$ m .....	280
Figure 188 Colour plot of time-averaged pressure at $z=2$ m .....	281
Figure 189 Colour plot of time-averaged pressure at $z=4$ m .....	282
Figure 190 Instantaneous pressure transient magnitudes (blue) for $y=1.59$ m and $z=2$ m with mean values (red).....	283
Figure 191 Instantaneous pressure transient magnitudes (blue) for $y=1.84$ m and $z=2$ m with mean values (red).....	283
Figure 192 Instantaneous pressure transient magnitudes (blue) for $y=2.34$ m and $z=2$ m with mean values (red).....	284
Figure 193 Instantaneous pressure transient magnitudes (blue) for $y=3.34$ m and $z=2$ m with mean values (red).....	285
Figure 194 Drag force coefficient against loading position for the no-crosswind (blue), $10^\circ$ crosswind (red) and $30^\circ$ crosswind (green) cases .....	286
Figure 195 Side force coefficient against loading position for the no-crosswind (blue), $10^\circ$ crosswind (red) and $30^\circ$ crosswind (green) cases .....	287

Figure 196 Lift force coefficient against loading position for the no-crosswind (blue), 10° crosswind (red) and 30° crosswind (green) cases .....	287
Figure 197 Cuboid subjected to a wind-induced load in original and displaced positions....	292
Figure 198 Mass-spring-damper stability model of person .....	294
Figure 199 Wind speed profiles generated in the wind tunnel (Jordan et al., 2008) .....	294
Figure 200 Instantaneous velocities from Chapter 4 at y=3 m and z=2 m (black) and Jordan (2008) (red) .....	296
Figure 201 Instantaneous velocities at y=3 m and z=2 m.....	298
Figure 202 Height and weight of randomly-generated people in the mathematical model...	300
Figure 203 Distribution of heights and weights for persons used in wind tunnel experiments (Penwarden et al., 1978) .....	300
Figure 204 Percentage chance of person instability against distance from train side for the no-crosswind, 10° and 30° crosswind cases, yellow line is positioned at y=2.95 m.....	305

## List of symbols

$b$  – cube half-width

$\widetilde{S}_{ij}$  – filtered rate-of-strain tensor

$\widetilde{\Delta}$  - filter cut-off width

$\bar{S}$  – characteristic filtered rate of strain

$k_r$  – kinetic energy of the residual components

$\bar{u}(x)$  – normalised ensemble-averaged velocity

$u_r(x)$  – normalised velocity signal for a single run

$A_{\text{ref}}$  – reference area (10 m<sup>2</sup>)

ABL – atmospheric boundary layer

$A_{\text{Du}}$  – Dubois area

$w_p$  – weight of person (N)

$h_p$  – height of person (m)

$C_d, C_s, C_l$  – drag, side and lift force coefficients

$a_e$  and  $a_w$  – neighbour cell coefficients

$C_{\text{DES}} = 0.65$

$C_F$  – force coefficient

$C_M$  – moment coefficient

$C_p$  – pressure coefficient

$C_s$  – Smagorinsky constant (0.07)

$D$  – diffusion coefficient (m<sup>2</sup>s<sup>-1</sup>)

$d$  – nodal distance to the nearest wall

$e, w$  – east and west of cell

$F$  – force (N)

$H$  – locomotive height (m)

$H_f$  – form parameter

$I$  - Turbulence intensity

$L$  – reference length (3 m)  
 $l_0$  – scale of flow  
 $L_c$  – characteristic cell length (m)  
 $l_s$  – Smagorinsky length scale  
 $Lx$  – turbulence length-scale (m)  
 $n$  – total size of ensemble  
 $p$  – static pressure (Pa)  
 $p_0$  – ambient pressure (Pa)  
 $Pe$  – Péclet number  
 $r$  – run number  
 $t$  – time (s)  
 $t^*$  – convective time  
 $Re$  – Reynolds number  
 $Re_{\max}$  – maximum Reynolds number  
 $Re_{\min}$  – minimum Reynolds number  
 $S$  – source term  
 $St$  – Strouhal number  
 $U$  – normalised velocity magnitude  
 $u(x)$  – normalised longitudinal velocity at longitudinal position  
 $u_*$  – friction velocity (m/s)  
 $u, v$  and  $w$  – longitudinal, lateral and vertical velocity  
 $u_{2\sigma}$  – TSI limiting velocity  
 $u_{2\sigma_{wt}}$  – TSI limiting velocity in wind tunnel  
 $U_c$  – velocity in cell ( $\text{ms}^{-1}$ )  
 $U_h$  – horizontal velocity  
 $U_{\text{mean}}$  – mean of instantaneous peak values  
 $V$  – cell volume ( $\text{m}^3$ )

$u_r$  – resultant velocity  
 $u_{\text{train}}$  – train speed (m/s)  
 $X$  – distance behind train (m)  
 $x$  – longitudinal distance from front face of train (m)  
 $y_d$  – distance from wall DDES  
 $y$  – lateral position from centre of track (m)  
 $y'$  – lateral distance from train side (m)  
 $y''$  – lateral distance from platform edge (m)  
 $y^+$  – non-dimensional wall distance  
 $z$  – vertical position from top of rail (m)  
 $z_0$  – roughness length (m)  
 $\Delta C_p$  – peak-to-peak pressure transient  
 $\Delta P_{2\sigma}$  – TSI limiting pressure value  
 $G(\dots)$  - filter function

## **Abbreviations**

ATM – aerodynamic train model  
CAD – computer-aided design  
CD – central differencing  
CFD – computational fluid dynamics  
CFL - Courant-Friedrichs-Lewy number  
COT – centre of track  
CWG – crosswind generator  
DES – detached-eddy simulation  
DDES – delayed detached-eddy simulation  
DMD - dynamic mode decomposition  
HST – high speed train  
IDDES - improved delayed detached-eddy simulation  
LES – large-eddy simulation

LEVM – linear eddy-viscosity model  
NLEVM – non-linear eddy-viscosity model  
POD - proper-orthogonal decomposition  
RANS – Reynolds-averaged Navier-Stokes  
RNG – renormalised group  
TOR – top of rail  
TSI – technical specification for interoperability

### **Greek symbols**

$\phi(\acute{x}, t)$  – unfiltered function

$\bar{\phi}(x, t)$  – filtered function

$\sigma_u(x)$  – standard deviation of the normalised velocity

$\sigma_{TSI}$  – standard deviation of peak one-second filtered values

$u_\tau$  – friction velocity (m/s)

$\delta_{ij}$  – Kronecker delta function

$\nu_t$  – eddy-viscosity

$\tilde{\nu}$  – viscosity-like term

$\Delta$  – chosen grid spacing

$\delta^*$  - displacement thickness (m)

$\eta$  – Kolmogorov micro-scale (m)

$\theta$  – yaw angle (degrees)

$\theta_M$  – momentum thickness (m)

$\kappa$  – Karman constant ( $\approx 0.41$ )

$\mu$  – dynamic viscosity ( $\text{kg m}^{-1}\text{s}^{-1}$ )

$\nu_r$  – eddy-viscosity of the residual motions

$\rho_\infty$  – freestream density ( $\text{kg/m}^3$ )

$\tau_w$  – wall shear stress ( $\text{N/m}^2$ )

$\phi$  – transported quantity

$\Psi(r)$  – Sweby limiter

# Chapter 1 Introduction

## 1.1 *Outline of studies*

This work consists of results obtained from numerical simulations which were conducted in order to investigate the effect of crosswinds on the slipstream of a model-scale freight train. This thesis draws on research from previously-conducted physical experiments for validation, as well as a mathematical model which predicts a human's response to a wind gust.

Results from the slipstream simulation without a crosswind applied were published in the *Journal of Wind Engineering and Industrial Aerodynamics* (Appendix A). Initial results concerning the effect of crosswinds on the slipstream properties around the train are collated in conference papers which were presented at the 11th UK Conference on Wind Engineering in Birmingham and the 6th International Symposium on Computational Wind Engineering in Hamburg.

A separate piece of work conducted by the author was the production of a report documenting a finite-element method consultancy project in which the design of a new track stretcher bar was tested for multiple train weights and track configurations for Network Rail.

## 1.2 *Research background*

When a train moves through the air it generates a slipstream which, to a static observer, appears as a gradually-building gust punctuated by pressure and velocity transients. The concept of a slipstream is well known by the general public and is colloquially referred to as 'air turbulence'. In recent years, the drive for faster trains has led to an increased risk of person instability because slipstream velocities increase approximately with train speed and hence faster trains produce higher slipstream velocities. Considering that the force experienced by an object subjected to a wind increases nearly proportionally with the square

of the resultant velocity, any increase in train speed can drastically increase the forces experienced by a person in close proximity to a train.

The study of train slipstreams has largely been directed towards high speed passenger trains, although these vehicles are generally very streamlined to reduce drag and hence the air which is locally deformed when the train passes through it is minimised. The contrary is the case for freight trains where geometries are generally bluffer making them responsible for thicker slipstreams and thus higher slipstream velocities are obtained for given distances from train side than would be from faster-travelling passenger trains (Pope, 2006).

Reports documenting the effect of train slipstreams on trackside infrastructure, people and objects on platforms, over a three decade period showed that train slipstreams have the potential to pose a safety threat. Incidents include empty pushchairs being moved into passing trains causing them to be destroyed and on one occasion a person's jacket was caught by the slipstream of a passing train and the person was subsequently spun around causing a whiplash-like injury (Pope, 2006). These incidents are fairly minor and so far there have been no fatalities on the UK rail network, however there is the potential for fatalities to occur. In Germany, an infant was killed when their pushchair was pulled towards an Inter-City Express 2 train passing through a station (Pope, 2006). Such incidents are expensive financially due to compensation costs but also have further implications on the reputation on the rail network which could affect it as a business.

Full-scale data suggest that when train slipstreams are subjected to ambient winds, an increase in slipstream properties can be observed on the leeward side which is hypothesised to be a result of the slipstream being convected to the leeward side of the train (Baker et al., 2007). The rate of increase in slipstream velocities with resultant yaw angle has been shown to be greater for freight trains than for passenger trains although due to the scarcity of this

data the effect of crosswinds on the slipstreams of freight trains at full-scale is poorly understood due to the range of vehicles which operate on the rail networks which all have unique aerodynamic characteristics.

Under the current Technical Specification for Interoperability (TSI) (2008) and European Norm (CEN, 2011), there are no limits for the slipstream velocities which a freight train can generate. Recent work has shown that the slipstream velocities produced by some freight trains with low loading efficiencies border on the maximum values allowed for high speed passenger trains (Soper et al., 2014). It is anticipated that these limits will be violated by even moderate ambient winds, considering the previously-observed behaviour of slipstreams in crosswinds (Baker et al., 2007, Baker et al., 2013b, Baker et al., 2013a).

A recent study collated data which showed that even at yaw angles ( $\theta < 1.5^\circ$ ) the effect of the crosswinds on the slipstream of a high speed passenger was significant for both ensemble-averaged, and peak one second moving-average velocities (Baker et al., 2013a, 2013b). With the effects of slipstream amplification apparent but difficult to quantify, the potential risk associated with slipstream amplification may have implications for the safety of persons in close proximity to the train. Furthermore, the lack of consideration of this effect in the current codes of practice allows for the designs of rolling stock which fail to mitigate, or even intensify this effect.

Investigating how crosswinds affect train slipstreams is difficult to achieve at full-scale because of the variability of ambient winds, however approaches such as numerical and physical modelling offer controlled environments in which to carry out such experiments. Numerical modelling has the main advantage of providing vast amounts of data from a single simulation which would otherwise require lengthy physical experiments to obtain. Numerical simulations have proved an effective tool for crosswind assessment and slipstream

calculation of trains (Diedrichs et al., 2007, Diedrichs, 2003, Golovanevskiy et al., 2012, Bouferrouk et al., 2012, Hemida and Baker, 2010, Hemida and Krajnovic, 2005, Hemida et al., 2012a, Huang et al., 2014, Pii et al., 2014). This being said, numerical simulations must be validated against physical experiments in order to prove that the numerical model produces physical results; therefore the two methods are most effective when used in unison.

The current available literature shows that in general, freight trains produce larger slipstream velocities than passenger trains for a given train speed. It is also known from full-scale experiments that the rate of increase of slipstream velocity with yaw angle is greater for freight trains than for passenger trains; however the data on this subject are sparse. Therefore to provide the literature with more data, and move towards a consensus on the subject, the current work uses numerical simulations to investigate the effect of crosswinds on the slipstream of a model-scale freight train. The potential effect of the slipstream amplification caused by the crosswinds on the stability of persons in close proximity to the train is also considered and provides context to the results, giving motivation for the inclusion of crosswind-affected slipstream in the codes of practice.

### *1.3 Aims and objectives*

#### **Research Aim**

The main aim of the research presented in this thesis is to investigate the effect of crosswinds on the slipstream of a model-scale freight train and predict possible consequences on persons within close proximity.

The following objectives have been set to achieve this aim:

- Conduct and validate numerical simulations of a model-scale Class 66 locomotive-hauled freight train subjected to no crosswind, 10° and 30° crosswinds in order to determine their effect on the slipstream of the train
- Use slipstream velocities obtained from the numerical simulations as inputs to spring-mass-damper model in order to predict effect of slipstream amplification on the stability of a randomly-generated representative sample of the population

## 1.4 *Structure of thesis*

This thesis is laid out as follows:

- In Chapter 2 the relevant literature concerning freight and passenger train slipstreams is discussed and a brief introduction to the basic concepts of computational fluid dynamics (CFD) are presented which gives context later when considering the application of CFD in train aerodynamics. Model- and full-scale experiments which investigate how winds affect train slipstreams are discussed and also the aerodynamic loading of passenger and freight trains is considered. A review of the current knowledge regarding the effect of winds on the stability of persons is also given.
- Chapter 3 contains a description of the full computational methodology used to undertake this work with specific focus on turbulence modelling as well as a discussion of the assumption made and limitations of CFD.
- Chapter 4 presents results from the simulation of the flow around the freight train when travelling in ambient conditions i.e. where no crosswind is present. The solution is verified both in terms of validation against physical experiment as well as by mesh sensitivity testing. Instantaneous and time-averaged pressures and velocities from positions within the slipstream are presented and the assumption of the

appropriateness of directly comparing ensemble-averaged data to time-averaged data is also tested. The conformance of the train's slipstream to the current safety standard limits was also assessed and the force coefficients on the locomotive and each container are given.

- Chapter 5 presents the results and validation from the first crosswind simulation at 30° yaw. The solution is verified by against physical experiment and mesh sensitivity; levels of sub-grid viscosity are also tested due to the high strain-rates which occur in recirculation in the wake and have the potential to have a detrimental effect on the results. The time-averaged velocity and pressure fields on the windward and leeward sides of the train are investigated as well as the mean and instantaneous forces on the locomotive and container wagons.
- Chapter 6 presents an analysis of the slipstream when the freight train is subjected to a 10° crosswind which was nearly-identical to that performed for the 30° crosswind case.
- In chapter 7 slipstream properties and force coefficients from all cases are directly compared in order to provide some insight into the effect of crosswinds on the slipstream of a freight train and for the first time, instantaneous velocities and pressures are considered.
- Chapter 8 presents the application of a previously-developed spring-mass-damper model of human response to a wind gust. The chapter gives an insight into the potential effect of slipstream amplification on the stability of a representative sample of the population standing in close proximity to a passing train as well as pushchair movement.

- In chapter 9 conclusions are drawn and recommendations for future work are made based on the findings in the preceding chapters.

# Chapter 2 Literature Review

## 2.1 *Introduction*

The present chapter contains an overview of the literature concerning the aerodynamics of trains, with a specific focus towards the slipstreams of freight trains. The majority of the research presented in this thesis is conducted using numerical modelling and so some fundamental considerations of the workings of CFD, as well as previous applications in the fields of train and bluff-body aerodynamics, will also be performed in Section 2.2. A review of the behaviour of model- and full-scale passenger and freight train slipstreams is conducted in Section 2.3 and the data concerning the effect of crosswinds on train slipstreams are examined in Section 2.6. A general discussion of the behaviour of persons subjected to wind gusts is conducted in Section 2.7 and a review of the aerodynamic loading of freight trains is performed in Section 2.8.

## 2.2 *The application of computational fluid dynamics modeling to train aerodynamics*

Computational fluid dynamics is used in this thesis to investigate the effect of crosswinds on the slipstream of a model-scale freight train. CFD is a tool which numerically solves the governing equations of fluid dynamics for flow variables such as pressure and velocity with given boundary conditions in a prescribed computational domain. CFD has developed from its earliest form which assumed inviscid, incompressible and irrotational flow (Hess and Smith, 1967) to become a versatile method of predicting fluid flows for a wide range of applications.

Nearly every flow of engineering interest is turbulent in nature, that is to say the flow is characterised by an apparently-random and chaotic motion. To solve the Navier-Stokes equations directly for a turbulent flow is incredibly costly because of the large range of

turbulent scales which must be accounted for. The smallest turbulent scales within a flow have very high frequencies and as such require very small time-steps to capture their behaviour which is extremely computationally expensive. This method of CFD is called direct numerical simulation (DNS) and is usually reserved for fundamental research problems at low Reynolds numbers. To overcome the challenges of resolving turbulence directly, the Navier-Stokes equations are often time-averaged and therefore are used to calculate the mean flow behaviour; this method of CFD simulation is known as the Reynolds-Averaged Navier-Stokes (RANS) approach.

The difficulty in obtaining accurate solutions using RANS lies in the prediction of the mean flow, because during the time-averaging procedure a turbulent stress tensor, known as the Reynolds stress tensor, is produced. The Reynolds stress tensor represents the effect of the turbulent fluctuations on the mean flow and is a crucial aspect of time-averaged simulations. Turbulence models are used to model the Reynolds stress tensor generally fall into two categories: eddy-viscosity and Reynolds-stress models. At present there is no universal turbulence model and therefore models are applied based on either previous experience or by comparison to similar cases in the literature.

With the ever-increasing affordability of computational power, CFD is quickly becoming a popular and affordable method of assessing the aerodynamic characteristics of a vehicle. Methods such as large-eddy simulation (LES) resolve the larger turbulent scales within a flow whereas the smaller-scales, which have little effect on the overall flow, are modelled using a type of eddy-viscosity model known as a sub-grid model. LES is significantly more computationally expensive than the more commonly-used RANS methods, although because the majority of the turbulence is directly resolved the results obtained are generally more accurate.

CFD has been applied to all facets of train aerodynamics such as slipstream analysis (Huang et al., 2014, Hemida et al., 2012a), crosswind loading assessment (Hemida and Krajnovic, 2005, 2005, Diedrichs, 2003, Diedrichs et al., 2007), tunnel aerodynamics (Ogawa and Fujii, 1997) and ballast flight and under body flow (Saussine et al., 2013, García et al., 2011). The application of CFD to each relevant aerodynamic topic in this literature review will be discussed in the applicable subsections below.

## **2.3 Slipstreams**

### **2.3.1 Preliminaries**

The locations at which slipstream measurements are taken can vary between studies depending on the purpose, and country of origin, of the research. A schematic of the positions of the different reference frames used in this work is shown in Figure 1.

The origin in the longitudinal direction ( $x$ ) is taken as the front of the train in question and is positive along train length. Trackside measurements are usually made relative to the centre of track (COT) for lateral ( $y$ ) positions and top of rail (TOR) for vertical ( $z$ ) positions. For platform measurements, the lateral reference ( $y'$ ) will be train side or platform edge ( $y''$ ) and the vertical reference ( $z'$ ) will be height above platform.

In the present work, COT and TOR will be considered as the primary reference frame for trackside measurements in accordance with CEN (2011).

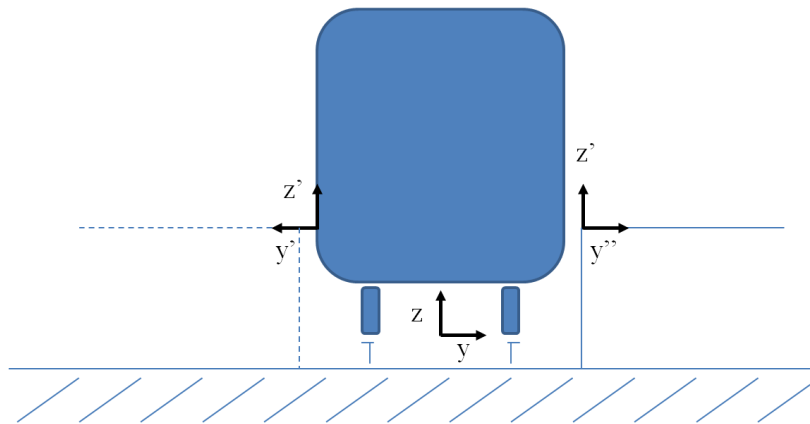


Figure 1 Schematic of slipstream measurement coordinate systems for trackside and platform measurements.

## 2.4 *Slipstream-induced accidents*

When a train moves through the air there is a region of air that moves along with the train at approximately the same speed: this region of air is called the ‘slipstream’. The concept of a slipstream is well known by the general public and is colloquially referred to as ‘air turbulence’ on station platforms in the form of audible announcements and signs (Figure 2).



Figure 2 Sign on a station platform warning passengers to keep clear of the platform edge because of possible train slipstream effects (© www.geograph.org.uk)

Throughout the world, there is a trend of increasing train speeds and although high speed rail in the UK is limited to 200 km/h, nations such as China, Japan and France are currently operating high-speed trains (HST) at speeds as high as 320 km/h. With higher train speeds come associated aerodynamic effects which would be otherwise negligible at lower speeds such as those for slower commuter trains.

Aerodynamic forces increase with the square of the resultant velocity vector thus increases in train speed can cause significant increases in the forces experienced by objects subjected to a train's slipstream. Between 1972 and 2005 there were 26 reported slipstream-induced incidents on the UK rail network; these incidents included movement of trackside equipment, pushchairs and luggage (Pope, 2006). So far there have been no fatalities due to slipstream-induced incidents on the UK rail network; however this is not the case in Germany where an infant's pushchair was moved by the slipstream of an Inter-City Express (ICE) passenger train and the child was subsequently killed (Pope, 2006).

Injuries or deaths on a rail network are disruptive to services and have the potential to damage the reputation of the railway and consequently affect it as a business. To avoid such incidents and restrict the aerodynamic loads experienced by people, limiting values of slipstream velocities and pressures generated by trains are placed on new train designs entering service (TSI, 2008, CEN, 2011). By applying these limits it is ensured that the likelihood of a person becoming injured or killed as a result of a train's slipstream is as low as reasonably possible.

## *2.5 Characteristic features of train slipstreams*

Relative to a static observer, train slipstreams are highly-turbulent non-stationary flows punctuated by pressure and velocity transients. The pressure and velocity transients are caused by the nose and tail of a train but also by geometric discontinuities on the trains such as bogies and inter-carriage spacings. These features are necessary for train operation and occur in one form or another even for very streamlined trains.

Passenger trains commonly travel at speeds greater than 160 km/h and are often streamlined to reduce their drag which in turn reduces their energy consumption. Freight trains on the UK rail network are restricted to a maximum line speed of 120 km/h (33 m/s) and therefore

generally travel at much lower speeds than passenger trains which have operational speeds of up to 200 km/h (56 m/s). Because aerodynamic drag is nearly proportional to the square of velocity it is regarded as a less significant factor in freight train operation and performing aerodynamic refinement on the vehicles could be disadvantageous to operators in terms of cost to benefit. Similar modifications were proposed to reduce the leaf movement onto the tracks under multiple unit trains such as the Class 158, however these modifications were deemed to require too long before the scheme ‘paid back’ (RSSB, 2007). Considering the significant annual effect that leaves have on the UK rail network and the fact that these modifications were not implemented due to cost makes it unlikely that aerodynamic drag reduction would be considered suitable for retro-fitting of freight trains.

As well as incurring relatively high drag, poor aerodynamic refinement and sparse container loading of freight trains can induce rapid slipstream growth, causing relatively large velocities at trackside which are often greater than those of faster-moving passenger trains (Soper, 2014, Sterling et al., 2008, Figura-Hardy, 2005).

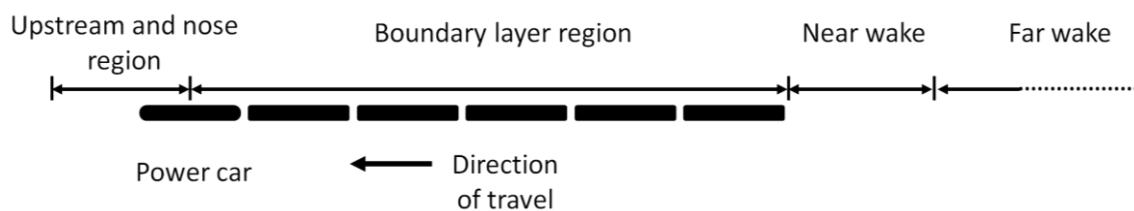


Figure 3 Schematic of the flow regions in a train's slipstream

The slipstream of a freight train is similar to that of a passenger train, in the sense that they can generally be characterised by four distinct flow regions (as shown in Figure 3) (Soper, 2014, Baker, 2010), namely: the upstream and nose region, the boundary layer region, the near wake and far wake regions. In the subsequent sections these flow regions will be discussed individually.

### 2.5.1.1 Upstream and nose region

The first region in a train's slipstream is the upstream and nose region which is characterised by essentially inviscid flow (Sanz-Andrés and Santiago-Prowald, 2002). The pressure transient observed in Figure 4 occurs because of the positive pressure field around the front of the train which is followed by a low pressure region caused by the flow accelerating around the curved roof in the case of passenger trains or separating around the front face of the locomotive in the case of freight trains (Soper, 2014). The repeatability, i.e. the very low run-to-run variation, of the nose region of streamlined passenger trains is due to the inherent steadiness in the stagnation process and is also due to the absence of large-scale flow separation which has been observed for freight trains. In the case of freight trains, only the flow ahead of the locomotive can be considered inviscid.

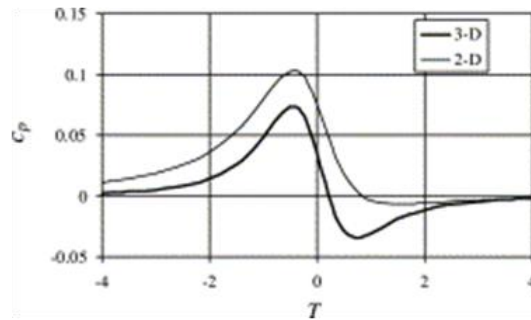


Figure 4 Idealised nose pressure coefficients obtained from potential flow calculations (Sanz-Andrés and Santiago-Prowald, 2002)

The pressure coefficient ( $C_p$ ) in the upstream and nose region of trains exhibits a positive-negative transient, where  $C_p$  is defined as

$$C_p = \frac{p_{\text{tot}} - p_0}{\frac{1}{2} \rho U_f^2} \quad (2.1)$$

where

$p_{\text{tot}}$  – total pressure (Pa)

$p_0$  – ambient pressure (Pa)

$\rho$  – density ( $\text{kg/m}^3$ )

$U_r$  – resultant wind speed (m/s).

Freight and passenger train cases exhibit similar behaviour, although for freight trains the magnitude is greater because of the generally bluffer cross section causing greater stagnation and flow separation. Typical values for peak-to-peak pressure coefficients ( $\Delta C_p$ ) for passenger trains are  $\Delta C_p = 0.45$  whereas for freight trains values approximately twice as great are seen,  $\Delta C_p = 0.9$  (Baker et al., 2012b).



Figure 5 Operational Class 66 locomotive hauling FEA-B container wagons through Virginia Water station (Tagishsimon, 2004).

The flow in the nose region of a freight train's slipstream is subject to the locomotive used and thus different locomotives will produce different nose-region characteristics. The choice of locomotive also has the potential to influence the slipstream further along the train. In the nose region of the Class 66 locomotive (Figure 5) ( $0 \text{ m} < x < 18 \text{ m}$ ) the flow is dominated by massive separation which induces velocities greater than train speed (Soper, 2014). It was

postulated that the nose region of the Class 66 locomotive extended up to  $x=18$  m which is several meters longer than for full-scale passenger trains (Sterling et al., 2008), however the definition is somewhat arbitrary.

### *2.5.1.2 Boundary layer region*

The second intrinsic region in a train's slipstream is the boundary layer region which usually exists for the majority of the train length. The boundary layer region is characterised by a gradual increase in slipstream velocity and is punctuated by pressure and velocity transients which occur due to the container or carriage spacings. For passenger trains the growth of the boundary layer region is somewhat gradual (Baker, 2010), however this can be more abrupt for freight trains, especially those with partially-loaded container wagons (Soper, 2014). The growth of the boundary layer region has been shown to depend heavily on train geometry, loading configuration and Reynolds number (Sterling et al., 2008, Soper, 2014).

Displacement thickness has been widely used as a means of approximating the thickness of the boundary layer around trains (Baker et al., 2001, Pii et al., 2014, Sterling et al., 2008, Hemida et al., 2010, Bell et al., 2014, Muld et al., 2013). Displacement thickness can be considered as a measure of the 'missing' mass flow due to the presence of a boundary layer as opposed to the mass flow which would exist in the same region without a boundary layer in a two-dimensional flow (Anderson, 2001) and is schematically described in Figure 6.

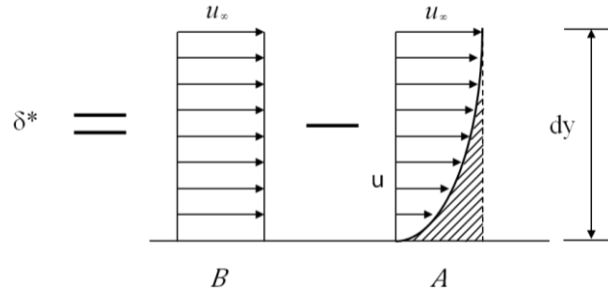


Figure 6 Schematic of the velocity profile from the flow over a slip wall and in a 2-dimensional boundary layer. Free-stream velocity, longitudinal velocity and height position from wall are given as  $u_\infty$ ,  $u$  and  $dy$ , respectively. Hashed area indicates missing mass and momentum flux from the presence of the boundary layer.

The mass flow across  $dy$  in an idealised two-dimensional flow over a slip wall is given by

$$B = \rho_\infty u_\infty dy \quad (2.2)$$

where

$u_\infty$  – freestream velocity (m/s)

$\rho_\infty$  – freestream density ( $\text{kg/m}^3$ ).

The mass flow across  $dy$  over a no-slip wall is given by

$$A = \rho u dy \quad (2.3)$$

where

$u$  – longitudinal velocity (m/s).

By defining the missing mass flow as

$$\text{missing mass flow} = \rho_\infty u_\infty \delta^* \quad (2.4)$$

and equating it to the difference between B and A we get

$$\rho_{\infty} u_{\infty} \delta^* = \int_0^y (\rho_{\infty} u_{\infty} - \rho u) dy. \quad (2.5)$$

Substituting the speed of the train as the freestream velocity and setting  $\rho_{\infty}$  equal to  $\rho$  because the flow is incompressible we get

$$\delta^* = \int_0^{y'} \left( 1 - \frac{u}{u_{\text{train}}} \right) dy' \quad (2.6)$$

where

$u_{\text{train}}$  – train speed (m/s)

$dy'$  – distance from train side (m).

The slipstreams of trains are highly-turbulent three-dimensional flows and thus it can be seen from the analysis above that the use of a two-dimensional flat plate boundary layer parameter such as displacement thickness as a method of calculating the thickness of a boundary layer is a rough approximation at best. The unsuitability of the displacement thickness parameter to three-dimensional flows is acknowledged by researchers in the literature, however this deficiency is often overlooked because of the lack of a better method of analysis to approximate the thickness of the slipstream.

Figure 7 shows the displacement thickness of the slipstreams of full- and model-scale Inter-City Express2 (ICE2) high-speed passenger trains measured from station platforms and at trackside. It can be seen that the rate of growth of the boundary layer region in the model-scale tests is approximately 50% greater than for the 8 car full-scale train. This observation is hypothesised to be due to the development of the actual boundary layer on the surface of the

model-scale train which is 25 times greater in relation to the size of the train for the model-scale case than it would be for the full-scale case, assuming no Reynolds number effects.

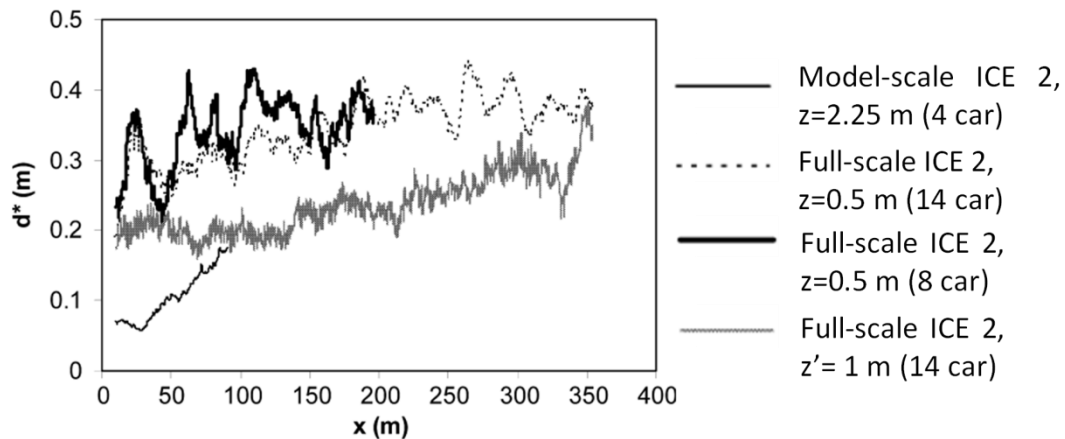


Figure 7 A comparison between displacement thicknesses of model-scale and full-scale ICE2 slipstreams (Sterling et al., 2008) (modified)

The thickness of the boundary layer region for the ICE2s shown in Figure 7 are less than half of those observed for the various loading configurations considered in Soper (2014). It is shown in Figure 8 that freight trains with lower-loading efficiencies produce more rapid slipstream growth than those with higher loading efficiencies (Figure 9). Loading efficiency is defined as the ratio of container size to useable space on the flat bed wagons. Even for the fully-loaded consist, the displacement thickness is greater for the freight train than for all of the ICE2 cases due to their smaller inter-carriage gaps ( $\approx 0.625$  m) and more aerodynamically refined power car.

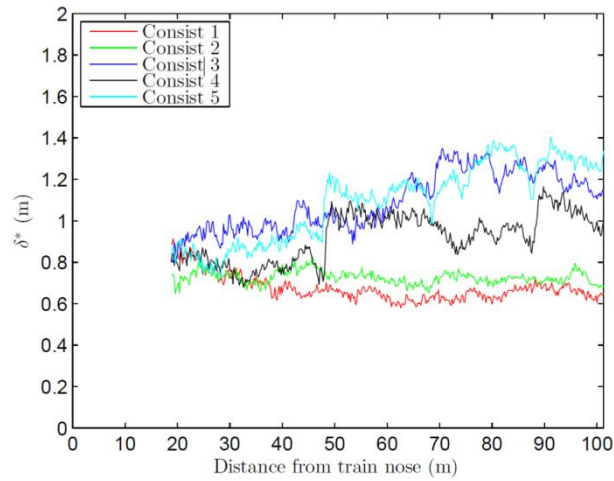


Figure 8 Displacement thickness,  $\delta^*$ , (m) along the train length for freight consists 1 (red), 2 (green), 3 (blue), 4 (black), 5 (cyan) (Soper, 2014). Loading configurations are shown in Figure 9.

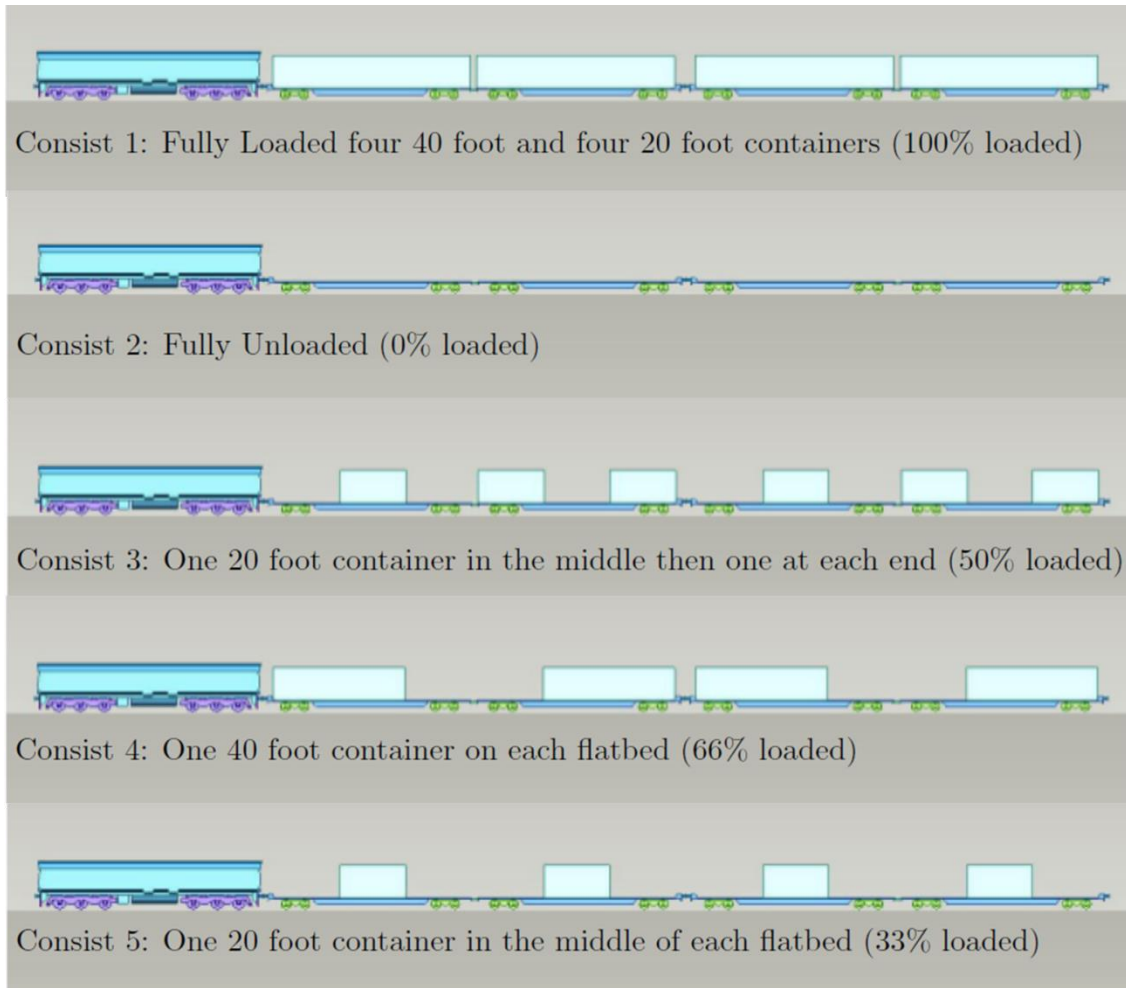


Figure 9 Loading configurations used by Soper (2014)

Momentum thickness is another parameter which is used in boundary layer analysis and is a measure of the momentum flux displaced by the presence of the boundary layer in comparison to what would have been the case over a slip surface. The momentum thickness,  $\theta_M$ , will not be derived here but it is defined as

$$\theta_M = \int_0^{y_n} \frac{u}{u_{\text{train}}} \left( 1 - \frac{u}{u_{\text{train}}} \right) dy'. \quad (2.7)$$

From the displacement and momentum thicknesses, the form parameter,  $H_f$ , can be defined as

$$H_f = \frac{\delta^*}{\theta_M}. \quad (2.8)$$

For conventional boundary layers, higher values of the form parameter indicate that an adverse pressure gradient is present and separation is imminent. In a standard, zero-pressure gradient boundary layer typical values of the form factor are 1.3-1.4 (Munson et al., 1990). The slipstream around the model-scale ICE2 (Baker et al., 2001) show values of the form parameter between 1.05 and 1.5 (Figure 10), however because less than eight measurement positions were used at train side (some of which were faulty) the error in the overall value of the form parameter should be treated with some circumspection. For the entirety of the train length, the form parameter is nearly identical for the flow around the train side as it is over the train roof.

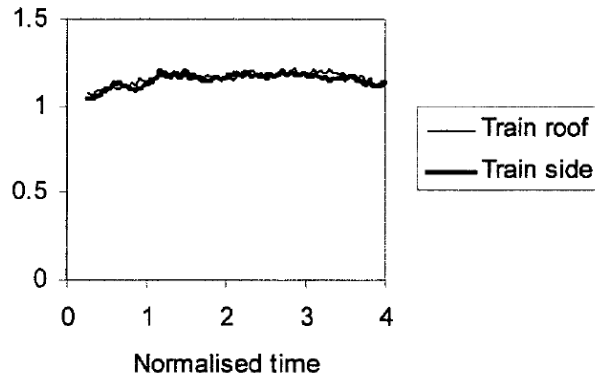


Figure 10 Form parameter over the roof and around the side of a 1/25<sup>th</sup> scale ICE2 (Baker et al., 2001)

### 2.5.1.3 *Near wake region*

The penultimate flow region in a train's slipstream is the near wake and is the region where the presence of coherent flow structures have been detected experimentally (Sterling et al., 2008) and observed in numerical simulations (Muld et al., 2012, Huang et al., 2014). In the case of passenger trains, it is common for the maximum velocities to occur in the near wake as a result of these trailing longitudinal vortices produced behind the vehicle and spreading-out from train side, as shown in Figure 11.

The trailing vortices in the wake of passenger trains are a familiar sight in vehicle aerodynamics and also occur in the wake of the frequently-studied Ahmed body (Hinterberger et al., 2004, Minguez et al., 2008, Fares, 2006) because of the downwash produced by the rear-sloping roof. The deviation of the trailing vortices from behind the train has been shown to be affected by the presence, or absence, of a ballast shoulder (Bell et al., 2014).

For freight trains, peak velocities are rarely observed in the near wake as a result of the absence of trailing vortex structures due to the geometry of the freight containers lacking the rear-sloped roofs which generate such flow mechanisms (Sterling et al., 2008).

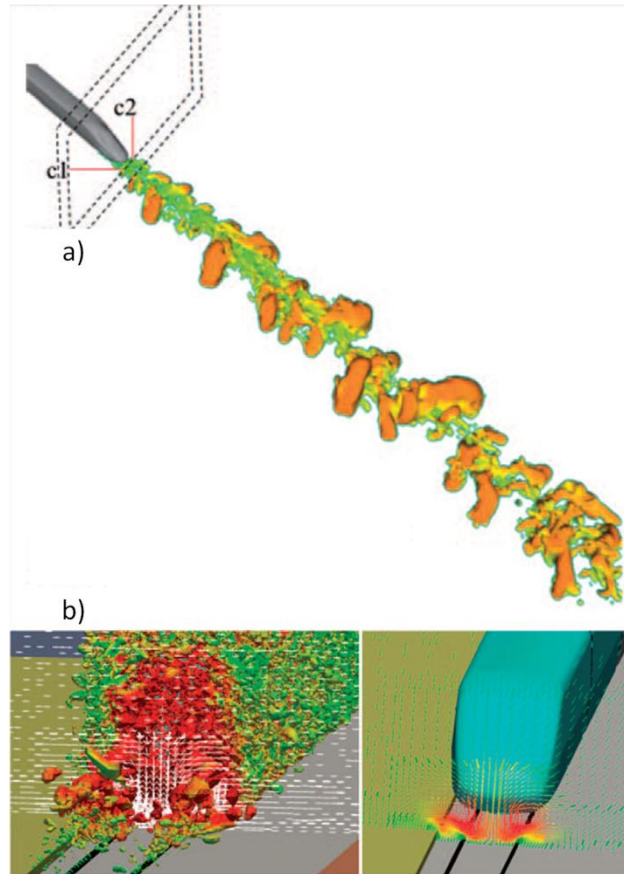


Figure 11 Flow structures obtained using CFD in near wake of the a) CRH2 Chinese passenger train (Huang et al., 2014) and b) the near wake of a simplified ICE2 (Hemida et al., 2012a)

#### 2.5.1.4 Far wake region

The final region in a train's slipstream is the far wake region and is characterised by a gradual decrease in velocity and can be observed for sometimes hundreds of metres behind the train (Sterling et al., 2008). In the case of some passenger trains the velocity in the far wake decays according to a power law (Eskridge and Hunt, 1979, Baker et al., 2013b) of the form

$$u = \frac{b}{X} e^{-\frac{c}{X^{0.5}}} \quad (2.9)$$

where

$X$  - distance behind the train (m)

$b$  and  $c$  - constants.

It can be seen from equation 1.9 that the velocity in the far wake takes the form of a decaying exponential function. From this it can be inferred that the in the far wake velocities should be significantly low so as not to pose a safety threat such as affecting a person's stability in the same way that higher velocities in the nose or boundary layer regions might and are thus of little interest in this work.

### ***2.5.2 Train slipstreams and experimental methodologies***

There are a number of methods commonly used to investigate the aerodynamics associated of trains by full-scale experiment, model-scale experiment and numerical simulations. The sections below detail uses of both kinds of physical experiment in train slipstream analysis and consider the shortfall of each method. Numerical simulations will then be introduced and their applications and limitations within slipstream analysis will also be discussed.

#### ***Full-scale freight slipstream measurements***

Full-scale measurements can be difficult to perform and can provide limited data during a measurement campaign. Full-scale slipstream measurement campaigns are often limited by site access, atmospheric conditions, availability of equipment and safety restrictions (Baker and Quinn, 2012) but the data are essential as validation for physical and numerical models. In the current section, a review of the full-scale slipstream measurement campaigns for freight trains will be performed with brief consideration of passenger train slipstreams. In order to aid perspective as passenger trains have been significantly more studied in this field.

The slipstream velocities of two freight trains measured on a station platform and normalised by train speed are shown in Figure 12. The data are taken from measurements of two container-hauled freight trains which consisted of a mixture of 12 m and 6 m containers on

FEA-B wagons with corresponding loading efficiencies of 66% and 33%, respectively. The velocity profiles exhibit a similar rate of increase along the train length, even though the loading configurations differ somewhat. The velocity peak in the nose region reaches a maximum value of only 0.08 of train speed which is due to the Class 92 locomotive's more rounded design than the Class 66 locomotive used by Soper (2014).

The boundary layer region development is observed for both trains until approximately  $x=400$  m where equilibrium is reached. The wakes of the trains differ due to the differing loading configurations, although the general trend of gradual decay is shown.

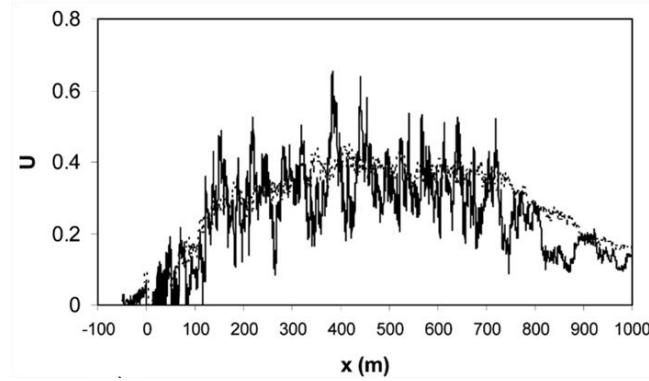


Figure 12 Normalised longitudinal slipstream velocities for a) two freight consists  $y''=1.5$  m and  $z'=1$  m (Sterling et al., 2008)

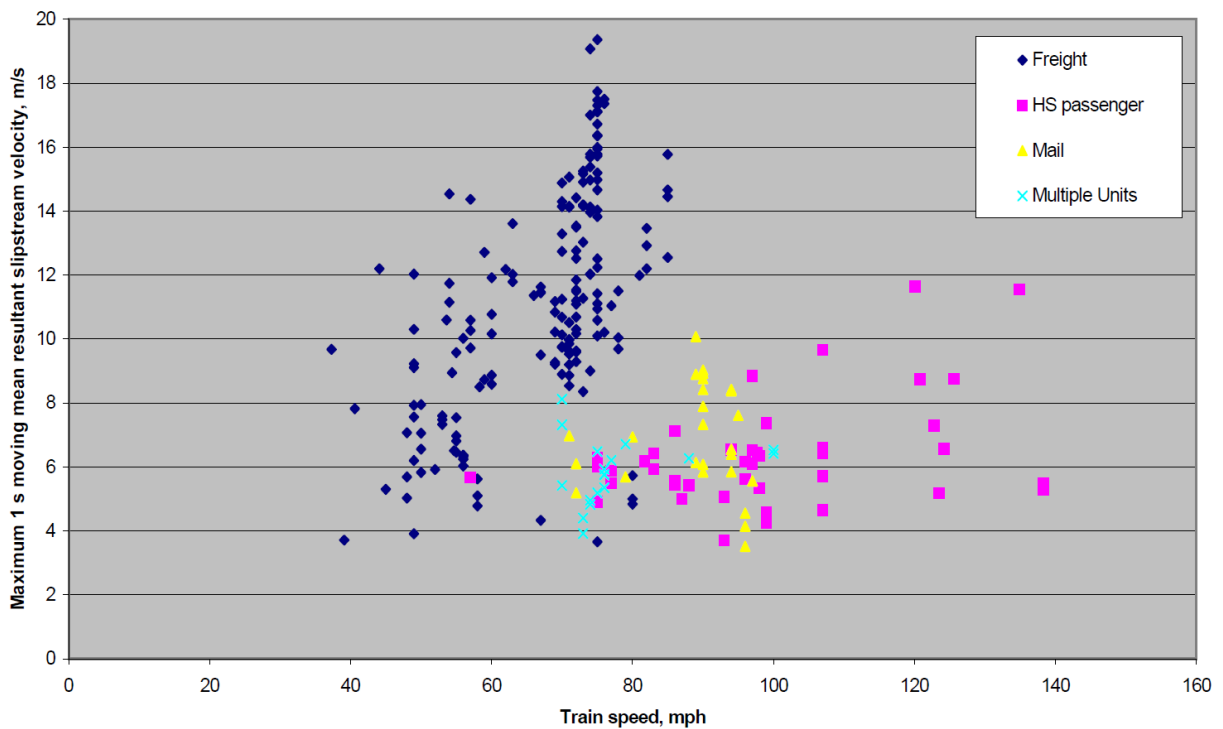


Figure 13 Peak one second moving averages  $y''=1.5$  m ( $z'$  unknown) (Figura-Hardy, 2005)

Figure 13 shows peak one second moving averages of slipstream data from a variety of trains which have been broadly categorised as freight, HST, mail train and multiple units (Figura-Hardy, 2005). The data are taken from  $y''=1.5$  m, although the height above the platform is not stated. The effect of applying one-second moving averages to instantaneous slipstream data is discussed in Section 2.5.4.

The general trend in the data is that even though the HSTs travel nearly twice the speed of the freight trains, their peak one second moving averages are still often lower than those of the freight trains. The majority of the multiple units are travelling at around 120 km/h and produce a peak maximum one second moving average velocities of approximately 8 m/s. The peak one second moving average velocity produced by the freight trains is up to 2.5 times greater when travelling at the same train speed as the multiple units.

Despite large scatter in the full-scale data it is possible to draw broad conclusions about the behaviour of train slipstreams. The spread of the velocities produced in the slipstreams of the freight trains, even after the smoothing effect of the moving average has been applied, is still great which is a testament to how unsteady the slipstreams are. Measurements on platforms showed that, in general, freight trains caused higher slipstream velocities than passenger trains even though, in some cases, they travelled at approximately half the speed of the passenger trains (Figura-Hardy, 2005) such that freight train slipstream velocities were as high as 19.4 m/s whereas velocities in passenger train slipstreams only reached 11.7 m/s.

The higher slipstream velocities produced by freight trains is due to their higher 'relative roughness' compared to passenger trains. The term 'relative roughness', in the current context, relates to the discontinuities of the train's geometry such as the inter-wagon spacings and bogies. The data in Figure 13 are taken from platform measurements and therefore the greatest source of roughness for a passenger train (the bogies) is shielded by the platform causing the only 'visible' roughness to be the inter-carriage gaps. The inter-wagon spacings of freight trains are generally much larger than the inter-carriage gaps of passenger trains and thus a greater level of discontinuity will cause higher velocities to be generated.

The effect of the inter-wagon spacings on the slipstream flow is broadly analogous to the flow over urban street canyons (Oke, 1988) where varying the spacing size has a direct

impact on the flow characteristics in, and around, the spacings (Figure 14). The limitations of the analogy are that the slipstream flow is three-dimensional due to all sides of the inter-wagon spacings being open unlike in the urban street canyon where the flow is either two-dimensional or the ground provides a mean of blockage. The regimes that Oke (1988) identified were skimming flow, wake interference and isolated roughness flow. The slipstreams around freight trains with low loading efficiency are thus more likely to be considered more closely comparable to isolated roughness elements than to skimming flow regimes which are most applicable to fully-loaded wagons.

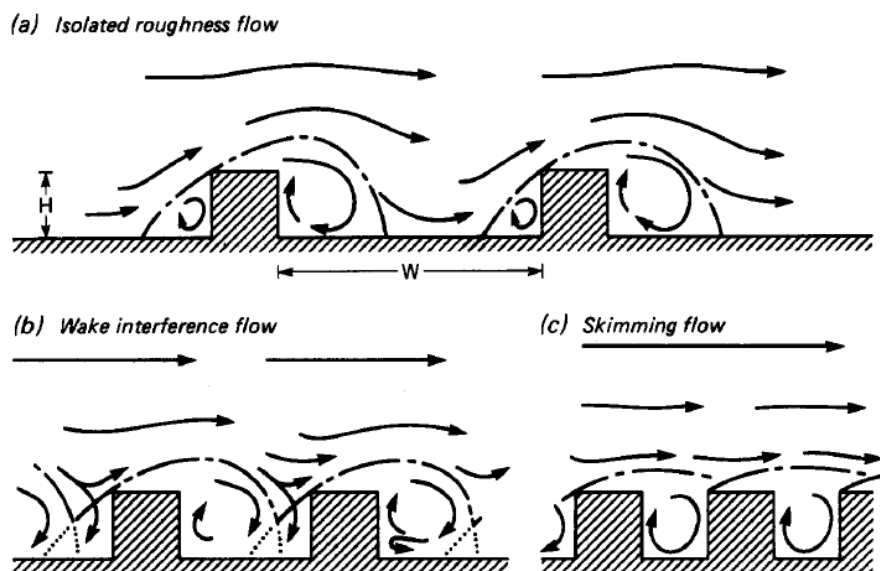


Figure 14 Flow regimes around representative street canyons for differing H/W ratios (Oke, 1988)

Turbulence intensity is monitored in train slipstreams as a measure of the gustiness of the flow. The turbulence intensities in the slipstreams of freight and passenger trains are shown in Figure 15. The standard method of calculating turbulence intensity is to take the ratio of the standard deviation of the velocity to a constant velocity such as train speed (Davidson, 2004). The turbulence intensity,  $I$ , used in the cases shown in Figure 15 is calculated by

$$I = \frac{\sigma_u(x)}{(1 - u(x))'} \quad (2.10)$$

where

$\sigma_u(x)$  –standard deviation of the normalised velocity

$u(x)$  – normalised longitudinal velocity at longitudinal position.

The method of calculating turbulence intensity employed in Figure 15 is used because it allows for local values to be calculated relative to the reference frame of the train.

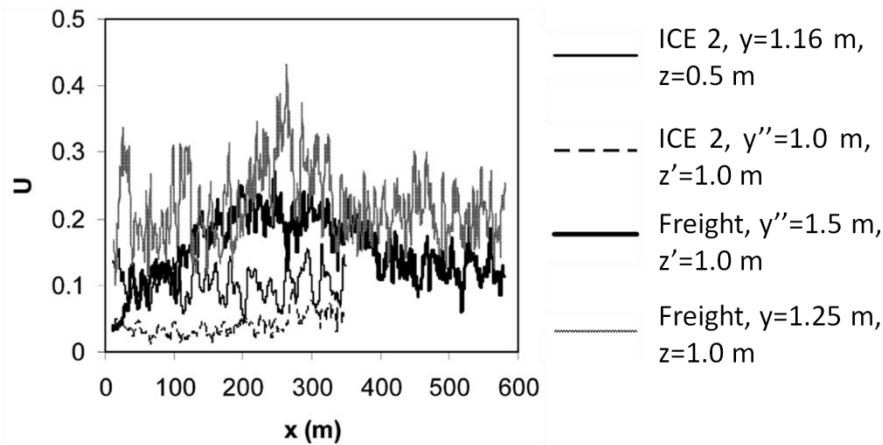


Figure 15 Turbulence intensities in the slipstreams of ICE2 and a freight consist on platforms and at trackside (Sterling et al., 2008) (Modified)

It can be seen from Figure 15 that the peak value of turbulence intensity in the boundary layer region of a freight train is  $I=43\%$  and occurs at  $x=263\text{ m}$ ,  $y=2.69\text{ m}$  and  $z=1\text{ m}$ . Turbulence intensity measurements from the same consist at  $z'=1\text{ m}$ , on a platform which is  $1\text{ m}$  high, reaches a peak value of only  $I=27\%$ . The turbulence intensity in the slipstream of the ICE2 reaches a peak value of  $I=16\%$  at trackside, which is  $62\%$  and  $40\%$  lower than the freight measurements at trackside and on a platform, respectively. The turbulence intensity in the slipstream of the ICE2 on the platform reaches  $I=9\%$  as a result of the platform shielding the energetic flow which is generated by the bogies and in the under body region. Overall it is observed that the greatest turbulence intensities occur closer to the bogies for both types of

train. It is also evident that the platform measurements for the freight train are greater than the trackside measurements for the passenger train which highlights the effect of the relative roughness of container wagons in generating turbulence in comparison to passenger train's bogies.

### *Model-scale train slipstreams*

Model-scale aerodynamic investigations are popular amongst researchers because they are relatively simple and inexpensive to conduct in comparison to full-scale tests (Baker et al., 2001, Gil et al., 2010, Baker et al., 2012a, Bell et al., 2015). Model-scale testing does have a fundamental weakness in that the Reynolds number of the case is rarely in the same order of magnitude as the full-scale case which is being modelled.

A recent example of physical modelling in train aerodynamics is an investigation of the slipstream development around a model-scale Class 66 locomotive container-hauled freight train using moving-model experiments at the Transient Railway Aerodynamic INvestigation (TRAIN) rig in Derby, UK (Soper, 2014).

The Reynolds number,  $Re$ , of a full-scale Class 66 locomotive-hauled freight train travelling at operational speed would be approximately  $Re=11.5 \times 10^6$ , where

$$Re = \frac{uH}{\nu} \quad (2.11)$$

and

$H$  – locomotive height (m).

Due to experimental constraints of the TRAIN rig and concerns about model fragility, the maximum Reynolds number used by Soper et al.(2014) was limited to  $Re=2.5 \times 10^5$  which is only 2.2% of the full-scale case.

In order to match the Reynolds numbers between the model- and full-scale cases, either the moving-model train would need to be much larger in scale, which would then affect operation of the TRAIN rig, or the model would need to travel 45 times faster, which would be approximately 3.5 times the speed of sound. It is evident then, that the relatively low Reynolds number of the model-scale tests cannot be increased to the same order or magnitude as the full-scale case, thus a compromise must be made.

Even with massive differences in Reynolds number, it is common practice for researchers to assume a level of independence as this allows for simpler testing to be conducted. The concept of Reynolds number independence assumes that the flow does not change as a function of Reynolds number above a certain value; however this notion is fundamentally flawed because of the nature of turbulent flows.

Turbulent flows are characterised by apparently-random fluctuations in velocity and pressure, and are comprised of a tangle of eddies which, at present, lack a formal definition. The largest-scales within a turbulent flow extract their energy from the mean flow and their size is determined by the geometry of the problem. The energy from the largest scales is transferred from the larger-scales to the smaller scales by shear and this continues until the smallest scale is reached, where viscosity dominates and the energy is then dissipated in the form of heat.

The Reynolds number of a turbulent flow is essentially a definition of the range of turbulent scales within that flow such that

$$\frac{\eta}{l_0} \sim Re^{-\frac{3}{4}} \quad (2.12)$$

where

$\eta$  – Kolmogorov micro-scale (m)

$l_0$  – scale of the flow (m).

From the definition of turbulence above it can be seen that model- and full-scale train slipstreams contain differing ranges of turbulent scales. It is the case then, that in a full-scale train's slipstream, energy is transferred through a much greater range of turbulent scales than would be the case for model-scale train's slipstream and so some statistical variation between results is anticipated.

Reynolds number dependence of force coefficients has been shown to occur below  $Re=85,000$  for sharper-edged vehicles, such as lorries (Coleman and Baker, 1990). For more rounded train shapes, such as streamlined passenger trains, force coefficients experience a higher degree of Reynolds number dependence because their value is a result of the separation and reattachment points which are sensitive to Reynolds number (Copley, 1987). For vehicles such as freight trains this sensitivity to Reynolds number is reduced because separation is forced by the sharp edges which decreases the dependence on Reynolds number.

The CEN (2011) code of practice states that model-scale train slipstream tests must be conducted at a minimum Reynolds number,  $Re_{min}=2.5 \times 10^5$ , in order to ensure independence has been achieved and evidence must also be provided of similarity between data sets from  $0.6 Re_{max}$  to  $1.0 Re_{max}$ .

Soper (2014) showed the vast difference in slipstream growth between consists with differing loading configurations. The slipstream development of a partially-loaded train was observed to reach equilibrium by the sixth wagon, whereas the fully-loaded case reached equilibrium by the fourth wagon. The slipstream velocities generated by one of the mixed-loading consists bordered on the maximum gusts allowed by the TSI and CEN. Although not

technically exceeding the limiting values, the gusts magnitudes are in accordance with those considered sufficient to cause person instability (Jordan, 2008).

Validation of the physical model was conducted against full-scale data obtained during a full-scale measurement campaign at the site of the former Uffington Junction railway station (Baker and Quinn, 2012). The longitudinal velocity component and pressure coefficient from the full- and model-scale cases were compared at  $y=3\text{m}$  and  $z=0.2\text{ m}$ . The peak positive and negative  $C_p$  showed agreement within 30 % and 12 %, respectively. The discrepancy between the positive nose-region pressure coefficients was conjectured to be due to the influence of the ballast shoulder in the full-scale case.

Of the slipstream velocities measured at full-scale, only one useable run was obtained for a fully-loaded container freight train. The longitudinal velocity component in the full-scale data was plotted alongside 25 instantaneous velocities from the four wagon model-scale train. The comparison of the longitudinal velocities from the full- and model-scale cases showed that the full-scale velocities remained within the maximum and minimum bounds of the 25 model-scale velocities for the entirety of the model-scale train's length. The validation of the model-scale data against the full-scale case is an inherent sign that the slipstream flow around the moving-model has achieved Reynolds number independence although, as discussed above the flow does differ from the full-scale case.

Wind tunnels can also be used for train slipstream analysis and can be preferable to moving-model experiments because specialist facilities are not required, unlike in moving-model tests. Recent tests to obtain slipstream velocities around a  $1/10^{\text{th}}$  scale aerodynamic train model (ATM) (loosely based on the ICE2) were conducted in Monash University's 450 kW wind tunnel (Bell et al., 2014).

The ATM used in the wind tunnel tests is intended to be representative of an ICE2, although there are a lower number of bogies than would be on an operational train and lower than was the case for previously-used models (Baker et al., 2001). The slipstream around the train was sampled at discrete positions using a robotic arm which allowed for frequencies in the slipstream relative to the train to be easily obtained.

Two ground configurations were used for the slipstream cases, namely the flat ground and single track and ballast. The single track and ballast was used in order to comply with the (CEN, 2010) regulations but also allowed for a comparison between the effect of the two ground configurations on the slipstream velocities.

The effect of Reynolds number on the slipstream velocities for the flat ground and single track and ballast case was tested between  $Re=4 \times 10^5$  and  $Re=7 \times 10^5$ . The velocity profiles from both cases showed maximum variations in velocity between 8.5 % and 23 % in the Reynolds number range although this was deemed to be within experimental error.

Due to the wind tunnel model being fixed to the ground, the wake flow was accessible unlike in moving model experiments where the movement of the train makes this impractical. Although the wake flow directly behind a train is of academic interest, its practicality in terms of slipstream safety, which was a key feature of the work, is negligible because this is far from where a pedestrian would stand and thus will have no direct effect on waiting passengers.

Perhaps a more novel method which has been employed to rapidly obtain slipstream measurements is a rotating rail rig (Gil et al., 2010). The scale of the model used on the rotating rail rig is half of those used in the TRAIN rig experiments (Baker et al., 2001, Soper et al., 2014, Dorigatti, 2013, Gilbert et al., 2013) or in CFD simulations (Hemida et al., 2012a, Huang et al., 2014) and therefore scaling effects will become increasingly prevalent.

Reynolds numbers between  $Re=30,000$  and  $Re=50,000$  were tested and slipstream velocities at the nose peak showed a significant change across a relatively small Reynolds number range thus suggesting that although convenient, this method does not provide realistic slipstream data due to the scale of the model.

### ***2.5.3 CFD slipstream investigations***

Another tool at a researcher's disposal in the investigation of train slipstream behaviour is numerical modelling. CFD provides the researcher with the capability to extract vast amounts of data from a single simulation that wouldn't be practically possible from a model-scale physical experiment.

Very specialised test facilities are required in order to conduct train slipstream analyses on moving models and although it is possible to use a static-ground configuration such as in a wind tunnel this method brings further uncertainties into the accuracy of the results (Bell et al., 2014). In CFD the correct relative motion between the train and the ground can be easily achieved by setting a velocity to the ground plane.

The slipstream of a model-scale ICE2 was investigated numerically using LES at a Reynolds number of 300,000 (Hemida et al., 2012a). The slipstream velocities were compared to full-scale data from the AEROTRAIN project and results show a large degree of difference. Factors besides Reynolds number may have also added to the discrepancy between the results but as it is not possible to quantify these, scale is considered a large contributing factor.

Huang et al.(2014) used improved delayed detached-eddy simulation (IDDES) to obtain velocities and pressures in the slipstream and wake of the Chinese CRH2 high speed train. The simulations are validated against full-scale experimental data where velocities at the nose and tail of the train are within 7 % and 12 %, respectively. Although, in the far wake the simulations miss two increases in static pressure 100 m apart as a result of a coarser mesh in

that region. The research found that the slipstream velocities generated in the train's slipstream under normal operational conditions are below recommended safety limits.

Muld et al. (2012) applied delayed detached-eddy simulation (DES) in order to obtain velocities in the near wake of an ATM. The instantaneous flow field in the near wake of the train model was decomposed into proper-orthogonal decomposition (POD) and dynamic mode decomposition (DMD) modes. The decomposition of the instantaneous wake flow into its respective modes allows for the dominant flow structures to be identified. A significant frequency of  $St=0.085$  was observed in the spectrum for both the POD and DMD methods, where  $St$  is the Strouhal number defined as

$$St = \frac{fl}{u} \quad (2.13)$$

where

$f$  – frequency ( $s^{-1}$ )

$l$  – length dimension (m).

The Reynolds number of the case was  $Re=60,000$  which is only 20% of the value used in other slipstream simulations (Hemida et al., 2012a, Huang et al., 2014). Because the Reynolds number is approximately a quarter of the lower limit recommended by CEN (2011), it is unclear what implications such a low-speed train will have on the modes within the slipstream and therefore it is unlikely that the data have any relevance to full-scale train slipstreams.

Numerical simulations have been used by many researchers and have been shown to not only elucidate the flow features of train slipstreams but also produce slipstream data that are comparable to data obtained in physical experiments (Pii et al., 2014). Although the data

from CFD simulations may not be credible enough to use without validation, once simulations are validated, CFD can be a highly effective tool which allows researchers to expand on an already existing data set which has been obtained experimentally. This extraction of further data from the simulations is advantageous because it can reduce the length and cost of physical experiments without extra work on behalf of the user.

#### ***2.5.4 Data analysis methods for slipstream measurements***

In train slipstream aerodynamics there are two methods of data interpretation that are prevalent: ensemble-averaging and the maximum one second moving average (MOSMA) technique.

Ensemble-averaging is the process of taking discrete measurements of flow variables from independent runs, normalising them and then averaging at specific positions relative to a fixed reference point (Deeg et al., 2008). Ensemble-averaging is defined mathematically as

$$\bar{u}(x) = \frac{1}{n} \sum_{r=1}^n u_r(x) \quad (2.14)$$

where

$\bar{u}(x)$  – normalised ensemble-averaged velocity

$u_r(x)$  – normalised velocity signal for a single run

$n$  – total size of ensemble

$r$  – run number.

In order to perform ensemble-averaging, the data must be aligned about a consistent feature in a train's slipstream such as the inviscid nose peak (Baker et al., 2001, Quinn et al., 2009, Soper, 2014, Sanz-Andrés and Santiago-Prowald, 2002). At least 20 runs are recommended for velocity by TSI (2008) and CEN (2011) in order to reduce the standard deviation in the

data. Due to the highly-unsteady nature of the slipstream of a container freight train, Soper (2014) opted to use 25 runs for the ensemble size to reduce the standard deviation of the ensemble.

Although ensemble-averaging can provide a view of the mean flow properties in a slipstream it was noted by Sterling et al.(2008) that periodic flow mechanisms can be overlooked. When applying ensemble-averaging, periodic flow mechanisms such as those in the near wake of HSTs are phase-averaged leading to misrepresentative data. However, the locations of high variability can be determined by examining the standard deviations of the flow properties.

The second method of slipstream velocity interpretation is the MOSMA technique which is used in CEN (2011) and TSI (2008) and consists of the following steps:

1. Sample 20 independent runs at  $y=3$  m and  $z=0.2$  m for velocity
2. Perform a one second moving average on each run
3. Take the mean,  $\bar{u}$ , and standard deviation,  $\sigma_u$ , of the peak velocities from each run obtained in step 2
4. Calculate the characteristic velocity,  $u_{2\sigma}$ , by

$$u_{2\sigma} = \bar{u} + 2\sigma_u \quad (2.15)$$

where  $u_{2\sigma}$  should be below 20 m/s for trains travelling between 160 km/h and 250 km/h or less than 22 m/s for trains travelling above 250 km/h. These velocities are usually obtained for full-scale or moving-model tests, although a recent investigation suggested that wind tunnel experiments could be used to obtain the limiting value of velocity based around an empirical fit. After applying a spatial average equivalent to a one-second moving-average, the characteristic velocity from wind tunnel experiments,  $u_{2\sigma_{wt}}$ , becomes

$$u_{2\sigma_{wt}} = \max(\bar{u}(x) + 0.9\sigma_u(x)). \quad (2.16)$$

The evaluation of pressure is performed for the peak-to-peak pressure transient at the nose of the train and consists of the following steps:

1. Sample at least 10 peak-to-peak pressure transients at  $y=2.5$  m and between  $z=1.5$  m and  $z=3.3$  m, at 0.3 m increments
2. Take the mean and standard deviations of the peak-to-peak pressure values
3. Calculate the characteristic pressure transient,  $\Delta P_{2\sigma}$ ,

$$\Delta P_{2\sigma} = \overline{\Delta p} + 2\sigma_p. \quad (2.17)$$

which should be lower than  $\Delta P_{2\sigma} = 720$  Pa for trains travelling below 160 km/h and below  $\Delta P_{2\sigma} = 795$  Pa for trains travelling at 250 km/h or higher. For trains that travelling below 160 km/h, there is no requirement for the train to conform to pressure and velocity limits.

Although the CEN and TSI methodology, detailed above, does not give a physical representation of the flow, it does provide a simple method of determining limiting values of slipstream velocities and pressures. This being said, the limiting value of slipstream velocities is somewhat arbitrary and has no physical significance such as to the stability of persons. Although this is the case, incidents of slipstream-induced accidents are rare and therefore the current limits should be considered adequate from a safety standpoint. The limits cannot be changed without sufficient justification such as they are overly-conservative and cause line speeds to be unnecessarily restricted.

## 2.6 *Crosswind effects on train slipstreams*

When a train is in service it will be subjected to winds of differing incidence, magnitude and duration. In the following section, the standard logarithmic profile of mean ambient winds

and its variation relative to a moving vehicle is described (Section 2.6.1) as well as the data concerning crosswind effects on train slipstreams at full-scale, model-scale and in CFD simulations (Section 2.6.2). Finally, the implications of these crosswinds with respect to current safety guidelines will be briefly considered in Section 2.6.3.

### **2.6.1 Relative crosswind profile**

When atmospheric winds travel over the earth the frictional effect of the ground causes wind speeds closer to the earth's surface to be slower than those higher up. This behaviour is much the same as boundary layers which form on flat plates but with negligible viscous effects. The region of flow that conforms to this velocity profile is called the atmospheric boundary layer (ABL). The logarithmic approximation of the ABL profile (Holmes, 2007) is defined as

$$\bar{U}(z) = \frac{u_\tau}{\kappa} \ln\left(\frac{z}{z_0}\right) \quad (2.18)$$

where

$u_\tau$  – friction velocity (m/s)

$\bar{U}(z)$  – mean velocity as a function of height (m/s)

$\kappa$  – Karman constant ( $\approx 0.41$ )

$z$  – height above ground (m)

$z_0$  – roughness length (m).

Moving vehicles which experience a crosswind will 'see' a different velocity profile to that which a static vehicle experiencing the same crosswind, will 'see' (Baker, 2010). Figure 16 shows the effective addition which occurs, between the negative vector of train speed and the ABL profile of a crosswind.

Due to the crosswind velocity being a function of height, close to the ground the contribution of the train's velocity to the resultant wind is dominant however, higher above the ground the contribution of the crosswind velocity component increases which results in a greater yaw angle (Figure 17).

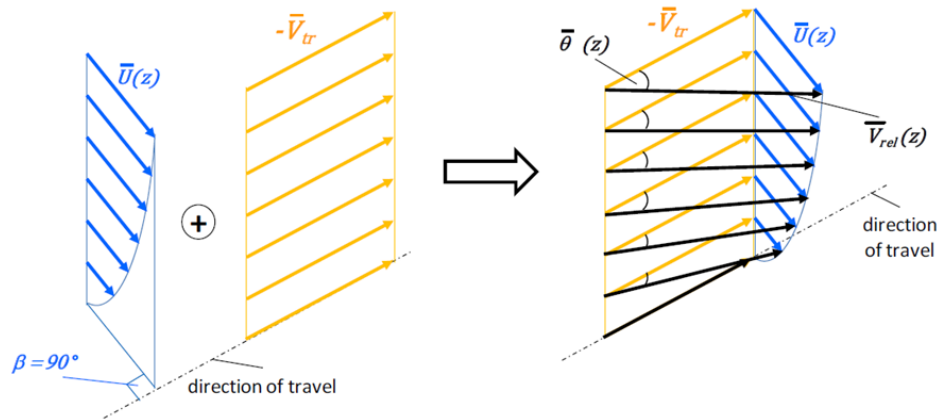


Figure 16 Skewed velocity profile relative to a moving vehicle (Dorigatti, 2013)

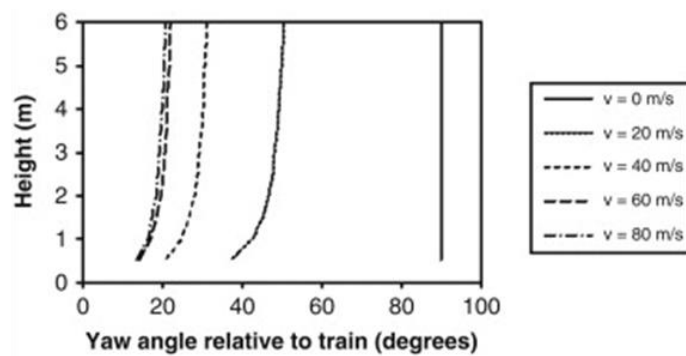


Figure 17 Relative yaw angle of crosswind experienced by train for differing train speeds

(Baker, 2010)

In the same way that the velocity profile seen by static and moving vehicles in crosswinds differs, this is also true for turbulence intensity (Baker, 2010). Figure 18 shows the effect of increasing train speed on the turbulence intensity experienced by that train in a crosswind. For the static train, the turbulence intensity profile is consistent with that of a flat-plate

boundary layer. As vehicle speed increases the gradient of the turbulence intensity below  $z=2$  m decreases and the profiles for  $u_{\text{train}} = 60$  m/s and  $u_{\text{train}} = 80$  m/s are nearly identical.

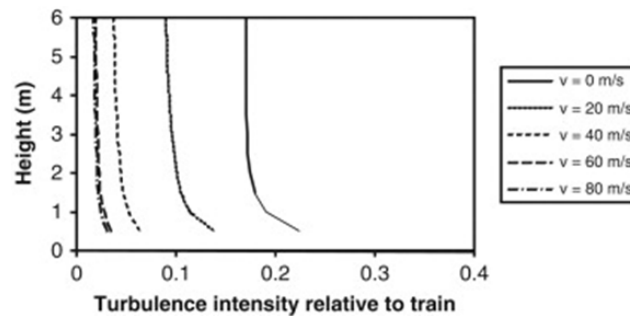


Figure 18 Turbulence intensity profile relative to a vehicle moving at differing speeds (Baker, 2010)

### 2.6.2 Crosswind-affected slipstreams

#### Full-scale experiment

When a train's slipstream is subjected to a crosswind, the flow around the train is convected towards the leeward side thus changing the flow properties at a given measurement point from what would occur if no crosswind was present. Slipstream amplification is the term used to describe the increase in slipstream velocity due to the effect of crosswinds on a train's slipstream. The effect of slipstream amplification has been reported in a number of full-scale measurement campaigns where ambient winds were present (Baker et al., 2013b, Figura-Hardy, 2002a, Rigby, 1982, Temple and Howlett, 1994, Figura et al., 1993, Figura-Hardy, 2002b, Bell, 1991).

Due to the variability of ambient winds, limited measurement campaign lengths and the variety of operational trains, it would be difficult to obtain sufficient full-scale slipstream data to understand the effect of crosswinds on train slipstreams. Because of the lack of available data at full scale, there is currently no firm consensus on the effect of crosswinds on the slipstreams of trains, although it has long been conjectured that there is a potential safety risk associated with the increased peak velocities (Sterling et al., 2008, Baker, 2010).

RSSB project T425 collated a vast amount of slipstream data which were obtained over several decades and from a variety of full-scale measurement campaigns (Rigby, 1982, Temple and Howlett, 1994, Figura et al., 1993, Figura-Hardy, 2002a, Figura-Hardy, 2002b, Bell, 1991). Figure 19 shows a selection of peak one second moving average velocities measured in the slipstreams of the broadly-named category of ‘freight trains’ subjected to different crosswind speeds. The majority of the data were obtained for crosswinds below 2 m/s, suggesting that either the measurement campaigns have been scheduled to coincide with calm weather or that slipstream data with crosswinds was discarded. Either way, it is the scarcity of such data which is the motivation for conducting the current research.

The slipstream velocities from trains travelling at 17 m/s and 18 m/s, in the crosswind range of 0-2 m/s, are 9.7 and 3.9 m/s, respectively. Of the data presented in Figure 19, only one peak velocity is in the 2-4 m/s range which is 8.9 m/s and is obtained for a train travelling at 15 m/s. In the crosswind range 4-6 m/s, trains travelling at 24 and 27 m/s produced slipstream velocities of 18 and 13 m/s, respectively. In the highest crosswind range, 6-8 m/s, velocities of 10 and 16 m/s are obtained from train speed of 19 and 21 m/s, respectively.

The run to run variability of freight train slipstream velocities is inherently large as a result of being comprised of large turbulent scales (Soper, 2014, Sterling et al., 2008). This variability is evident in the scatter in the crosswind data shown in Figure 19, especially considering that one second moving averages were applied which generally have a smoothing effect which increases conformity between runs. The data are presented as only crosswind speeds and as such, the resultant angle between the train and the wind is unknown. However, the data are useful to highlight that there is some effect of crosswinds on freight train slipstreams.

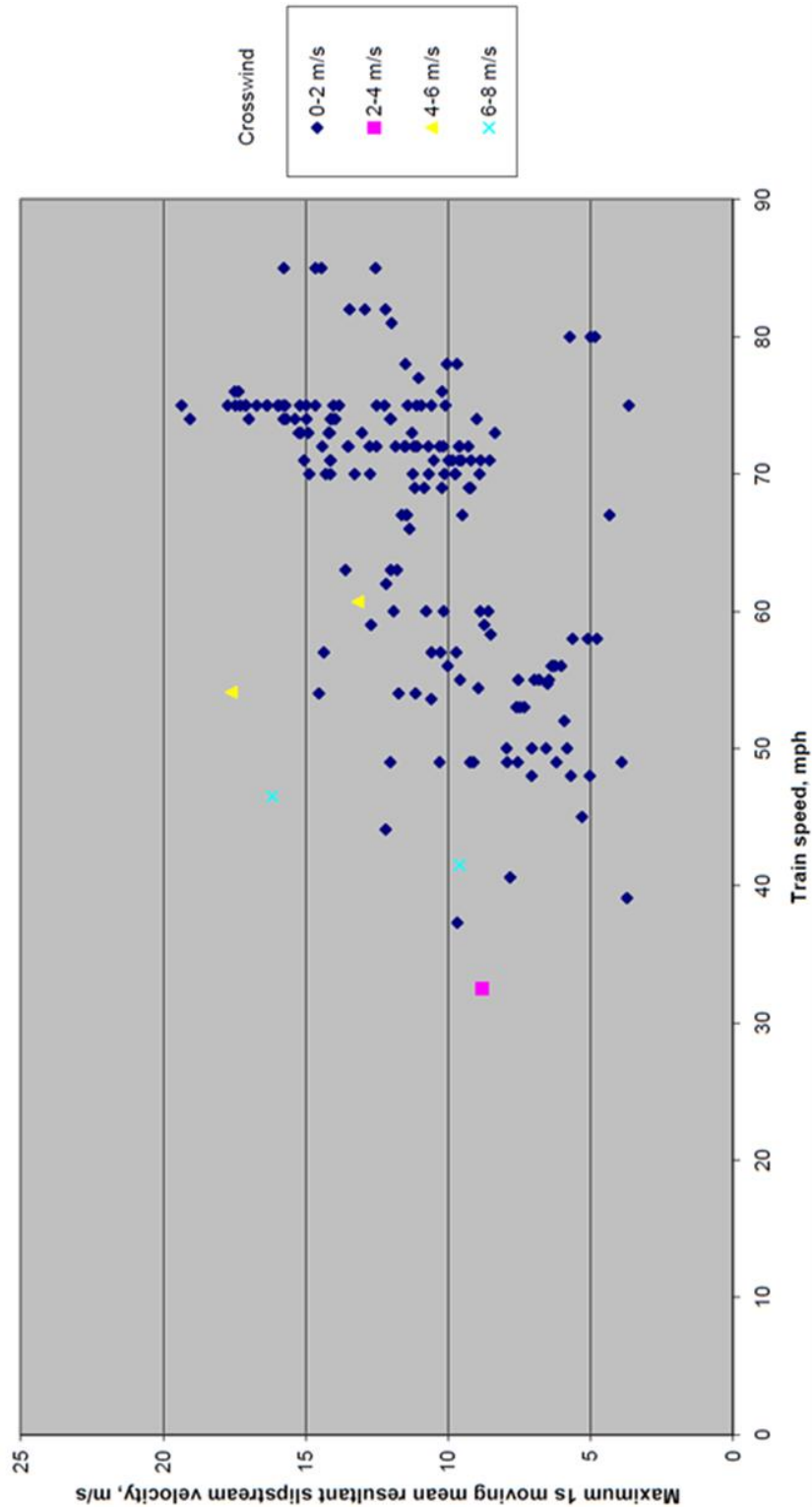


Figure 19 Maximum one second moving average velocities from freight trains 1.5 m from the platform edge (Figura-Hardy, 2005).

Figure 20 shows peak one second moving averages from Figura-Hardy (2005) and presented in Baker et al. (2007). The peak velocities are plotted against the resultant vector between the

wind and the train. In the case of the passenger train data (Figure 20a) it is observed that the best-fit line has a gradient of 0.02 of train speed per degree. It is acknowledged that the line of best-fit is somewhat of an approximation as there are only 33 data points above  $0^\circ$ , although this does indicate a general trend of increasing velocity with yaw angle.

The freight data shown in Figure 20b exhibit a similar trend to the passenger data, however the gradient of the best-fit line is 0.03 of train speed per degree. The rate of increase in the peak velocities with yaw angle are 50% greater for freight trains than for passenger trains in the data considered, although it is also acknowledged that there are only 13 data points in the  $\theta > 0^\circ$  yaw angle range, whereas the passenger train data has 33 within a shorter yaw angle range.

The data presented in Figure 20 show a general trend of increasing peak velocity with increasing yaw angle. The greatest rate of increase is observed to occur for freight trains although the data are relatively sparse and as a consequence of using the MOSMA technique, the true instantaneous peak velocities are unknown as are the locations of the peak velocities.

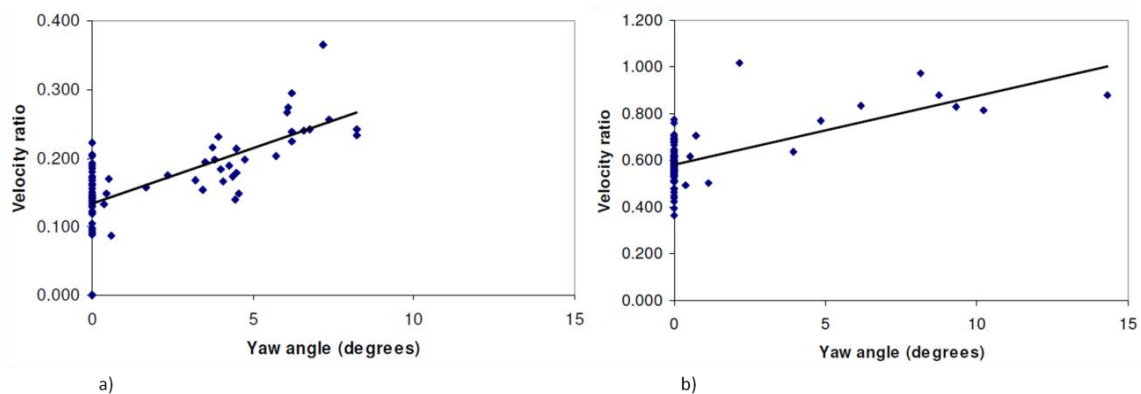


Figure 20 Maximum normalised slipstream velocities on the leeward side of a) passenger trains and b) freight trains (Baker et al., 2007)

The TSI and CEN standards require ambient wind to be below 2 m/s while measuring slipstream velocities at full-scale. Baker et al. (2013a, 2013b) collated data from the AEROTRAIN project (Sima et al., 2011) in order to determine the effect of minor winds on the slipstream of a high speed train. Slipstream velocities from approximately 300 runs in the presence of ambient winds were available for the Velaro S-103 passenger train which allowed for the analysis to be performed.

Individual slipstream measurements were made for each train pass and the yaw angle was determined from the resultant vector between the train speed and the wind. The wind speed and direction were approximated from the mean wind 3 s before the trains passed. The slipstream data were separated into yaw angle bands of  $1.5^\circ$  to  $0.5^\circ$ ,  $0.5^\circ$  to  $-0.5^\circ$  and  $-0.5^\circ$  to  $-1.5^\circ$ . The negative yaw angles signify that the instrumentation is on the leeward side of the train and for the positive yaw angles the instrumentation is on the windward side. The approximation of yaw angles into range bands was necessary because of the inherent measurement uncertainties associated with using unsteady winds.

Figure 21 shows ensemble-averaged velocities in the slipstream of the Velaro S-103 for each yaw angle band at  $z=0.2$  m and  $z=1.2$  m. The effect of the crosswind on the slipstream velocities is most evident on the leeward side of the train. The ensemble peak velocities at  $z=0.2$  m for the leeward, neutral and windward measurements are  $U=0.079$ ,  $0.062$  and  $0.054$ , respectively.

For slipstream measurements where there is no ambient wind present, it is often observed that the highest velocities occur in the near wake of passenger trains (Sterling et al., 2008). The peak velocities for the neutral and windward cases, at  $z=0.2$  m, both occur in the near wake of the train. The peak velocity in the leeward measurements occurs at  $x=180$  m and is more than 20 % greater than the nose peak. The near wake velocities are lower for the neutral and

windward cases at  $z=1.2$  m than were seen for  $z=0.2$  m, and the leeward velocities are more than 25% higher than were observed at  $z=0.2$  m.

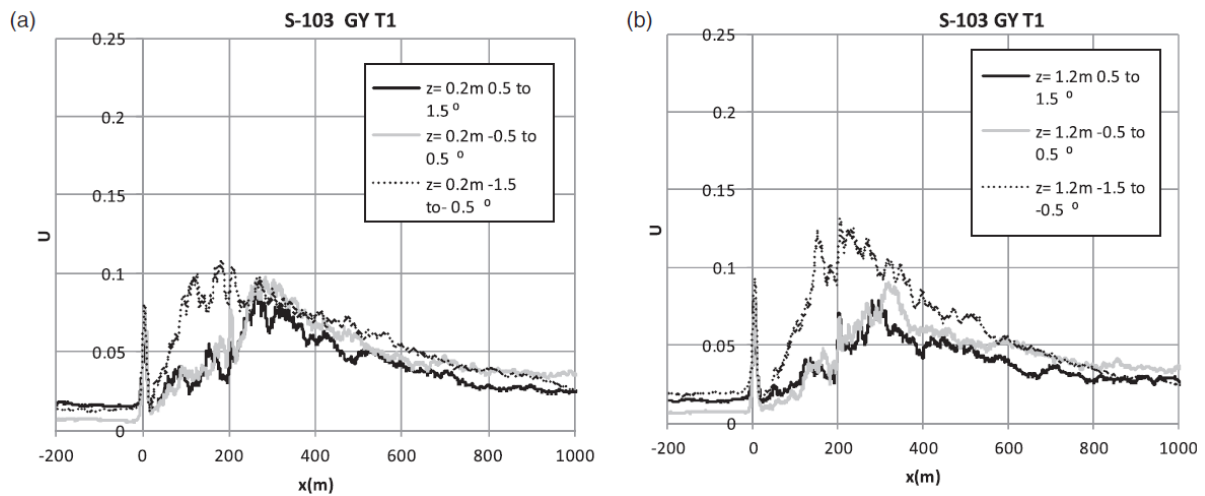


Figure 21 Normalised ensemble-averaged slipstream velocities of the S-103 at a)  $z=0.2$  m and b)  $z=1.2$  m (Baker et al., 2013b)

Normalised peak one second moving average velocities are shown in Figure 22 for a yaw angle range of  $-2.6^\circ$  to  $2.0^\circ$ . The data exhibit scatter reminiscent of that shown in Figure 20 although the yaw angles investigated in the research are significantly lower than those considered by Baker et al. (2007). The scatter in the data highlights the variability of instantaneous data insomuch as, for a given yaw angle, the velocities have a range of 0.1 of train speed. The data also show that even minor differences in yaw angle can cause relatively significant changes in peak velocities.

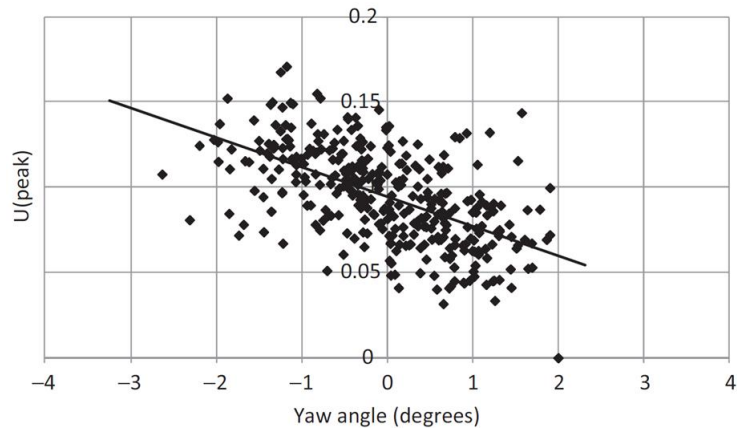


Figure 22 Normalised MOSMA velocities from the slipstream of the Velaro S-103 ET (Baker et al., 2013a)

The complications associated with measuring the effect of crosswinds on the slipstreams of full-scale passenger trains were highlighted by Quinn et al. (2011). The variability of natural wind means that the yaw angle experienced by a train will never remain constant for an entire train passage. The wind speed used to calculate the resultant yaw angle was approximated from the wind speed 3 s before the train passed and could have changed during the pass. This method of approximating the yaw angle is the most robust method available to researchers; however the yaw angles are at best approximated and the uncertainties associated with approximation should be taken into account.

### *Model-scale experiment*

The effect of a crosswind on the slipstream of a model-scale ICE2 was investigated by Baker et al. (2001). The 1/25th scale four-car ICE2 was fired at 30 m/s and was subjected to a 6m/s track-normal wind from a crosswind generator (CWG) (Figure 23). The resultant yaw angle is approximately  $\theta=11^\circ$  although some variation occurs due to slightly differing train speeds between runs.

The CWG was rather crudely constructed in comparison to more recently-developed CWGs (Dorigatti, 2013) and consisted of only three fans. Furthermore, the turbulence length-scales generated by the CWG are in the order of 3 m at full-scale which is significantly lower than expected from atmospheric winds where length scales are often in the order of 50 m (Cooper, 1984).

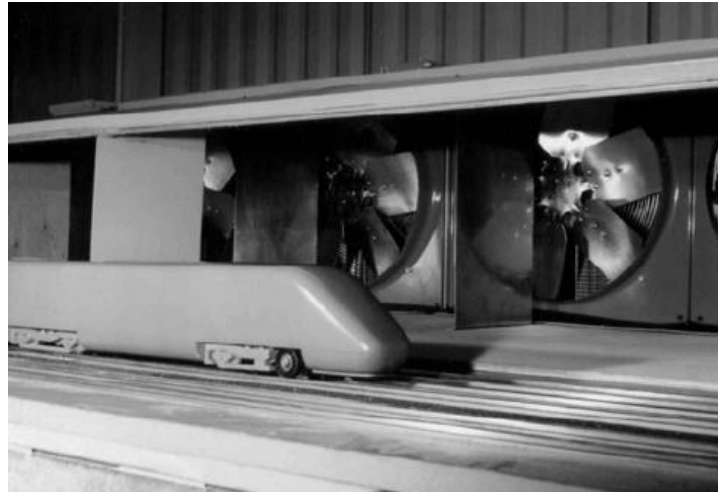


Figure 23 ICE2 model and crosswind generator used in (Baker et al., 2001)

Horizontal slipstream velocities were measured on the leeward side of the ICE2 by two-component hot-film anemometers at mid-height ( $z=2.25$  m) and lateral positions of  $y'=0.125$  m,  $y'=0.375$  m,  $y'=0.75$  m and  $y'=2.0$  m. The vertical component of velocity was neglected throughout due to the capability of the measuring equipment but also because there is no evidence in the literature to suggest that the vertical velocity component is significant in such flows.

The horizontal slipstream velocities generated by the model-scale ICE2 for the no-crosswind and crosswind cases are shown in Figure 24. At  $y'=0.125$  m the horizontal velocity in the no-crosswind case reaches a peak value of  $U_h=0.32$ , whereas in the crosswind case this peak is  $U_h=0.48$ . The velocity of the crosswind is  $U_h=0.16-0.18$ , so the leeward velocity is approximately the sum of the no-crosswind slipstream velocity and the crosswind velocity. It

is observed that at all distances from COT there is little variation between the sum of the crosswind speed and no-crosswind velocity and the velocities obtained from the crosswind case in the nose region. This behaviour is highlighted by the lack of discernible peak at 0 in Figure 25.

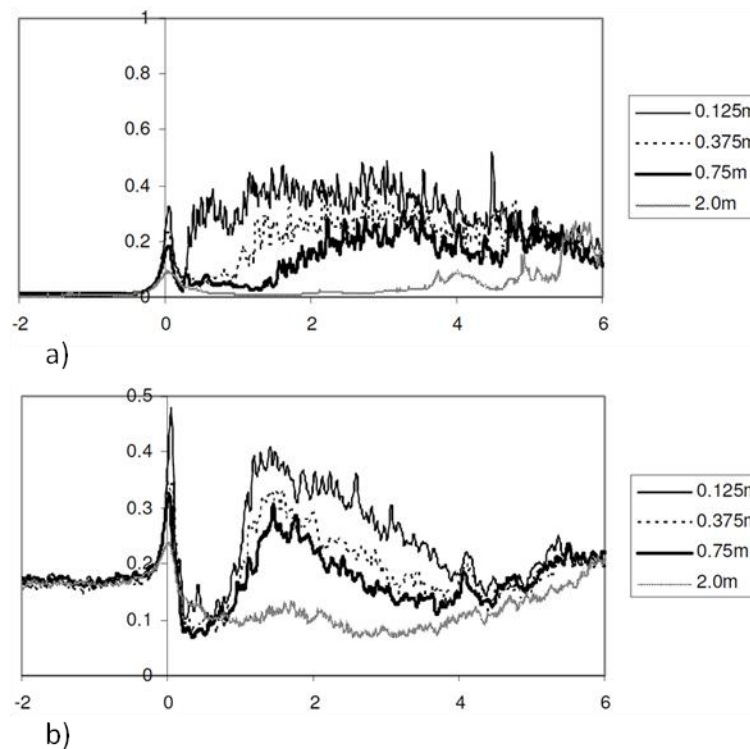


Figure 24 Horizontal velocities on the leeward side of a model-scale ICE 2 for a) no-crosswind and b) an  $11^\circ$  crosswind (Baker et al., 2007) (modified)

As the slipstream velocity begins to increase at approximately 0.3 in the no-crosswind case, the velocity in the no-crosswind case is observed to decrease for all distances from COT. The decrease in velocity is what Baker et al. (2007) referred to as the ‘shielding effect’ and is essentially a result of the train blocking the oncoming flow, much as it does in any bluff vehicle wake. At 1.8 m the crosswind case’s velocity is 0.25 greater than the no-crosswind case’s velocity for  $y'=0.5$  m and  $y'=1$  m. After the tail of the train, the slipstream velocity increases towards the velocity of the crosswind generator.

The most prominent feature of the crosswind case velocity is the peak-trough-peak behaviour between 0 and 1.5 (Figure 24). This is hypothesised to be the result of a vortex that is generated along the leeward side of the train similar to that found by Diedrichs (2003) at a yaw angle of  $\theta=30^\circ$  (Figure 26). It is unclear whether this rapidly-changing velocity could prove dangerous to persons on a station platform, but the variation is nonetheless significant.

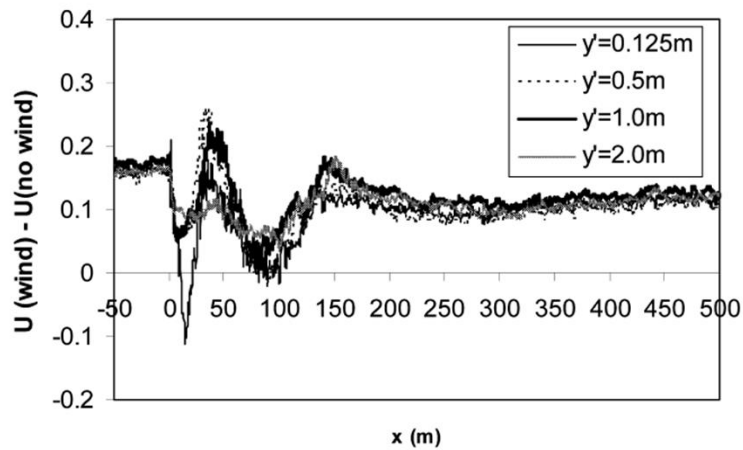


Figure 25 Crosswind  $U_h$  – no-crosswind  $U_h$  on the leeward side of model-scale ICE2 with crosswind at distances from train side and  $z=2.25$  m (Sterling et al. 2008)

The ‘ground’ surrounding the measurement hot wire anemometers was flat and level. Trains on the UK and European networks often run on ballasted track which have been shown to cause acceleration of crosswinds (Diedrichs et al., 2007), thus it is possible that the slipstream velocities observed in Figure 24 could be up to 30% higher with the inclusion of a ballast shoulder which, if true, would increase in slipstream velocities and also increase the forces experienced by a person at trackside.

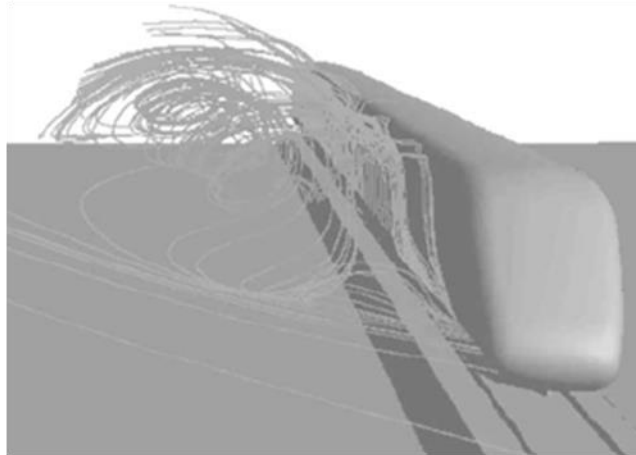


Figure 26 Leeward vortex along the length of an ICE 2 passenger train with a crosswind at 30° yaw (Diedrichs, 2003)

### *CFD for the crosswind effect on a train's slipstream*

A numerical investigation was commissioned as part of RSSB project T425 (Pope, 2006) in which the effect of crosswinds on the slipstreams of two generic train designs was studied (Bowman, 2005). The numerical work was intended to 'assist in bridging any gaps in the experimental data' but several issues with the methodology prevented the data collected from elucidating the behaviour of slipstreams when subjected to crosswinds.

The risk associated with the slipstreams of freight trains per train mile is ten times higher than for passenger trains (Pope, 2006), yet Bowman (2005) fails to use a train geometry that closely replicates a freight train. For the numerical simulations Bowman (2005) used two generic train geometries: the first consisting of only motor and passenger cars and the second was the same as the first except for the rear motor car which was altered to replicate a freight wagon. Due to the 'freight wagon' being at the rear of the train the effect of its geometry on slipstream growth could not be determined. The highest slipstream velocities are expected in the boundary layer region of a freight train's slipstream (Sterling et al., 2008), except around the Class 66 locomotive (Soper, 2014). By applying the 'freight wagon' at the rear of the

train, the study fails to capture the higher velocities that would otherwise have occurred due to rapid boundary layer growth in the slipstream of a freight train. Through a poor choice of geometry Bowman (2005) fails to address the concerns about which the study was first commissioned.

Bowman (2005) uses the RNG k- $\epsilon$  turbulence model which is a commonly-used linear eddy-viscosity model (LEVM) for bluff-body flows (Quinn and Richards, 2002, Revuz et al., 2009). The eddy-viscosity principle relates the larger-scale local strain-rate to the smaller-scale turbulent stresses and generally holds well for simple shear flows but weaknesses have been observed in the wakes of vehicles (Menter and Kuntz, 2004). Diedrichs (2003) subjected passenger train cars to crosswinds and noticed that in areas of flow with large strain rates (i.e. vehicle wakes), linear eddy-viscosity models had increased effective viscosity (kinematic + eddy viscosity), causing unphysical flow and leading to dubious solutions. In regions of large recirculation, non-linear eddy-viscosity models (NLEVM) produce much lower levels of effective viscosity, leading to more physical solutions and thus accurate results (Diedrichs, 2003). Further details about the weaknesses of eddy-viscosity models can be found in Wilcox (2003).

Verification is required to prove that the density of a mesh used in a CFD calculation does not affect the solution (Roache, 1998). To ensure this is the case, grid convergence studies should be conducted by varying the mesh density and monitoring several key variables, such as velocity and pressure. There is no evidence that Bowman (2005) conducts a mesh resolution check and as such the solution is not shown to be independent of mesh density.

A similar case to Bowman (2005) used CFD for the crosswind assessment of the German ICE2 passenger train (Diedrichs, 2003). Grid resolutions of 2.5 and 5 million cells per car were used, whereas Bowman (2005) uses only 0.27 million cells per car which is

approximately 10% of Diedrichs' (2003) coarsest mesh. The large difference in mesh density between the two cases suggests that the mesh resolution used by Bowman (2005) is not fine enough to ensure the high gradients of the flow are adequately resolved or that the wall function used by the RNG  $k$ - $\epsilon$  model is applied correctly. Failing to resolve the flow gradients or incorrectly applying wall functions makes the flow more unphysical and thus reduces the accuracy of a solution.

It is known from the literature that a person experiencing a mean wind speed of over 20 m/s is likely to become unstable or have difficulty walking (Penwarden, 1973). Bowman (2005) was aimed at determining whether the effects of crosswinds could increase the risk to persons produced by train slipstreams. By applying a mean 30 m/s crosswind Bowman (2005) renders the investigation redundant as the threshold for person becoming unsteady has already been exceeded and thus wind speeds are sufficient to prove dangerous to persons. Furthermore any loose objects on a platform are likely to have already been moved by the wind (Pope, 2006) and it is unlikely that the rail network would be operating in such high winds because of risks to vehicle overturning or trees falling on the lines (Network Rail, 2013).

When dealing with ground vehicle aerodynamics it is important to properly model the interaction of the ground and the air. Bowman (2005) applies a moving wall boundary condition to the ground plane in order to replicate the relative motion between the train and the ground. For cases with no crosswind the reference frame can be fixed on the train while the ground plane is given the same longitudinal velocity component as the inlet. When analysing the simulations, the longitudinal inlet velocity can be subtracted from the velocity in the computational domain replicating a train moving through still air. The use of a fixed reference frame negates the requirements for more complicated methods such as sliding meshes and has been successfully applied by (Hemida et al., 2012a, Huang et al., 2014).

Bowman (2005) suggested that future work should investigate the effect of crosswinds on passenger and freight trains using more accurate computational methods. So far no such work has been produced for freight trains despite Figura-Hardy (2005) and Baker et al. (2007) showing that their slipstream velocities are enhanced by additional crosswinds more so than passenger trains.

### ***2.6.3 Crosswinds, slipstreams and TSI***

The velocities measured in the slipstream of a high-speed passenger train travelling at 83.6 m/s, have been shown to be affected by even very low-speed crosswinds (< 2 m/s) (Baker et al., 2013b). If a crosswind was applied normal to track direction on a freight train operating on the UK network, and assuming line speeds of 120 km/h, the 2 m/s velocity would cause a yaw angle of 3.5°. It was seen in Figure 20 that the rate of increase of slipstream velocities is twice as great for freight trains as for passenger trains.

Using the lines of best fit from Figure 22, the normalised velocity as a function of yaw angle for the high speed passenger train would be

$$U = u_{\text{train}}(0.0114\theta + 0.113) \quad (2.19)$$

and using the best-fit line from Figure 20 for the freight train would be

$$U = u_{\text{train}}(0.029\theta + 0.58). \quad (2.20)$$

Assuming that the Velaro and freight trains were both travelling at maximum operating speeds then the peak velocities at the maximum possible yaw angles under the TSI ambient wind speed limit will be  $U=10.9$  m/s and  $U=22.5$  m/s, respectively. The velocity in the slipstream of the freight train is more than twice that shown for the Velaro.

It has been shown in the literature concerning full-scale train slipstream experiments that ambient winds are often higher than 2 m/s and so slipstream velocities greater than those which would be observed in the certification process will occur during operation. Forming a guideline for all eventualities of ambient wind speeds and yaw angles would be cumbersome and impractical especially considering that there is relatively little available data on the effect of slipstreams when subjected to crosswinds. A further consideration is the probability of incidents happening; this would be the product of the probability of a sufficient wind occurring and the train being at a place where pedestrians or trackside workers could be affected and also the persons' stance, height, weight etc. If the risk of person instability due to the above criteria is particularly low, no further action is likely to be taken.

To this end, it is clear that in order to define an industry standard by which train manufacturers should adhere to, firstly, the problem of slipstream amplification must be fully understood in order to provide a basis of knowledge for a statistical risk analysis to be performed. Such issues are the subject of the present thesis which, it is intended, will shed light on the issue of the effect of crosswinds on the slipstream of a freight train, but also give an insight into the potential risk to person stability associated with this phenomenon.

## *2.7 The effect of slipstreams on persons and objects at trackside*

In order to maximise route capacities it is desirable for train operators to increase the running speed of trains on rail networks. When the speed of a train is increased the slipstream velocity also increases at approximately the same rate. Aerodynamic forces increase nearly proportionally with the square of the velocity ergo at higher train speeds the forces experienced by persons and objects in close proximity to the train can be much greater than those at lower train speeds.

### ***2.7.1 Objects and persons on platforms***

Following documented reports of objects moving on platforms due to slipstream effects, Temple and Howlett (1994) investigated how objects moved when subjected to slipstream gusts. The experiments were aimed at replicating incidents from reports documented in reports compiled by Pope (2006). Objects such as pushchairs (single and double, loaded and unloaded), tools and trolleys were placed at distances of  $y \geq 1.5$  m from the platform edge and their motion was observed as regular line traffic passed by.

The operational speed of freight trains during the tests was as high as 126 km/h (34.9 m/s) whereas the Class 91s and HSTs had operational speeds of 151 km/h (42.0 m/s). Freight trains were found to cause the highest percentage of pushchair movement whereas the Class 94s and HSTs caused the least. The observations from Temple and Howlett (1994) agree well with slipstream data reviewed in Sterling et al.(2008), inasmuch as the slipstream velocities produced by freight trains are larger which explains the higher percentage of pushchair movement. It was also found that the orientation of the pushchairs had an effect on their mobility such that pushchairs facing or having their backs to the oncoming trains presented a larger surface area with which to convert the slipstream velocity into a force and induce movement.

Temple and Howlett (1994) showed that the slipstreams of passenger and freight trains are both capable of moving pushchairs on a station platform. In the event of a slipstream gust causing a pushchair to move resulting in the injury or death of an infant, the cost and negative publicity could have a detrimental impact on the railways as a business. To this end, the motivation for conducting research into the train slipstream velocities on station platforms is strong both in terms of financial loss and loss of life.

### ***2.7.2 Human stability in windy conditions***

Like all objects in the atmospheric boundary layer, people are often subjected to winds. In some cases, winds may be fast enough to cause discomfort or even affect a person's stability. Research from the field of person stability and wind comfort is yet to reach a consensus as to what constitutes a dangerous wind speed for a person. The reason for this is that there are a wide range of contributing factors to consider including gust duration, the person's age, weight, height, dress and physical fitness. Further complications include whether the person is walking or standing and their orientation to the wind. In the current work, dangerous winds speeds are considered to be those which cause a person to lose balance or change stance which is in line with the definition used by Jordan, (2008).

The level of disagreement of what wind speed is required to unsteady a person is highlighted by the range of wind speeds suggested in the literature. Melbourne (1978) and Penwarden et al. (1978) proposed mean wind speeds between 15 and 20 m/s whereas (Hunt et al., 1976) suggested that people would experience difficulty walking above wind speeds of 13-15 m/s. The consensus for person instability in gusty winds ranges between 11 and 28 m/s (Bottema, 1993, BRB, 1971, Durov, 1967, Hunt et al., 1976, Lawson, 1980, Melbourne, 1978, Penwarden et al., 1978, Peters, 1999, Soligo et al., 1998) (values quoted in Jordan et al.(2008)). As previously mentioned the large range of contributing factors to the stability of persons in windy conditions is highlighted by the range of wind speeds listed above and as such a method of approximating this behaviour is required.

In order to approximate the effect of winds from train slipstreams on passengers waiting on station platforms, Jordan (2008) developed a spring-mass-damper model to replicate a person's response to a gust. The model parameters were tuned against physical experiments where test subjects were subjected to gusts and had their motion observed. A full description

of the spring-mass-damper model and the experiments which it is validated against is given in Chapter 8.

### ***2.7.3 Risk***

In the event of train's slipstream causing injury to a passenger on a platform the network operator would be liable for the damages and compensation to the person injured. In order to assess the likelihood of these events occurring, risk must be calculated to predict a maximum likely expense. Baker et al. (2006) considered the risk to persons due to the effect of train slipstreams and it was found that of equivalent fatalities per year was 0.03, with an annual cost to the UK rail network of £41, 000 per year (2005 fatality worth £1.36 M).

With the increase in the use of the railways (DFT, 2007) there is likely to be an increase in the number of passengers waiting on station platforms and as such, the likelihood of an incident occurring will increase as will the number of equivalent fatalities.

The financial cost associated with the risk to persons on station platforms due to train slipstreams is not great enough to warrant expensive risk-averting systems such as barriers on platforms (RSSB, 2012). Alternative, and significantly cheaper, methods of reducing the risk of slipstream-related incidents which are currently deployed on the rail network are audible warnings of approaching trains and signs.

## ***2.8 Aerodynamic loading of container freight trains***

When a vehicle moves through the air it experiences forces and moments as a result of unbalanced pressures and frictional forces on its surface. In the absence of Reynolds number effects, the forces and moments experienced by a train will increase proportionally with square of the resultant velocity,

$$F = \frac{1}{2} \rho U_r^2 A C_F \quad (2.21)$$

$$M = \frac{1}{2} \rho U_r^2 A L C_M \quad (2.22)$$

where

A – specified area

L – reference length

$C_F$  – force coefficient

$C_M$  – moment coefficient.

Due to the quadratic relationship between wind speed and force coefficients, either increasing a vehicle's speed, or subjecting it to additional velocity components due to crosswinds, can significantly increase the aerodynamic forces experienced by vehicles.

The flow around bluff bodies, such as cubes, is dominated by large-scale separation and reattachment. Examples of bluff bodies in the world are buildings and many types of ground vehicles. Vehicles such as trains and lorries have bluffer cross-sections, due to requirements such as occupancy and storage capacity. Bluff vehicles such as freight trains generally have larger force and moment coefficients than more aerodynamically refined passenger trains.

### ***2.8.1 Aerodynamic drag of vehicles/trains***

Aerodynamic drag reduction is a key element of modern transport systems because reduced drag equates to reduced fuel consumption and thus making the mode more economical. Numerical simulations have been particularly prevalent in the reduction of aerodynamic drag for passenger and freight vehicles because they allow for easy identification of problem areas. Once the part of the geometry causing high drag it can be altered in CAD software and put

back into the CFD software and the simulations repeated. For some software this process is automated by way of parameter sweeping algorithms such as the Monte-Carlo method. Target parameters such as drag are set and the geometry is varied and optimised towards the desired parameter (Kumar et al., 2008).

Freight trains in the USA and Australia are often very long and travel may hundreds of miles across open country. Even though the trains do not travel very fast in comparison to passenger, the energy consumption because of the drag force experienced over such long distances can become significant. It was discussed earlier that the slipstream generated by freight trains with low loading efficiency can be particularly dangerous, but it is also the case that the drag they experience will be higher than trains with higher loading efficiency. Therefore it is the case that frugal operators will aim to load container wagons as efficiently as possible in order to reduce aerodynamic and fuel consumption.

Kumar et al. (2011) used computer sensors in order to assess the loading of a freight train passing out of a depot. From this information the fuel efficiency of the train during its operation could be predicted and hence lower values could be aimed for. Numerical simulations have been used alongside physical experiments to obtain the aerodynamic loading of each wagon in a freight train (Golovanevskiy et al., 2012).

### ***2.8.2 Crosswind loading on trains***

#### ***Incidents***

In the last 15 years there have been five container freight wagon overturning incidents in which crosswinds have either been cited as the sole, or major, contributing factors (ATSB, 2010, ATSB, 2011, RAIB, 2009, TSBC, 1999, Citynoise.org, 2006). The incidents in Canada and Australia (TSBC, 1999, ATSB, 2010, ATSB, 2011) all involved double-stacked container wagons which are not currently operational on UK rail networks. The height of the

wagons causes higher rolling moments than for single-stacked wagons which makes them particularly susceptible to overturning.

Although double-stacked container wagons are at greater risk of overturning than single-stacked wagons, crosswind incidents are not restricted to them. Similar, although not identical, incidents involving single-stacked container wagons have occurred in the UK. The accidents near Cheddington and Hardendale (RAIB, 2009) were both caused by strong winds affecting empty (or tare) container wagons. Unlike the incidents with double-stacked container wagons, the rolling moments experienced by the wagons were not sufficient to overturn them, however shedding of empty containers did occur as a result of decoupling from the flatbed wagons. Although no fatalities occurred during the incidents, the tracks were blocked and the overhead line equipment was damaged.

There are a number of factors that affect the flow around, and thus forces experienced by bluff bodies, namely; free-stream turbulence, interference effects from nearby objects, Reynolds number and shear (Holmes, 2007). Investigations of the flow around fundamental shapes often take the simplest form possible generally assuming steady, uniform velocity profile etc., however flows around real bluff bodies, such as trains in operational conditions, are seldom as straightforward and often include some or all of the factors mentioned above. The freight train investigations discussed below have all considered the factors mentioned above, to some extent, and the effect on the force coefficients are noted.

### *Freight wagon experiments*

The susceptibility of freight wagons to larger forces and moments than passenger trains is a consequence of their bluff geometries. The forces and moments experienced by different freight wagons in crosswinds have been investigated experimentally (Johnson, 2012, Krönke and Sockel, 1994, Watkins et al., 1992, Alam and Watkins, 2007, Alam and Watkins, 2006,

Soper, 2014) and numerically (Hemida and Baker, 2010, Liu et al., 2013, Golovanevskiy et al., 2012, Östh and Krajnović, 2014).

Following the container shedding incidents in Cheddington and Hardendale (RAIB, 2009) wind tunnel tests were conducted to establish the force and rolling moment coefficients on an FEA-B wagon loaded with a 60 ft International Shipping Organisation (ISO) shipping container (Johnson, 2012). The wind tunnel tests were conducted in accordance with the then current Railway Group Standard GM/RT 2142 (2009) in order to establish the intrinsic rollover wind speed of the container wagon. The mean rolling moment coefficients about the leeward rail were measured (Figure 27) and it was found that an error in the original Railway Group Standard GM/RT 2142 (2009) had overpredicted the required wind speed for rollover to take place. Had the wind speed been correctly set in the original standard, then evasive action could have been taken such as slowing the train and the incidents at Cheddington and Hardendale (RAIB, 2009) might have been averted.

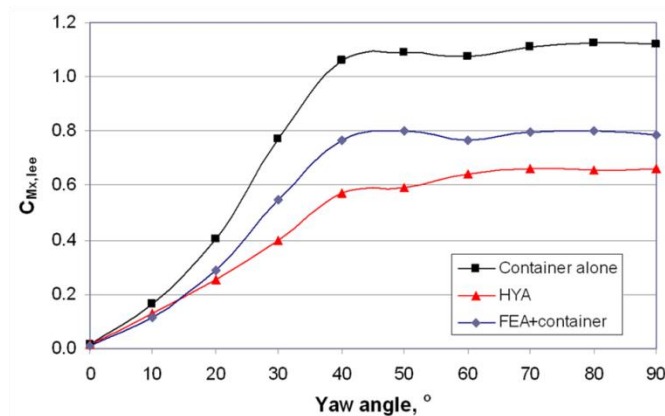


Figure 27 Rolling moments about the leeward rail (Johnson, 2012)

The cost and difficulties associated with full-scale aerodynamic testing were discussed in Section 2.5.2, as were the implications of model-scale testing. The Reynolds number of the flow around an operational freight train is generally one or two orders of magnitude greater

than can be achieved at model-scale and this deficiency is often assumed to have negligible effects on the similarity of the flows.

Watkins et al. (1992) and Alam and Watkins (2007) used wind-tunnel testing to obtain the aerodynamic forces experienced by 1/10<sup>th</sup> and 1/15<sup>th</sup> scale freight wagons, respectively, at varying yaw angles to the incident flow. Watkins et al. (1992) conducted a Reynolds number sensitivity analysis between  $Re=1 \times 10^5$  and  $Re=7 \times 10^5$ . At lower yaw angles, force coefficients were observed to be Reynolds number independent, although at yaw angles approaching  $\theta=15^\circ$ , some dependence on Reynolds number was observed; thereafter all tests were performed at  $Re=7 \times 10^5$ .

A similar wind tunnel investigation was performed by Krönke and Sockel (1994) using 1/7<sup>th</sup> and 1/3<sup>rd</sup> scale freight wagons. It was found that the Reynolds number had an effect on the force coefficients on the wagons tested; however as different wind tunnels were used, this effect cannot be solely attributed to Reynolds number effects, but more likely a combination of factors.

It is well known that adjacent objects will affect each other when subjected to winds as a result of, but not restricted to, wake flow interaction: this field of research is known as interference effects (Holmes, 2007). Watkins et al. (1992) studied the effect of position in a train on the drag force coefficients experienced by 1/10<sup>th</sup> scale hopper and gondola rail cars. Watkins et al. (1992) placed wagons upstream and downstream of an instrumented car which was attached to a force balance. The highest drag force was measured for the wagon with nothing upstream and half a wagon downstream, whereas the lowest drag force occurred for one wagon upstream and half a wagon downstream.

Wagons in the middle of long, regularly-loaded trains will experience similar aerodynamic loads once the slipstream becomes fully-developed and reaches equilibrium. Watkins et al.

(1992) proposed the concept of the ‘typical wagon’ to represent successive wagons experiencing regular flow. The force experienced by an entire train can be approximated by the product of the force on a typical wagon and the number of wagons in the train. Considerations must be made to account for the locomotive and the rear wagon which both experience higher forces than the other wagons (Watkins et al., 1992).

It was shown by Robinson and Baker (1990) that the force coefficients on an advanced passenger train (APT) were affected by the incident wind’s turbulence intensity,  $I$ , and length-scale,  $L_x$ . In the drag measurements made by Watkins et al.(1992) the effect of two turbulence intensities ( $I=1.5%$  and  $I=3%$ ) were investigated and were shown to have a negligible effect on the drag force coefficients. The intensity of the turbulence was very low in comparison to a natural wind in the ABL which is generally regarded as being approximately  $I=15%$ . Furthermore, the length-scale of the turbulence was not reported and as such, it is doubtful that the force coefficients presented are representative of the real-world scenario. This being said, Robinson and Baker (1990) showed that the effect of length-scale is negligible at yaw angles below  $30^\circ$ .

Wind tunnels and numerical simulations are both accepted methods of crosswind assessment for railway vehicles (CEN, 2010). Moving-model tests are a less conventional option for crosswind assessment of trains but have been successfully employed by Dorigatti (2013) and Soper (2014). The main advantage of using moving-models over static wind tunnel testing is that the relative movement between the train and the ground can be represented. A further advantage is that the ‘skewed’ velocity profile shown in Figure 16 can also be achieved. The major disadvantage of using a CWG is that there is no moving force balance and as such, forces must be approximated from discrete integration of surface pressures.

Soper (2014) subjected a Class 66 locomotive-hauled container freight train to a 30° crosswind in order to approximate the effect of adjacent container loading on the force coefficients experienced by an instrumented container. The containers used in the freight train are standard 60 foot ISO shipping containers with corrugations neglected. The forces on the instrumented container were approximated by pressure tapping the surface and performing discrete integration over a finite area around each pressure tap, as was done by Quinn et al. (2007) and Dorigatti (2013). For all of the merits of the moving model method, the main assumption of the work is that there is little spatial variation of surface pressure and that the number of pressure taps used is sufficient to capture representative surface pressures. The force coefficients were approximated from only 31 pressure taps which equates to 1 per 5.7 m<sup>2</sup> at full scale. The lack of resolution in terms of surface pressures on the container's surface means that potentially higher pressures could have been missed which reduces the accuracy of the approximation.

All of the crosswind analyses discussed above normalise the force coefficients by the container side area, front area or by the product of the length and height of the wagons. The current CEN (2010) guidelines recommend that forces on a train are normalised by a consistent area,  $A=10 \text{ m}^2$ , which allows for easy comparison to other vehicles. Using reference areas that are unique to a given vehicle restricts the applicability of the force coefficients thus making comparisons to other vehicles more difficult.

### ***2.8.3 CFD for crosswind assessment of trains***

CFD has been widely used for the aerodynamic load assessment of rail (Bouferrouk et al., 2012, Baker et al., 2011, Krajnovic, 2014) and road vehicles (Corin et al., 2008, Guilmineau et al., 2013) – especially high-sided vehicles such as lorries (Bettle et al., 2003, Hu et al., 2014) which are particularly susceptible to overturning (Baker, 1991b, Baker, 1991a). Using

CFD for the crosswind assessment of a vehicle allows for the aerodynamic loads to be obtained relatively quickly (depending on solution method) but also rapid design alterations can be made to a model in the development process (Krajnović, 2009b, Aïta et al., 1992).

With high speed passenger trains becoming lighter and travelling at higher speeds there has been research conducted over the last two decades to investigate whether incident winds have the potential to overturn HSTs (Sima et al., 2011). Freight trains are also susceptible to crosswind effects because they generally have much bluffer geometries and as such incur greater aerodynamic forces. Numerical modelling has been applied to the crosswind loading of passenger trains (Khier et al., 2000, Hemida and Krajnovic, 2005, Diedrichs et al., 2007, Cheli et al., 2010) and freight trains (Golovanevskiy et al., 2012, Hemida and Baker, 2010, Östh and Krajnović, 2014).

Some limitations of CFD when conducting the crosswind assessment of ground vehicles are scale for LES and DES, and accurate treatment for turbulence for RANS simulations. Discrepancies between CFD and experimental data can arise due to simulations assuming a different velocity profile to that used in the wind tunnel or no turbulence at the inlet for LES and DES (Guilmineau et al., 2013, Hemida and Krajnovic, 2005), even though wind tunnels always produce some level of turbulence and thus a greater difference in surface  $C_p$ s will occur than if turbulence levels were identical (Robinson and Baker, 1990).

The current work focuses on the effect of crosswinds on a freight train using CFD, although the literature of crosswind forces on freight trains is somewhat scarce due to the relative immaturity of CFD in comparison to wind tunnel testing.

Hemida and Baker (2010) used large-eddy simulation in order to investigate the force coefficients experienced by a 1/20<sup>th</sup> scale simplified FEA-B freight wagon (Figure 28). The work provided a previously-unseen view of the flow field around a stationary container

freight wagon subjected to a  $90^\circ$  wind in the presence of adjacent wagons which were simulated using periodic boundary conditions. The simulations conducted by Hemida and Baker (2010) lack validation against physical experiments, and as such the accuracy of the results cannot be verified.

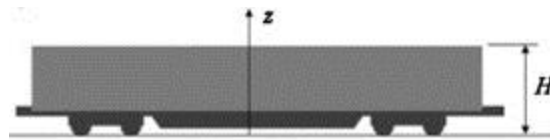


Figure 28 Freight wagon used by Hemida and Baker (2010) and flatliner

The inlet boundary condition used by Hemida and Baker (2010) was a uniform, steady velocity inlet even though Robinson and Baker (1990) showed that a low-turbulence approach can significantly affect force coefficients on a vehicle, especially at higher yaw angles. Numerical simulations require boundary conditions as inputs, although they often make assumptions of the flow which can be highly-idealised and can have a negative effect on the physicality of the solution. Without proper validation, the potential inaccuracies caused by the simplified boundary conditions used in this case cannot be quantified.

Golovanevskiy et al. (2012) used steady numerical simulations to determine the force coefficients on the wagons in a freight train when subjected to yaw angles at, and below,  $20^\circ$ . The weakness of using RANS simulations to perform crosswind assessment of bluff bodies is highlighted in the validation, where CFD results are up to 100 % greater than those obtained from the wind tunnel experiments. During the tests there is no evidence of mesh sensitivity tests being performed so the results may still be a function of the mesh density. Steady RANS simulations can be an effective method of obtaining mean force coefficients on trains however the methodology used must be robust as detailed by RSSB (2009).

# Chapter 3 Methodology

## 3.1 *Introduction*

The computational methodology applied in this thesis is described within the current chapter. A brief background of computational fluid dynamics is given in Section 3.2, followed by the case set-up for the crosswind and no-crosswind simulations Section 3.3, which in turn is followed by a description of the numerical method which was applied in those simulations Section 3.4.

## 3.2 *Computational fluid dynamics*

Computational fluid dynamics (CFD) is used in this thesis to investigate the effect of crosswinds on the slipstream of a model-scale freight train. CFD is a tool which numerically solves the governing equations of fluid dynamics for flow variables such as pressure and velocity with given boundary conditions in a prescribed computational domain. CFD has developed from its earliest form (Hess and Smith, 1967) where fluids were considered inviscid and irrotational to become a versatile method of predicting fluid flows for a wide range of applications.

Ever-advancing computer technology has, in recent years, allowed for more computationally expensive methods of fluid flow calculation, such as large-eddy simulation (LES) (discussed in Section 3.4.4), to be used, which allows for greater insight into the stochastic nature of turbulent flows by directly resolving large scales of the bulk flow. LES negates the reliance on Reynolds-Averaged Navier-Stokes (RANS) methods, which are based on the time-averaged Navier-Stokes equations and model the effect of turbulent fluctuations on the mean flow.

As accurate as CFD simulations become, engineers and scientists must not be solely reliant on numerical simulations as they are prone to errors which arise due to numerical approximation, assumptions of fluid behaviour, boundary conditions or human error. Verification and validation of numerical simulations is essential in order to determine the accuracy of the results obtained.

### **3.2.1 *OpenFOAM***

The present work utilises the open source CFD package, OpenFOAM 2.1.1 (Open Foundation, 2012). One of the main advantages of using an open-source code is that the requirement for licenses is bypassed. This is especially important considering that licenses are required for parallelisation of simulations across multiple nodes and can make larger simulations, such as those using LES, prohibitively expensive. Access to open source CFD codes allows scientists and engineers around the world to conduct advanced research without incurring large expenditure of licenses.

Open source codes such as OpenFOAM are often over-looked by companies on the grounds of their fidelity, however databases such as European Research Community on Flow, Turbulence and Combustion (ERCOFTAC, 2014) have allowed for some aspects of the code to be validated thus rendering concerns over the code's fidelity moot.

The other main advantage of using OpenFOAM over commercial codes is that the source code can be altered for specific applications as per the requirements of the user. Users also have a greater degree of control over the specific solvers and boundary conditions than they would with commercial codes which promotes user understanding of the fundamentals of CFD and prevents the software from being used as a 'black box'.

The mesh generation in the present work was performed using snappyHexMesh (SHM) which is a utility within OpenFOAM that generates unstructured hexahedral grids. SHM

allows for hexahedral cells to be generated for complex geometries where the use of structured grids would be unfeasibly difficult to generate.

SHM works by breaking a coarse ‘background’ mesh into smaller cells and removing cells that are entirely inside the geometry of the object that is being meshed. The cells that are partially inside the geometry are then broken down into smaller cells and again, those left inside the model are removed. This process is repeated to a specified tolerance and after which, prism layers, if needed, are added to the surface of the model.

### **3.3      *Slipstream Simulation setup***

From the literature, it is evident that freight trains have the most potential for generating slipstreams which are dangerous to persons (Sterling et al., 2008, Soper et al., 2014) . It has also been observed, from the limited available data, that freight trains exhibit a greater degree of slipstream amplification than passenger trains do. By reason of these observations, it has been decided that a freight train will be used to investigate the effect of crosswinds on train slipstreams. The British Class 66 locomotive has been chosen to head the container freight train because recent research has highlighted potential risks due to the high velocities generated around this vehicle (Soper et al., 2014) and also experimental data from this experiment can be used to validate the numerical simulations.

#### **3.3.1   *Geometry***

The train model used in the current work is a 1/25<sup>th</sup> scale British Class 66 locomotive with 4 fully-loaded FEA-B container wagons in tow. The present work was validated against moving-model physical experiments which were conducted at The University of Birmingham’s moving-model test facility in Derby.

In order to ensure a quality validation of the numerical simulations, the dimensions of the train model were matched as close as practically possible to the moving-model. The dimensions of the locomotive, containers and flatbed wagons will be considered separately, below.

The Class 66 locomotive has been operational in the UK since the year 2000, and is an extremely bluff railway vehicle (Figure 5), especially when compared to other vehicles on the UK rail network such as the Class 43 high speed train (HSTs). The Class 66 has a tractive effort of 409 kN, an operational speed of 120 km/h (33 m/s) and weighs of approximately 130 tonnes. The computer-aided design (CAD) model of the Class 66 locomotive used in this work is shown in Figure 29. The model has a full-scale height of 4.35 m, width of 2.68 m, the wheels are 1.20 m apart and the lowest point of clearance between the train and the ground is 0.25 m; henceforth all dimensions will be given at full-scale. The dimensions of the CAD model relate to the moving-model used in Soper (2014) and do not necessarily compare to the full-scale vehicle.

The origin in the present work is in line with the front face of the train, at the centre of track (COT) and at the top of rail (TOR). All distances in the present work will be given relative to the origin unless otherwise stated.

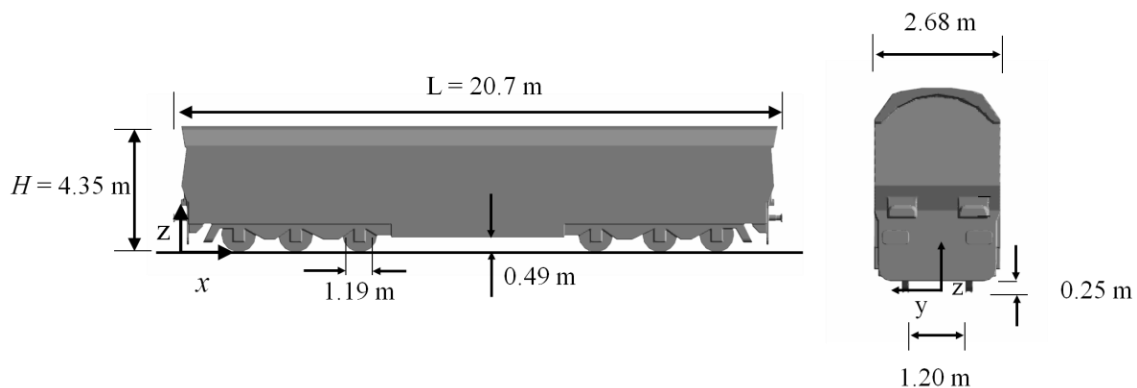


Figure 29 Dimensions of the CAD model of the Class 66 locomotive.

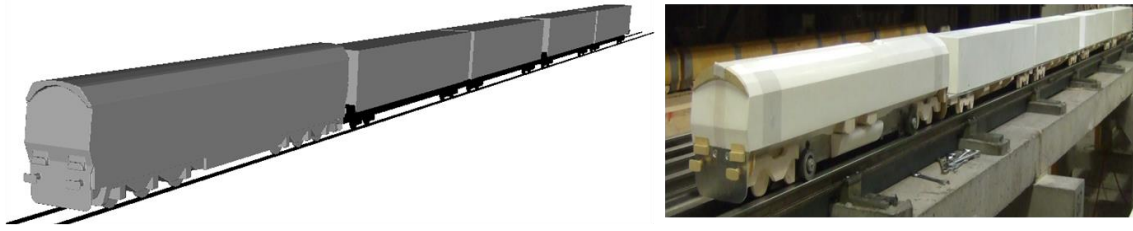


Figure 30 Numerical (left) and experimental (Soper, 2014) (right) Class 66 locomotive models with four fully-loaded FEA-type B container wagons.

Figure 30 presents a juxtaposition of the CAD model used in the present work and the physical model used in Soper (2014). The models have a good degree of similarity although some simplifications are made to the CAD model to allow for a higher-quality mesh. In order to propel the physical model, a rope must be attached to the underside of the locomotive. This mechanism requires a strong mounting point so it is looped around a hook attached to a metal block which has not been included in the CAD model. It is assumed that the blockage caused by the mounting point beneath the train does not affect the slipstream around the sides.

The FEA-B wagon used in the present work consists of two parts; a container (Figure 31) and a flatbed wagon (Figure 32). The wagon shown here differs very little compared to the model used in the physical experiments. The bogies on the CAD model are more complex than those in the physical experiments, which have dummy bogies to shield the functional wheels.

The container used on the wagons is a cuboid with external measurements of a standard 60 foot, ISO container (Figure 31). The containers used were simplified by neglecting the corrugations, which was also done by Alam and Watkins (2007) and Hemida and Baker (2010) with satisfactory results. The total height of each container wagon is 4 m above TOR.

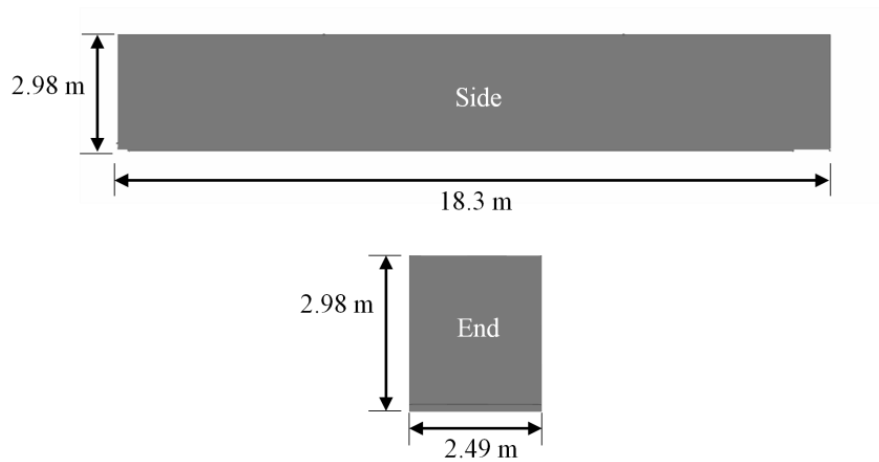


Figure 31 Dimensions of ISO container model.

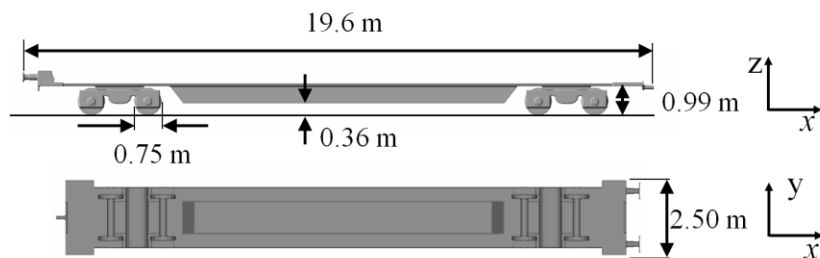


Figure 32 Dimensions of the flatbed wagon.

Close attention has been paid to the under floor construction of the locomotive (Figure 30) and subsequent container flats (Figure 32) because the largest boundary layer growth, and hence the highest slipstream velocities, are generally associated with measurements closer to the ground at trackside (Sterling et al., 2008, Baker et al., 2013b). By ensuring the vehicle has an appropriate level of under-floor complexity, the growth of a realistic slipstream is promoted.

In order to closely replicate the physical experiments, rails were added to the simulations and extended 8 locomotive heights ( $H$ ) ahead of, and behind, the train. The rails were modelled as simple blocks of 0.1 m high and 0.15 m wide. These are not the dimensions of full-scale rails but are intended to replicate those at the moving-model rig.

Figure 33 shows the positions of the front faces of the containers relative to the origin as well as the size of the inter-wagon spacings. The containers are positioned in pairs to replicate the coupling which occurs in operational conditions.

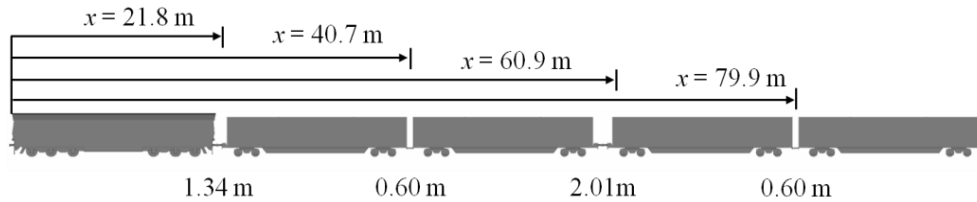


Figure 33 Distances of front faces of locomotive and containers from the origin and size of inter-wagon spacings

The container freight train considered in the present work is fully-loaded, which means that the containers are the largest size that can be fitted onto the flatbed wagons. The effect of lower loading efficiencies (size of load relative to wagon size) on slipstream development has been investigated by Soper (2014), however the fully-loaded configuration was chosen for the purpose of proving a baseline capability of CFD and allowing for the possibility of using lower loading efficiencies for future investigations.

### **3.3.2 No-crosswind case**

#### *Computational Domain and Boundary Conditions*

The computational domain used in the no-crosswind case is shown in Figure 34. The simulations replicate the relative movement between the train and the ground by specifying a moving-wall boundary condition for the ground plane and rails, which are given the same velocity as the inlet. By holding the train in a fixed reference frame, the correct relative movement between the train and the ground is achieved without the need for complex simulation methods such as sliding meshes and has been used successfully by Hemida et al. (2014) and Huang et al. (2014).

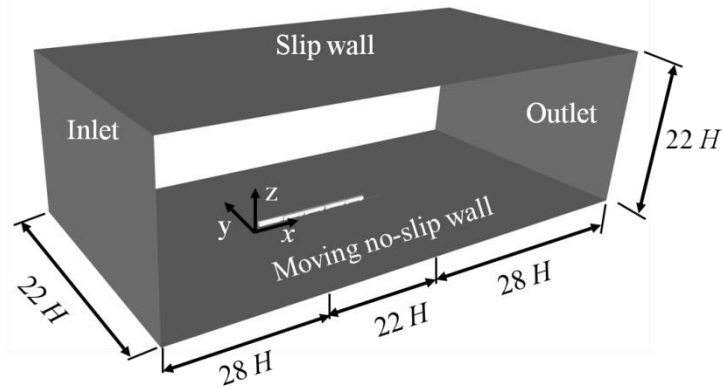


Figure 34 Computational domain used for no-crosswind simulations

The boundary conditions are a crucial aspect of a numerical simulation and therefore the boundary conditions used must be realistic and well-posed in order to ensure physical solution. An example of an unphysical boundary condition would be a ‘slip’ boundary condition on a flat plate with a fluid moving over it. The ‘slip’ boundary condition would not allow for the growth of a boundary layer on the plate’s surface, which is what would occur in a physical experiment, thereby creating an unphysical flow. In some cases however, it is possible to make assumptions of the flow behaviour without compromising the accuracy of the solution. For example, applying a slip condition on a boundary where the adjacent flow is steady, uniform and far enough from the object of interest such as the roof of the current computational domain.

The side walls of the computational domain were also set as slip walls and were deemed not to require periodic boundary conditions due to the size of the domain. The outlet is a zero pressure outlet and is  $28 H$  downstream of the last wagon. This distance has been used in previous studies (Hemida et al. 2012) and is sufficient to allow for wake development. The inlet condition is a block velocity profile with a value of 23 m/s and is  $28 H$  upstream of the locomotive. Based on the CEN (2011) recommendations for passenger trains, the inlet of the computational domain should be at least  $8 H$  from the nose of the train and the outlet section should be at least  $16 H$  from the tail of the train. Similar dimensions to these were used in the

slipstream simulations of a passenger train conducted by Hemida et al. (2012b). However, the Class 66 locomotive has a very bluff cross-section and to ensure a pressure build-up did not occur at the inlet, the domain was further enlarged upstream. The boundary conditions applied in the no-crosswind case are summarised in table 1.

Table 1 Boundary conditions applied in the no-crosswind case.

<b>Boundary</b>		<b>Boundary</b>	
<b>Inlet</b>	Constant velocity	<b>Roof</b>	slip wall
<b>Outlet</b>	Zero pressure	<b>Floor</b>	constant velocity
<b>Side 1</b>	slip wall	<b>Train</b>	no-slip wall
<b>Side 2</b>	slip wall	<b>Rails</b>	no-slip wall

The Reynolds number,  $Re$ , of the simulations in the present work based on height and resultant velocity is  $Re=300,000$ . As discussed in Chapter 2, the Reynolds number of the flow around an operational freight train would be approximately 40 times greater than in the present work. A Reynolds number sensitivity analysis was conducted at Reynolds numbers of  $Re=200,000$  and  $Re=240,000$  to determine their effect on velocity and pressure. For the majority of train length, the flow variables from each Reynolds number case showed differences below 10 %, although at further distances from train side the velocity nose peak's agreement was as far as 20 % between cases. A comparison of the results showed differences in the flow variables that were largely within the bounds of expected statistical variation (Soper, 2014) suggesting that Reynolds number independence could be assumed above  $Re=200,000$ .

### *Computational Mesh*

The computational meshes used in this work are unstructured hexahedral grids and the coarse and fine meshes consisted of 25 M and 34 M cells, respectively. The surface mesh on each container wagon for the coarse mesh consisted of 0.4 M cells whereas the surface mesh on the locomotive consisted of 0.6 M. The mesh is dominated by hexahedral cells but other polyhedral elements are also present due to the complexity of the geometry (Figure 35). The meshes were generated using the SHM utility within OpenFOAM. The quality of the meshes was verified using mesh metrics within OpenFOAM and it was ensured that the maximum skewness of every cell was below 4 and maximum non-orthogonality was less than 60: corrections were made for the non-orthogonality in the solver. Skewness in this case is defined as the distance from the face centre to the intersection of the line between the two adjacent cell centres which is then normalised by the centroid-to-centroid distance of the adjacent cell. Orthogonality is calculated as the dot product of the face area vector normalised with a vector from the centroid of the cell to the centroid of the adjacent cell.

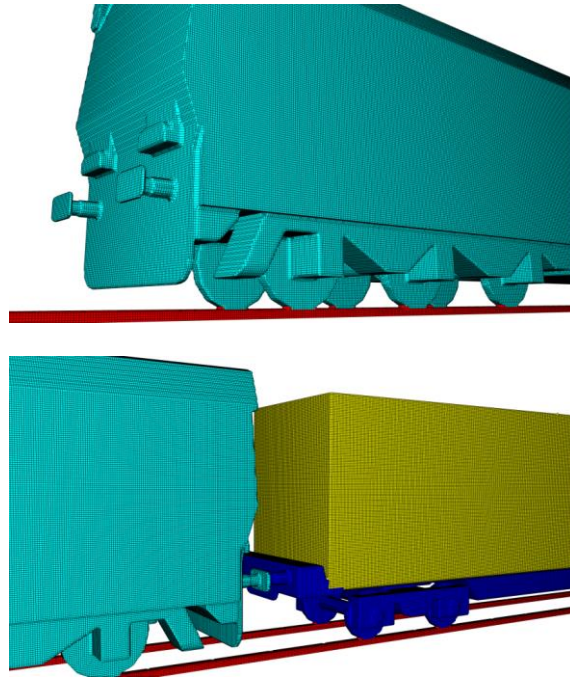


Figure 35 Surface mesh on the complex geometry of the Class 66 locomotive and first container wagon.

Figure 36 shows the mesh used in the no-crosswind simulations on a cut-plane positioned at  $y=0$  m. It should be noted that the cells which appear triangulated are hexahedral cells however the appearance of triangulation is a common visualisation error (Lewis et al., 2009) and does not represent the true geometry of the cells.

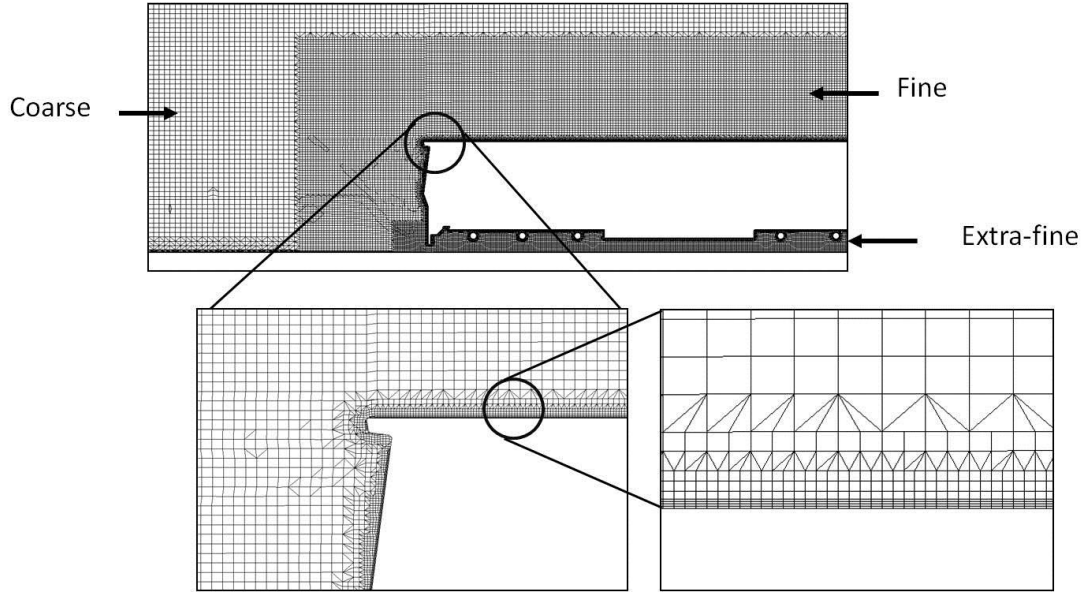


Figure 36 Mesh resolution around the Class 66 locomotive on a cut plane at  $y=0$  m.

In order to resolve the highly turbulent Couette-like flow, which exists beneath the freight train, an extra-fine refinement box was used, as seen in Figure 36. It is particularly important in this case to resolve the flow in the under-floor region because it has been associated with the highest slipstream velocities in the boundary layer region of various trains (Sterling et al. 2008, (Huang et al., 2014, Hemida et al., 2012a).

The boundary layer is a key flow feature in a turbulent flow and thus its resolution or representation is crucial to ensure the accuracy of the simulations. The turbulent boundary layer consists of four distinct regions viz: the laminar sub-layer ( $0 < y^+ < 5$ ), buffer region ( $10 < y^+ < 30$ ), log-law region ( $30 < y^+ < 500$ ) and the wake region ( $y^+ > 500$ ) where  $y^+$  is given as

$$y^+ = \frac{u_* y}{\nu}, \quad (3.1)$$

$$u_* = \sqrt{\frac{\tau_w}{\rho}}, \quad (3.2)$$

and 
$$\tau_w = \mu \left( \frac{\partial u}{\partial y} \right) \quad (3.3)$$

where

$\mu$  – dynamic viscosity ( $\text{kg m}^{-1}\text{s}^{-1}$ )

$\frac{\partial u}{\partial y}$  – wall-normal velocity gradient ( $\text{s}^{-1}$ ).

Figure 37 shows the mean velocity profile of an idealised two-dimensional turbulent boundary layer and a CFD representation of it for an inadequately coarse mesh. The closest cell to the wall is so large that the high velocity gradient is underestimated by the simulation. Neglecting the velocity gradient near the wall will misrepresent the shear stress at the wall which will affect factors such as turbulence production and separation.

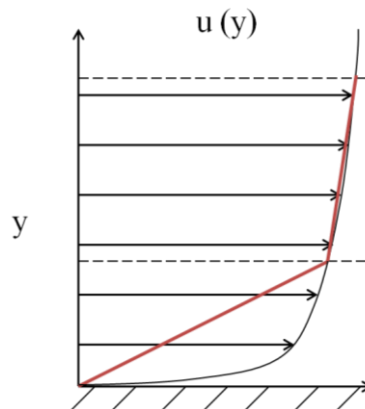


Figure 37 Time-averaged velocity profile of an idealised 2-D boundary layer: expected profile (black line) and simulated velocity profile in CFD (red line) using coarse mesh (dashed line).

To ensure that the velocity gradients near the wall are correctly represented, four prism layer cells were applied to the surface of the vehicle (Figure 36). The maximum distance between the centre of the first cell layer and the surface of the train is 0.1 mm. The  $y^+$  over the majority of the train's surface was between 10 and 50, with a small number of localised

exceptions occurring. The ‘Spalding wall function’ (Launder and Spalding, 1974) was applied because of the value of the average  $y^+$  on the surface of the train.

Wall functions are generally calibrated using channel flow experiments and have little physical relevance for general purpose cases where wall-normal flows exist, although neglecting the gradient entirely may have a worse effect on a solution’s accuracy and so a wall function is applied here.

### 3.3.3 Crosswind cases

#### Domain and Boundary Conditions

The computational domain used for the two crosswind cases is shown in Figure 38. The domain is sized so that it is large enough to be used for the  $10^\circ$  and  $30^\circ$  yaw angle crosswinds and it has two inlets and outlets to ensure that the flow covers the entire train.

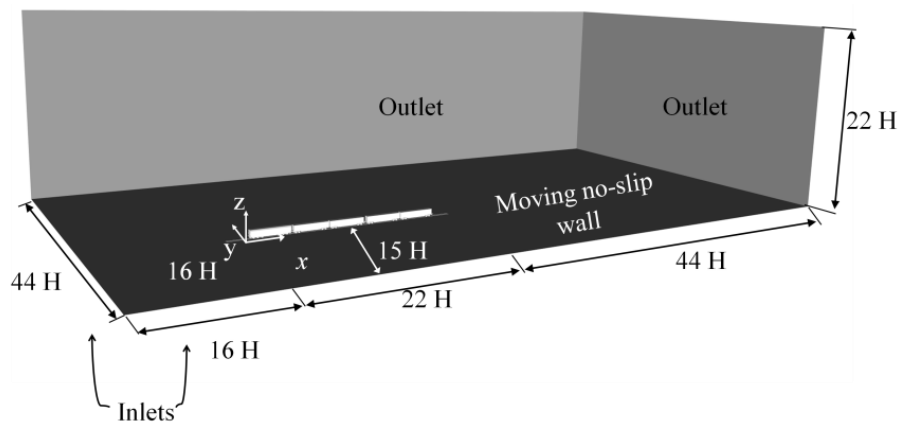


Figure 38 Computational domain for the crosswind simulations, missing walls are inlets and roof.

The inlets provide uniform velocity profiles at yaw angles of  $10^\circ$  and  $30^\circ$ , where the resultant inlet velocity is  $u_r=23$  m/s. The ground plane is a no-slip moving wall and is set to the longitudinal inlet velocity component,  $u_{train}$ , but it also acts as a no-slip wall for the lateral velocity components which affects the flow as it passes through the domain. The outlets are

zero-pressure outlets and the roof is set as a slip wall. The boundary conditions used for the crosswind cases are summarised in Table 2.

Table 2 Boundary conditions for the crosswind cases

Boundary		Boundary	
<b>Inlet</b>	Constant velocity	<b>Roof</b>	slip wall
<b>Outlet</b>	Zero pressure	<b>Floor</b>	constant velocity
<b>Inlet</b>	Constant velocity	<b>Train</b>	no-slip wall
<b>Outlet</b>	Zero pressure	<b>Rails</b>	no-slip wall

The numerical simulations are designed to adhere as closely as is reasonably possible to the moving-model crosswind experiments (Soper, 2014) although features such as the turbulent inlet characteristics are not attempted in the current work. The CWG used by Soper (2014) has an average span-wise and vertical turbulence intensity of approximately  $I=18\%$  which is broadly in accordance with turbulence intensities in natural wind (Holmes, 2007). Some turbulence at the inlet may be beneficial however a uniform inlet is specified for simplicity and to provide a basis of comparison for future work where turbulent inlets could be applied.

#### *Computational Mesh*

The computational domains contained coarse and fine meshes consisting of 45 M and 65 M cells, respectively. By generating a multi-purpose domain, which can be used for both yaw angle cases, the process of further mesh generation can be avoided which is advantageous for complex geometries where quality mesh generation can be very time-consuming. Another advantage of using the same meshes for both crosswind cases is that there is no difference in

mesh quality between the simulations. The fine surface mesh consisted of approximately 0.84 M cells on each container wagon and 1 M cells on the locomotive. The size of the meshes used for the crosswind cases are 80% greater than those in the no-crosswind case due to the much larger wake region, greater separation over the containers as well as the requirement for the meshes to be functional for multiple yaw angles. As with the no-crosswind meshes, it was ensured that the cells for the crosswind cases were not skewed and had non-orthogonality levels below 60.

Figure 39 shows the mesh refinement regions around the train and it can be seen that the mesh is biased towards leeward side of the train to ensure that the majority of the cells are placed in the wake, where resolution is most important.

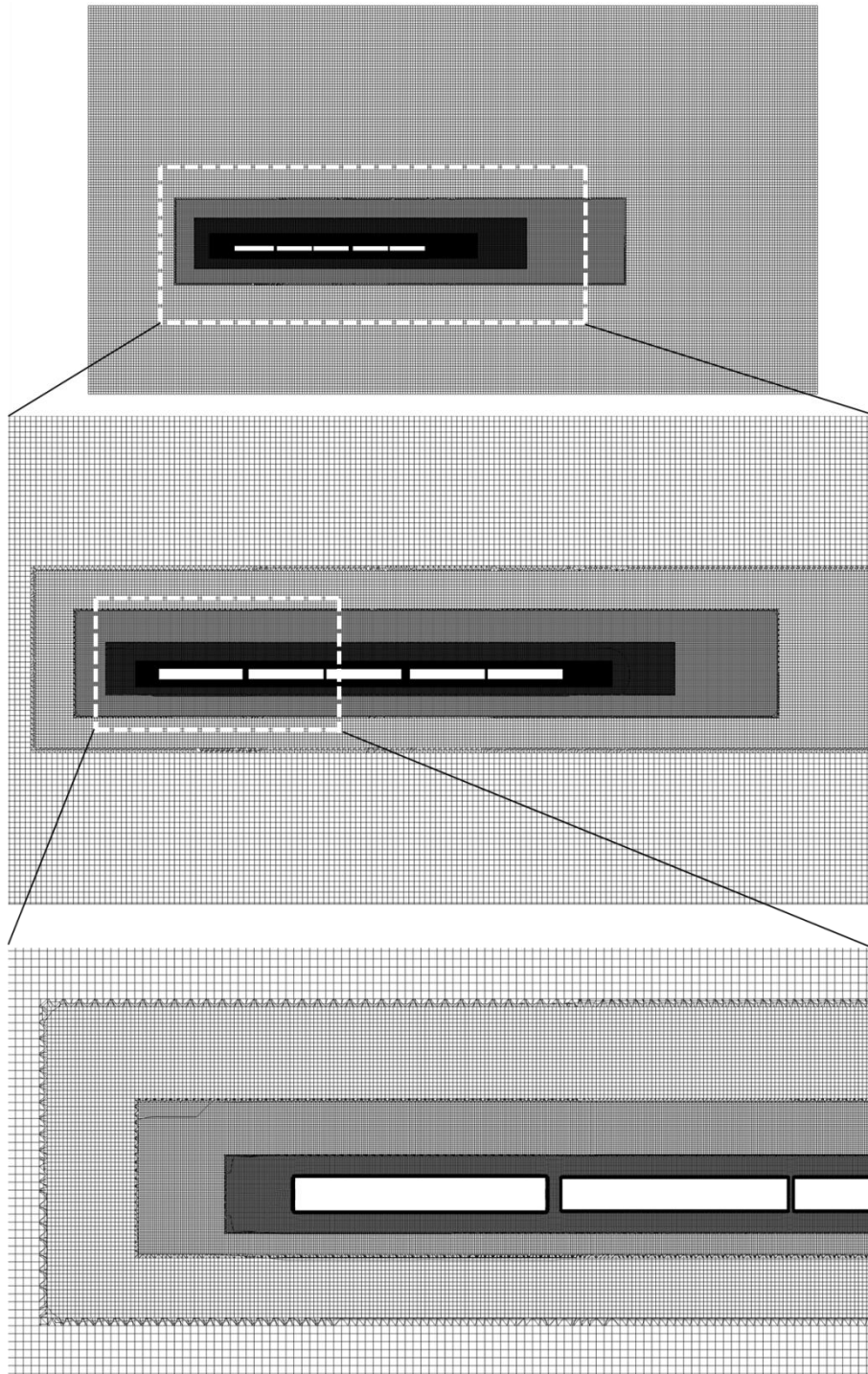


Figure 39 Mesh regions used in the crosswind cases

## 3.4 Numerical method

### 3.4.1 Discretisation

The finite volume method (FVM) is a discretisation method for partial differential equations and is based on control volume integration. FVM is widely used in fluid dynamics, heat and mass transfer. Due to the FVM using control volume integration, the flux across cells can be simply determined and hence conservation is also easily maintained. The incompressible momentum equation in the integral form is given as

$$\begin{aligned} \frac{\partial}{\partial t} \int_V u_i dV + \int_V u_j \frac{\partial u_i}{\partial x_j} dV = -\frac{1}{\rho} \int_V \frac{\partial p}{\partial x_i} dV \\ + \int_V \frac{\partial}{\partial x_j} \left( \nu \frac{\partial u_i}{\partial x_j} \right) dV + \int_V S dV \end{aligned} \quad (3.4)$$

where

$V$  – cell volume

$p$  – static pressure

$S$  – source term.

The method by which the values within the mesh are interpolated is known as discretisation and there are many ways to approximate the same gradient although each method will have different effects on the solution.

Consider the one-dimensional control volume in Figure 40. The node, P, is surrounded by node, W, and node E, signifying the west and east nodes, respectively. The west and east faces of the control volume are given as  $w$  and  $e$ , respectively. The velocity is considered to be positive when travelling from west to east and the velocity at western face of volume P is signified as  $u_w$ .

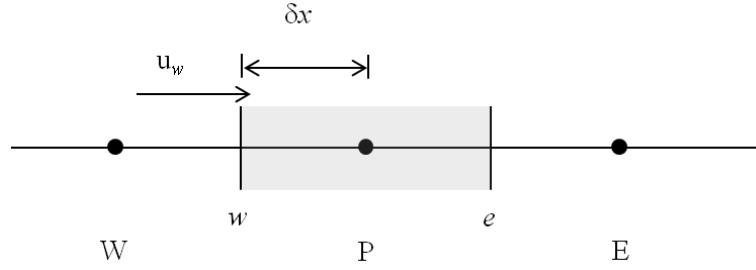


Figure 40 One-dimensional control volume

The convective flux across a cell can be approximated as by linear interpolation, otherwise known as central differencing (CD), and is given by

$$a_P \phi_P = a_W \phi_W + a_E \phi_E \quad (3.5)$$

where

$\phi$  - transported quantity

with central and neighbour coefficients given by

$$a_P = \rho u_e - \rho u_w, \quad a_W = \rho u_w, \quad a_E = \rho u_e. \quad (3.6)$$

Using pure central differencing in high-fidelity CFD simulations such as DNS, LES and DES is ideal as this allows the greatest amount of energy to be retained in the solution although CD is inherently unstable for general-purpose convection-diffusion problems and ‘wiggles’ or even massive instabilities can occur in the solutions (Versteeg and Malalasekera, 2007). The instabilities when using central differencing arise when Péclet numbers (cell Reynolds numbers) become greater than 2. The Péclet number,  $Pe$ , is defined as

$$Pe = \frac{\text{Advective transport}}{\text{Diffusive transport}} = \frac{U_c L_c}{D} \quad (3.7)$$

where

$L_c$  – characteristic cell length (m)

$U_c$  – velocity in cell (m)

$D$  – diffusion coefficient ( $m^2/s$ ).

Upwind differencing schemes assume an upwind bias, also unlike central differencing, first order upwind discretisation is sensitive to the flow direction and the central and neighbour coefficients are given by

$$\begin{aligned} a_P &= a_W + a_E + (\rho u_e - \rho u_w), & a_W &= \max(\rho u_w, 0), \\ a_E &= \max(0, -\rho u_e). \end{aligned} \tag{3.8}$$

Blended central-differencing (BCD) schemes combine the results at nodal points obtained for upwind differencing and central differencing. The formulation of the BCD scheme uses a weighting factor,  $\gamma$ , to control the contribution of the CD and UD schemes and is defined as

$$\phi_{BCD} = (1 - \gamma)\phi_{UD} + \gamma\phi_{CD}. \tag{3.9}$$

It can be seen that higher values of  $\gamma$  signify a greater contribution of central differencing to the solution. BCD has been successfully employed in large-eddy simulations for freight train aerodynamics (Östh and Krajnović, 2014), where a factor of  $\gamma=0.95$  was used. BCD was applied to the convection terms in the no-crosswind case and the blending factor was set to  $\gamma=0.95$  to aid the stability of the solution without compromising the accuracy of the results.

Central-differencing has been discussed as being the ideal choice for retaining the energy content of a turbulent flow although its main weakness is that it can become unstable in convection-diffusion problems. Total-variation diminishing (TVD) schemes are an alternative

to the conventional central differencing discretisation approach and can be applied to flows with higher Reynolds numbers without the developing numerical instabilities. The study of TVD schemes is a broad and highly-mathematical area but a brief review of the relevant fundamentals is presented below.

Direct interpolation between the nodes P and E, to obtain the value at of the property,  $\phi$ , at face, e, is given as

$$\phi_e = \frac{\phi_P + \phi_E}{2}. \quad (3.10)$$

An upwind-biased central-difference approximation of the eastern face value can be given as

$$\phi_e = \phi_P + \frac{1}{2}(\phi_E - \phi_P). \quad (3.11)$$

The upwind-biased CD scheme can be manipulated so that the general form of the convective flux though the east face can be given as

$$\phi_e = \phi_P + \frac{1}{2}\Psi(r)(\phi_E - \phi_P) \quad (3.12)$$

where

$\Psi(r)$  – Sweby limiter.

The Sweby limiter (Sweby, 1984) is a function of r, which is defined as

$$r = \left( \frac{\phi_P - \phi_W}{\phi_E - \phi_P} \right) \quad (3.13)$$

and is the ratio of the upwind to the downwind gradient of the property ,  $\phi$ .

This type of TVD scheme is referred to in OpenFOAM as the limitedLinear scheme as a reference to the Sweby limiter and linear interpolation. The limitedLinear scheme applied to the convection terms for both crosswind cases where the Sweby limiter was set to 0.6.

Due to the instantaneous nature of detached-eddy simulation, the temporal term in the momentum equations requires discretisation. The temporal terms for all cases were discretised by using a second order backward implicit scheme which is given as

$$\phi^n = 3\phi^n - 4\phi^{n-1} + 2\phi^{n-2} \quad (3.14)$$

where

$\phi^n$  – transported quantity at current time-step.

It can be seen from equation (1.36) that the solution at time step  $n$  is dependent on the solution at the previous two time-steps which has the implication of relatively high computational cost although the main benefit of the scheme is that it provides the solution with second-order temporal accuracy and increased numerical stability.

The time-step size was based around the value of the Courant-Friedrichs-Lewy (CFL) number. The CFL number is a stability criterion which is employed when solving partial differential equations and is often the limiting value of time-steps in CFD simulations.

Figure 41 is a schematic of a one-dimensional mesh with cell width,  $\delta x$ , and a fluid particle travelling at  $u_\infty$  through it. The CFL condition ostensibly states that the time-step,  $\Delta t$ , must be small enough to ensure that a fluid particle travelling at  $u_\infty$  should not travel further than  $\delta x$  in  $\Delta t$ . The CFL condition for stability is described mathematically as

$$\text{CFL} = \frac{u_{\infty} \Delta t}{\delta x} < 1. \quad (3.15)$$

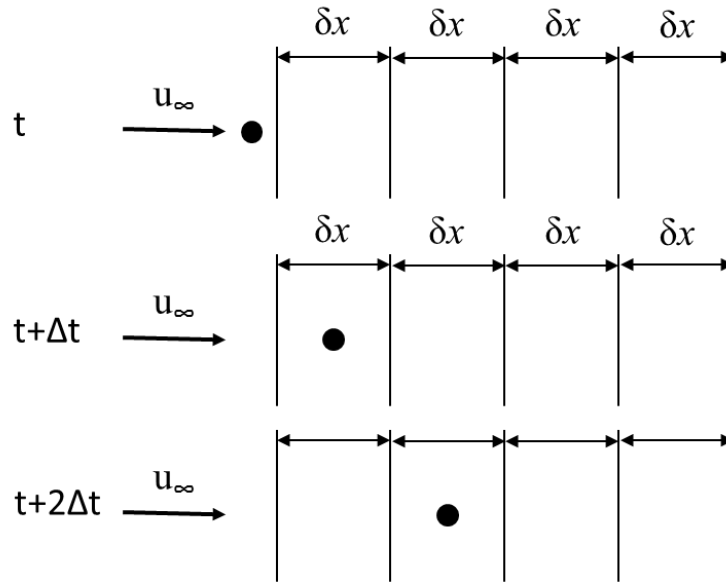


Figure 41 Schematic diagram of a particle travelling through a one-dimensional mesh over three time-steps and conforming to the CFL condition

The discretisation schemes used in CFD are often dependent on the flow variables in the adjacent cells and as such, if a particle, such as that shown in Figure 41, were to pass through more than one cell in a given time-step the results obtained from the discretisation scheme would have their accuracy affected. For explicit discretisation schemes, a violation of the CFL condition can cause numerical instabilities, although the temporal scheme used in this work is implicit.

The mean and maximum CFL numbers in both computational domains have approximate values of 0.001 and 2.0, respectively. The CFL number only exceeded 1 in approximately 1% of the cells around the train and the effect of the minor violation of the CFL condition was assumed to be negligible. The high computational cost associated with maintaining the low CFL number is compensated by the resolution of the high frequency/small-scale structures in the flow.

### ***3.4.2 Pressure/velocity decoupling***

By definition the Navier-Stokes equations are coupled, non-linear partial differential equations. Every component of velocity appears in each momentum equation as well as in the continuity equation; however pressure only appears in the momentum equations. In this sense, pressure and velocity are coupled variables and must be decoupled before they can be solved for.

Pressure-velocity decoupling was performed in this work using the pressure interpolated splitting of operators (PISO) algorithm (Issa, 1986). The PISO algorithm performs (usually) two pressure-correction steps and is non-iterative, unlike the semi-implicit method for pressure-linked equations (SIMPLE) (Patankar and Spalding, 1972), which only has one pressure correction step.

### ***3.4.3 Matrix Solution Algorithms***

Once the governing equations are discretised, they require solving so that the values of flow variables can be obtained. The solution of the discretised equations is obtained by using matrix solution algorithms and these methods are generally very efficient, robust and usually designed specifically for CFD purposes (Versteeg and Malalasekera, 2007). The two algorithms used in the current work were the geometric algebraic multi-grid (GAMG) method for pressure (Mavriplis and Venkatakrishnan, 1995) and the pre-conditioned bi-conjugate (PBiCG) solver for velocity. Each algorithm was chosen for its respective flow variable on the basis of efficiency i.e. whichever algorithm was fastest was employed, providing the set tolerances were met.

The solutions to the discretised equations in each time step were deemed to be converged when the absolute value of the residual was  $10^{-8}$  for both the momentum and continuity equations. The relatively high tolerance was chosen to ensure minimal effects of rounding

error which could otherwise prove significant because of the large number of time-steps in the solution.

#### ***3.4.4 Large-eddy simulation***

Solving the Navier-Stokes equations directly is called direct numerical simulation (DNS) and provides very high resolution data because all of the turbulent scales in a given flow are resolved. In order to resolve all of the turbulent eddies in a given flow, the mesh resolution requirement increases proportionally with  $Re^{9/4}$  (Davidson, 2004). For flows of engineering interest, Reynolds numbers are often very high ( $Re > 100,000$ ) so applying DNS is prohibitively expensive and is expected to be for many decades to come (Davidson, 2004).

The principle of large-eddy simulation is that the larger energy-containing turbulent scales within a flow are directly resolved and the effect of the smaller scales are accounted for using a ‘sub-grid’ model. It is assumed in LES that the smaller scales will have little effect on the flow and that neglecting them will not significantly alter the solution. Pope (2000) suggested that 80 % of the turbulence kinetic energy within a given flow should be directly resolved, although this figure appears somewhat arbitrary and is not supported by a justification.

The concept of large-eddy simulation was first proposed in the twentieth century by Joseph Smagorinsky (1963) and was originally intended for meteorological flows. In the last two decades, researchers have applied large-eddy simulation to bluff-body vehicle aerodynamics (Krajnović, 2009a, Hemida and Krajnovic, 2005, Liu et al., 2013, Hemida and Baker, 2010, Östh and Krajnović, 2014). LES is ideal for simulating the flow around bluff model-scale vehicles because the wake flow is dominated by large turbulent scales which are then directly resolved giving greater accuracy than would otherwise be achieved by modelling them. The smaller scales in the flow are modelled because they have low energy content and their contribution to the force coefficients is negligible. The resolution of the wake flow is

important to vehicle aerodynamicists because its size determines the magnitude of the force coefficients experienced by shorter vehicles (Baker, 1991a). The downside of LES is that with current computing power, the flow simulations are generally restricted to model-scale testing and hence the Reynolds numbers are significantly lower than operational cases.

The first conceptual step of LES is the definition of the filtering operation where the flow variables are decomposed into the filtered and residual components. The filtered components are resolved directly whereas the residual components are accounted for by using a sub-grid scale turbulence model.

The filtering operation is used to decompose the flow variables is defined by

$$\bar{\phi}(x, t) \equiv \int_{-\infty}^{\infty} \int_{-\infty}^{\infty} \int_{-\infty}^{\infty} G(x, \acute{x}, \tilde{\Delta}) \phi(\acute{x}, t) d\acute{x}d\acute{y}d\acute{z} \quad (3.16)$$

where

$G(\dots)$  - filter function

$\bar{\phi}(x, t)$  – filtered function

$\phi(\acute{x}, t)$  – unfiltered function

$\tilde{\Delta}$  - filter cut-off width.

The filter cut-off width,  $\tilde{\Delta}$ , is the length at which the scales will no longer be resolved and the sub-grid model is applied for scales below this value. There are many ways to select the filter cut-off width but the most common and robust method is to use the cube root of the volume of the smallest cell size which is given as

$$\tilde{\Delta} = \sqrt[3]{\Delta x \Delta y \Delta z} \quad (3.17)$$

where

$\Delta x \Delta y \Delta z$  - volume of the smallest cell.

By selecting the cut-off width approximately the size of the smallest cell, it is ensured that the sub-grid model will not be applied where turbulent eddies can be directly resolved.

The velocity field is decomposed into the filtered,  $\tilde{u}$ , and residual,  $u'$ , components by

$$u = \tilde{u} + u' \quad (3.18)$$

and the same operation is performed for the pressure field

$$p = \tilde{p} + p'. \quad (3.19)$$

The filtering method is analogous to the Reynolds-averaging procedure used for RANS but in this case  $\overline{\tilde{u}} \neq 0$  and  $\overline{\tilde{p}} \neq 0$ , where the over-bar denotes time-averaging

Once the filtering method has been selected it must be applied to the governing equations.

Applying equation 1.40 to the continuity equation we get the filtered continuity equation

$$\frac{d\tilde{u}_i}{dx_i} = 0 \quad (3.20)$$

and applying equation 1.40 and 1.41 to the momentum equation yields

Equation

$$\frac{\partial \tilde{u}_i}{\partial t} + \tilde{u}_j \frac{\partial \tilde{u}_i}{\partial x_j} = -\frac{1}{\rho} \frac{\partial \tilde{p}_i}{\partial x_i} + \frac{\partial}{\partial x_j} \left( \nu \frac{\partial \tilde{u}_i}{\partial x_j} \right) + \frac{1}{\rho} \frac{\tau_{ij}}{\partial x_j}, \quad (3.21)$$

where

$\tau_{ij}$  – anisotropic residual stress tensor.

In a similar way that the RANS equations require closure, the filtered Navier-Stokes equations also require closure. The isotropic and anisotropic components of the residual stress tensor can be equated to the eddy-viscosity hypothesis by

$$\tau_{ij} = \tau_{ij}^R - \frac{1}{3}k_r \delta_{ij} = -2\nu_{sgs}\widetilde{S}_{ij} \quad (3.22)$$

where

$\delta_{ij}$  – Kronecker delta function

$k_r$  – kinetic energy of the residual components

$\nu_{sgs}$  – eddy-viscosity of the residual motions

$\widetilde{S}_{ij}$  – filtered rate-of-strain tensor.

The eddy-viscosity or ‘sub-grid’ viscosity,  $\nu_{sgs}$ , is derived from the mixing length hypothesis and is modelled as

$$\nu_{sgs} = l_s^2 \bar{S} \quad (3.23)$$

where

$l_s$  – Smagorinsky length scale

$\bar{S}$  – characteristic filtered rate of strain.

The Smagorinsky length-scale,  $l_s$ , is analogous to the mixing length in Prantl’s mixing length model and is taken to be proportional to the filter cutoff width,  $\tilde{\Delta}$ , by the Smagorinsky constant,  $C_s$ , thus

$$v_{sgs} = (C_s \tilde{\Delta})^2 \bar{S} \quad (3.24)$$

where

$$C_s = 0.07.$$

The simplicity of the standard Smagorinsky model makes it an attractive choice to researchers even though the model does not account for backscatter (energy transfer from the residual motions to the resolved motions), assumes isotropy at small-scales and  $C_s$  is considered to be constant although it has been shown to vary in homogeneous turbulence (Schumann, 1975).

Although the above assumptions are made, the standard Smagorinsky model has been successfully used in bluff body vehicle aerodynamics (Krajnović, 2010, Krajnović, 2009a, Hemida and Krajnovic, 2005, Hemida et al., 2012a) and was chosen in this work because it is also less computationally expensive than the dynamic Smagorinsky model (Germano et al., 1991) where  $C_s$  is locally calculated at each time-step.

### ***3.4.5 Delayed Detached-Eddy Simulation***

Using LES can be very computationally expensive, especially at higher Reynolds numbers where the computational cost of resolving the boundary layer increases proportionally with  $Re^{1.8}$  (Piomelli, 2008). To overcome the high cost of LES, delayed detached-eddy simulation (DDES) (Spalart et al., 2006) was used in the present work. The principle of DDES is that the detached flow is resolved using LES and the attached flow on the walls is simulated using a RANS model. The Spalart-Allmaras one equation turbulence model (Spalart and Allmaras, 1992) was used to simulate the attached flow on no-slip walls in the DDES calculations in

this work. The model was chosen because of the relatively low computational expense in comparison to standard two-equation models such as the k- $\epsilon$  and k- $\omega$  models. The Spalart-Allmaras model used in this work is different from the original model and the distinctions will be discussed in Section 3.4.5.2.

DDES is an improvement over the original DES method which suffered from grid-induced flow separation. It was observed by users of DES that thickening boundary layers or ‘ambiguous’ grids promoted early flow separation caused by a premature switch between RANS and LES modes in the upper region of the boundary layer (Deck, 2005). The premature switch between modes RANS and LES modes lead to a reduced eddy-viscosity because the grid refinement was not fine enough to support Reynolds stress resolution of LES, in that region. This phenomenon is known as modelled stress depletion (MSD) (Spalart et al., 2006). It is considered unlikely that premature flow separation will occur in the present work due to the sharp edges of the freight train forcing separation, however DDES is applied as a precautionary measure.

#### 3.4.5.1 *DDES length scale*

The problems with DES was the definition of the position of the end of the boundary layer (Spalart et al., 2006). The switch between RANS and LES modes occurs at the edge of the boundary layer and is defined by a length-scale, which in DES, is  $\tilde{d}$ , and given by

$$\tilde{d} \equiv \min(d, C_{DES}\Delta) \quad (3.25)$$

where

d – nodal distance to the nearest wall

$$C_{DES} = 0.65$$

$\Delta$  – chosen grid spacing.

For wall parallel grid spacings where,  $x/\delta \gg 1$ , the RANS mode was active in the boundary layer and the model functioned as intended.

The issue of unphysical flow separation was addressed by amendments to DES (Spalart et al., 2006). The DDES limiter,  $\tilde{d}_{DDES}$ , triggers the switch between RANS and LES modes at the very edge of the boundary layer and is defined as

$$\tilde{d}_{DDES} \equiv y_d - f_d \max(0, d - C_{DES}\Delta) \quad (3.26)$$

and the switching action is performed by a combination of the  $f_d$  and  $r_d$  functions,

$$f_d \equiv 1 - \tanh([8r_d]^3) \quad (3.27)$$

$$r_d \equiv \frac{\nu_t + \nu}{\sqrt{U_{ij}U_{ij}}\kappa^2 y_d^2} \quad (3.28)$$

where

$\nu_t$  – eddy-viscosity

$y_d$  – distance from wall.

The hyperbolic function ensures that the trigger occurs at the very edge of the boundary layer. Kinematic viscosity,  $\nu$ , is added to the numerator of  $r_d$  to prevent it from going to zero close to a wall, where the eddy viscosity is inherently low.

### 3.4.5.2 Spalart-Allmaras one equation model

The Spalart-Allmaras (S-A) one equation turbulence model was originally intended for use in aerospace applications (Spalart and Allmaras, 1992) and was chosen due to it being less computationally expensive than standard two-equation models.

In DDES, the purpose of the RANS model is purely to model the boundary layer and so at higher Reynolds numbers the boundary layer becomes very thin and thus the RANS model is applied to very little of the bulk flow. It is conjectured by the author that due to the thickness of the boundary layer, and the fact that bluff body flows are dominated by massive flow separation, the effect of the choice of RANS model on the free-stream flow will be negligible.

The model used in OpenFOAM is the Ashford (1996) formulation of the S-A model and is written as

$$\begin{aligned} \left( \frac{\partial}{\partial t} + u \cdot \nabla \right) \tilde{\nu} &= \frac{1}{\sigma} \nabla \cdot \left( (\nu + (1 + c_{b2})\tilde{\nu}) \nabla \tilde{\nu} \right) - \frac{c_{b2}}{\sigma} \tilde{\nu} \Delta \tilde{\nu} \\ &+ c_{b1} (1 - f_{t2}) \hat{S} \tilde{\nu} - \left( c_{w1} f_w - \frac{c_{b1}}{\kappa^2} f_{t2} \right) \left( \frac{\tilde{\nu}}{d} \right)^2 \\ &+ f_{t1} \Delta U^2 \end{aligned} \quad (3.29)$$

The left hand side of equation 1.51 is the advection term along a particle path. The right hand side has the diffusion, anti-diffusion, production, destruction and trip terms, respectively. The production term is made from the following functions:

Equation

Equation

Equation

Equation

$$\chi = \frac{\tilde{\nu}}{\nu} \quad (3.30)$$

$$f_{v1} = \frac{\chi^3}{\chi^3 + C_{v1}^3} \quad (3.31)$$

$$f_{v2} = \frac{1}{(1 + \chi/C_{v2})^3} \quad (3.32)$$

$$f_{v3} = \frac{(1 + \chi f_{v1})(1 - f_{v2})}{\chi} \quad (3.33)$$

$$S = \|\text{curl } \mathbf{u}\| \quad (3.34)$$

$$\hat{S} \equiv f_{v3}S + \frac{\tilde{\nu}}{\kappa^2 d^2} f_{v2} \quad (3.35)$$

where

$d$  – distance from the first node to the wall.

$\tilde{\nu}$  – viscosity-like term.

The destruction term is comprised of the following functions

$$f_w = g \left[ \frac{1 + C_{w3}^6}{g^6 + C_{w3}^6} \right]^{1/6} \quad (3.36)$$

$$r = \min \left( \frac{\tilde{\nu}}{\hat{S}k^2 d^2}, 10 \right) \quad (3.37)$$

$$g = r + C_{w2}(r^6 - r). \quad (3.38)$$

The function  $f_{t2}$  stabilises the production and destruction terms when  $\tilde{\nu} = 0$ ,

$$f_{t2} = c_{t3} e^{(-c_{t4} \chi^2)}. \quad (3.39)$$

and the trip term is used to calculate the location of the boundary layer transition and is given by

$$f_{t1} = c_{t1} g_t e^{\left( -c_{t2} \frac{\omega_t^2}{\Delta U^2} (d^2 + g_t^2 d_t^2) \right)} \quad (3.40)$$

where

$d_t$  – distance to the nearest trip point

$\omega_t$  – vorticity at the wall at the trip point

$\Delta U$  – normalised velocity difference between the wall and the point under consideration

$$g_t = \min (0.1, \Delta U / \omega_t x) \quad (3.41)$$

where

$x$  – wall-parallel spacing at the trip point.

Eddy-viscosity is given by

$$\nu_t = \tilde{\nu} f_{\nu 1} \quad (3.42)$$

and the constants of the turbulence model are:

$$\sigma = \frac{2}{3}, \quad C_{b1} = 0.1355, \quad C_{b2} = 0.622, \quad C_{\nu 1} = 7.1$$

$$C_{w1} = \frac{C_{b1}}{\kappa^2} + \frac{(1 + C_{b2})}{\sigma}, \quad \kappa = 0.41, \quad C_{w2} = 0.3, \quad C_{w3} = 2, \quad C_{\nu 2} = 5$$

Model constants were attained largely empirically in order to give physically representative results. However, model calibration was not conducted for bluff bodies therefore the applicability to the present work is not entirely clear, although Muld et al.(Muld et al., 2013) applied the S-A model in DDES slipstream calculations and showed it to be effective.

# Chapter 4 The slipstream flow around a freight train in no wind conditions

## 4.1 *Introduction*

The present chapter reports on data obtained from delayed detached-eddy simulations of the slipstream of a 1/25<sup>th</sup> scale freight train consisting of a Class 66 locomotive and four fully-loaded container wagons. It is acknowledged by the author that a lower loading efficiency is likely to produce higher leeward slipstream velocities in the crosswind cases however the present case is used as a baseline case with potential for future work.

The no-crosswind simulations were conducted in order to understand the behaviour of the slipstream of a freight train with no atmospheric wind, which could then be compared with the data from crosswind simulations, thus allowing the effects of crosswinds on the slipstreams of freight trains to be quantified.

This chapter is laid out as follows, Section 4.2 shows the solution verification, Section 4.3 presents the time-averaged flow around the train and in Section 4.4 the instantaneous flow is exhibited. In Section 4.5, the TSI compliance of the slipstream generated around the train is tested and in Section 4.6 conclusions are drawn.

## 4.2 *Solution verification and validation*

To ensure the results of numerical simulations are physical and accurate, it is standard practice in industry and academia to perform validation against physical experiments. Furthermore, results from simulations with at least two different mesh densities should be compared in order to confirm that the results are in fact independent of mesh density (Roache, 1998).

### 4.2.1 Mesh sensitivity

The sensitivity of the longitudinal velocity component to the mesh for the current case is shown in Figure 42. The longitudinal component of velocity is converted to the frame of reference of a static observer by

$$\mathbf{u} = \frac{(\mathbf{u}_{\text{train}} - \mathbf{u})}{u_{\text{train}}} \quad (4.1)$$

where

$\mathbf{u}$  – longitudinal velocity component in the computational domain.

The results show little difference between the cases, so it can be determined that the results are not a function of mesh density and it can be assumed that the important energy containing scales have been resolved.

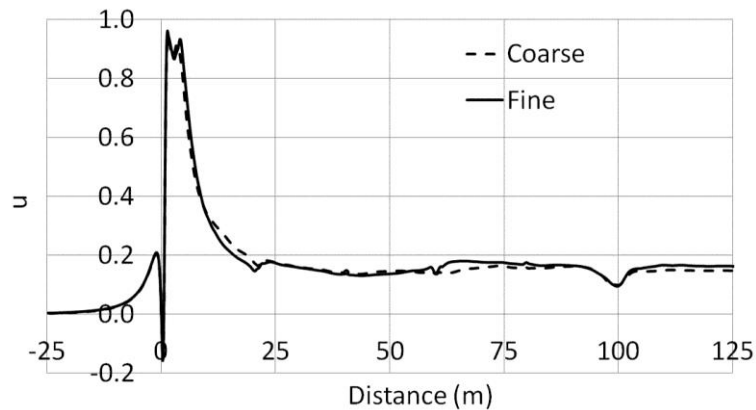


Figure 42 Longitudinal velocity component for the coarse (25 million cells) and fine (34 million cells) meshes

Pope (2000) stated that the energy that should be resolved in a good quality LES is 80%. Figure 43 shows the percentage of the turbulence kinetic energy (TKE) that has been resolved in the slipstream around the freight train. Due to the zero-turbulence inlet condition, at  $x < -25$

m, there is no turbulence to resolve hence the very low values. For the entirety of train length, the level of TKE that has been resolved is above the value stated by Pope (2000).

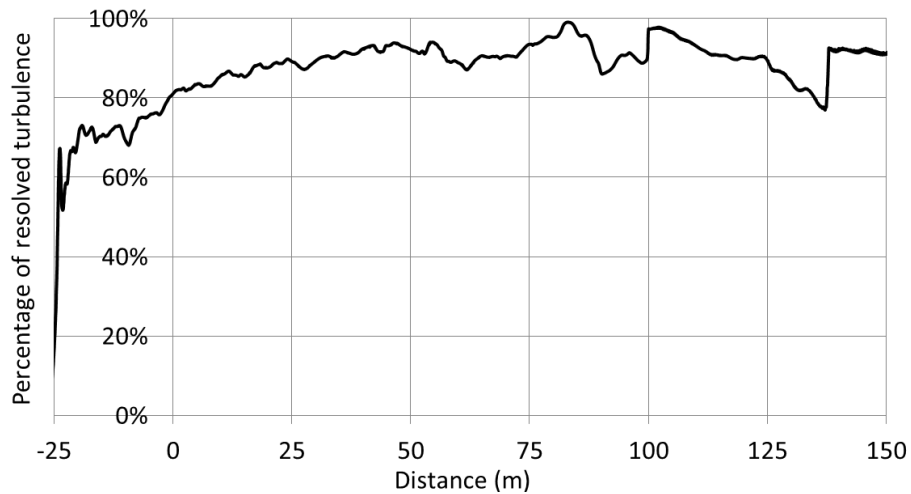


Figure 43 Percentage of resolved turbulence kinetic energy around the Freight train at  $y=2.34$  m and  $z=2$  m.

#### 4.2.2 Validation

Validation of the present simulations was performed against experimental data (Soper, 2014) where the pressure coefficients ( $C_p$ ) and the normalised longitudinal component of velocity,  $u$ , are compared in Figure 44 and Figure 45, respectively.

To aid the interpretation of the data with regards to expected error, bounds of  $\pm$  one standard deviation have been applied to the experimental data: hereon in referred to as  $\pm$  1SD. The positive peak at  $x \approx 0$  m for the CFD reaches a maximum value of  $C_p=0.37$  whereas the experimental data reaches a peak positive value of  $C_p=0.31$ . The increase in the pressure field ahead of the train ( $x < 0$  m) is more rapid for the CFD data which is hypothesised to be due to the probe which only measure velocities and pressures when the flow is above 2 m/s. They also have an accuracy of  $\pm$  1 m/s.

The minimum peak pressure coefficient values are  $C_p=0.86$  and  $C_p=0.66$  for the CFD and experimental data, respectively. It is evident that the negative peak CFD value is outside of

the  $\pm 1$ SD bound, signifying a much lower degree of agreement than was seen for the positive peak which could be due to reverse flow affecting the operation of the probes. For the remainder of train length, the CFD value remains comparable to the experimental work with minor discrepancy in the near wake which is attributed to the inherent differences between the ensemble and time-averaging methods and will be discussed further in Section 4.2.3.

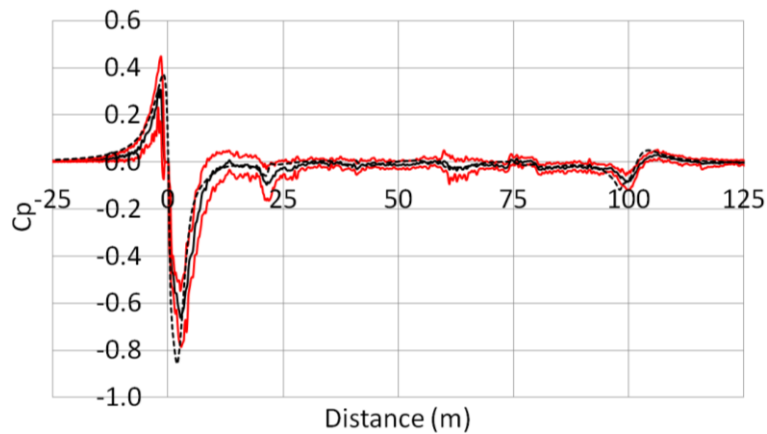


Figure 44 Time and ensemble-averaged  $C_p$  at  $y=1.75$  m and  $z=2.25$  m, for the numerical (dashed line) time-average and experimental ensemble average (solid black line) with  $\pm 1$  standard deviation of the ensemble in red.

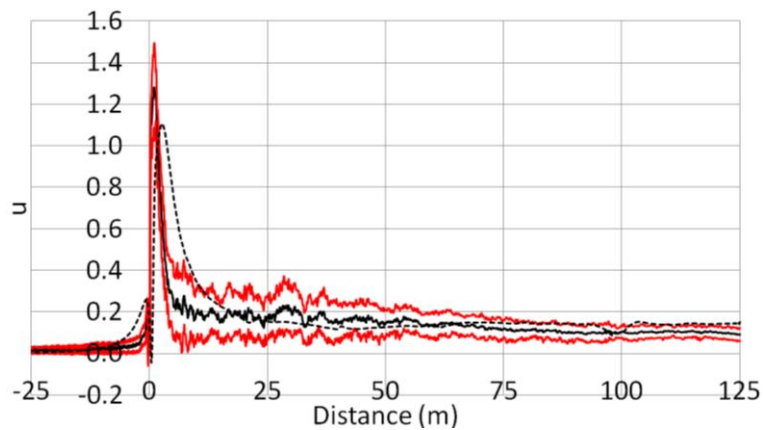


Figure 45 Time and ensemble-averaged longitudinal components of velocity at  $y=1.75$  m and  $z=2.25$  m, for the numerical (dashed line) time-average and experimental ensemble average (solid black line) with  $\pm 1$  standard deviation of the ensemble in red.

Figure 45 shows the longitudinal velocity component from the CFD and experimental cases. The rise in the longitudinal velocity does not begin until the train is approximately 10 m before it reaches the probe. Even for very streamlined trains this increase has been shown to begin much earlier (Baker et al., 2013b, Hemida et al., 2014). It would therefore be expected that such a bluff train would cause an increase in velocity further ahead of the train, although as discussed above this is likely to be due to the minimum measurable velocity of the probes.

The maximum longitudinal velocity components for the CFD and experimental cases are  $u=1.1$  and  $u=1.3$ , respectively. The positions of the maximum values also differs with the experimental work's peak value occurring at  $x=0.9$  m and the CFD's peak value occurring at  $x=1.7$  m. Between  $x=1$  m and  $x=10$  m, the numerical value for  $u$  remains greater than the upper standard deviation bound for the experimental data. The flow in the nose region is highly three-dimensional and as such the Cobra probes will not register velocity outside of its 'cone of influence' which is within  $45^\circ$  of the front face (see (Soper, 2014)). For the remainder of the slipstream good agreement is seen between the numerical and experimental data.

The effect of the different measurement techniques must be considered when comparing data insomuch as in the CFD case, the model remains static the inlet velocity has no effect on its position or movement. The experimental model is subjected to transient aerodynamic loads as well as vibration from the running mechanism. Although this movement is not anticipated to have a significant effect on the slipstream around the train it would be naive to assume that this movement contributed nothing to the slipstream flow.

### ***4.2.3 Ensemble-averaging vs. time-averaging***

In train aerodynamic experiments, where the relative movement between the vehicle and the ground is considered important, methods such as moving-models can be employed (Soper, 2014, Baker et al., 2001, Baker et al., 2012a). With moving model experiments, the slipstream properties are measured as the train passes and are therefore instantaneous. In turbulent flows which are dominated by large turbulent scales, the run-to-run variability of instantaneous measurements can be large and thus the behaviour of the mean flow is not apparent. In order to obtain velocities and pressures close to that of the mean flow the values obtained at a given distance along the train are averaged. It is recommended by CEN (2011) and TSI (2008) that when ensemble-averaging slipstream velocities, 20 runs used and when ensemble-averaging pressure at least 10 are required in order to reduce the standard deviation of the data. It is also a requirement that the ambient wind speed must be lower than 2 m/s. At model-scale Soper (2014) found that for the highly turbulent slipstream of the freight train, 25 runs were required to reduce the standard deviation of the velocity ensemble-average to a point where the ensemble didn't change with increased ensemble size.

When making a direct comparison between ensemble-averaged data from experiments and time-averaged data from CFD simulations it could be assumed that it is appropriate to directly compare each data set even though they include different errors and uncertainties. In order to demonstrate the equivalence of ensemble-averaging with respect to time-averaging, a comparison must be made between data from a single source that has the ability to carry out both techniques, thus this method is applied in the present work.

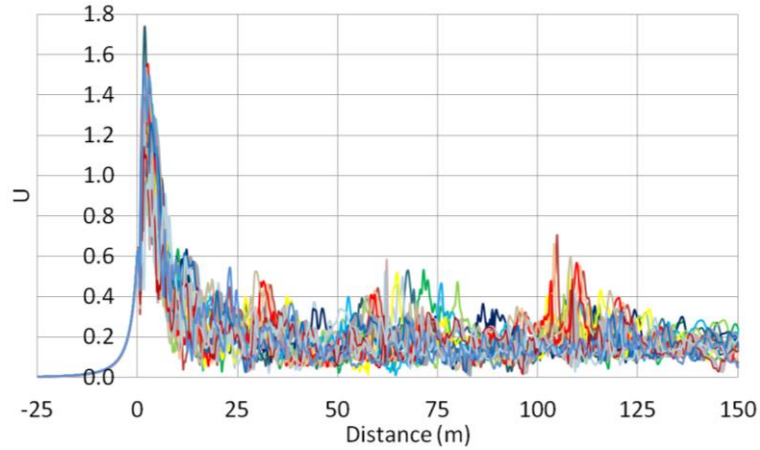


Figure 46 Instantaneous  $U_h$  at the validation at  $y=1.75$  and  $z=2.25$  m

In Figure 46 instantaneous horizontal velocities,  $U_h$ , from 20 independent time-steps in the DDES simulation are plotted to replicate the instantaneous slipstream velocities that would be obtained from moving-model experiments. The horizontal velocity,  $U_h$ , is used because this is the recommended velocity in the technical codes of practice and is given as

$$U_h = \frac{\sqrt{(u_{in} - \mathbf{u})^2 + \mathbf{v}^2}}{u_{in}} \quad (4.2)$$

where

$\mathbf{v}$  – lateral velocity component in the computational domain.

The instantaneous velocity samples from the simulations are not the same as velocity measured from a train moving past a static probe however for the current work it is assumed to be the same.

The ensemble-average, time-average and standard deviation of  $U_h$  at the validation probe position are shown in Figure 47. The ensemble-averaged velocity has a peak value of  $U_h=1.2$  at  $x=2$  m which is 10% greater than the time-averaged value. For the majority of the length of

the locomotive, the ensemble predicts higher horizontal velocity and is only lower than the time-averaged value for 8 % of the train's length.

Locations where the ensemble is consistently greater than the time-average mainly occur at the inter-wagon spacings, especially the third inter-wagon spacing. Furthermore, a decrease in the slipstream velocity is not observed in the wake for the ensemble-averaged data, a feature which is exhibited in the experimental data used for validation (Figure 45). The time-averaged data from the CFD generally remains within one standard deviation of the ensemble mean which is taken to be the confidence limit of the data. Therefore it can be concluded that the ensemble- and time-averaged data are similar enough to be used interchangeably.

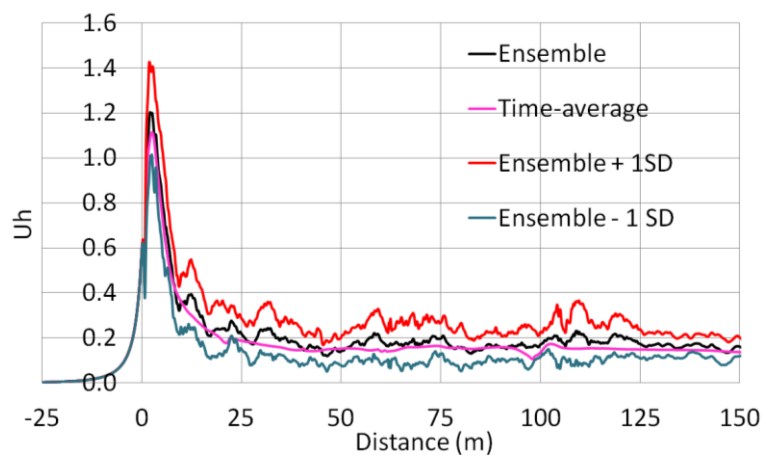


Figure 47  $U_h$  at probe position 2 for time-averaged, ensemble-averaged and +/- 1 standard deviation from the ensemble-average

### 4.3 Time-averaged flow

#### 4.3.1 Slipstream measurement positions

The slipstream velocities (components and magnitudes), pressure coefficients and turbulence intensities were sampled at the side and above the roof of the train at different distances from the COT and TOR as shown in Figure 48 and Figure 49. The lateral sampling positions at

train side, used in the present work, are  $y=1.59$  m,  $y=1.84$  m,  $y=2.34$  m and  $y=3.34$  m from COT, which corresponds to  $y'=0.25$  m,  $y'=0.5$  m,  $y'=1$  m and  $y'=2$  m from train side which correspond to some of the locations used by Baker et al.(2001) to allow for comparison between data sets.

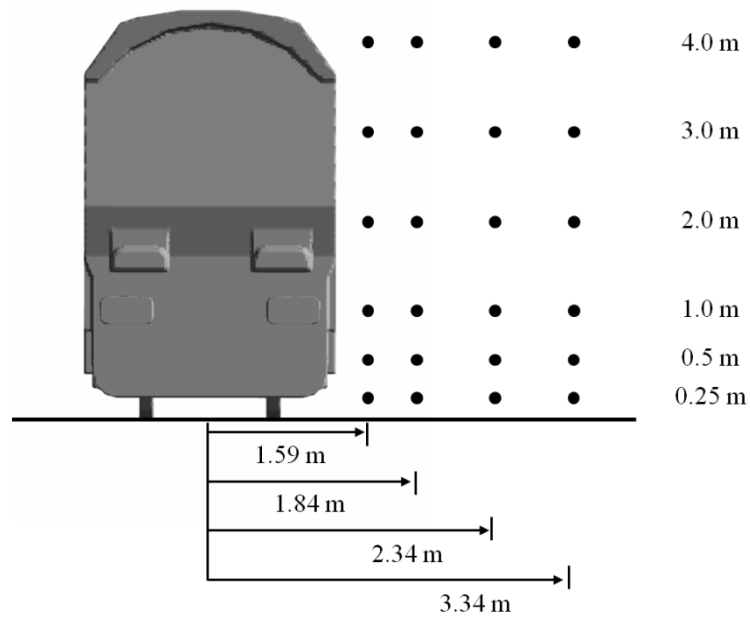


Figure 48 Locations of slipstream measurement at train side relative to COT and TOR

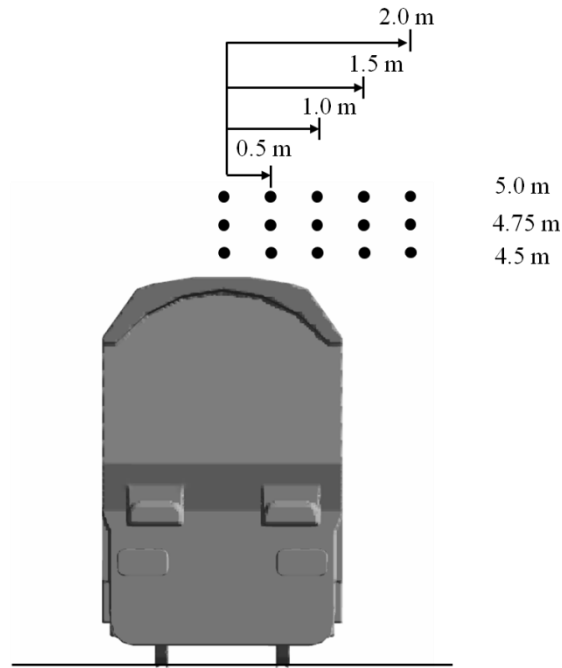


Figure 49 Locations of slipstream measurement above the roof of the train relative to COT and TOR

### 4.3.2 Velocity magnitude at train side

Time-averaged normalised slipstream velocity magnitudes at train side are presented in Figure 50. The normalised velocity magnitude,  $U$ , is calculated by

$$U = \frac{\sqrt{(u_{\text{train}} - \mathbf{u})^2 + \mathbf{v}^2 + \mathbf{w}^2}}{u_{\text{train}}} \quad (4.3)$$

where

$\mathbf{w}$  –vertical component in the computational domain.

Three of the four characteristic flow regions of the slipstream of a train are visible from Figure 50 namely: the upstream and nose region, the boundary layer region as well as the near wake. The far wake is not considered to be of great interest here as this work focuses on the slipstream adjacent to the train.

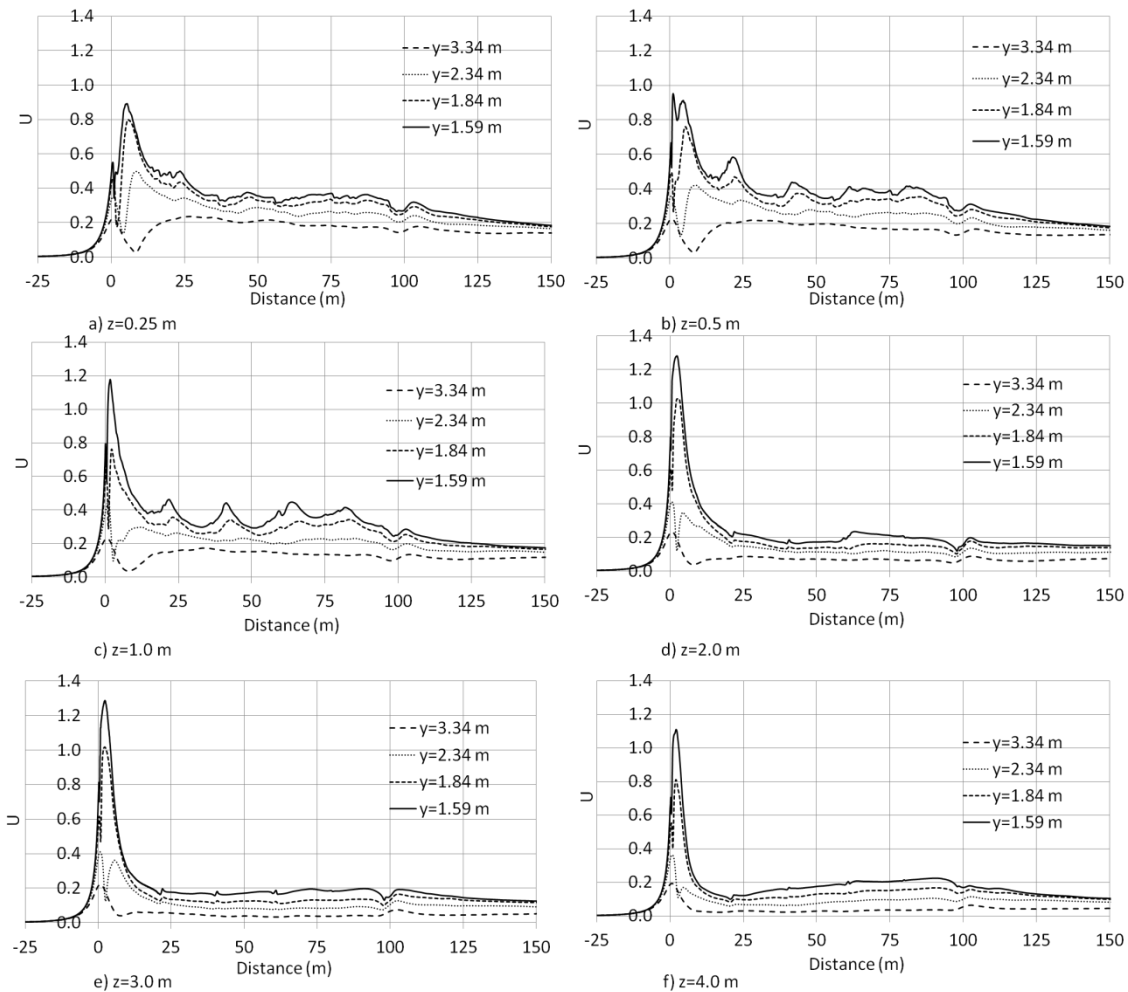


Figure 50 Normalised velocity magnitude,  $U$ , at varying distances from COT at a)  $z=0.25$  m, b)  $z=0.5$  m, c)  $z=1$  m, d)  $z=2$  m, e)  $z=3$  m and f)  $z=4$  m

The characteristic aerodynamic feature of the Class 66 locomotive is the large velocity peak at the front face of the locomotive which is many times greater than relative velocity peaks observed at model-scale for other vehicles such as the ICE2 (Baker et al., 2001, Hemida et al., 2014) or for other full-scale trains (Baker et al., 2013b).

The largest velocity peaks consistently occur at  $y=1.59$  m for all heights, between  $x=1$  m and  $x=5$  m. The velocity peaks are a result of the flow separating around the relatively sharp corners of the locomotive, causing it to accelerate. The greatest velocity magnitude along the length of the locomotive is  $U=1.29$  and occurs at  $y=1.59$  m and  $z=3$  m. Figure 51 shows

recirculation regions that are formed around the sides of the locomotive and reattachment occurs at approximately  $x=6$  m.

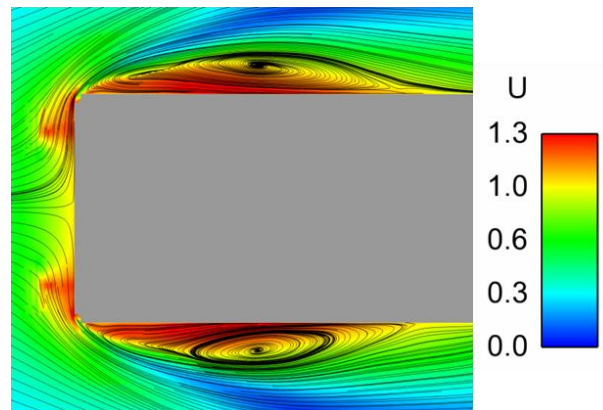


Figure 51 Time-averaged velocity streamlines projected onto a horizontal cut-plane at  $z=1$  m, coloured by velocity magnitude

At lower heights above TOR, the variation in velocity magnitude along train length is greater than at higher positions above TOR. Transients are observed at inter-wagon spacings; however these are negligible for  $z \geq 2$  m. The transients which occur at  $z=1$  m are the greatest in the slipstream and are a result of the coupling between the flat liner and the container. Station platforms in the UK are approximately 1 m above the TOR so it is possible, in the presence of a platform, a waiting person may only experience the lower velocity wind. For the case of people at trackside,  $z=1$  m would be approximately  $2/3^{\text{rd}}$  of the height of an average person and could pose more of an issue to stability. The influence of the slipstream velocities on person stability will be discussed in Chapter 8.

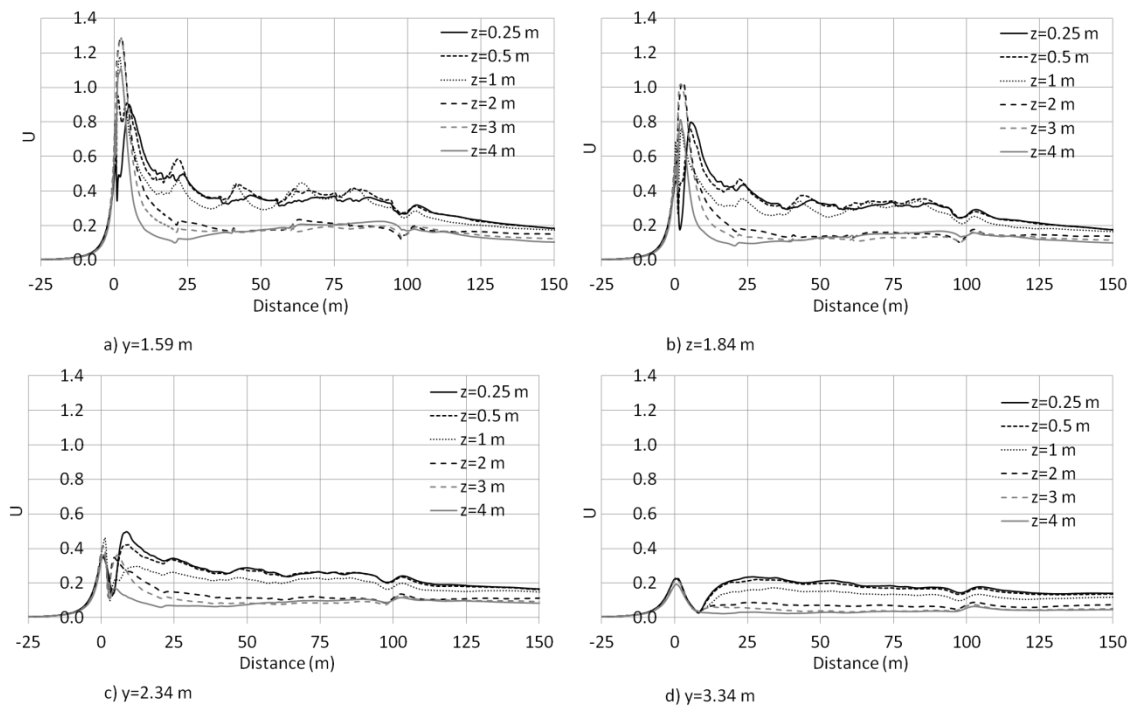


Figure 52 Normalised velocity magnitude,  $U$ , at varying distances above TOR at a)  $y=1.59$  m, b)  $y=1.84$  m, c)  $y=2.34$  m and d)  $y=3.34$  m

The slipstream velocity magnitudes shown in Figure 50 were re-plotted with respect to height (Figure 52). The greatest change in velocity with respect to height occurs between  $z=1$  m and  $z=2$  m. The variation in velocity magnitude is due to the difference in effective roughness between the ‘smooth’ sides of the containers and the relatively ‘rougher’ bogies, with the ‘rougher’ geometry producing higher slipstream velocities; this observation has been made in the literature (Sterling et al., 2008).

It is observed from Figure 52 that there are greater similarities between velocity magnitudes in the nose region at further distances from COT than at closer distances from COT. This is because the influence of the local geometry of the train on the mean flow is most prevalent close to train side, whereas further from train side the general effect of the bulk geometry is observed.

### 4.3.3 Velocity magnitude above train roof

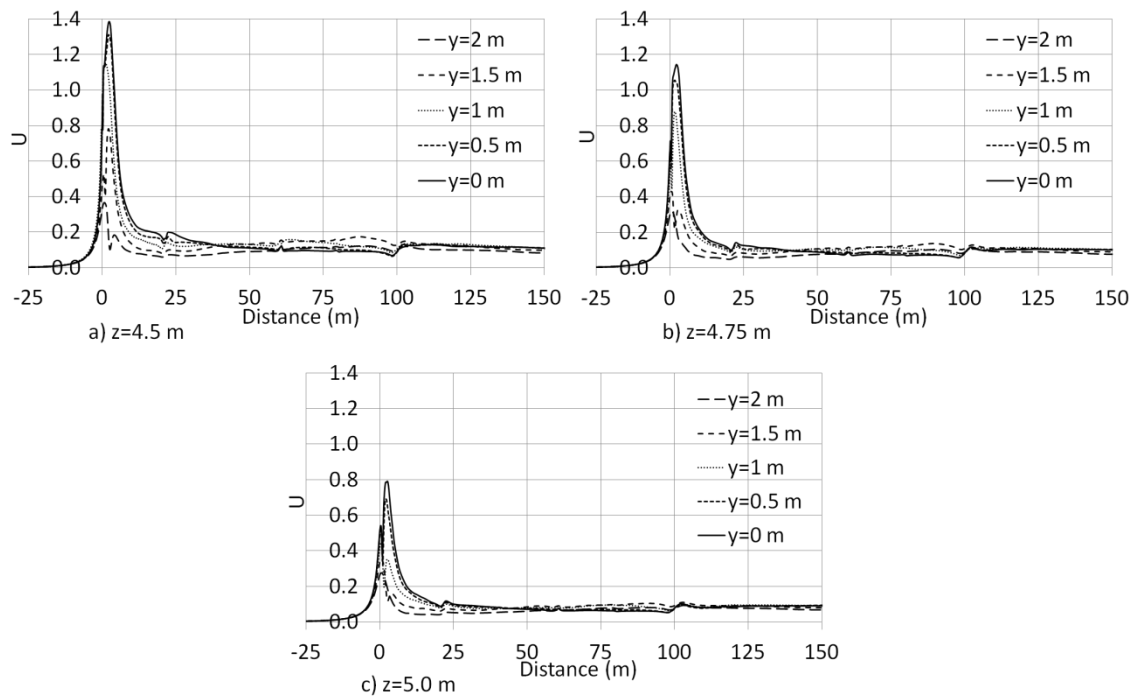


Figure 53 Normalised velocity magnitude,  $U$ , above the train roof at varying distances from COT at (a)  $z=4.5$  m, (b)  $z=4.75$  m and (c)  $z=5.0$  m.

The velocity magnitudes in Figure 53 were sampled at 0.15 m, 0.4 m and 0.65 m above the roof of the locomotive, corresponding to 0.5 m, 0.75 m and 1 m above the containers.

As was seen with samples along the train side (Figure 50), velocity magnitude peaks are observed above the roof of the train. The greatest peak is  $U=1.38$  and occurs at  $x=2$  m,  $y=0$  m and  $z=4.5$  m. The slipstream velocities in the boundary layer region are much lower than those measured at train side which is due to the probes being a greater distance from a ‘moving’ surface because of the difference in height between the locomotive and the container wagons.

Slipstream velocities in the boundary layer region at  $y=0$  m decrease over the length of the train, whereas increasing  $U$  is observed at greater distances from COT. This change is due to the effect of an interaction with the slipstream at the side of the train increasing the lateral

velocity components and thus the overall value of U. Due to the near-symmetry of the vehicle, the resultant of the mean lateral velocity at y=0 m is very close to zero, hence a lower overall magnitude.

#### ***4.3.4 Velocity components at train side***

When considering U, all three components of velocity are included. TSI and CEN only require the horizontal velocity magnitude to be considered, and thus assume w to be zero or negligible. By investigating each velocity component individually the assumption of the vertical component being negligible, made by the certification standards and previous research (Baker et al., 2001), can be evaluated.

The normalised lateral, v, and vertical, w, components are given by

$$v = \frac{\mathbf{v}}{u_{\text{train}}} \quad (4.4)$$

and

$$w = \frac{\mathbf{w}}{u_{\text{train}}} . \quad (4.5)$$

In this section the velocity components on the windward side of the freight train are presented. The lateral velocity is positive ahead of the train due to the crosswind component and is thus negative when the flow is moving away from the train. On the leeward side of the train negative lateral velocity will signify that the flow is moving towards the train. This convention is used to ensure that the crosswind is always positive however the aforementioned consequences should be borne in mind when inspecting the data.

The slipstream components upstream and in the nose region at  $z=0.25$  m and  $y=1.59$  m are shown in Figure 54. It can be observed the longitudinal component is dominant and reaches a peak value of  $u=0.88$  at  $x=5$  m. The second largest peak is the lateral velocity, whose maximum value is  $v=-0.54$ , where the negative value signifies this is away from the train. The vertical velocity component around the front face of the locomotive is negligible, suggesting that the slipstream could be adequately represented by a two-dimensional flow at  $z=0.25$  m.

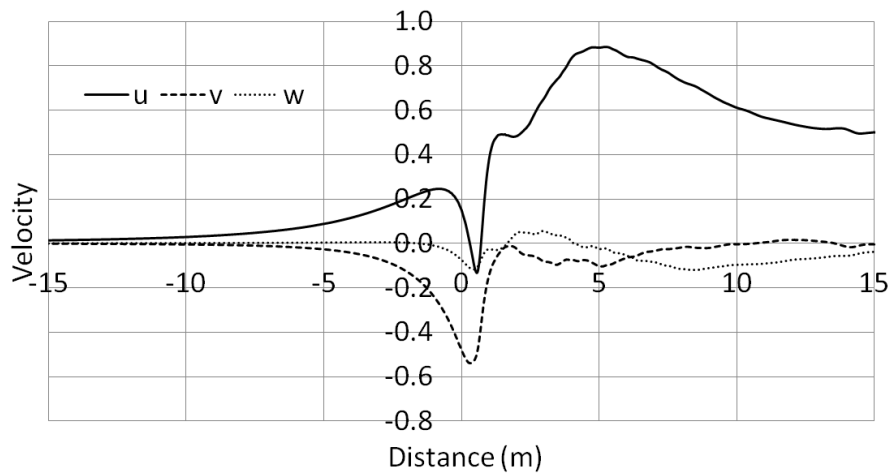


Figure 54 Upstream and nose region velocity components at  $y=1.59$  m and  $z=0.25$  m

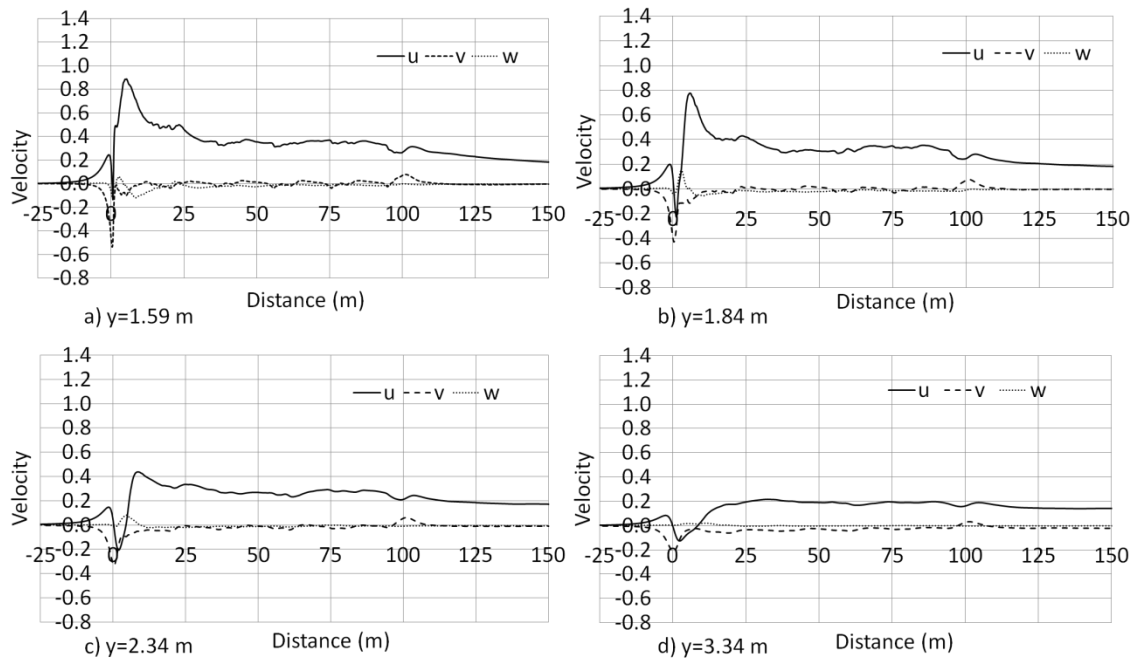


Figure 55 Velocity components at  $z=0.25$  m above TOR and at a)  $y=1.59$  m, b)  $y=1.84$  m, c)  $y=2.34$  m and d)  $y=3.34$  m

The mean slipstream velocity components at  $z=0.25$  m are presented in Figure 55. At  $y=1.59$  m and  $y=1.84$  m two  $u$  peaks are observed which reach maximum values of  $u=0.21$  and  $u=0.85$  for the first and second peaks, respectively (Figure 55a). The first peak is caused by the pressure field on the front face of the locomotive whereas the second is due to flow separation around the sides of the train. After the secondary peak the longitudinal velocity generally reduces to boundary layer region values at most of the sampling positions. At  $y=3.34$  m, the second nose peak does not occur and  $u$  is seen to increase along the length of the locomotive and plateau into the boundary layer region. At all distances from COT,  $u$  exhibits a gradual decrease along the length of the train.

The negative lateral velocity,  $v$ , at  $x=0$  m for all distances from COT, indicates that the air is moving away from the train side due to the high pressure field on the front face of the locomotive. Along the length of the train there are minor changes in  $v$  at inter-wagon gaps. The greatest lateral velocity away from the train occurs at  $y=1.59$  m and is  $v=-0.54$  whereas

the largest  $v$  towards the train is in the near wake and is a result of the low pressure region behind the last wagon entraining the air.

The vertical velocity exhibits a negative-positive transient in the nose region whose negative peak is greatest at  $y=1.59$  m and positive peak is greatest at  $y=1.84$  m. The vertical component of velocity,  $w$ , generally remains negligible in comparison to  $u$  and  $v$  along train length and the greatest vertical peak velocity is  $w=0.13$  and occurs at  $y=1.84$  m.

### $z=0.5$ m

The longitudinal velocity at  $y=1.59$  m exhibits a double peak as shown in Figure 56a at  $x=1$  m and  $x=5$  m. It is observed in Figure 57 that the first velocity peak at  $x=1$  m is located behind the air dam and the second peak occurs further along the locomotive and is a result of the relative roughness of the bogies. A comparison between the velocities at the two heights can be seen in Figure 58. Aside from the double nose peak, the slipstream velocities at  $z=0.5$  m behave very similarly to  $z=0.25$  m with all peak component values occurring at  $y=1.59$  m.

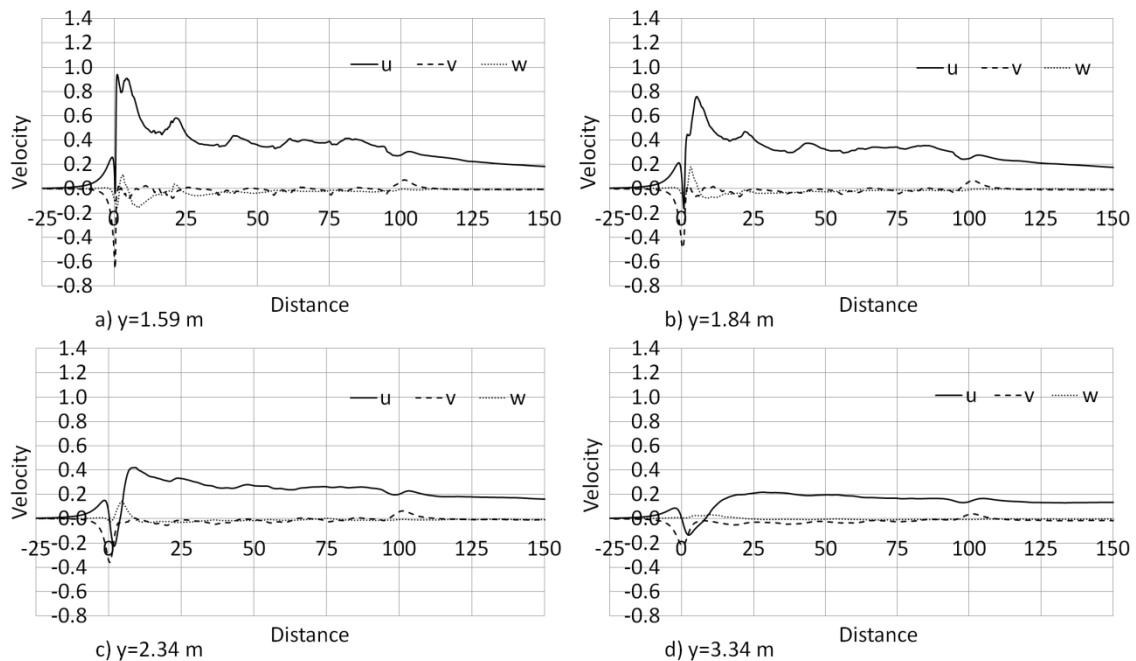


Figure 56 Velocity components at  $z=0.5$  m above TOR and at a)  $y=1.59$  m, b)  $y=1.84$  m, c)  $2.34$  m and d)  $y=3.34$  m

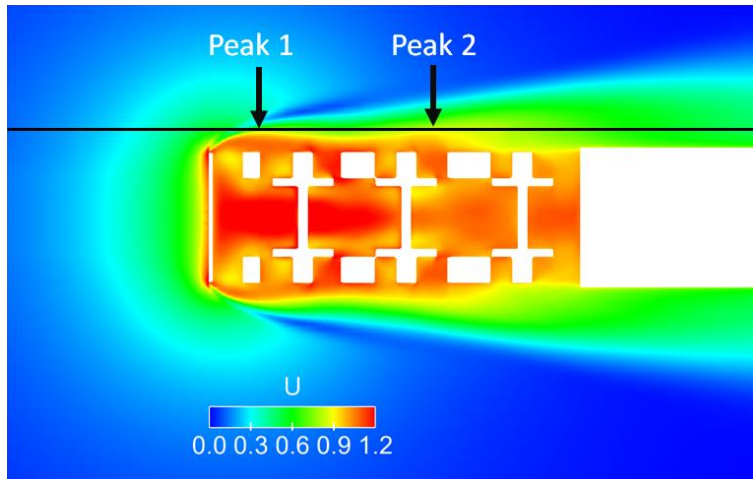


Figure 57 Mean velocity magnitude showing locations of sharp double peak at  $z=0.5$  m where black line is sampling location at  $y=1.59$  m (train travelling from right to left)

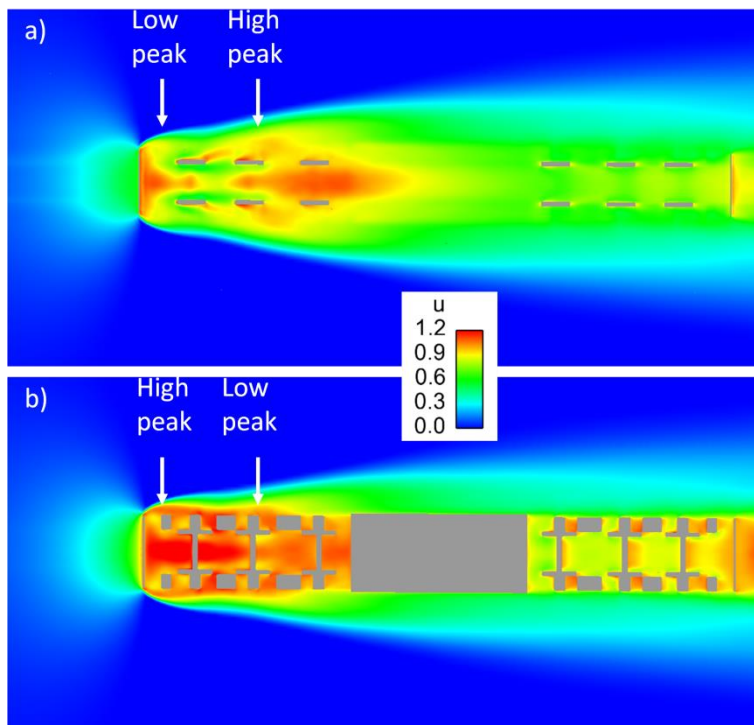


Figure 58 Longitudinal velocity components on a plane at a)  $z=0.25$  m and b)  $z=0.5$  m

**z=1.0 m**

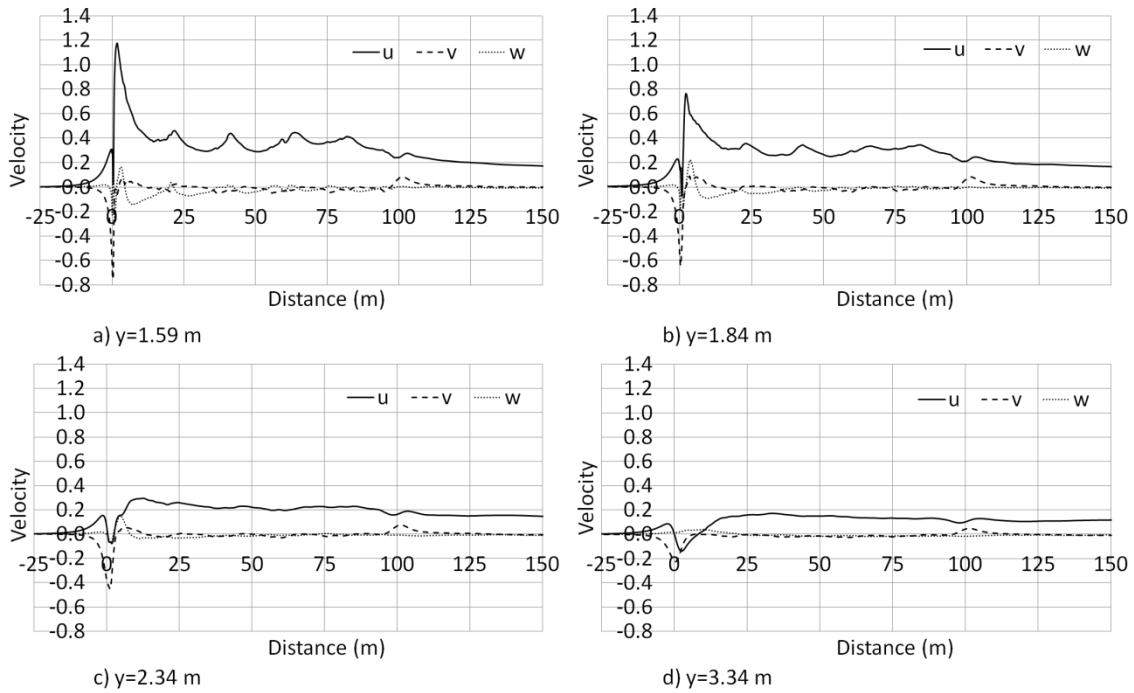


Figure 59 Velocity components at  $z=1.0$  m above TOR and at a)  $y=1.59$  m, b)  $y=1.84$  m, c)  $y=2.34$  m and d)  $y=3.34$  m

At  $z=1$  m, the  $u$  and  $v$  peak values are greater than those observed at  $z=0.5$  m for  $y=1.59$  m (Figure 59). The longitudinal velocity remains nearly constant in the boundary layer region with the exception of peaks at the inter-wagon spacings. Furthermore, the longitudinal velocity is lower in the boundary layer region for all distances from train side than it was at  $z=0.5$  m. The peak lateral velocity is greater than the peak longitudinal velocities for  $y=2.34$  m and  $y=3.34$  m. The peak vertical velocity occurs at  $y=1.84$  m and is  $w=0.22$ : 4% lower than the primary longitudinal velocity peak.

**z=2.0 m**

The u velocity at y=1.59 m does not become 0 or negative in the nose region for the first time which is a result of the differing geometry at that height above TOR (Figure 60). At y=3.34 m, u remains relatively constant in the wake after x=125 m because the air is entrained by the low pressure region behind the train.

Generally, the u component of velocity is approximately half of that observed at lower heights and the locations of the inter-wagon spacings are visible as much-less pronounced transients. The lateral velocity is the greatest sampled in the slipstream so far and is v=-0.78.

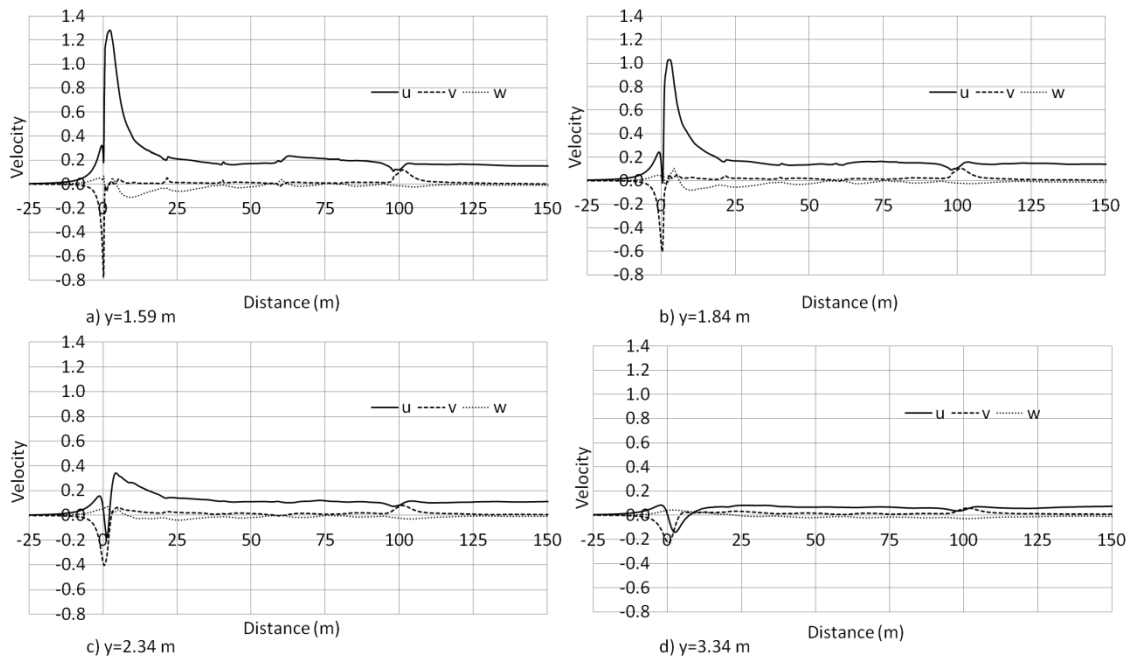


Figure 60 Velocity components at z=2.0 m above TOR and at a) y=1.59 m, b) y=1.84 m, c) 2.34 m and d) y=3.34 m

**z=3.0 m**

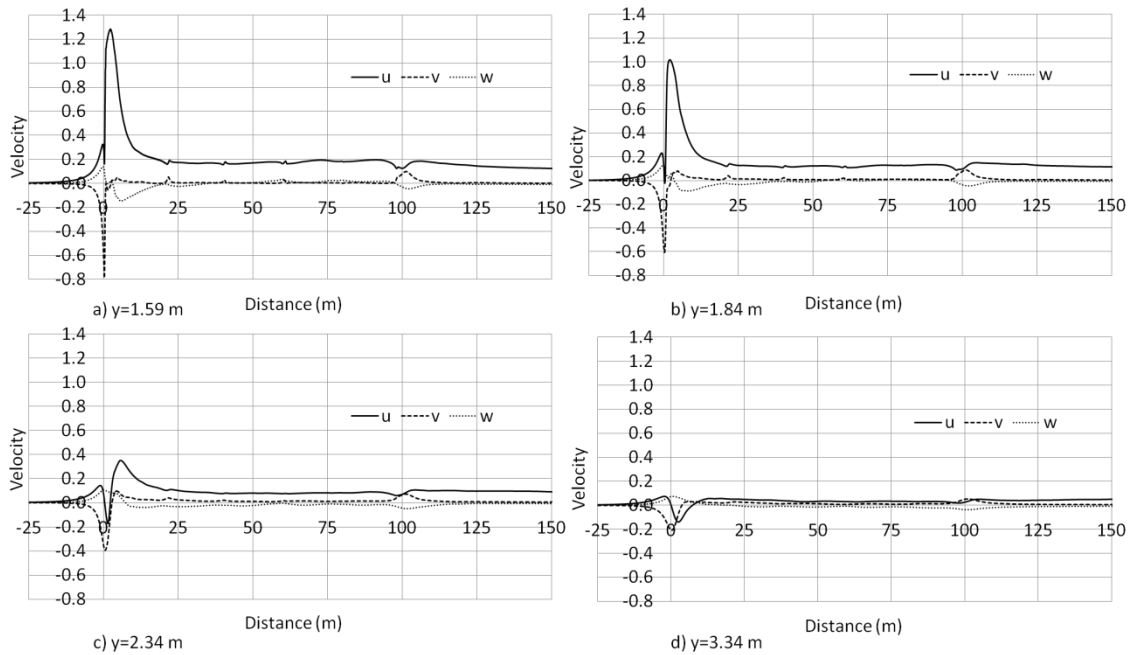


Figure 61 Velocity components at  $z=3.0$  m above TOR and at a)  $y=1.59$  m, b)  $y=1.84$  m, c)  $2.34$  m and d)  $y=3.34$  m

The data presented in Figure 61 shows very little change in comparison to the data sampled at  $z=2$  m, thus suggesting little change occurs in the structure of the slipstream between  $z=2$  m and  $z=3$  m as was shown for velocity magnitude in Figure 52. The longitudinal velocity remains fairly constant in the boundary layer region between  $x=25$  m and  $x=90$  m. The peak lateral velocity is  $v=-0.78$ .

**z=4.0 m**

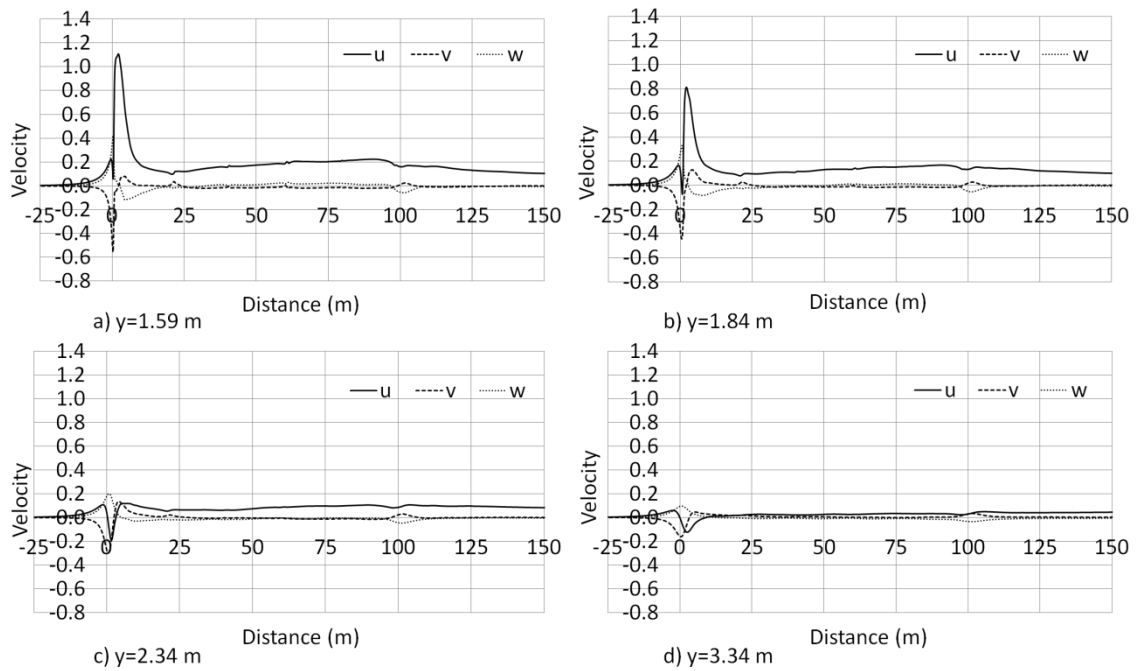


Figure 62 Velocity components at z=4.0 m above TOR and at a) y=1.59 m, b) y=1.84 m, c) 2.34 m and d) y=3.34 m

For the first time u is seen to increase steadily in the boundary layer region for all distances COT. For the first time the vertical velocity has become a significant component with a peak value of  $w=0.42$  at  $y=1.59$  m. The vertical velocity is also the greatest positive component at  $y=2.34$  m and  $y=3.34$  m, whereas the lateral velocity is the greatest negative component for all distances from COT.

#### 4.3.4.1 Component summary

The overall trends observed for the components of velocity are:

- Longitudinal peaks (and double velocity peaks close to train side) are observed at all heights above TOR between  $x=0$  m and  $x=5$  m.
- For all measurement positions, the lateral velocity increases away from train side (negatively) in the range of  $-5$  m  $< x < 1$  m.

- Vertical velocity is negligible in the boundary layer region for all measurement positions at train side
- Vertical velocity becomes significant at  $z=4$  m in the nose region
- The longitudinal velocity decays, or remains nearly constant, along train length for all heights except  $z=4$  m
- A positive lateral velocity transient is observed in the near wake for all cases due to the low-pressure region which exists there

### 4.3.5 Boundary layer profiles

Longitudinal velocity profiles normal to container sides are shown in Figure 63. The measurements are made halfway along the length of each container at heights of  $z=1$  m,  $z=2$  m and  $z=3$  m. The loading positions of the containers in the train are denoted by 1, 2, 3 or 4, with 1 being at the front and 4 at the rear of the train.

The profiles in

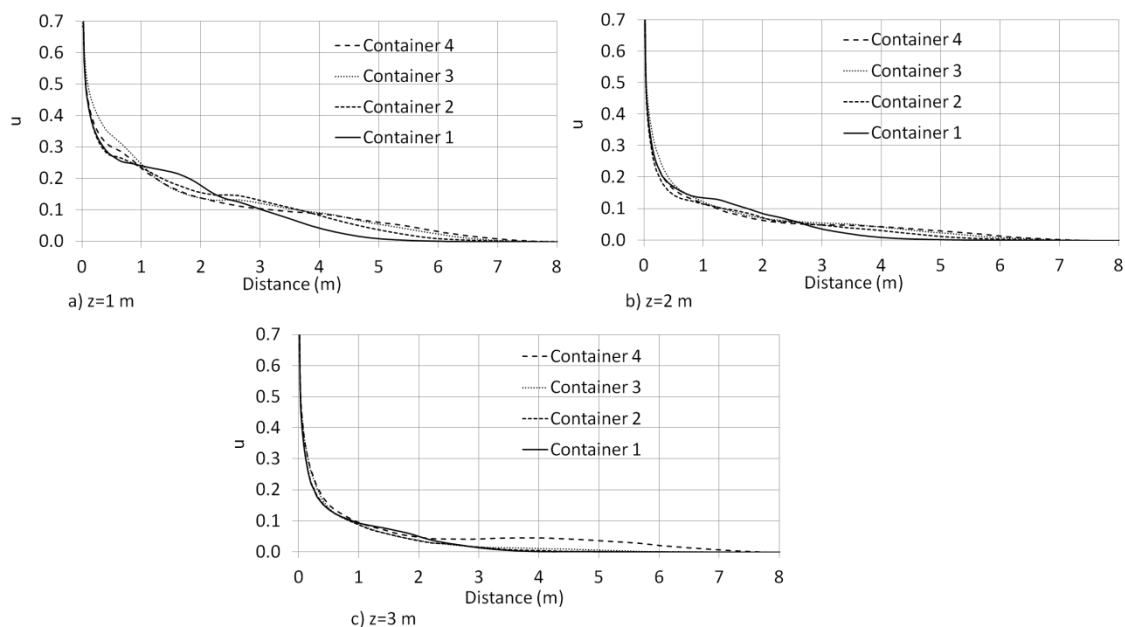


Figure 63 show a general trend of decreasing velocity with distance from the container sides with the approximate shape of

$$u = e^{-ky'} \quad (4.6)$$

where

$k$  – positive constant.

At  $z=1$  m and  $z=2$  m above TOR the velocity in the range  $0 < y' < 1$  m is greatest at the middle of container 3 because of the unsteady ejections that occur from the shear layer that forms at the largest inter-wagon spacing between wagons 2 and 3. Such ejections are a common occurrence in cavity flows and can be observed at two instances in time in Figure 64.

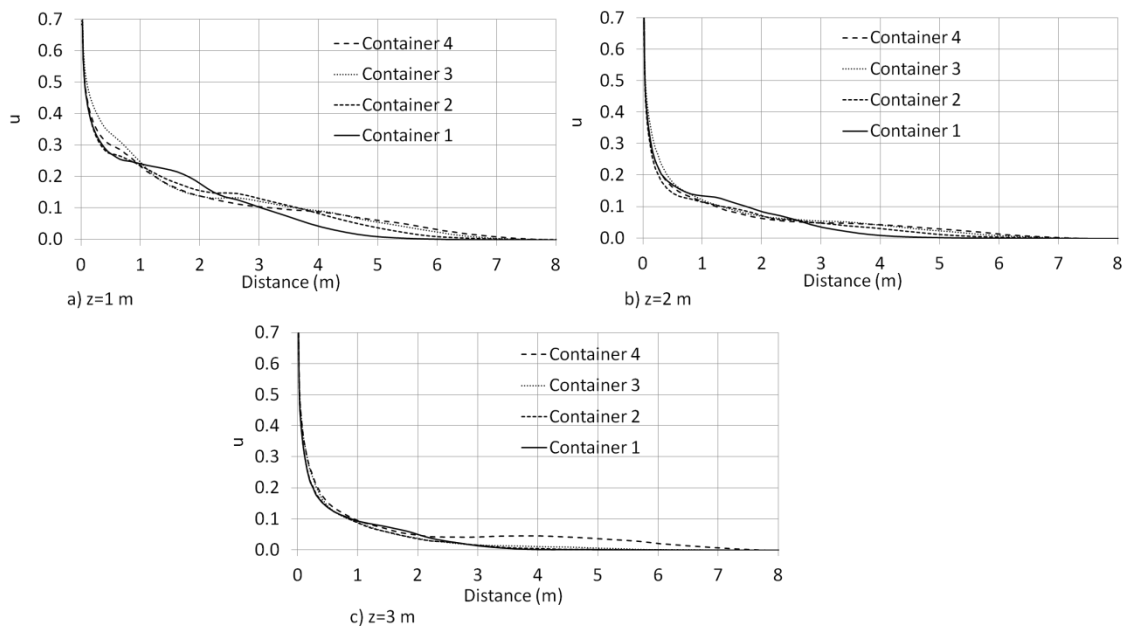


Figure 63 Longitudinal velocity profiles with distance from the side of each container (1, 2, 3 or 4) at a)  $z=1$  m, b)  $z=2$  m and c)  $z=3$  m.

At further distances from the container sides ( $y' > 4$  m), the largest slipstream velocities occur at the middle of the 4<sup>th</sup> container as a result of boundary layer growth. Greater slipstream velocities towards the rear of a train are commonly reported in the literature both at full and model scale (Sterling et al., 2008, Hemida et al., 2014, Baker, 2010). It is expected

that the slipstream of a sufficiently long train would exhibit growth up to a limiting value and then subsequent boundary layer profiles at each container would be almost identical providing that the geometry of subsequent container wagons remained constant.

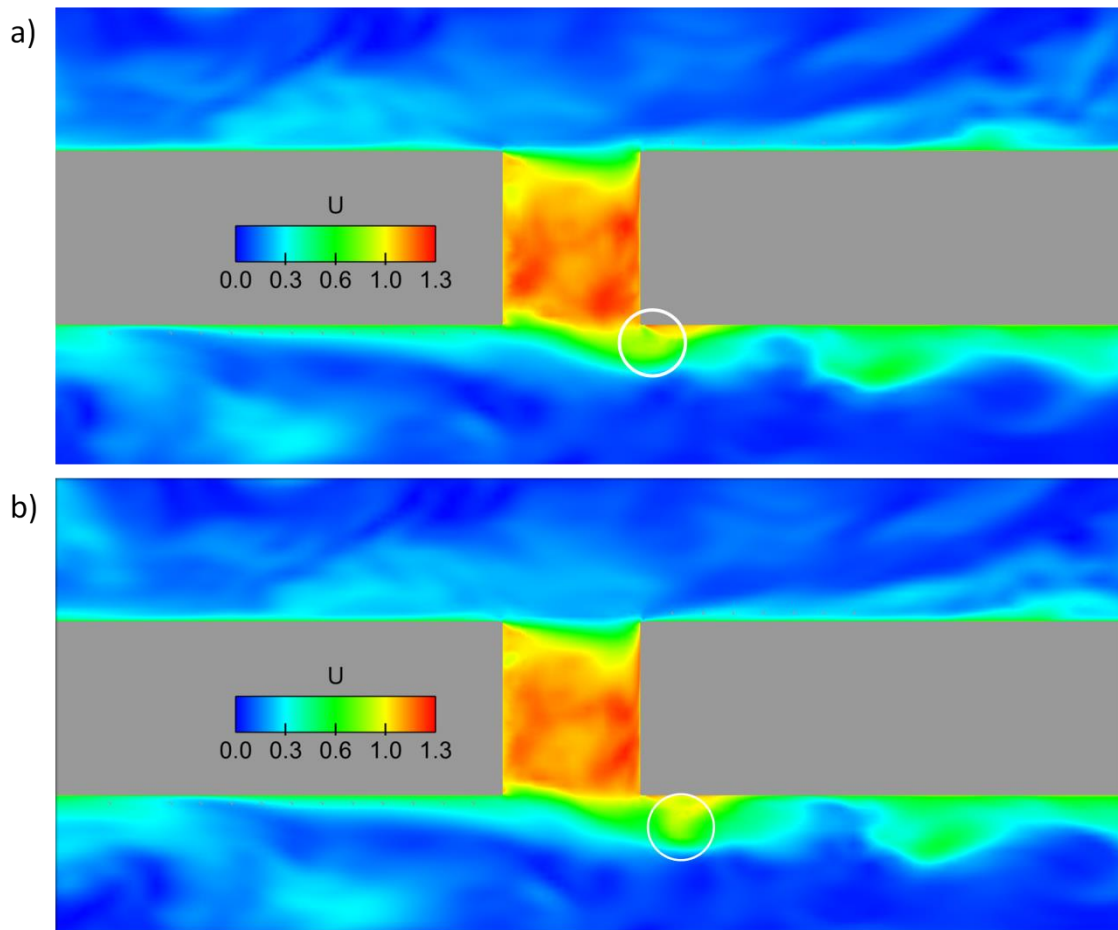


Figure 64 Colour plot of velocity magnitude showing ejections from largest inter-wagon spacing at  $z=2$  m for a)  $t_1$  and b)  $t_2$ .

Figure 65 shows the container-normal velocities presented in Figure 63 but the data are plotted with respect to distance from TOR normal to each container. By plotting the data in this way, the effect of height on  $u$  at each measurement position can be elucidated.

The profiles in Figure 65 show that with increasing distance above TOR velocity decreases. The velocities at  $z=2$  m and  $z=3$  m are much more comparable than  $z=1$  m and  $z=2$  m

because the geometry at  $z=2$  m and  $z=3$  m are comparable and are further away from the relatively rough bogies.

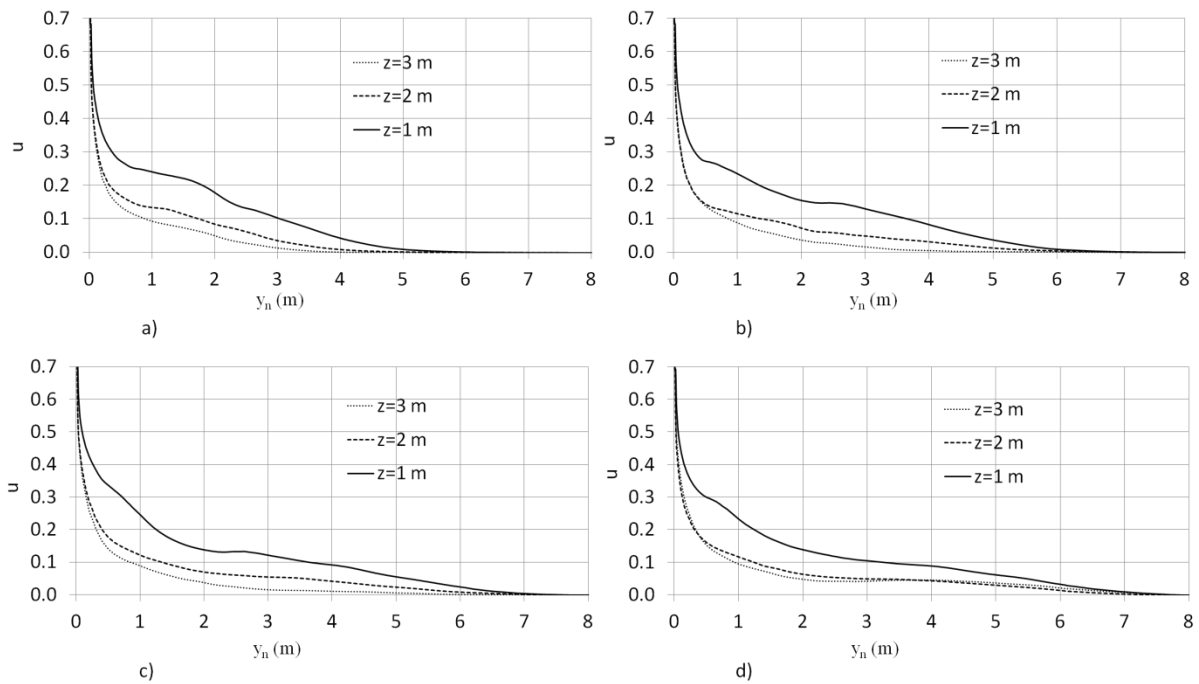


Figure 65 Longitudinal velocity profiles normal to train side at the centre of a) container 1, b) container 2, c) container 3 and d) container 4 at 3 heights above TOR

#### 4.3.6 Inter-wagon spacings

This section shows the mean flow structures that exist in the inter-wagon spacings and for ease of recognition these are labelled in Figure 66. Figure 67 shows mean streamlines projected onto a plane coloured by velocity magnitude at  $y=0$  m. The flow structures in the first inter-wagon spacing differ with respect to those in the other inter-wagon spacings as a result of the taller, preceding locomotive (Figure 67 a). The mean flow in the gap recirculates in the top third and the flow below that is either heading towards the ground or is recirculating as a result of the air dam at the rear of the locomotive.



Figure 66 Designation of inter-wagon spacings

The identical inter-wagon spacings (2 & 4) shown in Figure 67 b & d, display a coherent mean flow structure approximately 20 % of the container height. The difference between the mean flow structures in spacings two and four is a result of the developing boundary layer around the train. In the third inter-wagon spacing, the flow recirculates in the upper quarter of the spacing and further recirculation is caused by the buffers at the fore and aft of wagons two and three, respectively.

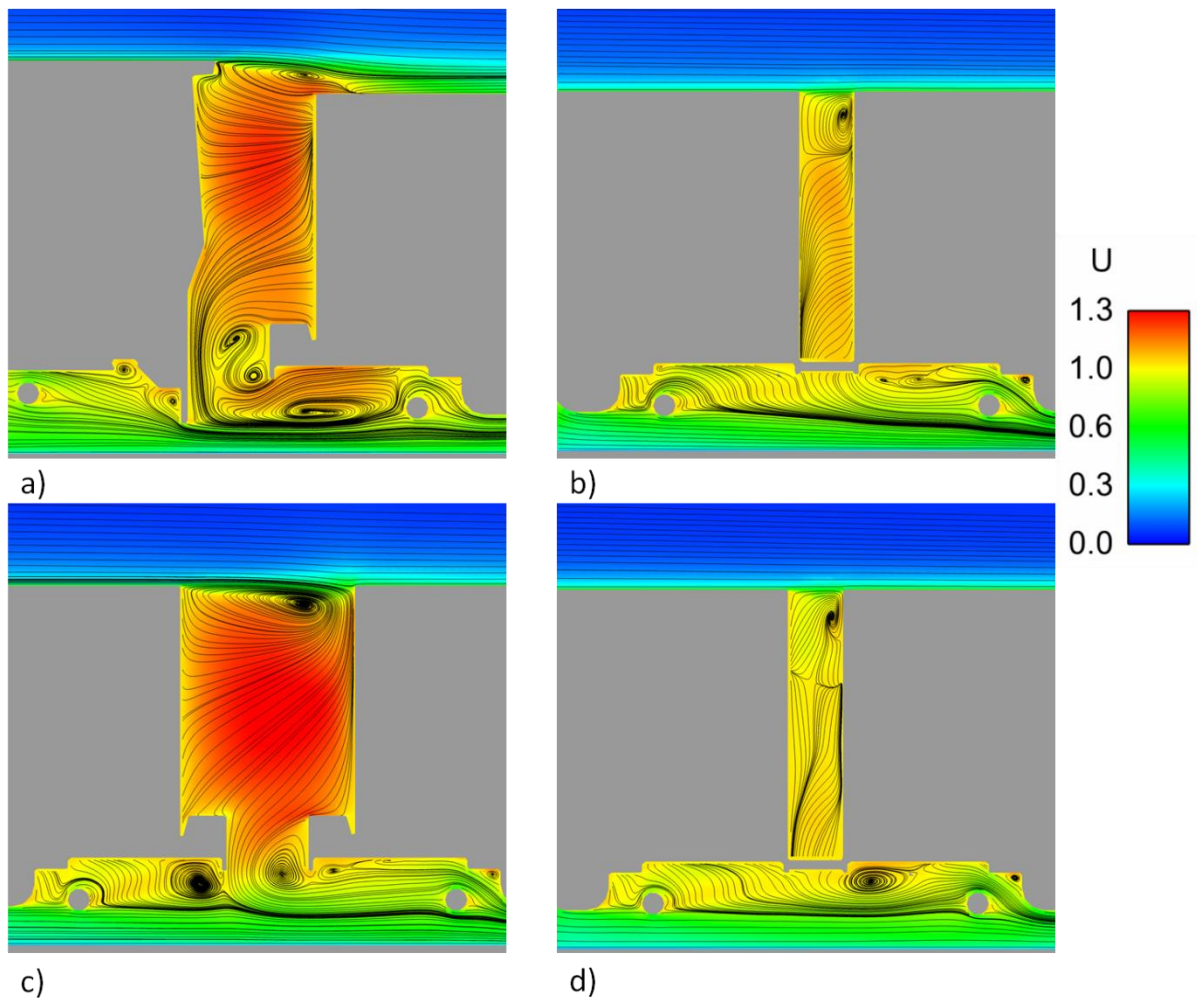


Figure 67 Time-averaged streamlines projected on a plane at  $y=0$  m coloured by  $U$

Figure 68 show mean streamlines projected onto a plane coloured by velocity magnitude at  $z=2$  m. Due to the symmetrical nature of the flow in the horizontal plane, it is expected that the mean flow vortices are also symmetrical. Figure 68a & c show large vortices with length

to width ratios of approximately 1, whereas Figure 68b & d show much more confined vortices with aspect ratios of approximately 2.

The effect of vortex dimensions on the drag of open-top freight wagons was discussed by Saunders et al.(1993). It was found that by altering the proportions of the inside of the wagon, the stability of the vortices inside could be increased, thus reducing the perturbation on the external flow, thereby reducing drag. It was found that cavities with approximately equal depth and streamwise proportions produced more stable-vortices than cases with unequal proportions. In the present case, inter-wagon spacings 1 & 3 are more likely to produce lower perturbation on the slipstream than 2 & 4, because the length and width ratio is closer to unity. It is acknowledged by the author that Saunders et al.(1993) were considering open-top hopper wagons although the theory appears to be relevant.

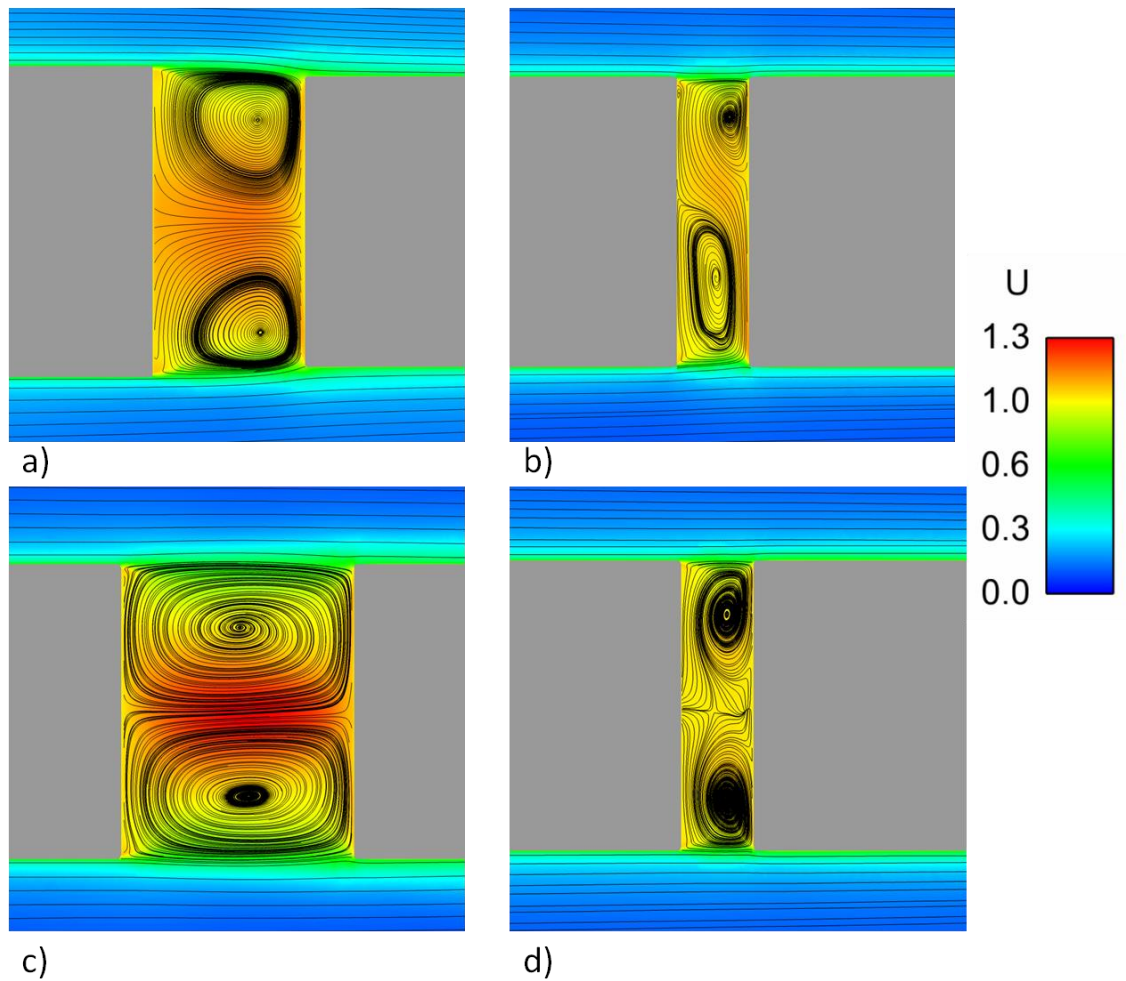


Figure 68 Time-averaged streamlines projected on a plane at half train height coloured by  $U$

The flow structures inside the inter-wagon spacings shown in Figure 68 can be considered analogous to the flow in representative urban street canyons shown in Figure 14; especially the skimming flow in Figure 14c. A degree of asymmetry is present in Figure 68 which is attributed to minor asymmetry in the CAD model. If the distance between the containers is  $W$  and the half-width of the containers is considered to be  $H$  due to the symmetrical nature of the flow then  $H/W$  ratios for the first, second, third and fourth inter-wagon spacings are 0.96, 2, 0.64 and 2, respectively.

A broad comparison can be drawn between the flow behaviour over the containers and that of urban street canyons although it should be stressed that the length of the containers with respect to the inter-wagon spacings are much larger in the present case. From the information

in Figure 69 it is evident that that flow around the majority of the containers can be considered as skimming flow although the largest inter-wagon spacings are close to the size of wake-interference flow. If lower container loading efficiencies were considered the flow could be more like wake interference or isolated roughness flow.

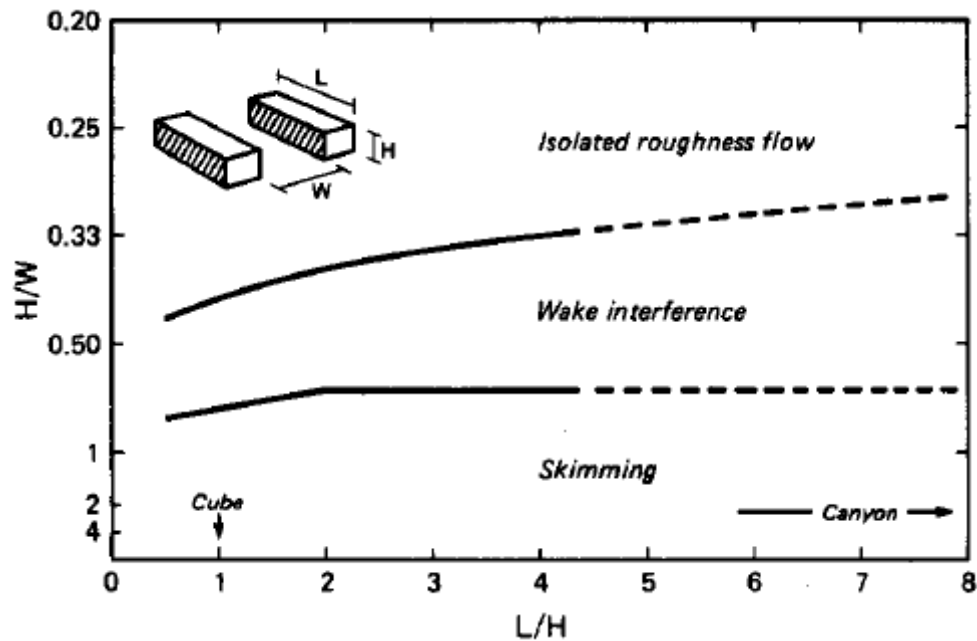


Figure 69 The behaviour of flow in street canyons as functions of H/W and L/H ratios (Oke, 1988)

#### 4.3.7 Displacement thickness

Displacement thickness,  $\delta^*$ , is a parameter which approximates the depth of a 2-dimensional boundary layer over a flat-plate. Displacement thickness has also been widely used in train slipstream analysis as an approximation of slipstream thickness (Baker et al., 2001, Sterling et al., 2008, Soper, 2014, Pii et al., 2014), although this method can produce spurious results due to the lack of samples normal to train side. The derivation and application of the displacement thickness was presented in Section 2.5.1.2.

The displacement thickness in the present work was generated by using 11 slipstream velocity samples at distances between 0.025 m and 2.5 m from train side. Figure 70 shows

that the displacement thickness varies very little along the length of the train. The mean displacement thickness along train length is  $\delta^*=0.61$  m which is in broad agreement with Soper (2014) which had a displacement thickness of  $\delta^*=0.6-0.8$  m for the majority of train length. The difference between the results is likely to be due to the work only using 3 probes at train side. A minor increase is observed in the near wake of the train however, this is not considered to be part of the boundary layer. From the data presented in Figure 70 it appears that the displacement thickness is largely fixed by the flow separation around the locomotive and not from slipstream growth in the boundary layer region.

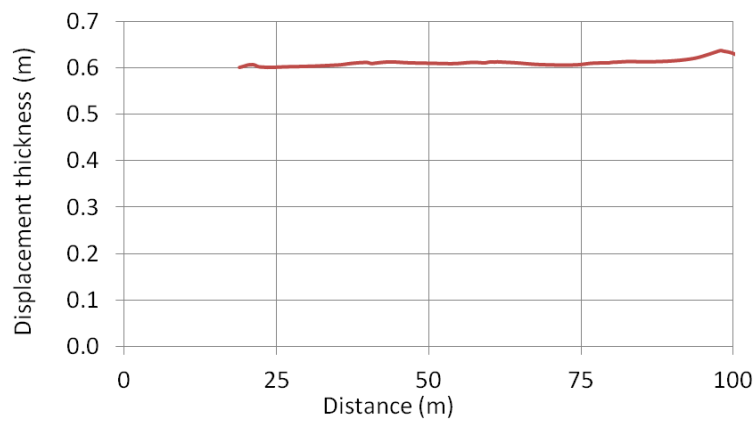


Figure 70 Displacement thickness of the slipstream at mid-height

### 4.3.8 Pressure coefficients at train side

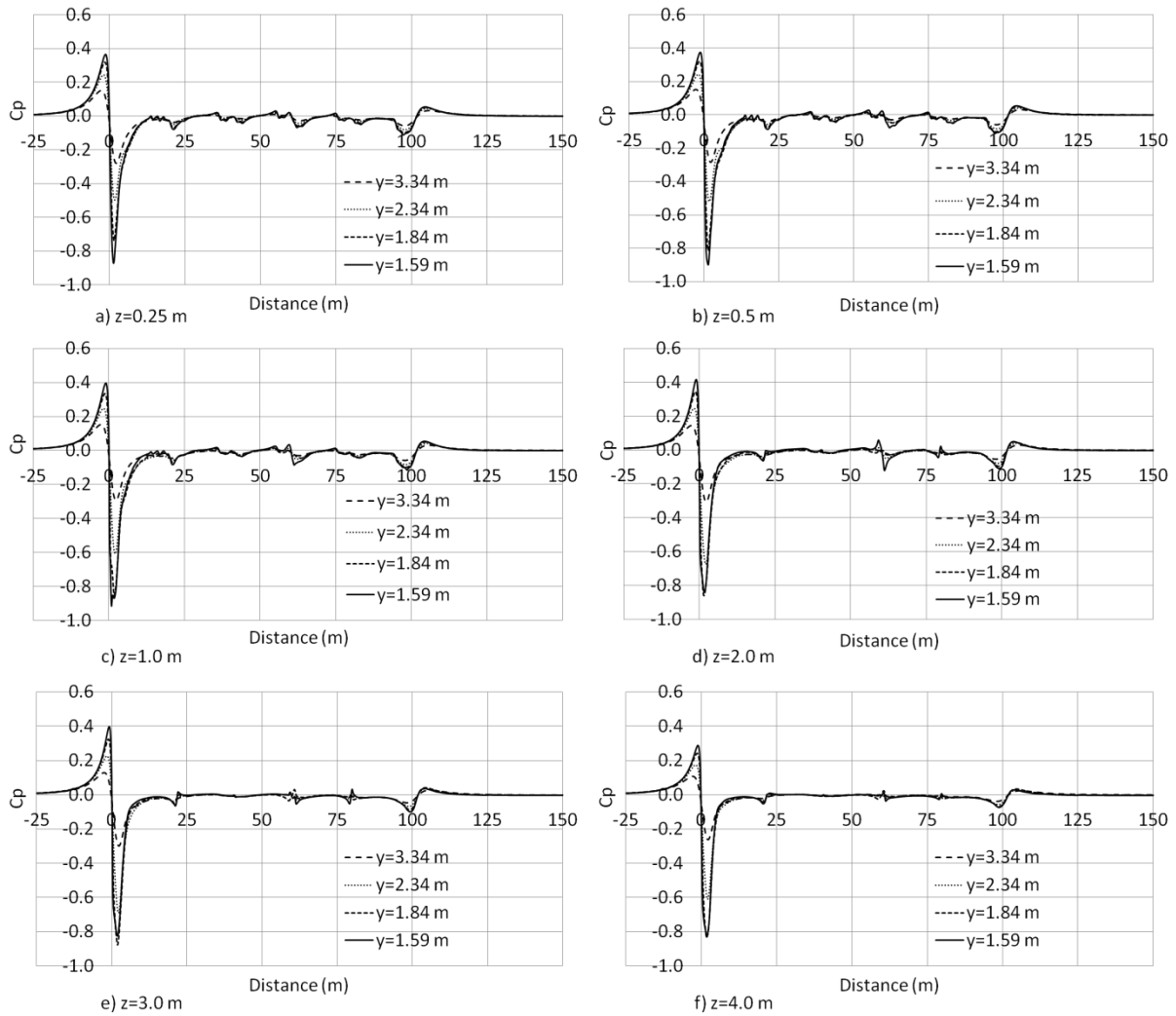


Figure 71 Pressure coefficients at distances from COT and at varying distances above TOR a)  $z=0.25$  m, b)  $z=0.5$  m, c)  $z=1.0$  m, d)  $z=2.0$  m, e)  $z=3.0$  m and f)  $z=4.0$  m

Figure 71 shows the pressure coefficients sampled at train side at the locations shown in Figure 48. The effect of the bogies on the pressure coefficient is visible at  $z=0.25$  m and  $z=0.5$  m as roughness on the curves. The distinction between flow regimes occurs between  $z=1$  m and  $z=2$  m, where the additional roughness of the bogies disappears from the plots. The pressure transient,  $\Delta C_p$ , at the largest inter-wagon spacing is greatest at  $z=2$  m, with a magnitude of  $\Delta C_p=0.18$ .

The maximum peak-to-peak pressure occurs at  $y=1.59$  m,  $z=1$  m and is approximately  $\Delta C_p=1.31$ . For all heights above TOR the maximum peak values of pressure occur closest to train side except at  $z=2$  m and  $z=3$  m, where this happens at  $y=1.84$  m. It can be observed in Figure 72 that the greatest negative pressure region migrates away from train side with height due to the changing profile of the locomotive. The largest wake pressure transient occurs at  $y=1.59$  m and  $z=1$  m and is  $\Delta C_p=0.17$ .

The pressure transients in the nose region are significantly greater than have been observed in the literature for passenger trains where values closer  $\Delta C_p=0.4$  are expected due to the more streamlined shape of the trains.

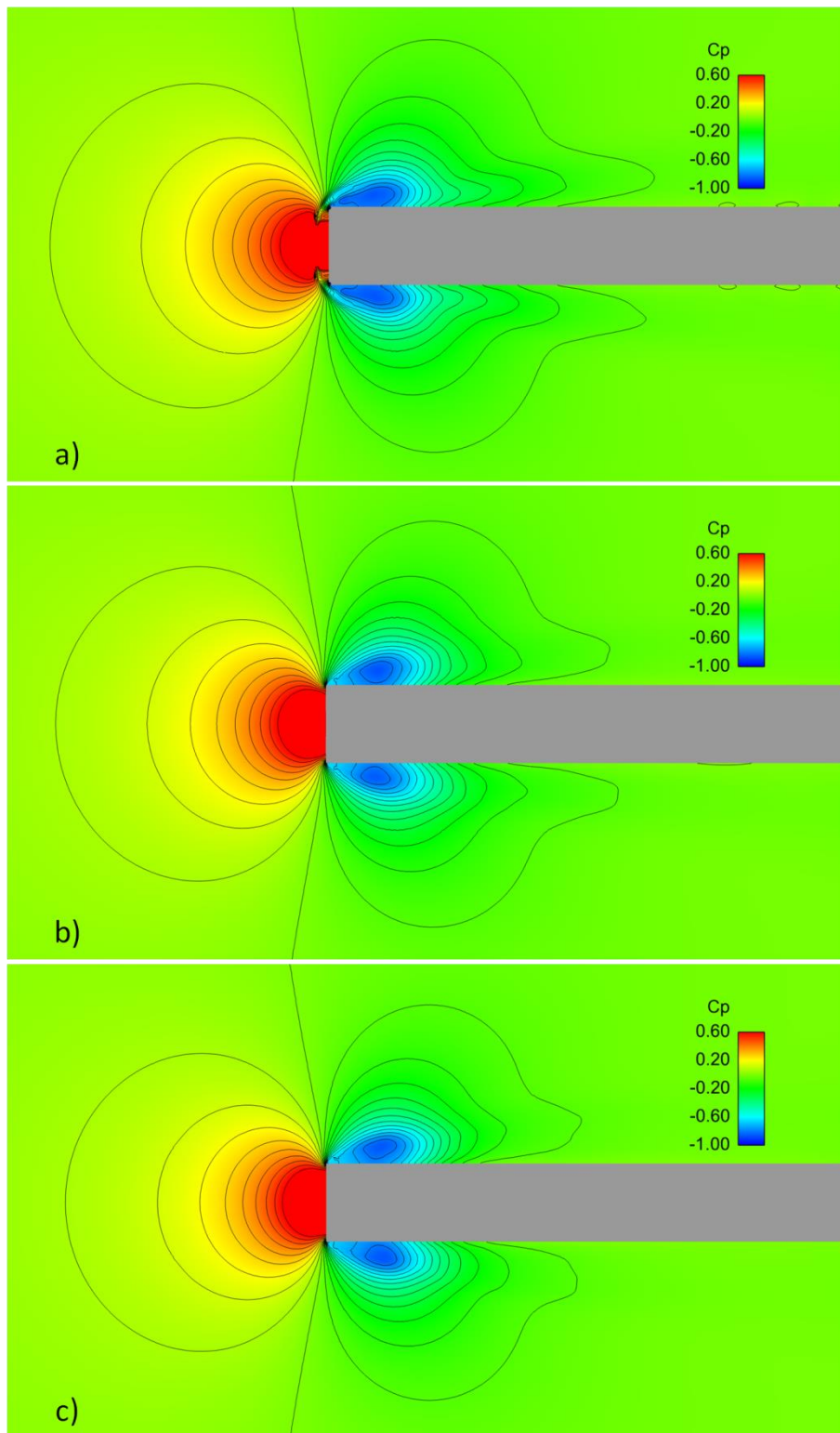


Figure 72 Colour contour plot of pressure coefficient on planes at a)  $z=1$  m b)  $z=2$  m and c)  $z=3$  m

Figure 73 shows the positive and negative pressure fields in front of, and around the Class 66 locomotive. The adjacent pressure fields form a negative pressure gradient at the front of the

train causing flow acceleration towards the rear. The negative pressure region extends further towards the rear of the locomotive closer to the top of rail due to the influence of the air dam and the under body complexities. Furthermore, the greatest difference between pressure coefficients at  $x=8$  m for  $z=0.5$  m and  $z=4$  m which can be seen from the shape of the pressure isosurface in Figure 73.

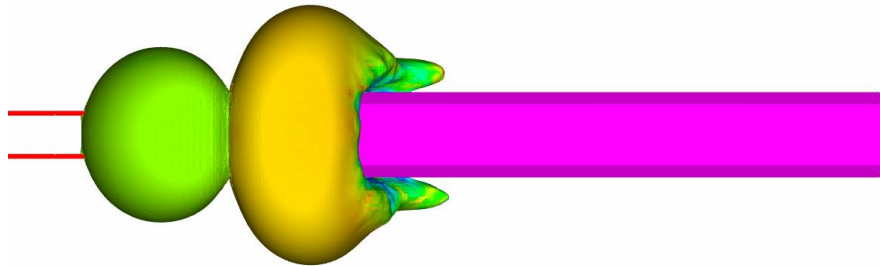


Figure 73 Mean pressure isosurfaces around the front of the locomotive for  $C_p=0.2$  (left) and  $C_p=-0.2$  (right), coloured by velocity magnitude

The pressure coefficients shown in Figure 71 are re-plotted in Figure 74 to allow for the effect of height on  $C_p$  to be investigated. The most significant differences between the  $\Delta C_p$  in the nose region occur at  $y=1.84$  and  $y=2.34$  m.

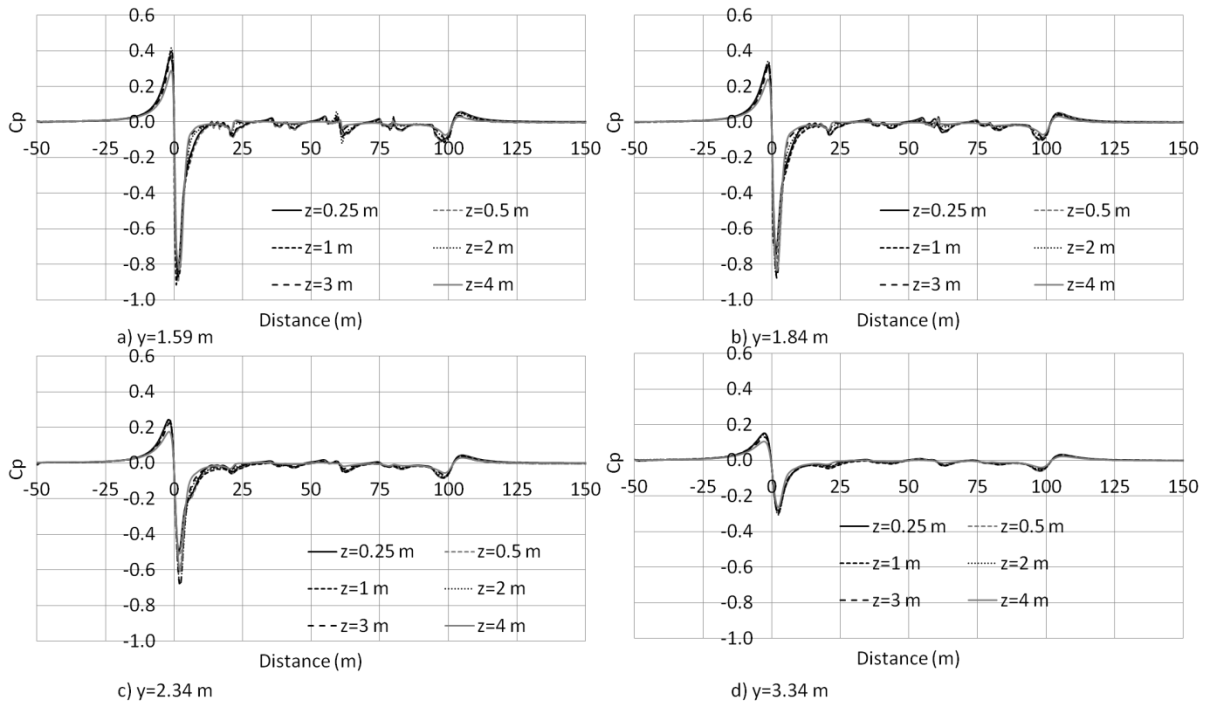


Figure 74 Pressure coefficients at distances above TOR and at varying distances from COT  
(a)  $y=1.59$  m, (b)  $y=1.84$  m, (c)  $y=2.34$  m and (d)  $y=3.34$  m

#### 4.3.9 Nose region visualisation

In order to improve the understanding of the behaviour of the slipstream ahead of and around the locomotive, the present section uses time-averaged velocity vectors projected onto planes coloured by velocity magnitude (Figure 75 and Figure 76).

The images in Figure 75 are at the same vertical positions as the sampling locations shown in Figure 48, namely  $z=0.25$  m,  $z=0.5$  m,  $z=1$  m,  $z=2$  m,  $z=3$  m and  $z=4$  m. Velocity magnitude in the colour plots increases ahead of the locomotive until it reaches stagnation on the face and is then at train speed. In the under-floor region, higher velocities are observed on the outer regions of the wheels and at the COT. The recirculation region around the side of the locomotive is visible at all heights above  $z=0.5$  m.

In the underbody region, at  $z=0.5$  m, higher velocity magnitudes are observed than at  $z=0.25$  m, because the plane is closer to the locomotive's surface thus having a more comparable

velocity to train speed than it would if it were further away. As well as higher velocities, there is also a significant increase in recirculation due to the underbody geometry.

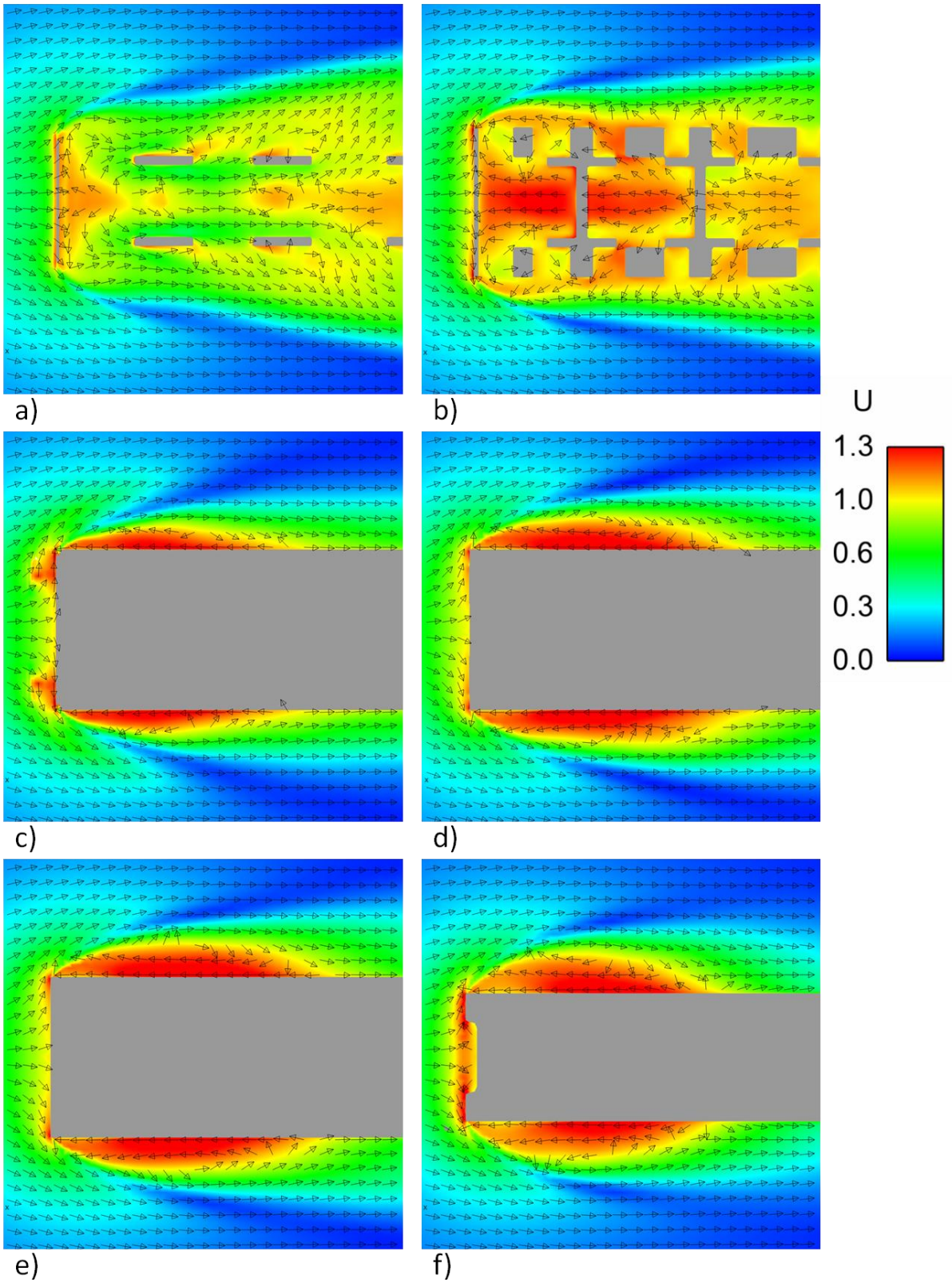


Figure 75 Time-averaged velocity vectors on cut planes (coloured by velocity magnitude) at distances above TOR a)  $z=0.25$  m, b)  $z=0.5$  m, c)  $z=1.0$  m, d)  $z=2.0$  m, e)  $z=3.0$  m and f)  $z=4.0$  m

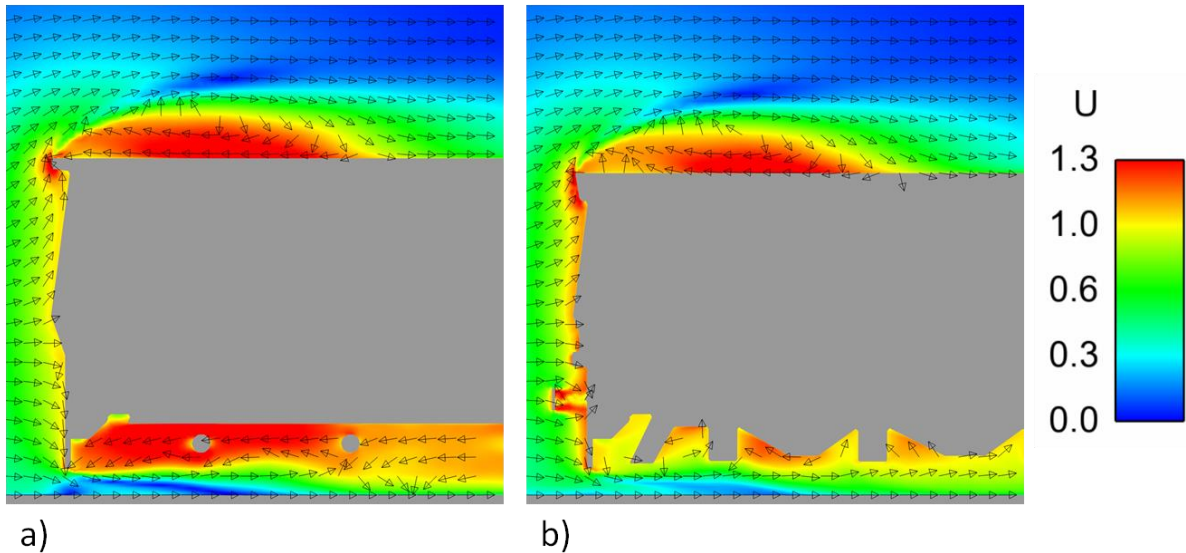


Figure 76 Time-averaged velocity vectors on cut planes (coloured by velocity magnitude) at distances from COT, a)  $y=0$  m and b)  $y=1$  m

Figure 76 shows the velocity vectors at two cuts in the lateral plane. At  $y=0$  m, the velocity vectors near the train underbody and the ground are ‘opposing’ which signifies the presence of a turbulent Couette-like flow as observed by Ido et al.(2008) underneath a high-speed train.

#### 4.4 *Instantaneous flow*

The behaviour of the mean flow around the train was considered in depth in the previous section. However, in the real world a person does not experience the mean flow they experience instantaneous flow. In the following section, the instantaneous nature of the slipstream of a freight train will be presented.

##### 4.4.1 *Vortex generation*

Figure 77 presents an instantaneous view of the vortices generated in the three main regions of the freight train’s slipstream. The flow visualisation are isosurfaces of the second invariant of the velocity gradient tensor , Q-Criteria (Jeong and Hussain, 1995), coloured by velocity magnitude. Q-Criteria is defined as

$$Q = \frac{1}{2}(\Omega_{ij}\Omega_{ij} - S_{ij}S_{ij}) \quad (4.7)$$

where

$S_{ij}$  – strain–rate tensor

$\Omega_{ij}$  – vorticity tensor

and is chosen as a means of visualising vortices over similar methods such as vorticity isosurfaces because Q-Criteria allows for the balance between strain rate and vorticity components to be quantified. Vorticity can occur in flows where no vortices are present and hence visualising vortices using this method is somewhat flawed (Jeong and Hussain, 1995).

Around the front face of the locomotive a large degree of vortex generation is observed as a result of the inherently unsteady process of flow separation (Figure 77). In the boundary layer region the majority of the vortices are generated in the under-floor region due to the turbulent Couette-like flow that exists there. A superficial comparison of the vortices generated around the locomotive and those generated in the under-floor region displays the general difference in the scale of the turbulent flow structures. The vortices around the locomotive are generally larger than those in the under-floor region due to their lack of confinement which allows for unimpeded development. In the near wake region, a combination of large- and smaller-scales is exhibited at  $z \approx 1$  m where the flow from the under-floor region interacts with the larger-scale structures in the wake.

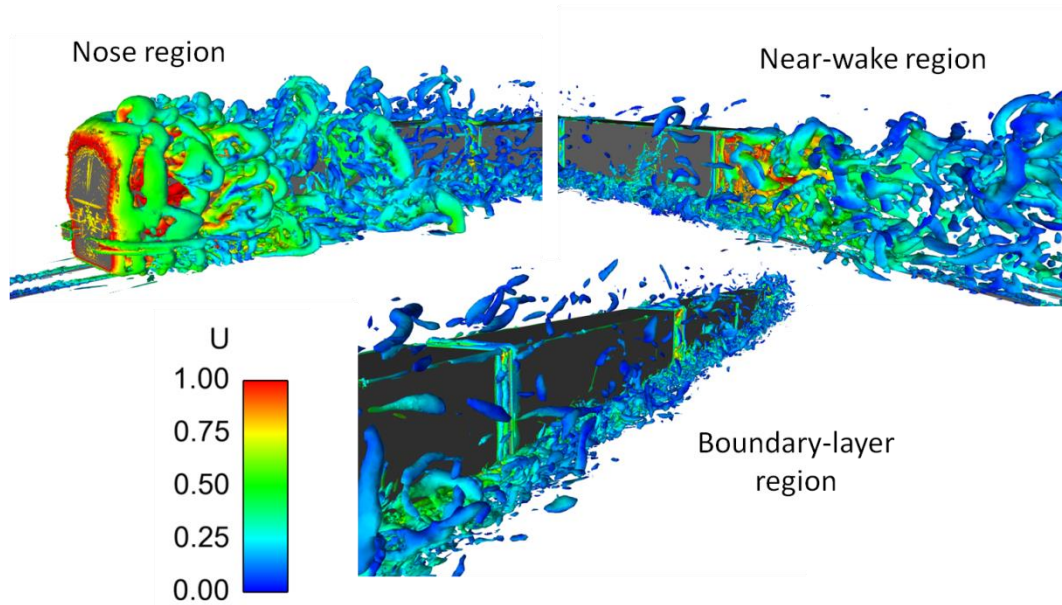


Figure 77 Isosurfaces of second invariant of the velocity gradient tensor,  $Q=50,000$ , coloured by velocity magnitude.

#### ***4.4.2 Turbulence intensity at train side***

The turbulence intensities at train side are shown in Figure 78. In the region of flow around the locomotive, extremely high turbulence intensities were observed as a result of massive flow separation. It has been determined that for the present work turbulence intensities greater than 100% may be misleading and are thus neglected from the present analysis.

The standard method of calculating the turbulence intensity is the ratio of the standard deviation to the mean wind speed (Davidson, 2004). In the present work, the mean velocity and standard deviation are calculated locally as has previously been performed in train slipstream analysis (Sterling et al., 2008, Baker et al., 2001, Soper, 2014) and thus turbulence intensity,  $I$ , is given by equation 1.10.

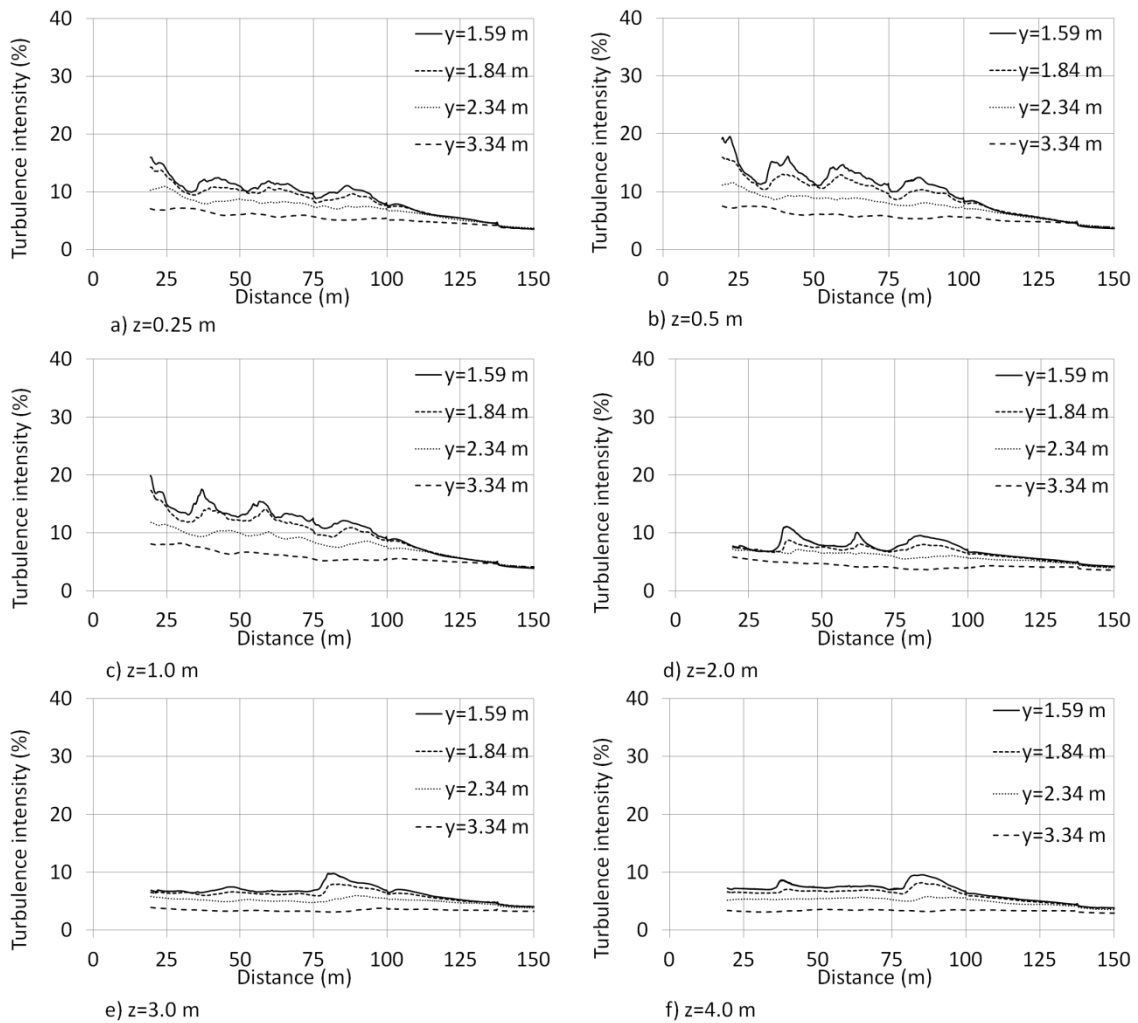


Figure 78 Turbulence intensity at distances from the COT and at varying distances above TOR a)  $z=0.25$  m, b)  $z=0.5$  m, c)  $z=1.0$  m, d)  $z=2.0$  m, e)  $z=3.0$  m and f)  $z=4.0$  m

There is a general decay in turbulence intensity along train length with peaks occurring at inter-wagon gaps, as was observed with velocity magnitude in Section 4.3.2. Turbulence intensity is greatest at the closest measurement position to the train,  $y=1.59$  m and the maximum value of turbulence intensity in the boundary layer region is  $I=18\%$  at  $x=37$  m and  $z=1$  m. The second inter-wagon spacing has the highest turbulence intensity peak at all heights above TOR due to the lower mean velocity than at the largest inter-wagon spacing. For  $x > 100$  m the turbulence intensities converge towards the value at  $y=3.34$  m at all heights above TOR. The intensity of the turbulence generated from the locomotive increases with height until  $z=1$  m, after which it decreases with height above TOR.

As was shown for the mean velocities at train side, the turbulence intensities also decay along train length. This observation again suggests that the locomotive is the main cause of the turbulence generation in the slipstream although contributions are also evident from the inter-wagon spacings.

For the same consist in Soper (2014), the peak turbulence intensity in the boundary layer region is approximately  $I=90\%$ , more than four times greater than the turbulence intensity in the present work. It is hypothesised that this massive difference is a result of the variation in the methods of calculating the normal turbulent stresses as well as additional fluctuations in the velocity due to vibration of the Cobra probes. In the present work, the normal turbulent stresses are averaged arithmetically at each time step, whereas in Soper (2014) there are only 25 samples to take these values from. In the present work the turbulent stresses are calculated and averaged over more than 100,000 time steps and will thus provide a more representative standard deviation than is possible to obtain from 25 realisations.

The turbulence intensities obtained in the present work are much lower than those obtained from full-scale measurements shown in Figure 15. In the boundary layer region of the present freight train's slipstream turbulence intensity is in the order of  $I=5-25\%$  and is significantly lower observed in Figure 15, which range from  $I=5-45\%$ . Effects such as atmospheric conditions, scale, measurement techniques and dynamic effects such as buffeting are all hypothesised to be responsible for the discrepancy.

#### ***4.4.3 Integral length scale***

The autocorrelation functions obtained from the velocity signal for each probe are shown in Figure 79. The auto-correlation function,  $\rho(t)$ , is defined as

$$\rho(\tau) = \frac{\dot{u}(t)\dot{u}(t + \tau)}{\sigma^2} \quad (4.8)$$

where

$\dot{u}$  – fluctuating velocity component

and the integral time-scale,  $\tau_l$ , is found by

$$\tau_l = \int_0^{\infty} \rho(\tau) d\tau . \quad (4.9)$$

The integral time-scale was found by using the trapezium rule to numerically integrate under the autocorrelation curves until the correlation is zero (Pope, 2000). The integral time-scale was then converted into the integral length-scale by multiplying by train speed.

The velocity time-series data were obtained from stationary velocity probes close to each inter-wagon spacing, at half train height. The velocity time-series used in full- (Sterling et al., 2008) and model-scale (Soper, 2014) experimental work are obtained as the train passes the static probe which means that the value of the integral time-scale is valid relative to a static observer. However, the integral time-scale in the current work is only valid for a single point relative to the train.

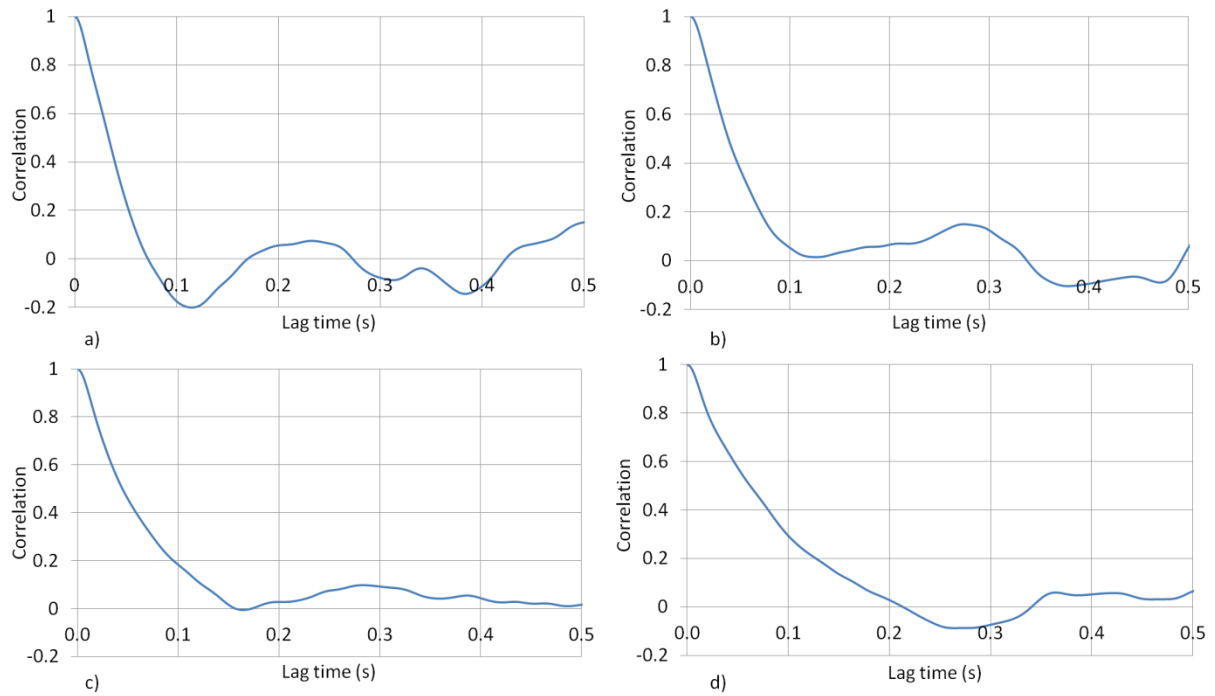


Figure 79 Correlation against lag-time for the probe at  $y=1.84$  m and  $z=2.1$  m for a)  $x=21$  m, b)  $x=40$  m, c)  $x=60$  m and d)  $x=80$  m

Table 3 Integral values at probe positions relative to train

Probe	$x$ (m)	$y$ (m)	$z$ (m)	Time-scale (s)	Length-scale (m)
1	21	1.84	2.1	0.034	1.12
2	40	1.84	2.1	0.061	2.02
3	60	1.84	2.1	0.056	1.86
4	80	1.84	2.1	0.038	1.24

Table 3 shows the probe coordinate positions, integral time-scale and integral length-scales in terms of full-scale. The data show integral length-scales from all four probe locations are within 1 m of one another. The largest integral time-scale in the flow is only 16% of the 0.375 s required for a person to become unsteady and therefore it is considered unlikely to be long enough in duration to have any effect on a person. This being said, the time-scales are

measured relative to the train so their applicability to the person unsteady scenario is currently unclear.

#### **4.4.4 Force coefficients**

Force coefficients exist as a result of unbalanced pressures and frictional forces on the surface of the flatbed wagons and containers. In train aerodynamics, the drag force experienced by a high-speed passenger train will be largely dominated by the frictional force of the air moving over the surface of the train. For shorter or bluffer trains, the drag force is dominated by pressure forces as a result of flow stagnating on or separating from the surfaces.

The container wagons in the present work consist of a flatbed wagon and a representative shipping container. The incidents at Cheddington and Hardendale (RAIB, 2009) were a result of container shedding and not due to the entire freight wagons rolling over as has been seen for double-stacked container wagons (ATSB, 2011, ATSB, 2010, TSBC, 1999). For this reason, the present section will mainly focus on the forces experienced by containers as they are most susceptible to wind-induced forces in their tare condition.

The area by which force coefficients are normalised are often different between cases, some choose container side area (Krönke and Sockel, 1994), the product of container length and height (Hemida and Baker, 2010) or the projected front area of the wagon (Östh and Krajnović, 2014). Due to the lack of consistency in normalising areas selected by researchers, comparison between the force coefficients is difficult. It is recommended by CEN (2010) that the normalising area should be standardised to  $10 \text{ m}^2$  to circumvent the above difficulties.

The total force coefficients experienced by the locomotive and each container are shown in Tables 2 & 3. The drag, side and lift force coefficients,  $C_d$ ,  $C_s$  and  $C_l$ , respectively, are calculated by

$$C_d = \frac{F_x}{\frac{1}{2}\rho u_{in}^2 A}, C_s = \frac{F_y}{\frac{1}{2}\rho u_{in}^2 A}, C_l = \frac{F_z}{\frac{1}{2}\rho u_{in}^2 A} \quad (4.10)$$

where

$F_x, F_y, F_z$  – total drag, lift and side force

$A_{ref} = 10 \text{ m}^2$ .

Due to the symmetry of the case the side force coefficient is negligibly small and is thus omitted from this analysis. The drag force coefficient,  $C_d$ , experienced by the Class 66 locomotive is 1.99 where 95% of the drag is contributed by pressure (Table 4). The  $C_d$  experienced by the first container wagon is 0.09, 38% of the force experienced by the subsequent wagon and 5 % of that experienced by the locomotive. In Golovanevskiy et al.(2012) the drag experienced by the locomotive is more than five times greater than the drag experienced by the first container wagon. In the present work the locomotive is much bluffer than other freight trains thus it will experience greater force coefficients due to effects such as flow separation. The effect of adjacent wagons on force coefficients was investigated by Watkins et al.(1992) and it was found that the drag experienced by a container wagon with 1 upstream wagon and 0.5 wagons downstream is approximately 1/3<sup>rd</sup> of the force experienced by a wagon with only 0.5 wagons downstream. The first container experiences a negative pressure drag as a result of being positioned in the wake region of the Class 66 locomotive and is the only container to experience negative pressure drag.

The general trend in  $C_d$  with loading position in the present work compares broadly to those experienced by the container wagons in Golovanevskiy et al.(2012). In the present work the drag force experienced by the entire second wagon is 2.5 times greater than the force experienced by the first wagon. Golovanevskiy et al.(2012) shows only a 36% increase

between the drag force on first and second containers, although this is most likely to be due to the difference in vehicle geometry.

Table 4 Drag force coefficients experienced by the locomotive, each container and each wagon

	<b>Total</b>	<b>Pressure</b>	<b>Viscous</b>	<b>Whole wagon</b>
<b>Class 66</b>	1.99	1.90	0.09	1.99
<b>Container 1</b>	0.04	-0.07	0.11	
<b>Flatbed wagon 1</b>	0.05	0.04	0.01	0.09
<b>Container 2</b>	0.15	0.04	0.11	
<b>Flatbed wagon 2</b>	0.09	0.08	0.01	0.24
<b>Container 3</b>	0.20	0.10	0.10	
<b>Flatbed wagon 3</b>	0.17	0.09	0.07	0.37
<b>Container 4</b>	0.26	0.15	0.11	
<b>Flatbed wagon 4</b>	0.14	0.12	0.02	0.40

The lift force coefficients on each container show a general trend of increasing towards the rear of the train. On the other hand, the total force experienced by the first and final wagons is negative as a result of the addition of the force on the flatbed wagons. The two intermediate wagons experience positive lift coefficients due to the positive forces experienced by the flatbed wagons. The locomotive, the first container and the fourth flatbed wagon all experience negative lift coefficients. The cause of the negative lift force coefficient from the locomotive is the low pressure which is dominant in the under floor region. The negative lift

force experienced by the first container is hypothesised to be a result of the downwash from the locomotive stagnating on the roof of the container, although the value is only 1/3<sup>rd</sup> of the force experienced by the Class 66 locomotive. The negative lift force experienced by the final flatbed wagon is half the value experienced by the Class 66 locomotive.

Table 5 Lift force coefficients experienced by the locomotive, each container and each wagon

	<b>Total</b>	<b>Pressure</b>	<b>Viscous</b>	<b>Whole wagon</b>
<b>Class 66</b>	-0.18	-0.18	0.00	-0.18
<b>Container 1</b>	-0.06	-0.06	0.00	
<b>Flatbed wagon 1</b>	0.04	0.04	0.00	-0.02
<b>Container 2</b>	0.04	0.04	0.00	
<b>Flatbed wagon 2</b>	0.01	0.01	0.00	0.05
<b>Container 3</b>	0.04	0.04	0.00	
<b>Flatbed wagon 3</b>	0.02	0.02	0.00	0.06
<b>Container 4</b>	0.14	0.14	0.00	
<b>Flatbed wagon 4</b>	-0.23	-0.23	0.00	-0.09

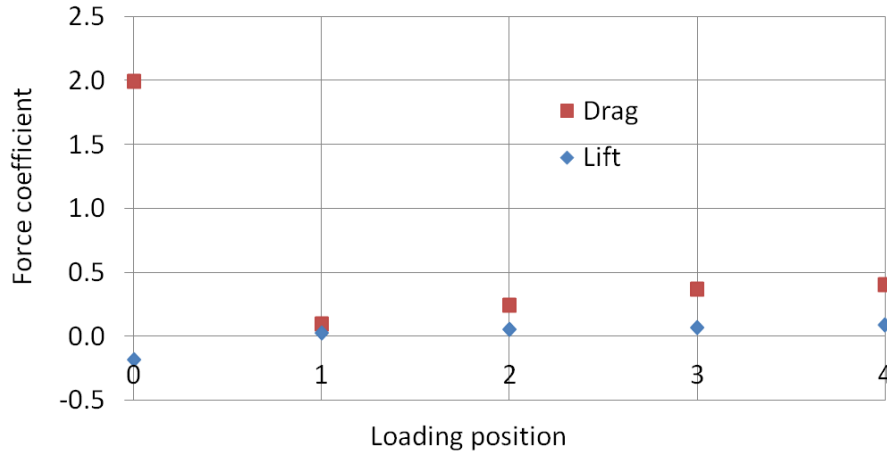


Figure 80 Force coefficients experienced by the locomotive and each container against loading position

Figure 80 shows the drag and lift force coefficients experienced by each container plotted against loading position in. A 95 % decrease is observed in drag force between the locomotive and first container. The  $C_d$  of the containers increases with a logarithmic trend as was seen in Golovanevskiy et al.(2012), however, as mentioned above, this increase is more rapid in the present work for the first two containers. The lift force coefficient increases with loading position although the overall values are very low in comparison to the drag force.

The instantaneous total force coefficients experienced by the locomotive and containers are shown in Figure 81. The force and moment coefficients are plotted against convective time,  $t^*$ , which is defined as

$$t^* = \frac{tu_r}{H} \quad (4.11)$$

where

$t$ , - physical time in the simulation.

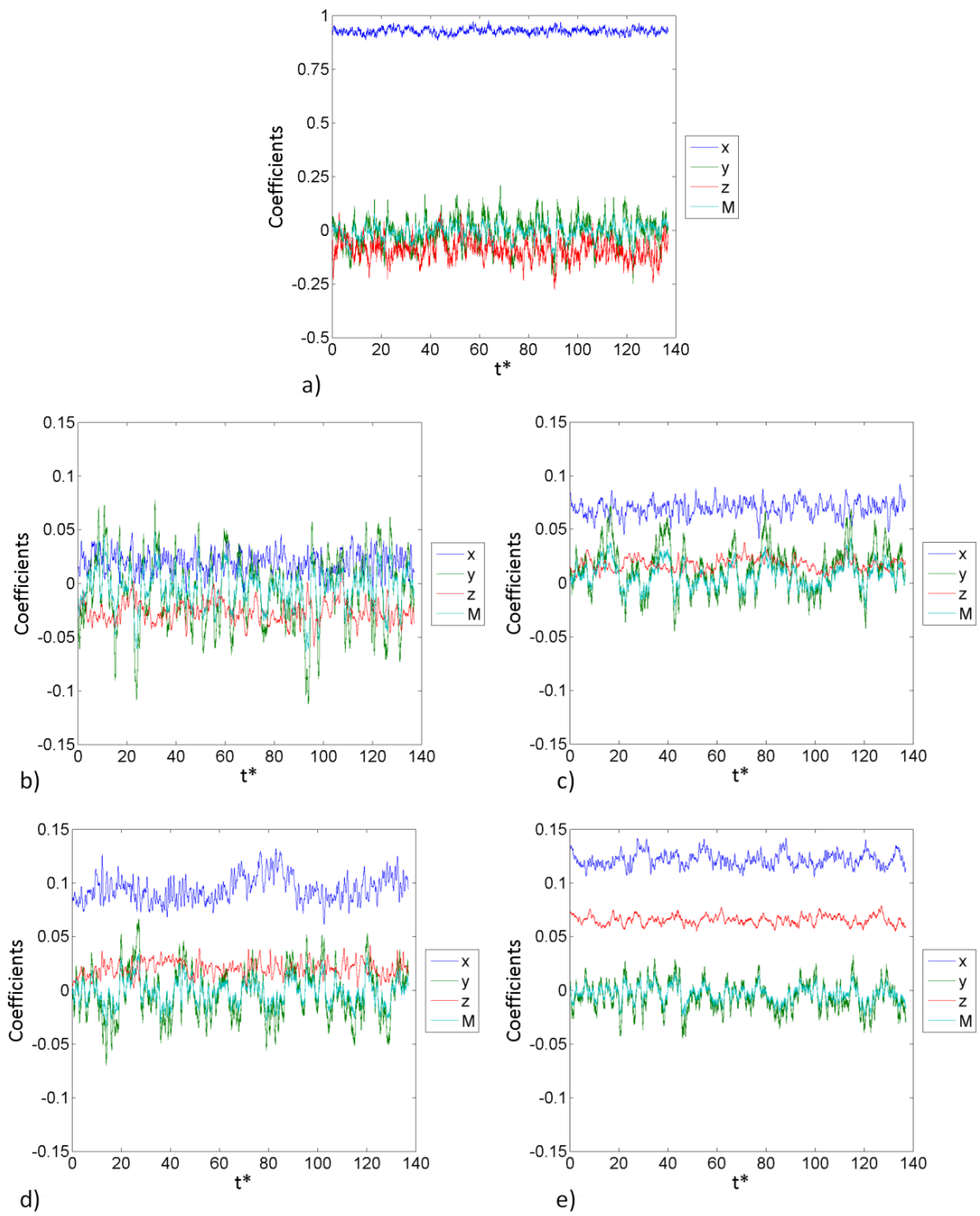


Figure 81 Force coefficients on a) Class 66 locomotive, b) container 1, c) container 2, d) container 3 and e) container 4

The drag force coefficient on the locomotive shown in Figure 81a appears to vary little about the mean value and on closer examination the root mean squared (RMS) of the drag force coefficient is 0.011. The side and lift force coefficients are visibly more variable than the drag force coefficient and have RMS values of 0.051 and 0.040, respectively.

The instantaneous drag force coefficient on the first container shows a similar degree of variation with time in comparison to the side force coefficient (Figure 81b). The RMS values of the drag, side and lift-force coefficients are 0.008, 0.025 and 0.008, respectively. The variation in the side force coefficient is large and is hypothesised to be due to vortex shedding from the locomotive affecting the flow field around the container.

The drag force coefficient on the second container again shows little variation with time as does the lift force coefficient (Figure 81c). However, the side force coefficient shows massive fluctuations about the mean in comparison. The RMS values of the drag, side and lift-force coefficients are 0.006, 0.016 and 0.005, respectively.

For the first time the drag force coefficient on the third container shows large variability about the mean value due to the adjacent inter-wagon spacing and the wake flow from the previous wagon (Figure 81d). The side force coefficient remains similarly variable as for the previous two containers although the lift force exhibits no discernible difference. The RMS values of the drag, side and lift-force coefficients are 0.01, 0.018 and 0.005, respectively.

The drag force coefficient on the fourth container is dominated by the unsteady wake behind it (Figure 81e). The lift force shows little variation, as does the side force coefficient. The RMS values of the drag, side and lift-force coefficients are 0.005, 0.01 and 0.003, respectively.

### *Container force summary*

The forces experienced by the containers and entire wagons are observed to vary with loading position as a result of slipstream development but also due to the presence of adjacent vehicles. The mean lift coefficient for the first container was negative although a trend of increasing lift force coefficient was observed with loading position which reached a maximum value at the fourth container. The mean lift coefficient of the Class 66 locomotive is negative as a result of the low-pressure region beneath the train.

The locomotive experiences the highest drag coefficient due to the flow stagnating on its front face. The first container wagon experiences a large amount of 'shielding' from the free stream flow which is responsible for the negative pressure drag it experiences. The total drag on the first container becomes positive only as a result of the frictional contribution.

The variability of the force coefficients on the locomotive and each container was approximated using RMS values. The drag force coefficient exhibited a consistently low RMS value for the majority of loadings position as a result of the presence of the preceding and subsequent wagons. The exception occurred at the third container where the drag force varied more than for other containers as a result of the larger preceding inter-wagon spacing.

The relatively high RMS side force coefficients are hypothesised to be due to the fact that the side forces are integrated over twice the amount of surface area as the lift force which may be a potential cause of this observation.

## *4.5 Technical standards for interoperability*

The Technical Specification for Interoperability (TSI, 2008) are accreditations which are required for rolling stock to operate in the European Union. The purpose of TSI is to ensure

trains which operate across borders have been determined safe to operate on each country's rail networks by undergoing a single certification method.

The requirements for the aerodynamics in open air (TSI, 2008) are that the characteristic velocity,  $U_{2\sigma}$ , within the slipstream of a train is must not exceed the 20 m/s, and the calculation is given in equation 1.15.

In the present case, 20 independent instantaneous velocity samples are made to replicate the passing of a train as shown in Figure 82. The velocities have been converted from model-scale to full-scale values, assuming that the train is running at the maximum operational speed of 120 km/h (33 m/s). The effect of applying a one second moving average to the instantaneous velocities is shown in Figure 83. The presence of the nose peak which was formally up to  $U_h=31$  m/s has been entirely filtered out by the one second moving-average. Means and standard deviations are taken of the peak velocities is calculated that

$$U_{2\sigma} = 9.98 \text{ m/s} \quad (4.12)$$

The value of  $U_{2\sigma}$  is half of the maximum allowable by TSI which is 20 m/s for trains travelling between 160 km/h and 200 km/h. The  $U_{2\sigma}$  attained from the numerical simulations is 26 % lower than was obtained by Soper (2014) , suggesting that the additional dynamic effects of the moving-model cause greater slipstream velocities. It is also possible, but not quantifiable, that the choice of discretisation scheme for the convection term caused sufficient damping to truncate potentially higher instantaneous velocity peaks, however his effect is considered unlikely because the level of damping was so minimal.

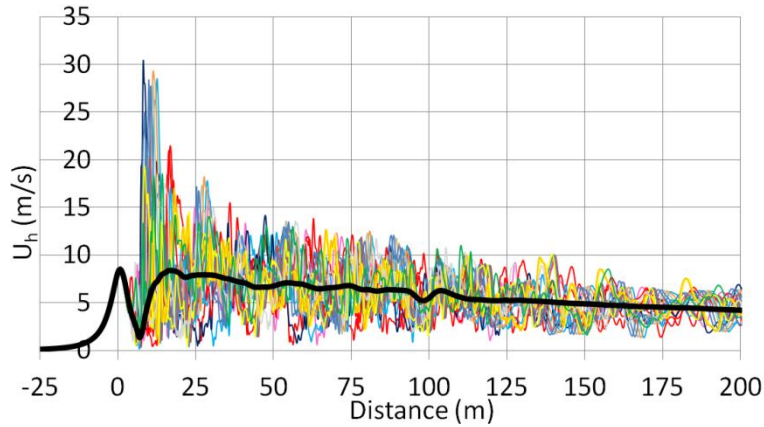


Figure 82 Horizontal velocity magnitudes at the TSI velocity measurement position ( $y=3$  m,  $z=0.2$  m) with time-averaged velocity (thick black line)

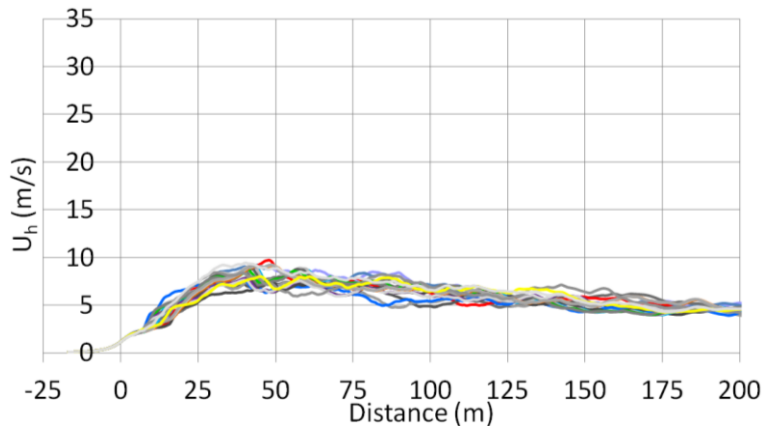


Figure 83 Horizontal velocities with one second moving averages applied at TSI measurement position ( $y=3$  m,  $z=0.2$  m)

#### 4.6 Summary

In the present chapter the behaviour of the slipstream and wake of a model-scale Class 66 locomotive with four fully-loaded container wagons in tow was analysed using DDES. The results of the numerical simulations were validated against physical experiments and the impact of the mesh resolution on the results was also verified.

The slipstream velocity, pressure and turbulence intensity were measured at train side and above the roof. From the time-averaged data, the following conclusions were drawn:

- Within 2 m of the train side, the highest slipstream velocities occur at  $x \approx 0$  m, as a result of flow separation around the locomotive
- In the boundary layer region, the highest slipstream velocities are observed at lower heights above TOR as a result of the underbody complexities such as bogies
- The inter-wagon spacings are visible in the pressure, velocity and turbulence intensity signals
- The force experienced by a container is a function of loading position
- The locomotive experiences the greatest drag, side and lift force coefficients
- The displacement thickness in the boundary layer region varies by less than 10% along train length
- Slipstream velocities may be under-predicted by using static models such as those used in CFD due to a lack of buffeting or a dynamic ‘pumping’ effect between wagons.

From analysis of the instantaneous data, the following conclusions were drawn:

- The greatest peak ensemble-averaged velocity is 10% greater than the time-averaged velocities
- The  $U_{2\sigma}$  value produced in the simulations was 26 % lower than the value calculated from moving-model experiments
- The greatest integral time-scale is 16% of the 0.375 s which is considered necessary in the literature to be a risk to person stability and is thus not likely to be dangerous
- Turbulence intensity decays along the train length for all measurement positions

# Chapter 5 Freight train subjected to a 30° crosswind

## 5.1 Introduction

The present chapter presents results obtained from DDESs of the slipstream of the model-scale freight train when subjected to a steady 30° crosswind. The 30° yaw angle was chosen because it allowed for validation of the numerical model against physical experiments which were originally intended for crosswind stability analysis of a container wagon in a freight train (Soper, 2014).

In Section 5.2 the accuracy of the simulations is verified, in Section 5.3 the time-averaged flow on the windward and leeward sides of the train is presented, and in Section 5.4 some instantaneous flow features are discussed.

## 5.2 Solution verification and validation

### 5.2.1 Mesh Sensitivity

A mesh sensitivity test was performed in order to determine whether the solution of the simulations was a function of mesh density. The comparison between the time-averaged surface pressure around the middle of each container, for the coarse and fine meshes is shown in Figure 84. The surface pressure on the windward faces of each container show very good agreement with differing only slightly between fine and coarse meshes. The pressures on the roof show slightly worse agreement although the greatest discrepancy is 17% on container 2. Generally good agreement is observed between the  $C_p$  from the coarse and fine meshes indicating that the energy-containing motions that will affect the solution have been resolved therefore a finer mesh is not required.

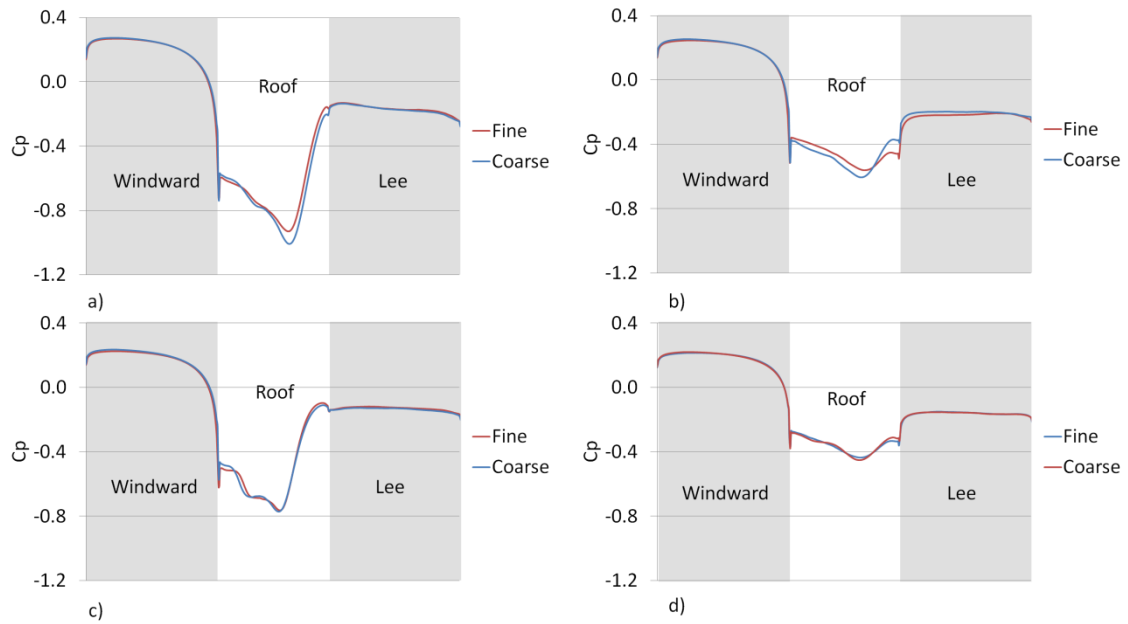


Figure 84 Pressure coefficients on each a) container 1, b) container 2, c) container 3 and d) container 4 at mid-length for fine and coarse meshes

### 5.2.2 Verification of sub-grid viscosity levels

In LES, sub-grid viscosity,  $\nu_{sgs}$ , is used to account for the absence of turbulent stresses that are smaller than the filter width. In highly turbulent flow regions, where  $S_{ij}$  are large, and especially where the mesh is coarse,  $\nu_{sgs}$  can build up to levels that is many orders of magnitude greater than the kinematic viscosity,  $\nu$ . High levels of effective viscosity ( $\nu + \nu_{sgs}$ ) can drastically affect the local flow physics and thus are not desirable for an accurate and representative solution. In order to reduce the effective viscosity, where  $S_{ij}$  are large, it is necessary to reduce the filter width so that fewer scales are ‘sub-grid’ which can be accomplished by refining the computational mesh.

Instantaneous values of  $\nu_{sgs}$  for the fine and coarse meshes on the leeward side of the train, at mid-height, are shown in Figure 85.  $\nu_{sgs}$  was not time-averaged during the simulation so only instantaneous values are available but it is assumed that this will be sufficient for discussion. Due to the uniform steady inlet there is no  $S_{ij}$  thus  $\nu_{sgs}$  ahead of the train is zero. The

maximum value of  $v_{sgs}$  occurs for the coarse mesh ( $v_{sgs}/v=52$ ) although the maximum  $v_{sgs}$  for the fine case is only 3% lower. Previous work which has discussed  $v_{sgs}/v$  levels in the field of train aerodynamics (Östh and Krajnović, 2014) showed  $v_{sgs}/v$  in the form of a colour plot with a maximum colour band of 10. It is quite possible that the  $v_{sgs}/v$  levels greatly exceeded this although using a qualitative method such as a colour plot can mask the true levels, whereas explicitly stating the levels as has been done here provides full disclosure

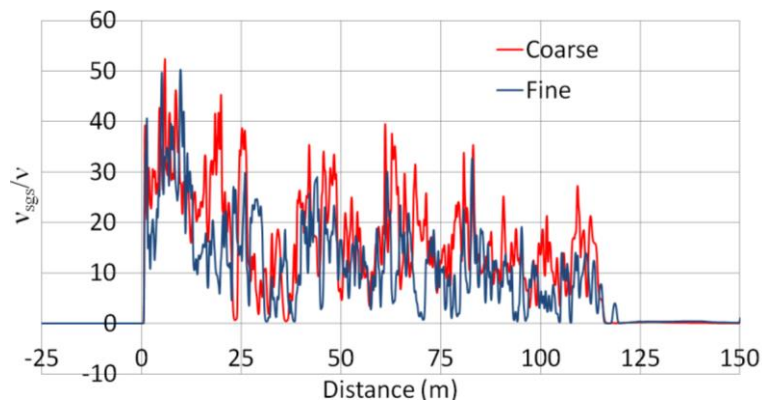


Figure 85 Sub-grid viscosity ratio,  $v_{sgs}/v$ , along train length at half-height at  $y=2.35$  m  $z=2$  m

### 5.2.3 Validation

To ensure physical realism, the 30° crosswind simulation was validated against experimental data from Soper (2014), using mean pressure coefficients on the surface of the third container. In the numerical simulations the crosswind is assumed to be a uniform steady velocity whereas in the experimental case, the train is subjected to a turbulent wind ( $I \approx 18\%$ ) produced by the CWG (Dorigatti, 2013). Turbulence intensity and length scale are known to have some effect on the surface  $C_p$ , and thus forces, experienced by vehicles (Robinson and Baker, 1990) and bluff bodies (Lee, 1975, Bearman and Morel, 1983) thus some degree of difference should be expected between the CFD and experimental data as a result of the turbulence.

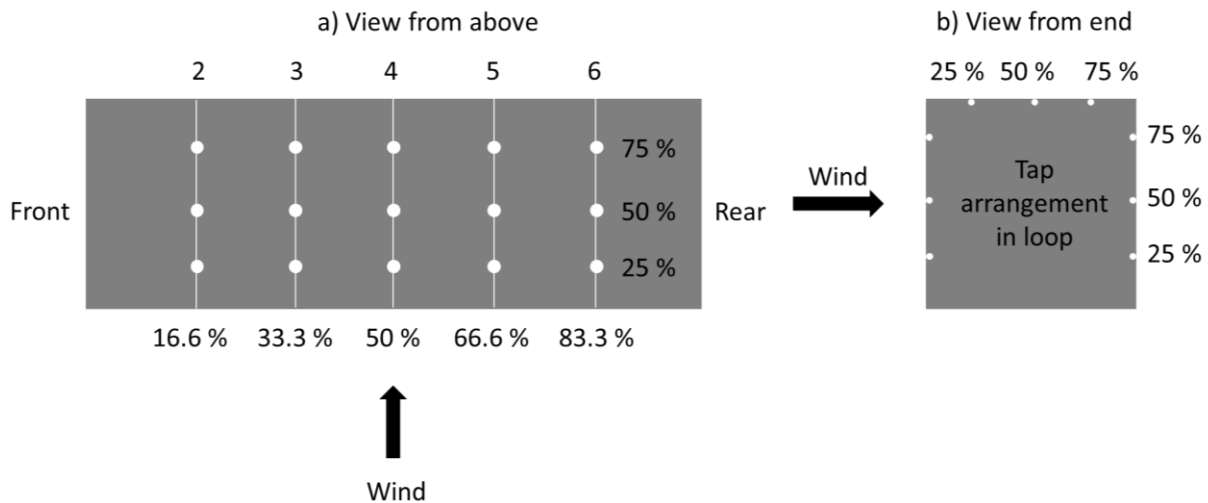


Figure 86 Tap and loop positions a) on the roof of container 3 and b) around the outside

Figure 86 shows the locations of the pressure taps on the surface moving model's third container. The taps are positioned at 25 %, 50 % and 75 % across the width of the container roof, and height of the container sides with loops occurring at 16.6 %, 33.3 %, 50 %, 66.6 % and 83.3 % along the length of the container.

Figure 87 shows the pressure coefficient data from the CFD and physical experiments on the windward, roof and lee sides of the third container. Representative error bars are provided on the figure with values of  $C_p = \pm 0.05$  which are assumed due to the absence of more meaningful values. For the first tap on the container roof at loop 2 the experimental data has a negative pressure with a 12% greater magnitude than the CFD. The next tap along the roof the experimental and CFD values are  $C_p = -0.19$  and  $C_p = -0.69$ , respectively. The massive difference between pressure magnitudes is due to the location of the roll vortex on the roof which will be discussed in Section 5.3.8.

On the roof of the container, at loop 6, the experiment produces pressures that are 23 %, 11% and 5% greater than the CFD for taps 1, 2 and 3, respectively. On the windward side of the

container, the CFD produces pressures which are 50%, 31% and 63% greater than the experiment at taps 1, 2 and 3, respectively.

The comparison between the results improves towards the rear of the container and thus it is hypothesised that free stream turbulence has the greatest effect on the flow separation at the windward corners and the effect decreases towards the rear of the container.

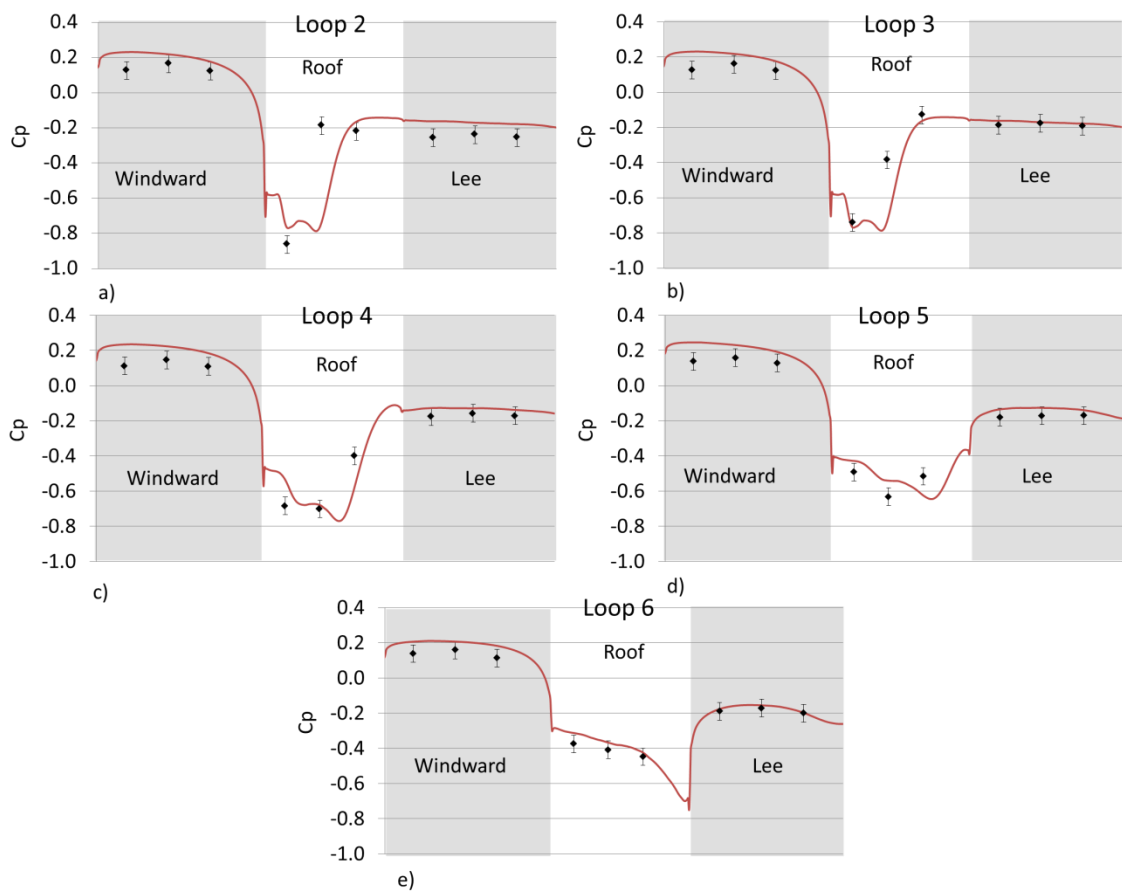


Figure 87 Pressure coefficients on the third container from numerical and experimental cases (Soper, 2014)

### 5.3 Time-averaged flow

#### 5.3.1 Boundary layer development in the computational domain

Moving-models subjected to crosswinds experience different velocity profiles and turbulence spectra compared to static wind tunnel models (Cooper, 1984). The ‘skewed’ velocity profile

that a moving-model experiences can be replicated in numerical simulations by setting the ground plane as a moving-wall boundary condition with the velocity of the vehicle's speed. If the ground-plane has the velocity component of the vehicle's speed, then it will behave as a no-slip wall for the lateral component of the wind, thus causing boundary layer development as was shown in Figure 16.

Figure 88 shows the components of velocity and resultant yaw angle with height relative to the train at  $x = -6.25$  m and  $y = -6.25$  m. This location was used to sample the velocity profile because it is far enough from the train not to be affected by the flow field around it but it is also close enough to show the level of boundary layer development that the train experiences. It is observed in Figure 88 that the lateral velocity reaches its maximum value at 1.5 m ( $\approx 1/3^{\text{rd}}$  of train height), whereas in the CWG the maximum lateral velocity was reached at twice train height. To properly generate the crosswind velocity profile in the numerical simulations, a larger fetch, a rough wall or an ABL inlet boundary condition is required. Due to the rate at which the lateral velocity increases towards its maximum value, the upstream velocity profile is not anticipated to greatly affect the results of the simulations.

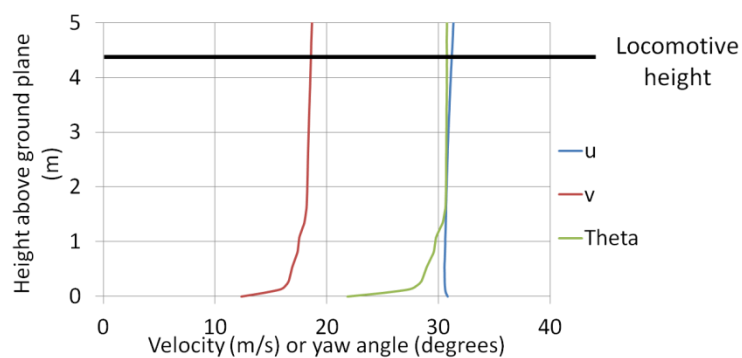


Figure 88 Crosswind component and resultant yaw angle with height above TOR

### 5.3.2 Velocity magnitude on the windward side of the train

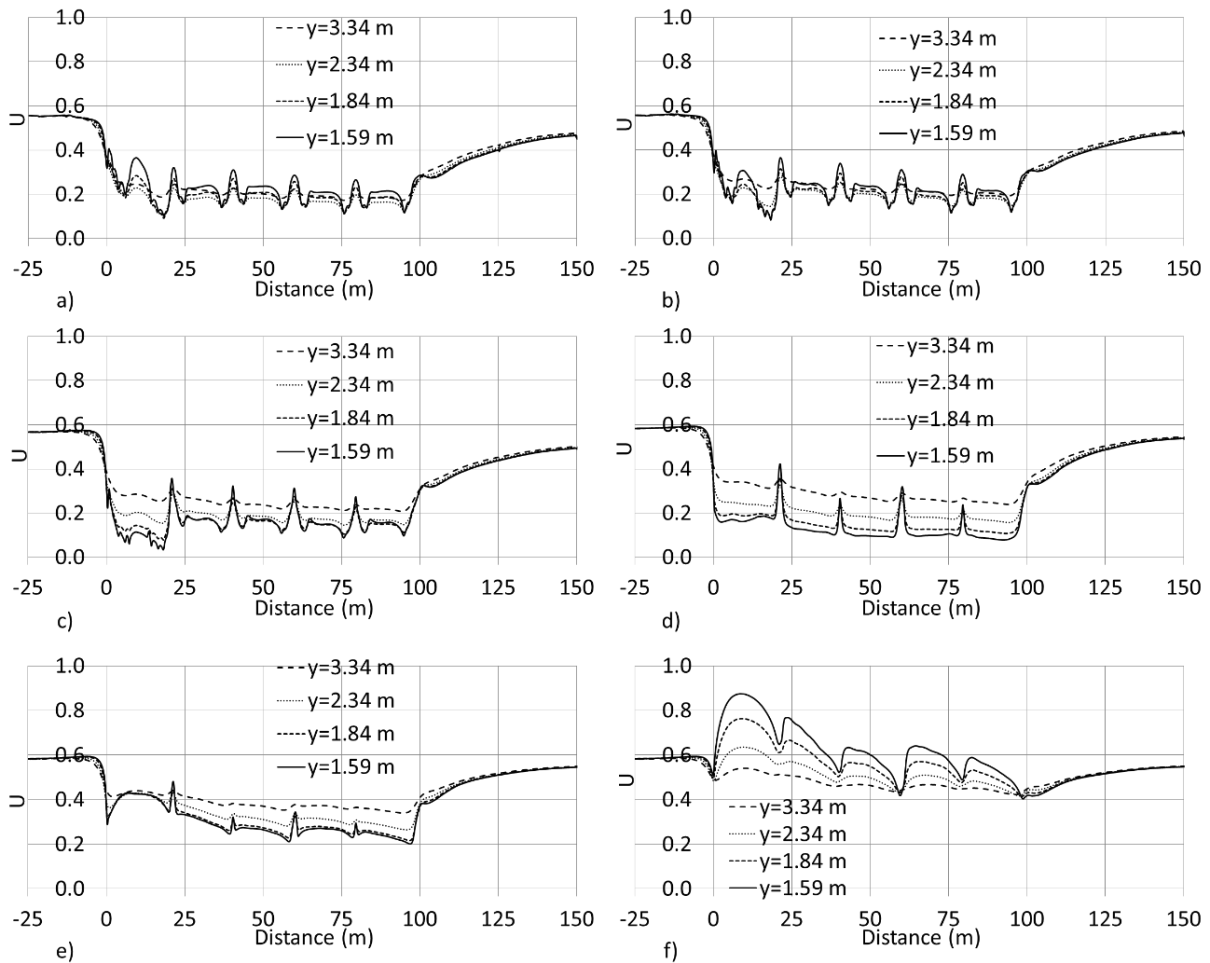


Figure 89 Slipstream velocity magnitudes relative to a static observer at a)  $z=0.25$  m, b)  $z=0.5$  m, c)  $z=1.0$  m, d)  $z=2.0$  m, e)  $z=3.0$  m and f)  $z=4.0$  m

Figure 89 shows the velocity magnitude,  $U$ , relative to a static observer, on the windward side of the train. The general trend is that  $U$  rapidly decreases at  $x \approx -3$  m and this is followed by lower-velocities in the boundary layer region punctuated by velocity pulses close to inter-wagon spacings. The lower-than-crosswind velocity is a result of the sampling locations being in the stagnation region. The greatest velocity magnitude in the slipstream occurs at  $x=10$  m,  $y=1.59$  m and  $z=4$  m where a higher-than-crosswind velocity is observed for the first time as a result of the flow separation around the roof of the locomotive. For all cases, the velocity in the wake takes over 50 m to return to the original crosswind value.

The variation of slipstream velocity magnitude with height is considered at each lateral sampling position (Figure 90). At  $z=0.25$  m and  $z=0.5$  m, a close degree of similarity is observed between velocity magnitudes at different distances from COT along train length. A significant difference is observed at  $z=2$  m where the velocity at  $y=3.34$  m is nearly twice that of  $y=1.59$  m due to the reduced effect of the stagnation region.

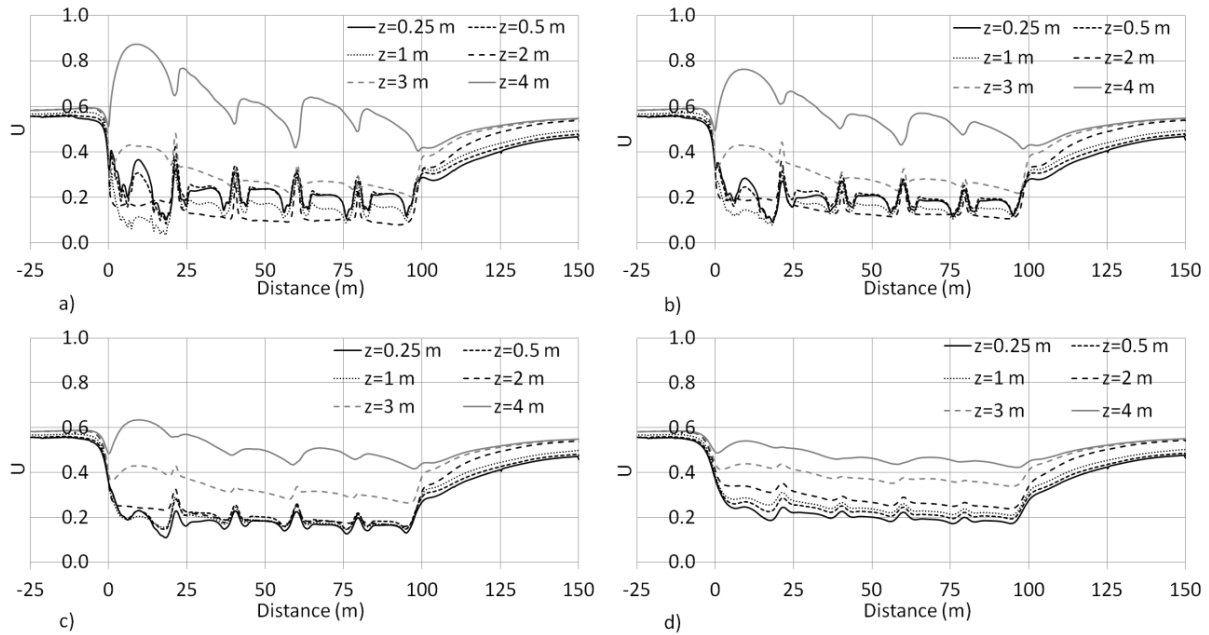


Figure 90 Slipstream velocity magnitudes relative to a static observer varying with height at a)  $y=1.59$  m, b)  $y=1.84$  m, c)  $y=2.34$  m and d)  $y=3.34$  m

For  $y=1.59$  m and  $y=1.84$  m significant difference is observed for velocity magnitude between  $z=2$  m and  $z=3$  m because of the local separation. At  $y=3.34$  m, the velocities magnitudes increase at a given position along train length increase monotonically with height above TOR. Ahead of the train ( $x < 0$  m) the effect of the boundary layer can be seen in the velocity magnitudes where  $z=4$  m has the highest velocity.

### 5.3.3 Velocity magnitude on the leeward side of the train

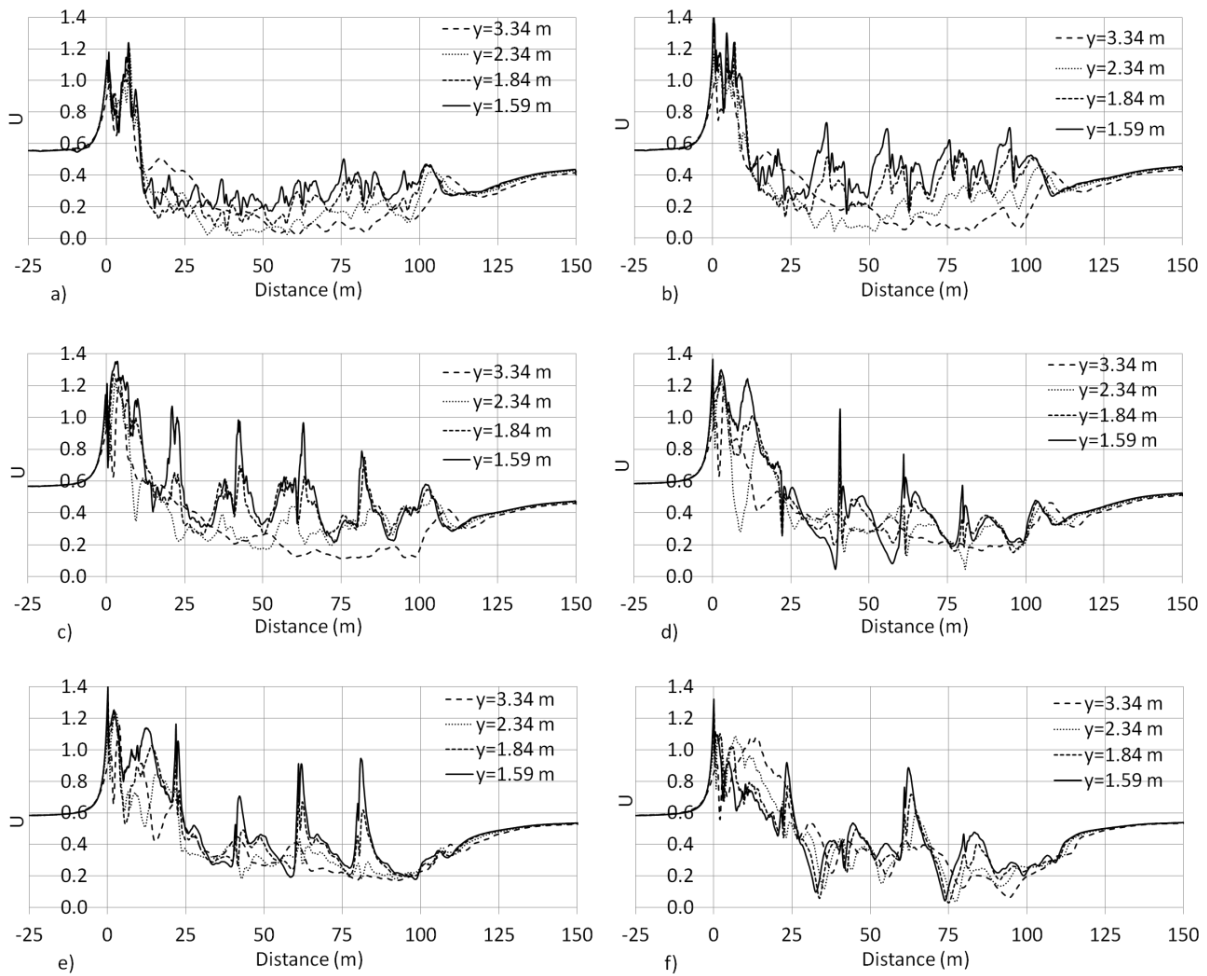


Figure 91 Slipstream velocity magnitudes relative to a static observer at a)  $z=0.25$  m, b)  $z=0.5$  m, c)  $z=1.0$  m, d)  $z=2.0$  m, e)  $z=3.0$  m and f)  $z=4.0$  m

The slipstream velocity magnitudes on the leeward side of the train are shown in Figure 91. The key feature in the slipstream on the leeward side of the train is the large velocity peaks in the nose region which are often followed by a general decrease in velocity until the middle of the train. The greatest velocity peak at the front of the train is 2.4 times the value of the crosswind velocity. Transients occur at inter-wagon spacings with greater magnitudes than were observed on the windward side of the train due to flow shearing around the front leeward corners of the containers (Figure 89). The greatest velocity transients at the inter-

wagon spacings occurs at mid-height due to the lack of obstruction to the flow ( $z=2$  m) by wagon couplings and buffers.

In some regions in the lee of the train, the velocity magnitude can be as low as  $U=0.05$ . The very low mean velocities occur in recirculation regions where there is no dominant flow direction thus the average is close to 0: this is observed to occur mostly at  $y=2.34$  m for  $z=0.25$  m and  $z=0.5$  m.

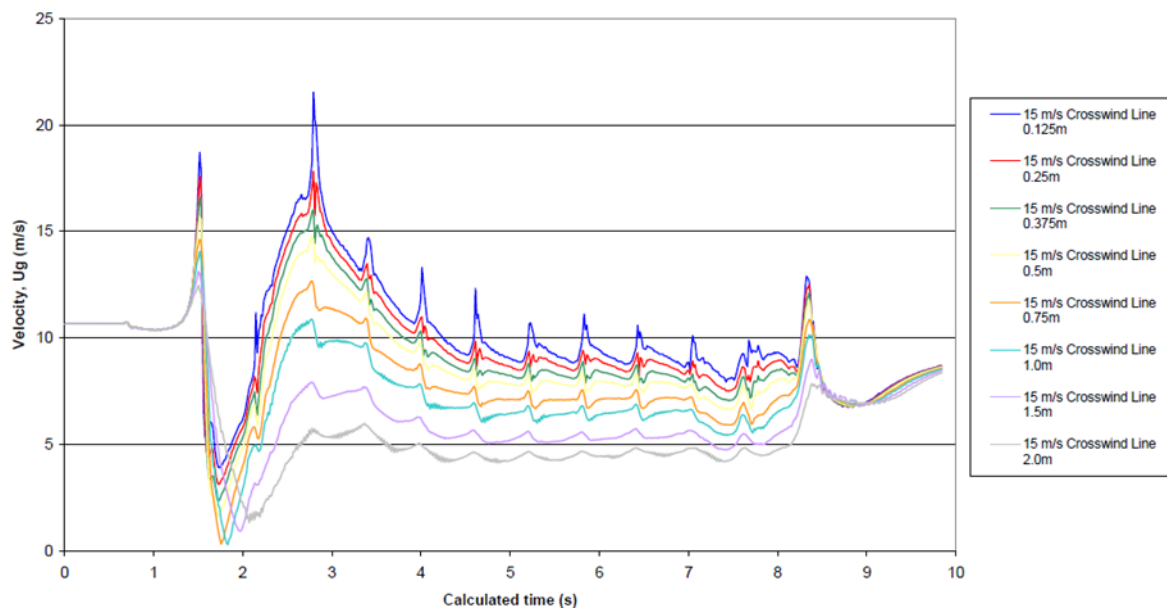


Figure 92 Velocity magnitude on the leeward side of the passenger train at mid-height (Bowman, 2005)

Figure 92 shows the velocity magnitude on the leeward side of the generic passenger train used in Bowman (2005). The velocities were obtained using steady RANS with the RNG  $k-\epsilon$  model applied for turbulence close. The weaknesses of Bowman’s work have been discussed extensively in Chapter 2 and it was concluded that the data should be considered as indicative of trends only. The 15 m/s crosswind makes a resultant yaw angle with the train of  $24^\circ$  which is broadly comparable with the present results. The distances are given relative to the side of the train so  $y=1.59$  m,  $y=1.84$  m,  $y=2.34$  m and  $y=3.34$  m in the present work correspond to

$y'=0.25$  m,  $y'=0.5$  m,  $y'=1$  m and  $y'=2$  m, respectively. At the closest position to train side the primary velocity peak shows a 63% amplification of the crosswind velocity, and the second peak shows a 100 % increase. At the furthest position from train side, the velocity exhibits a 25% increase whereas in the present work at the same position the peak value is 85% greater than the crosswind speed. It is also observed that the primary and secondary velocity peaks in the present work are closer together than for the passenger trains as a result of forced separation.

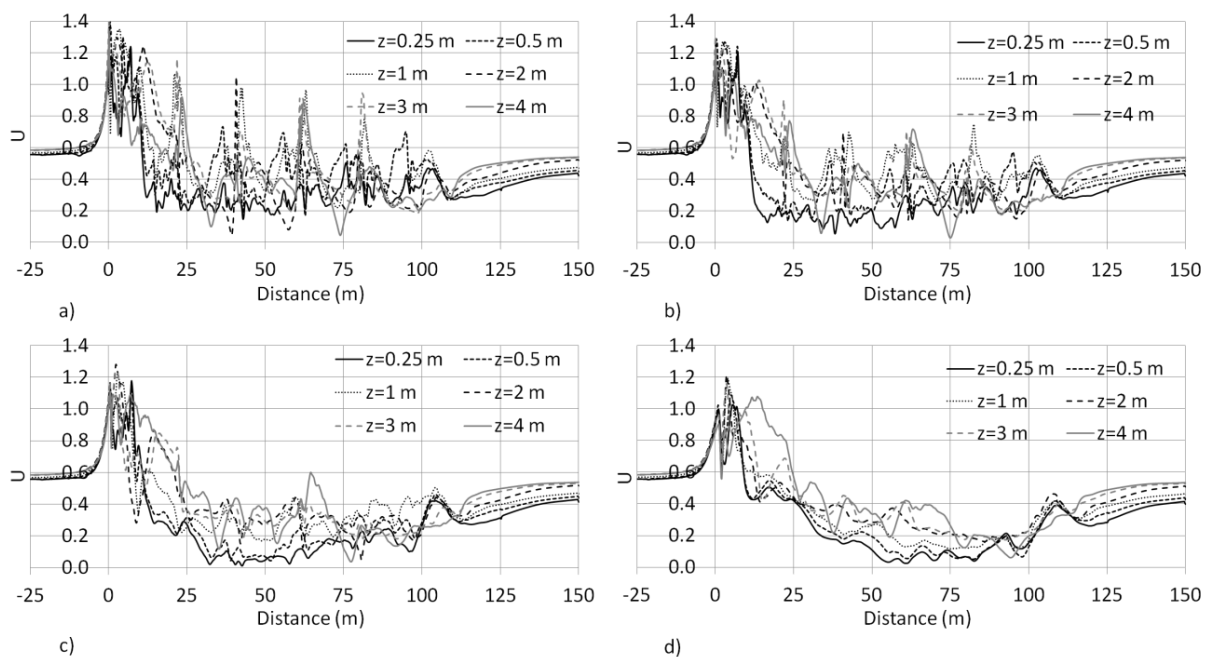


Figure 93 Slipstream velocity magnitudes relative to a static observer varying with height at a)  $y'=1.59$  m, b)  $y'=1.84$  m, c)  $y'=2.34$  m and d)  $y'=3.34$  m

Figure 93 shows the data from Figure 91 which are plotted in terms distance from COT in order to highlight the effect of height above TOR on U. The data show the massive variation in mean velocity magnitude at  $y'=1.59$  m whereas the variation is shown to decrease with distance from train side. It can be seen that the lowest velocities are often observed at the closest measurement positions to the ground although as previously mentioned this could be a result of recirculation.

### 5.3.4 Velocity components on the windward side of the train

Figure 94 to Figure 99 show the slipstream velocity components at each sampling location on the windward side of the train.

**$z = 0.25$  m**

Figure 94 shows the velocity components on the windward side of the train at  $z=0.25$  m. The vertical velocity has its greatest value of  $w=-0.14$  at  $x=10$  m and  $y=1.59$  m and is negative which signifies that it is towards the ground. The lateral velocity is shown to decrease in the nose region and remains almost constant at  $v=0.2$  along train length, with the exception of the transients at inter-wagon spacings. At all positions from COT the lateral velocity rapidly decreases in the nose region and the longitudinal velocity reaches a greatest peak value of  $v=0.27$  at  $y=1.59$  m. The peak longitudinal transient in the near wake is  $u=-0.18$  at  $y=1.59$  m. At  $y=3.34$  m, the longitudinal and vertical velocities are both negligible in the boundary layer region.

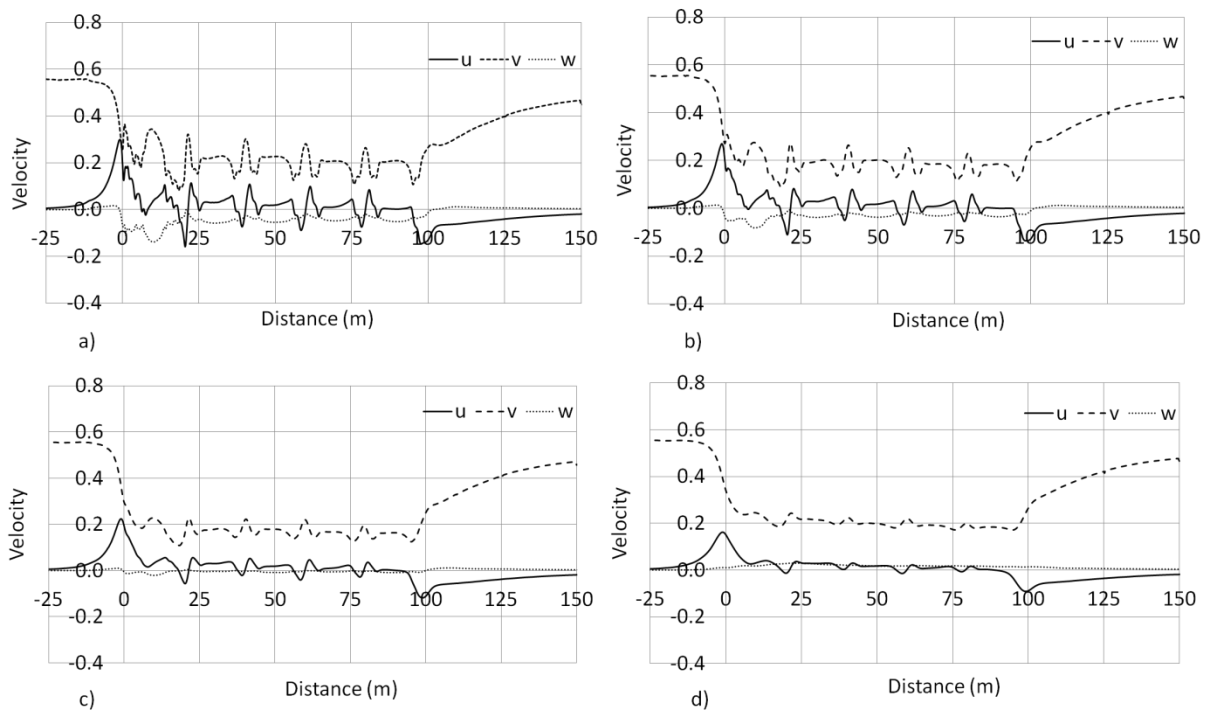


Figure 94 Slipstream velocity components at a)  $y=1.59$  m, b)  $y=1.84$  m, c)  $y=2.34$  m and d)  $y=3.34$  m

**z= 0.5 m**

Figure 95 shows the velocity components on the windward side of the train at  $z=0.5$  m. Similarly to  $z=0.25$  m, the longitudinal velocity shows a large degree of ‘sharpness’ in the signal due to the complex flow around the bogies. The recirculation at  $x=21$  m is preceded by a longitudinal peak at  $x=14$  m which was caused by the flow shearing around the rear bogie set. The vertical component at  $x=10$  m is  $w=-0.2$ , and is 43% greater than at  $z=0.25$  m. The vertical velocity in the boundary layer region is comparable to the longitudinal peak values at  $y=3.34$ m. The lateral and longitudinal transients at  $x=40, 60$  and  $80$  m are all of similar magnitude which suggests that the flow is fully-developed on the windward side of the train at  $z=0.5$  m.

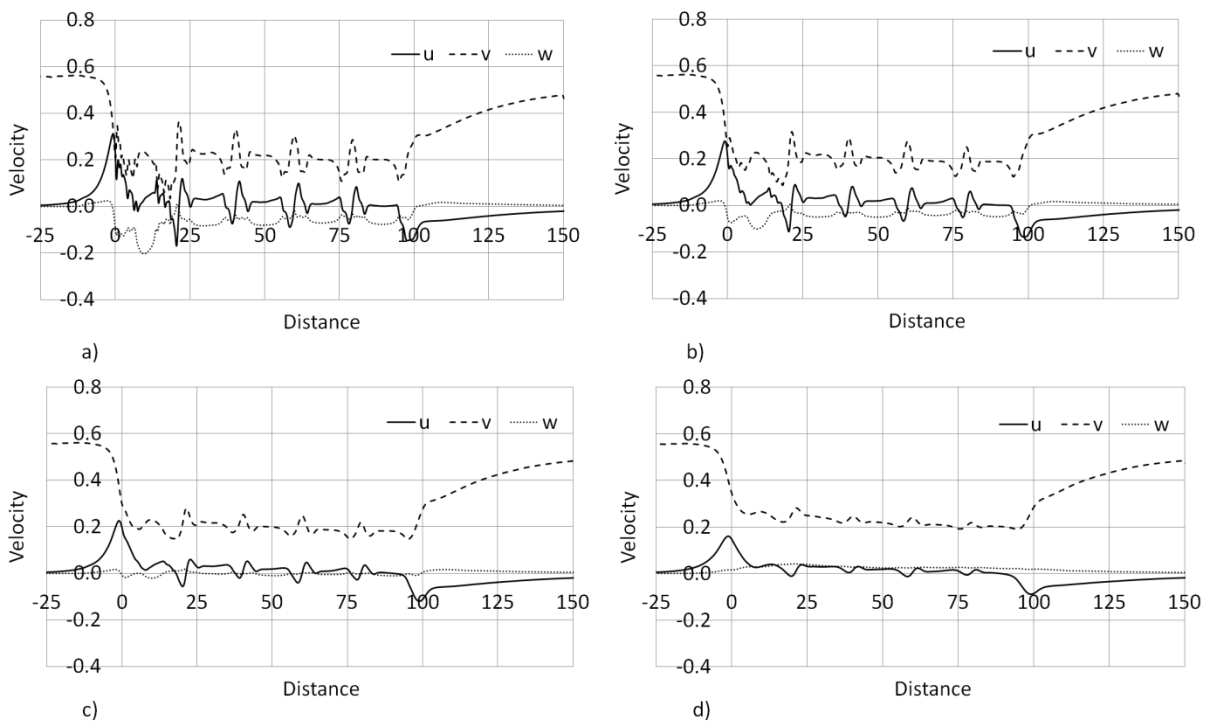


Figure 95 Slipstream velocity components at a)  $y=1.59$  m, b)  $y=1.84$  m, c)  $y=2.34$  m and d)  $y=3.34$  m

**z= 1 m**

Figure 96 shows the velocity components on the windward side of the train at  $z=1$  m. The lateral and longitudinal transients in the boundary layer region are greater at  $z=1$  m than were observed for  $z=0.25$  m and  $z=0.5$  m. Furthermore, the magnitudes of the transients are shown to undergo a gradual decay along train length which did not occur at lower heights above TOR. The vertical component reaches a negative peak at  $w=-0.15$  for  $x=1$  m and  $y=1.59$  m as opposed to  $x=10$  m for  $z=0.5$  m. The peak velocity in the boundary layer region is the longitudinal component which is  $u=0.35$  at  $x=21$  m and the longitudinal component also has a peak boundary layer region value at  $x=21$  m but is negative at  $u=-0.19$ . The longitudinal position of  $x=21$  m is the location of the spacing between the locomotive and the first container wagon.

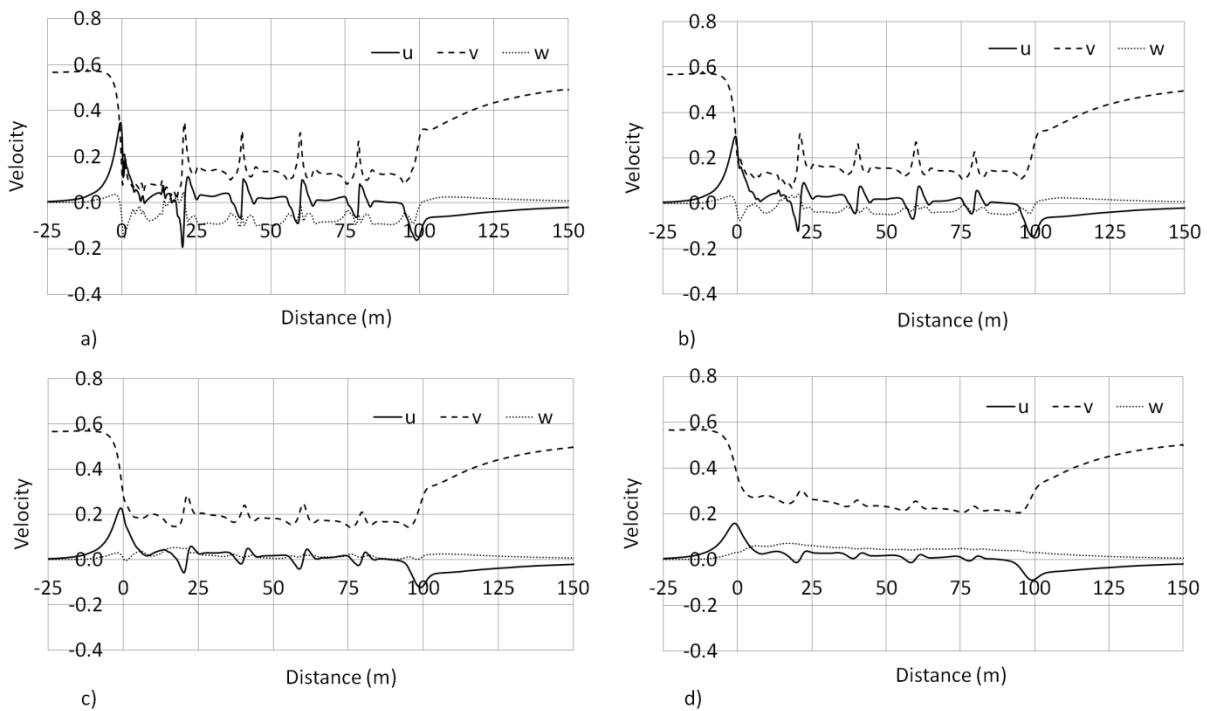


Figure 96 Slipstream velocity components at a)  $y=1.59$  m, b)  $y=1.84$  m, c)  $y=2.34$  m and d)  $y=3.34$  m

## $z = 2 \text{ m}$

Figure 97 shows the velocity components on the windward side of the train at  $z=2 \text{ m}$ . A significant shift in flow regime is observed at  $z=2 \text{ m}$  in comparison to  $z \leq 1 \text{ m}$ . As was seen at  $z=1 \text{ m}$ , the greatest lateral and longitudinal velocity components in the boundary layer region occur at  $x=21 \text{ m}$ . The near-linear decrease in lateral velocity on the windward side of the train suggests that the windward boundary layer development is likely to continue changing with longer train length which is contrary to what was observed at  $z=0.5 \text{ m}$ .

For the first height above TOR, the vertical velocity is not only positive but also greater than the longitudinal and lateral components along the locomotive for  $y=1.59 \text{ m}$  and  $y=1.84 \text{ m}$ . In the near wake region a rapid increase in lateral velocity is observed as a result of flow shearing around the rear windward corner of the last container wagon.

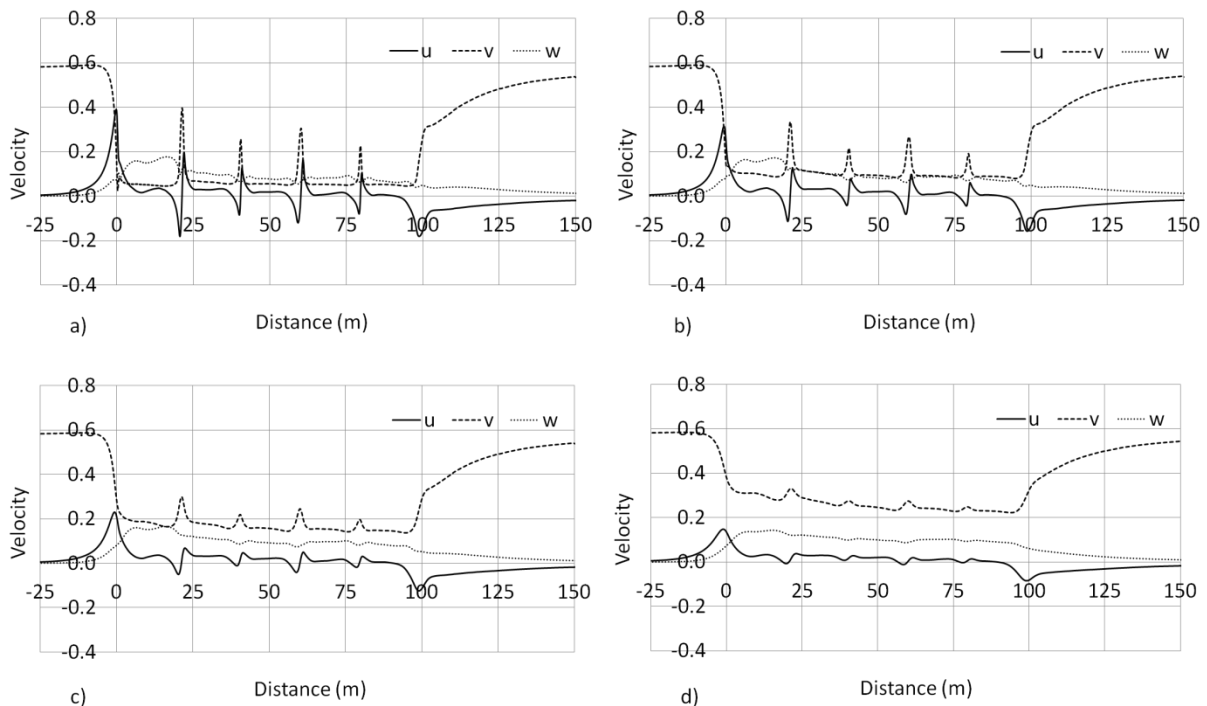


Figure 97 Slipstream velocity components at a)  $y=1.59 \text{ m}$ , b)  $y=1.84 \text{ m}$ , c)  $y=2.34 \text{ m}$  and d)  $y=3.34 \text{ m}$

### **z= 3 m**

Figure 98 shows the velocity components on the windward side of the train at  $z=3$  m. At  $y=1.59$  m, the vertical velocity is greater than the longitudinal and lateral components for the majority of train length. Between  $y=1.59$  m and  $y=3.34$  m, the lateral velocity is shown to increase, be approximately equal to, and then become greater than the vertical velocity component. At  $y=2.34$  m the lateral and vertical components of velocity are approximately equal in the boundary layer region.

As was shown at  $z=2$  m, the lateral velocity shows a step increase in the near wake, to a value between  $v=0.35$  and  $v=0.4$ , where the gradual increase towards the crosswind component continues.

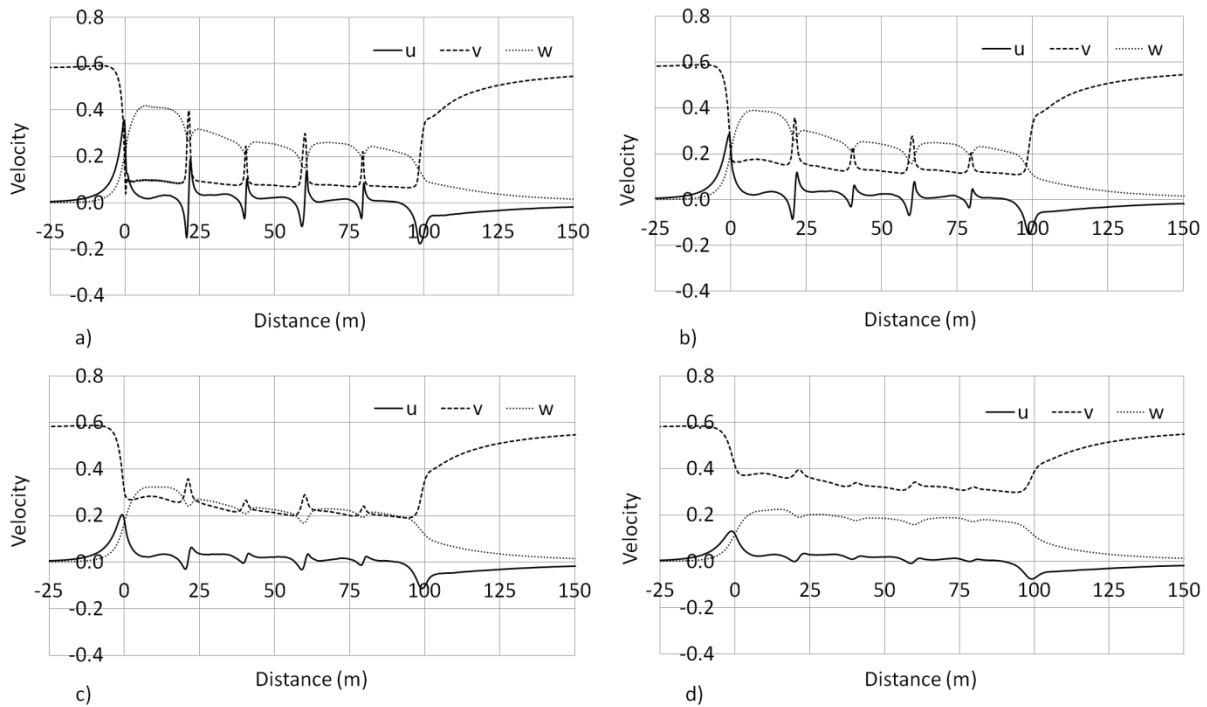


Figure 98 Slipstream velocity components at a)  $y=1.59$  m, b)  $y=1.84$  m, c)  $y=2.34$  m and d)  $y=3.34$  m

### **z= 4 m**

Figure 99 shows the velocity components on the windward side of the train at  $z=4$  m. The peak longitudinal velocity component occurs is  $u=0.21$  and occurs at  $x=0$  m and  $y=1.59$  m.

For the rest of train length the longitudinal velocity component can be considered negligible in comparison to the lateral and vertical components. At  $y=1.59$  m the peak vertical velocity occurs along the locomotive and is  $w=0.66$ . In the near wake a steep decay is observed in vertical velocity because the flow separation which drove the velocity is no longer present. The vertical velocity component at  $y=3.34$  m is constant along the length of the train.

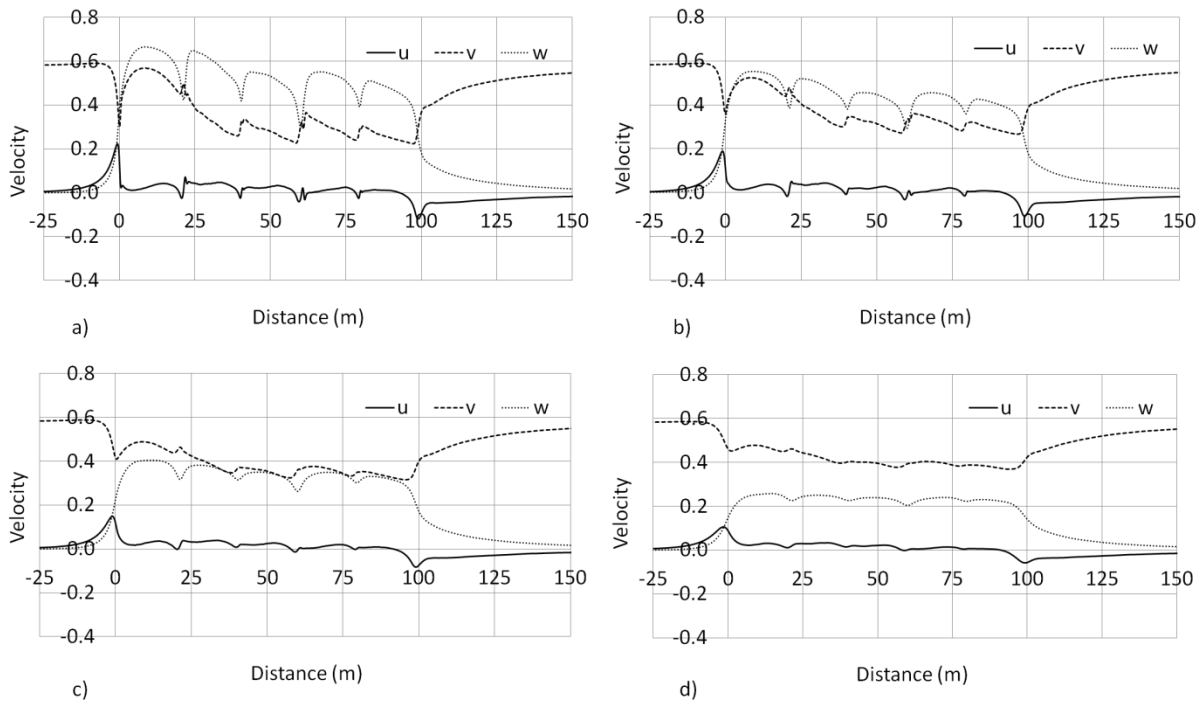


Figure 99 Slipstream velocity components at a)  $y=1.59$  m, b)  $y=1.84$  m, c)  $y=2.34$  m and d)  $y=3.34$  m

### Windward component summary

At lower heights above the ground ( $z < 2$  m) lateral velocity is the dominant component in the boundary layer region, followed by longitudinal and vertical, respectively. Whilst the lateral velocity decreases after  $x=0$  m, the longitudinal component increases as a result of acceleration around the windward corner of the locomotive. At greater heights above TOR ( $z \geq 2$  m) the vertical component becomes more significant and in some cases is the greatest, reaching a peak value of  $w=0.66$ . At  $z=4$  m in the boundary-layer region, the longitudinal velocity becomes almost negligible in comparison to the lateral and vertical components.

The near-linear decrease in lateral velocity suggests that the windward boundary layer is far from developed above  $z=0.5$  m. To investigate the effect of train length on crosswind slipstream development a longer train such as the eight wagon train used by Soper (2014) would be required.

### ***5.3.5 Velocity components on the leeward side of the train***

#### ***z=0.25***

Figure 100 shows the velocity components on the leeward side of the train at  $z=0.25$  m. The greatest peak velocity is the longitudinal component which is  $v=1.27$  and occurs at  $y=1.59$  m. The lateral velocity peaks in the nose region with maximum values of  $v=1.1$  at  $y=1.84$  m. In the boundary layer region at  $y=1.59$  m and  $y=1.84$  m the longitudinal and lateral components undulate with a general trend of increasing to peak values of approximately  $u=0.5$  and  $v=0.5$ , respectively at  $x=103$  m and  $x=95$  m, respectively.

The lateral velocity has values of  $v=-0.5$  along the length of the locomotive due to the recirculation in that region. The negative value of the component denotes that it is towards the train with a value that is within the range shown by Jordan (2008) to cause person instability.

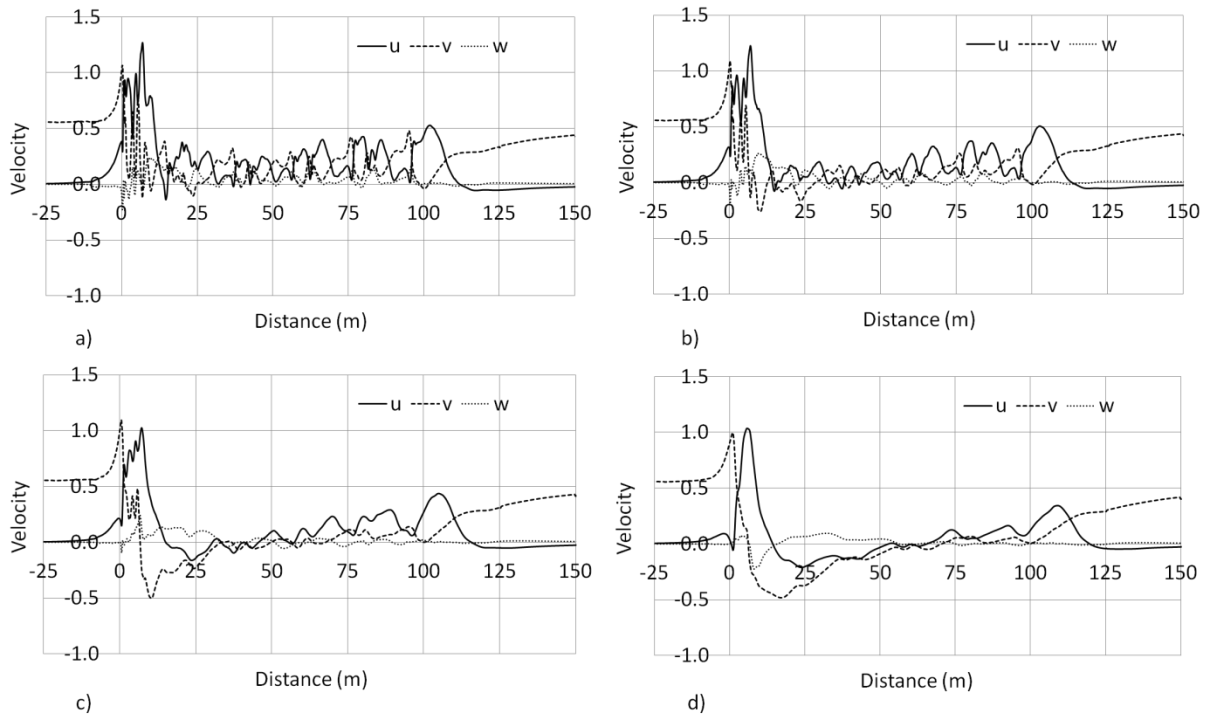
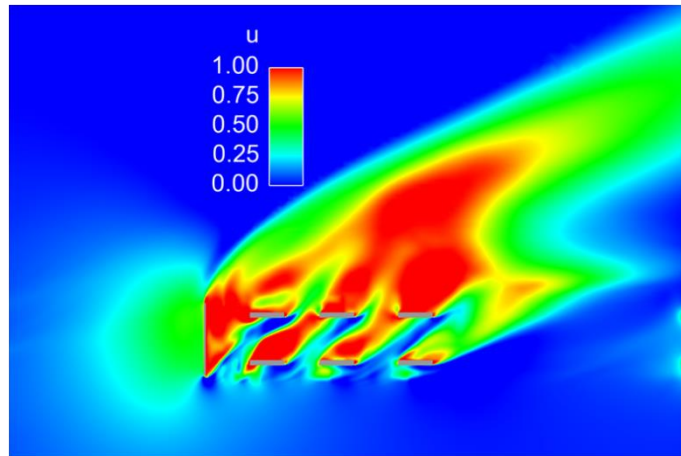
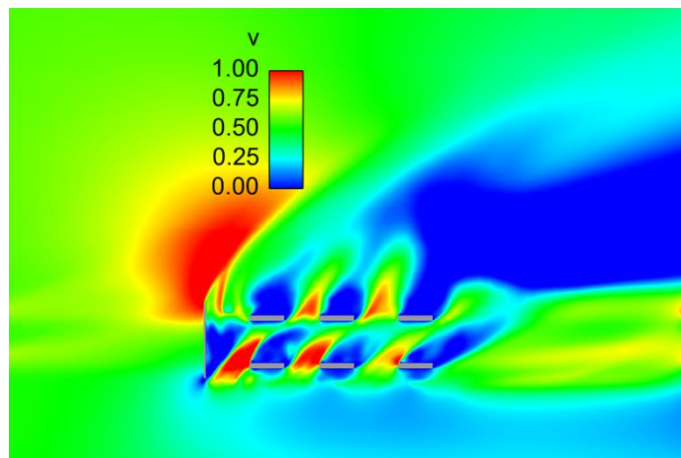


Figure 100 Slipstream velocity components at a)  $y=1.59$  m, b)  $y=1.84$  m, c)  $y=2.34$  m and d)  $y=3.34$  m

At all distances from COT the lateral velocity reaches a local maximum peak before the longitudinal velocity. Figure 101 shows the velocity components on a plane at  $z=0.25$  m, which shows the velocity field at that height around the locomotive. The figures are congruent with the data in Figure 100 in that the peak longitudinal velocity occurs further along the train than the lateral velocity peak does.



a)



b)

Figure 101 Colour plots of mean a) longitudinal and b) lateral velocity components on a plane at  $z=0.25$  m

**z=0.5**

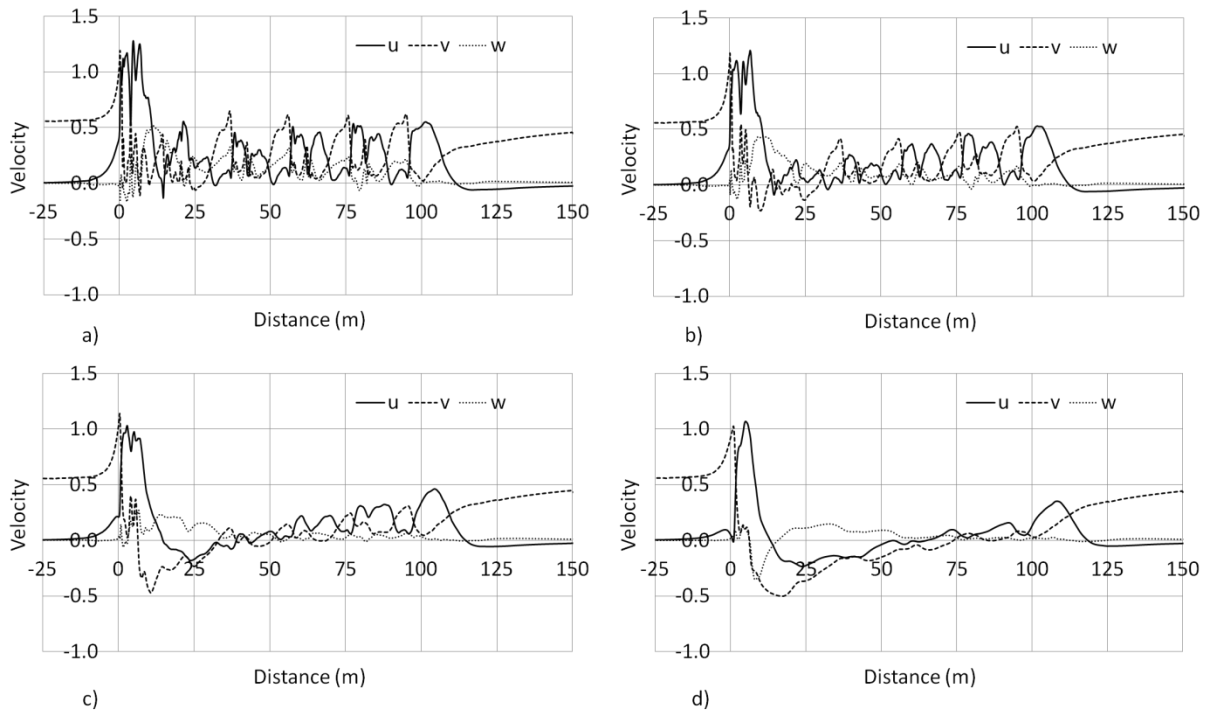


Figure 102 Slipstream velocity components at a)  $y=1.59$  m, b)  $y=1.84$  m, c)  $y=2.34$  m and d)  $y=3.34$  m

Figure 102 shows the velocity components on the leeward side of the train at  $z=0.5$  m. The undulating behaviour of the longitudinal and lateral components which was observed at  $z=0.25$  m occurs again at  $z=0.5$  m however the values in the boundary layer region are close to, or greater than,  $u=0.5$  and  $v=0.5$  at  $y=1.59$  m and  $y=1.84$  m. For all distances from COT the peak lateral and longitudinal velocities in the nose region are within 12 % of each other. At  $y=2.34$  and  $3.34$  m, the lateral velocity has a peak with a value of  $v=-0.5$  at  $x=11$  m and  $x=17$  m, respectively. The vertical velocity is shown to peak towards the ground at  $w=-0.35$  at  $y=3.34$  m which is a result of recirculation around the locomotive (discussed in Section 5.3.8). Positive longitudinal velocities are observed at all distances from COT, with the peak value of  $u=0.5$  occurring at  $y=1.59$  m. Peak longitudinal velocities in the near wake occurs further behind the train with increasing distance from train side, in accordance with the  $30^\circ$  wind.

### **z=1 m**

Figure 103 shows the velocity components on the windward side of the train at  $z=1$  m. The velocity components in the boundary layer region at all distances from COT are not only larger but exhibit more variability for  $z=1$  m than they did for  $z=0.5$  m. The peak component in the boundary layer region is the longitudinal velocity which reaches  $u=0.88$  and occurs at  $x=63$  m and  $y=1.59$  m. The peak vertical velocity occurs along the length of the locomotive and is  $w=0.7$  at  $y=1.59$  m.

The duration of the longitudinal nose peak is shown to be up to 15 m long and then fall to local minima which differ significantly from the no-crosswind case where the boundary layer development continues directly after the nose pulse and durations were approximately 0.5 m. The greatest component on the leeward side of the train occurs at  $z=1$  m is the longitudinal velocity and is  $u=1.32$ .

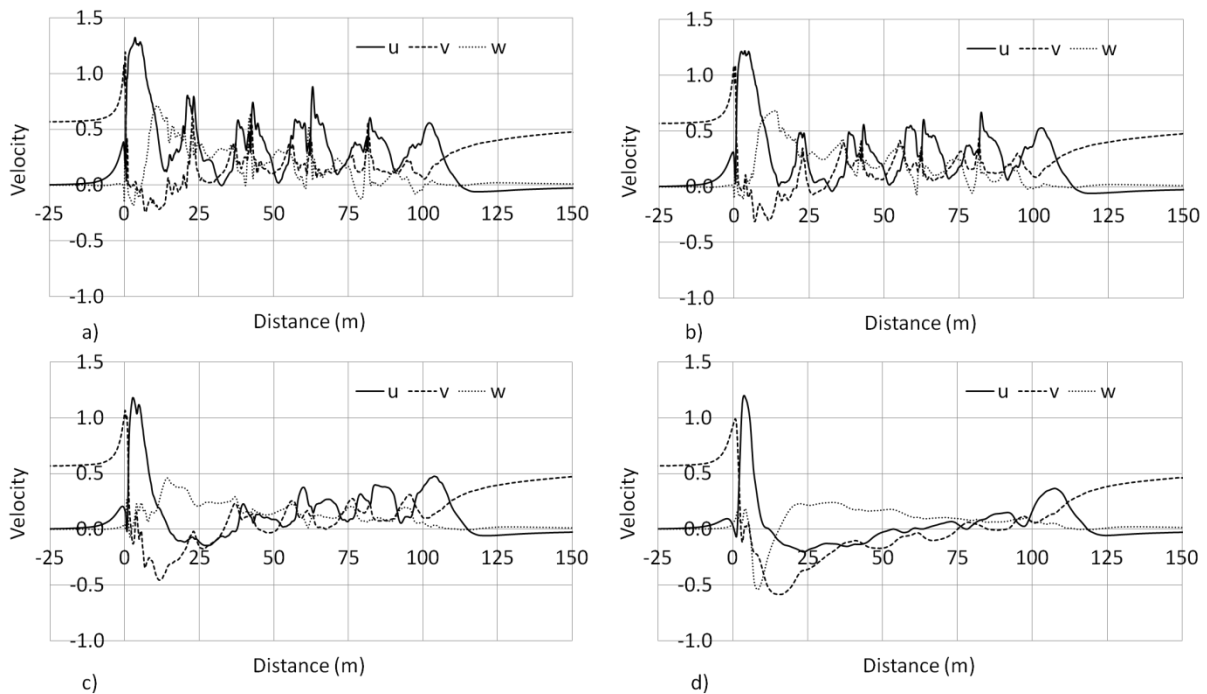


Figure 103 Slipstream velocity components at a)  $y=1.59$  m, b)  $y=1.84$  m, c)  $y=2.34$  m and d)  $y=3.34$  m

### **z=2 m**

Figure 104 shows the velocity components at  $z=2$  m. The greatest lateral velocity in the boundary layer region reaches a peak value of  $v=1.0$  at  $x=41$  m. The greatest lateral transient has a duration of 4 m which corresponds to a time-scale of 0.12s and is less than  $1/3^{\text{rd}}$  of the human response time suggested by Fukuchi (1961), thus it is unlikely to affect standing persons.

The vertical velocity at  $x=11$  m is the greatest vertical component above TOR with a value of 1. For all heights above TOR the lateral velocity is negated by the magnitude of the vertical velocity component.

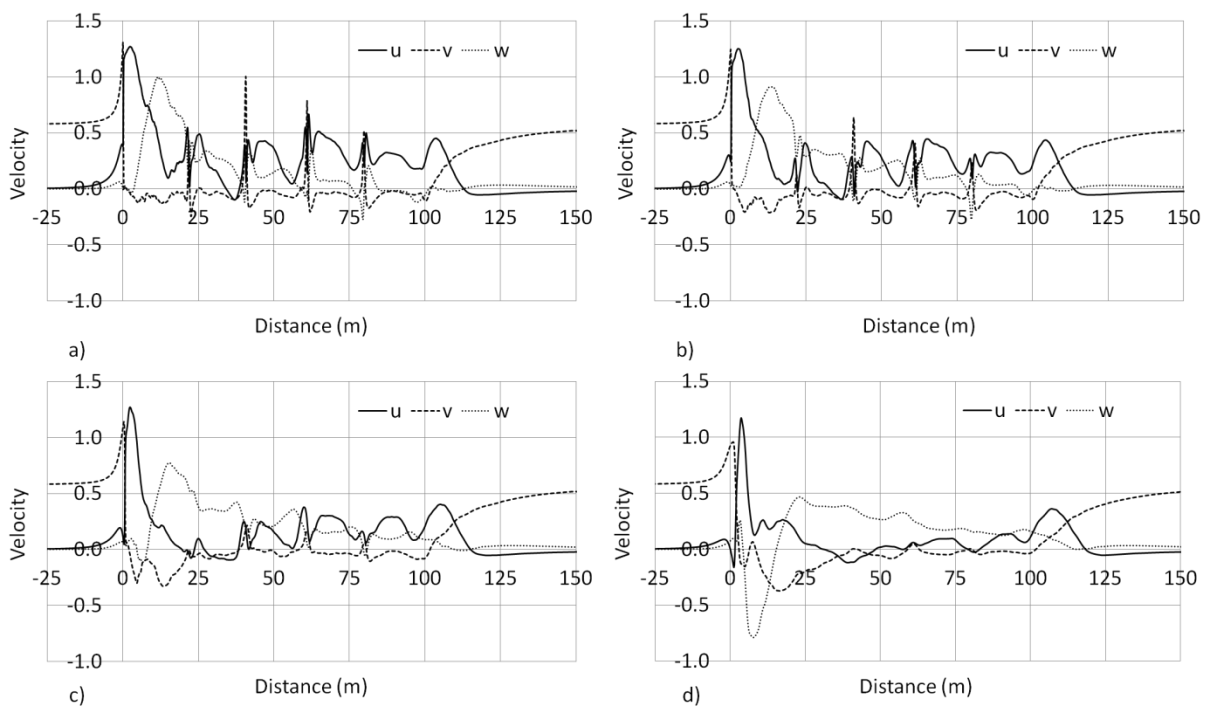


Figure 104 Slipstream velocity components at a)  $y=1.59$  m, b)  $y=1.84$  m, c)  $y=2.34$  m and d)  $y=3.34$  m

### **z=3 m**

Figure 105 shows the velocity components at  $z=3$  m. The peak longitudinal velocity in the boundary layer region is 54 % greater at  $z=3$  m than at  $z=2$  m. This dramatic increase in the

longitudinal velocity is hypothesised to be due to reduced blockage in the inter-wagon spacings.

A vertical velocity transient occurs at  $y=3.34$  m, shifting from  $w=-0.82$  at  $x=8$  m to  $w=-0.57$  at  $x=23$  m. This transient of  $\Delta w 1.39$  happens in only 15 m, which corresponds to a time-scale of 0.45 s and is also only 20% greater than the instability time-scale proposed by Fukuchi (1961). For  $x>20$  m, the lateral velocity remains negative for the majority of train length with magnitudes greater than at  $z=2$  m. This behaviour occurs for all distances from COT except  $y=3.34$  m.

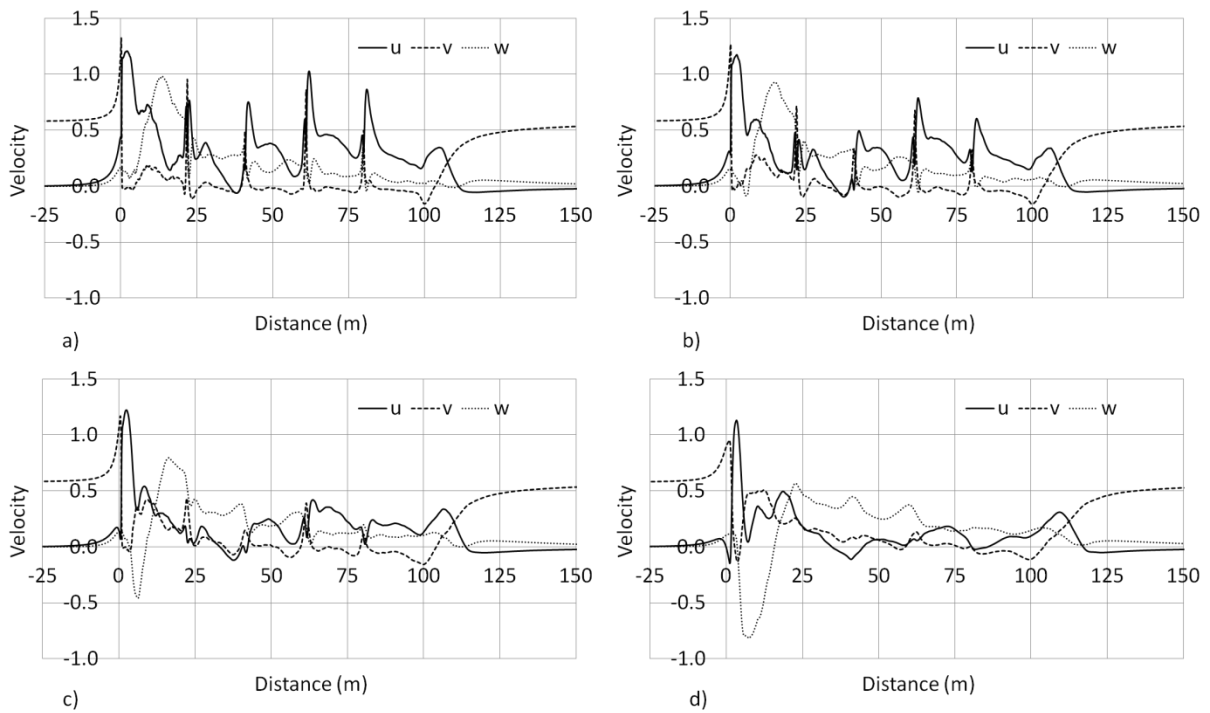


Figure 105 Slipstream velocity components at a)  $y=1.59$  m, b)  $y=1.84$  m, c)  $y=2.34$  m and d)  $y=3.34$  m

$z=4$  m

Figure 106 shows the velocity components at  $z=4$  m. The vertical velocity is observed to have peak values greater than  $w=-0.5$  along the locomotive for all distances from COT. A secondary lateral velocity peak exists at  $x=12$  m and  $y=3.34$  m, with a value of  $v=0.94$ . This

is the first example of a secondary peak being greater than the primary one for any component at any sampling position in the slipstream.

The nose region transients for the longitudinal velocity are between 4 and 6 m long although a secondary peak exists for all distances from train side which occur between 7 and 10 m after the first peak. In the near wake of the freight train the longitudinal velocity is observed to have peak values of up to  $u=0.32$  which rapidly fall away to  $u=0$  within 10 m.

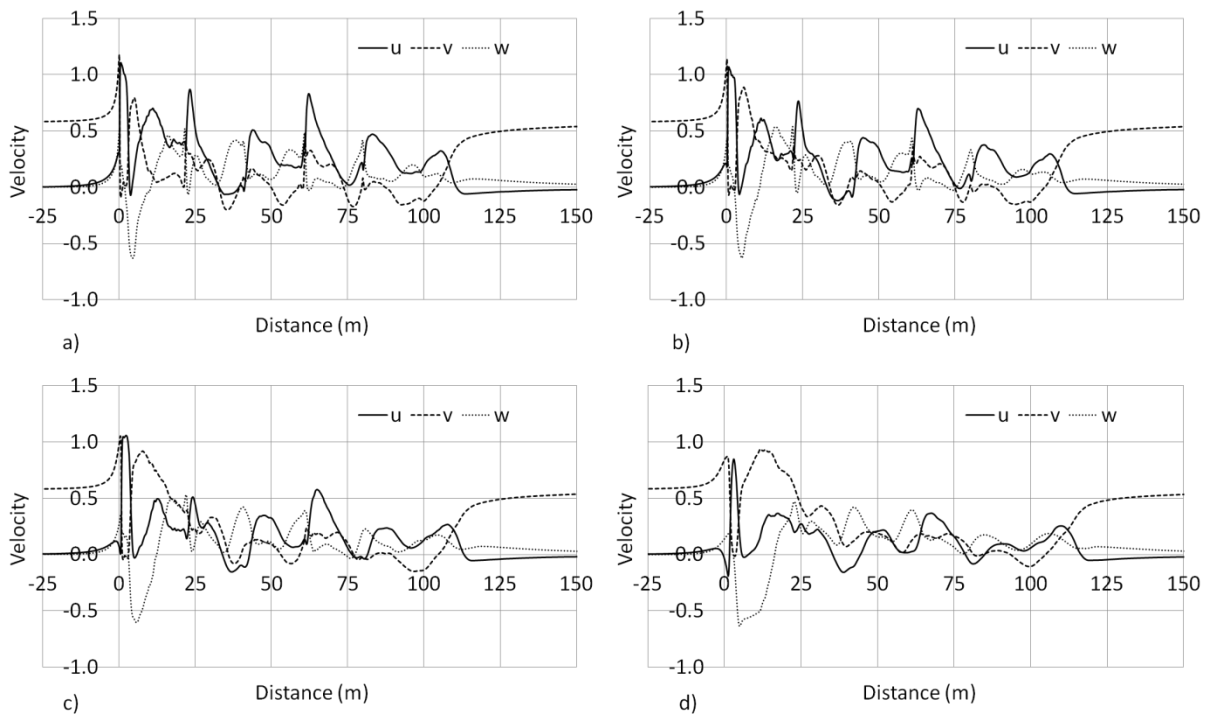


Figure 106 Slipstream velocity components at a)  $y=1.59$  m, b)  $y=1.84$  m, c)  $y=2.34$  m and d)  $y=3.34$  m

### Leeward component summary

Large variability is observed between velocity components in the slipstream due to the large-scale recirculation on the leeward side of the train. At all heights above the ground, in the nose region the longitudinal and lateral velocity peaks exceed train speed. For  $z \geq 1$  m the vertical velocity becomes a significant component within the slipstream. The maximum sampled component is the longitudinal velocity which is  $u=1.32$  and occurs at  $x=4$  m and  $z=1$  m.

### 5.3.6 Pressure on the windward side of the train

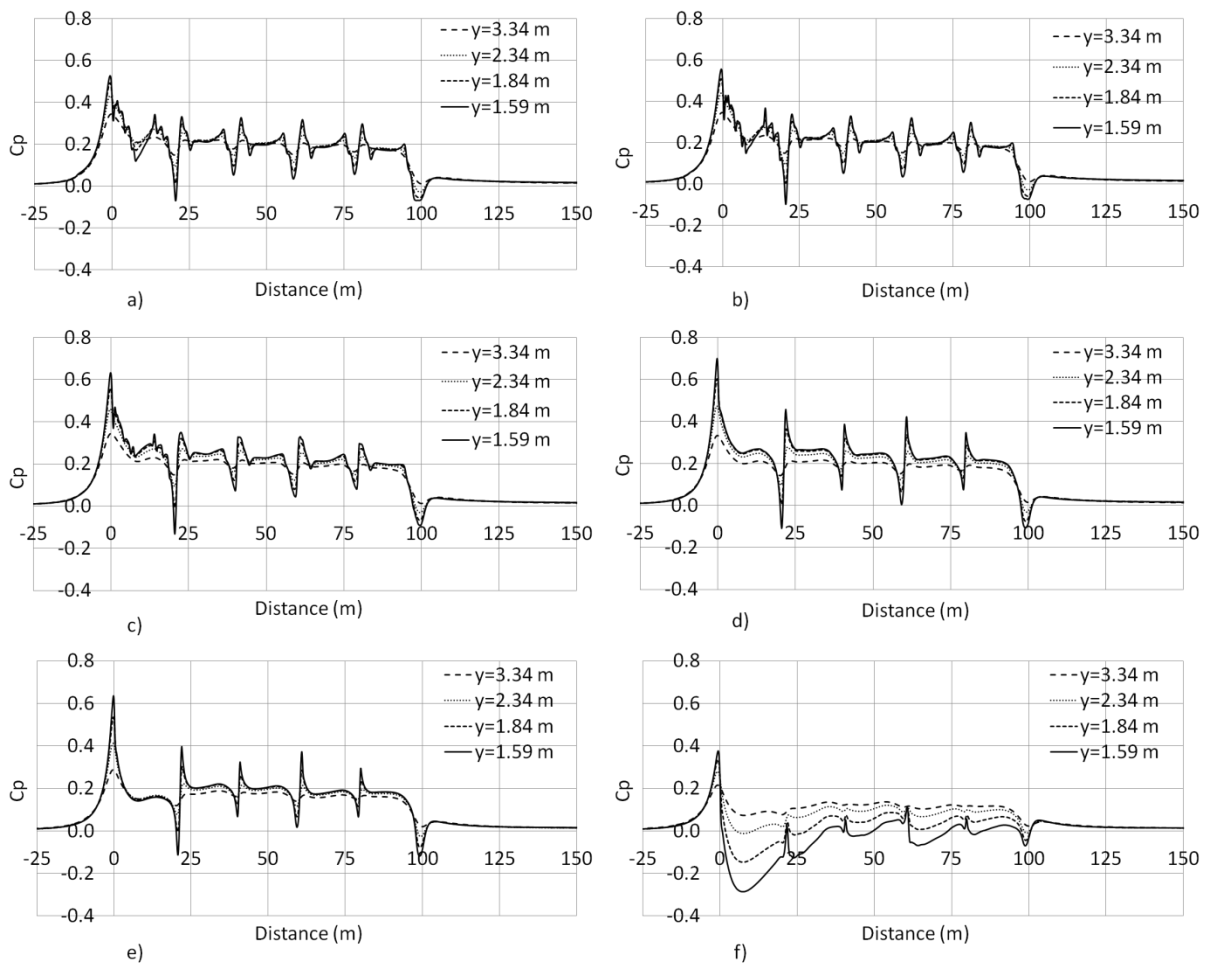


Figure 107 Pressure coefficients,  $C_p$ , on the windward side of the freight train at a)  $z=0.25$  m, b)  $z=0.5$  m, c)  $z=1.0$  m, d)  $z=2.0$  m, e)  $z=3.0$  m and f)  $z=4.0$  m

Figure 107 presents the pressure coefficients on the windward side of the freight train. The pressures on the windward side of the train are generally positive for the majority of train length as a result of the flow stagnating on the locomotive and container sides: exceptions occur at the first inter-wagon spacing as well as in the near wake. At  $z=4$  m the region of lowest pressure is observed as a result of the flow separating over the roof of the locomotive but further from the train side the positive pressure is dominant due to the extent of the stagnation region.

The relative roughness of the bogies is visible in the pressure signals for  $z > 2$  m, whereas at  $z \leq 2$  m the curves are smooth between transients due to the relative smoothness of the

container sides. Furthermore, at  $z=2$  m, the greatest positive pressure of  $C_p=0.7$  and occurs at  $x=0$  m. The greatest pressure transients occur at the two largest inter-wagon spacings due to the high pressure from the stagnation rapidly reducing because the pressure to diffuses through the spacings.

Figure 108 shows data from Figure 107 plotted with respect to height. The negative pressure coefficients at the first and third inter-wagon spacings, at  $z<4$  m show values within 10% of each other.

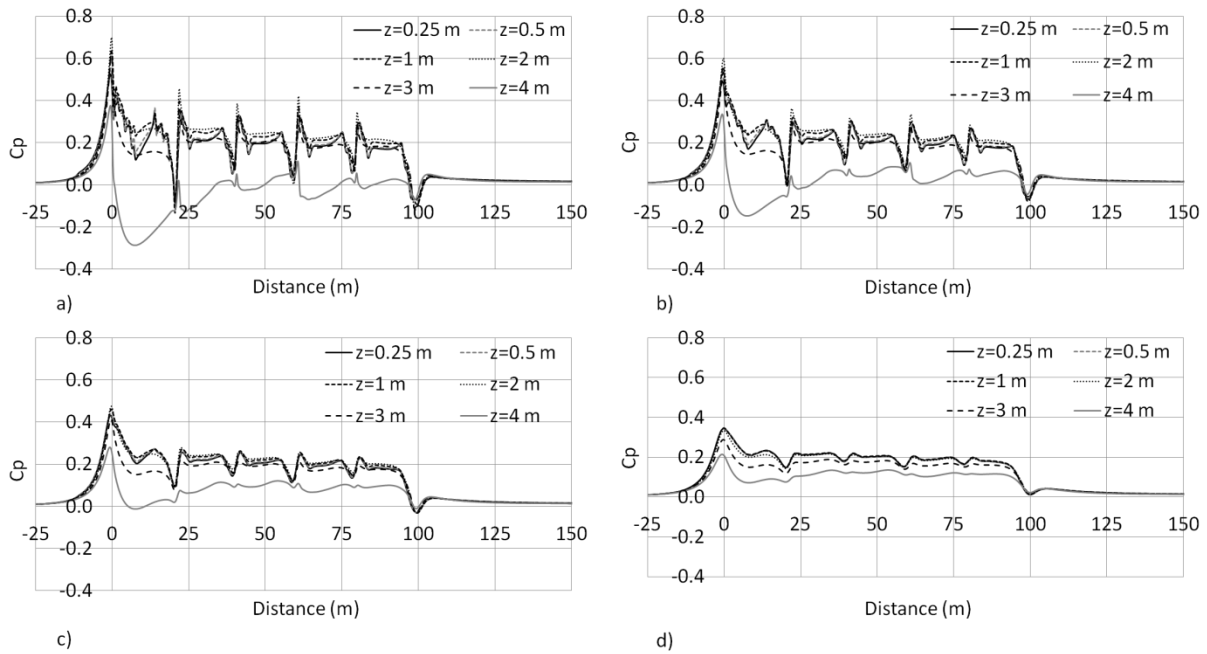


Figure 108 Pressure coefficient,  $C_p$ , windward varying with height at a)  $y=1.59$  m, b)  $y=1.84$  m, c)  $y=2.34$  m and d)  $y=3.34$  m

### 5.3.7 Pressure on the leeward side of the train

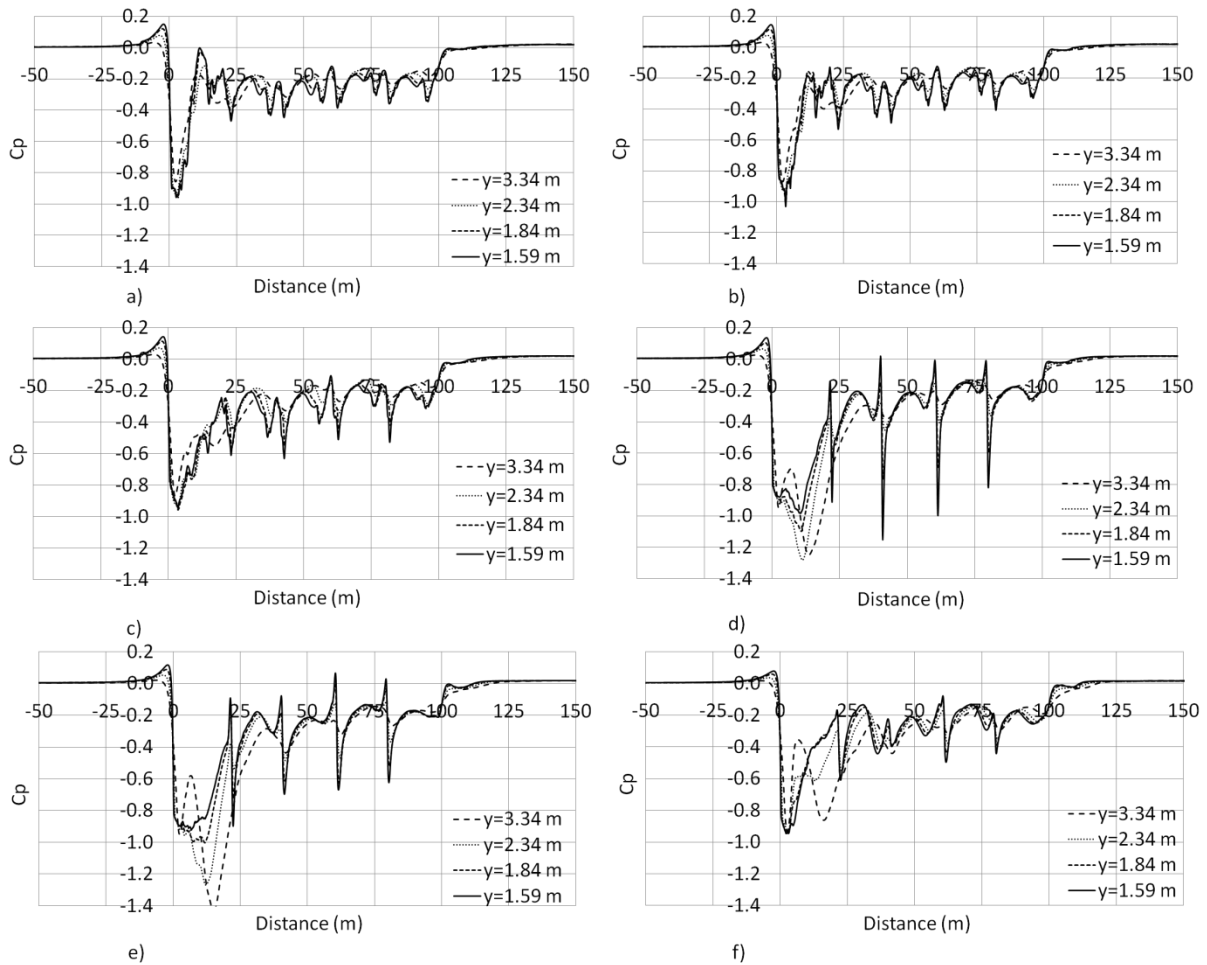


Figure 109 Pressure coefficient,  $C_p$ , downwind of the freight train at a)  $z=0.25$  m, b)  $z=0.5$  m, c)  $z=1.0$  m, d)  $z=2.0$  m, e)  $z=3.0$  m and f)  $z=4.0$  m

Figure 109 shows the pressure coefficients on the leeward side of the train. Large negative pressures are observed along the length of the locomotive due to massive flow separation over the roof and around the front face. The negative pressure coefficient is greater on the leeward side of the locomotive than the container wagons due to the larger blockage from the underbody region. The greatest negative pressure coefficient occurs at  $y=3.34$  m  $z=3$  m with a value of  $C_p=-1.42$  and the largest pressure transient occurs at the second inter-wagon spacing with a value of  $\Delta C_p=1.17$ .

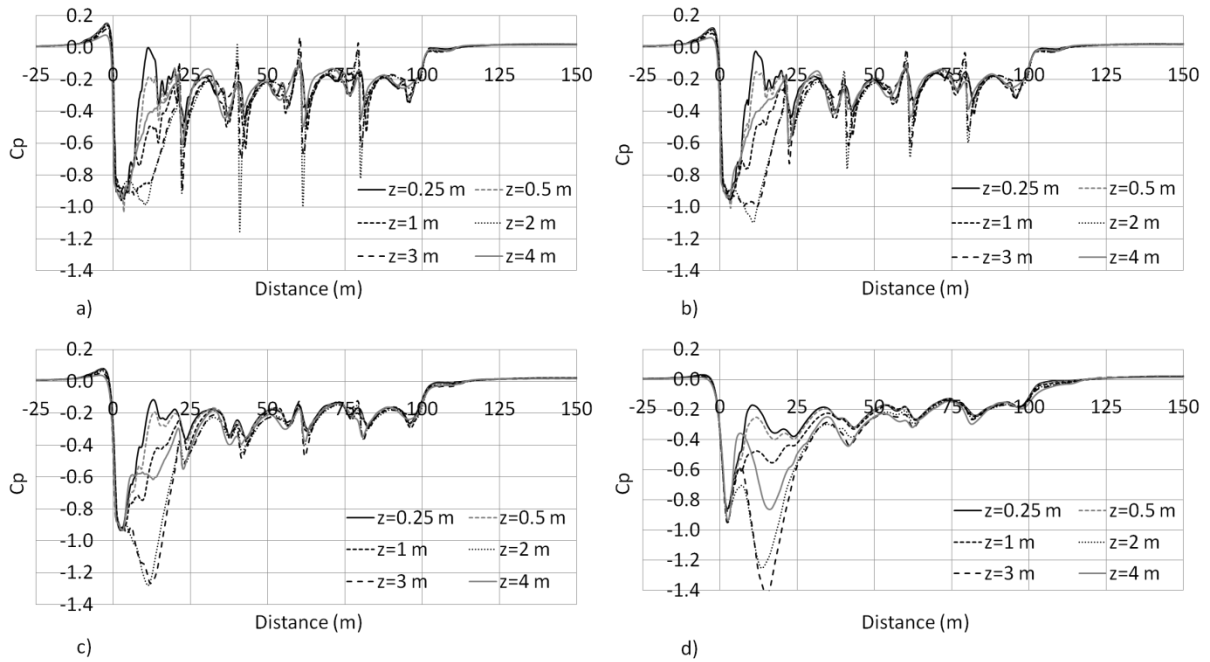


Figure 110 Pressure coefficient,  $C_p$ , downwind varying with height at a)  $y=1.59$  m, b)  $y=1.84$  m, c)  $y=2.34$  m and d)  $y=3.34$  m

Figure 110 shows the variation of  $C_p$  with height for different distances from train side. The most significant feature in the slipstream is the elongation of the nose pressure transient in comparison to what was observed in the no-crosswind case. The nose transients at  $z=2$  m and  $z=3$  m show a greater similarity to each other than for other distances above TOR due to the nearly-constant vehicle cross section in that region. At  $y=1.84$  m,  $y=2.34$  m and  $y=3.34$  m the pressure remains negative for the entire train length.

### 5.3.8 Flow structures

Figure 111 shows streamlines released  $6.25 \times 10^{-5}$  m from the containers' surfaces. The streamlines give an indication of the behaviour of the mean flow close to the surface of the containers, especially regions of flow separation and recirculation. The streamlines replicate surface oil flow patterns that would occur on the containers and was used for an idealised passenger train in Hemida and Krajnović (2005). The locations of flow separation and reattachment are visible in the streamlines with the approximate shape of the roll vortices shown by  $C_p$  in Figure 112.

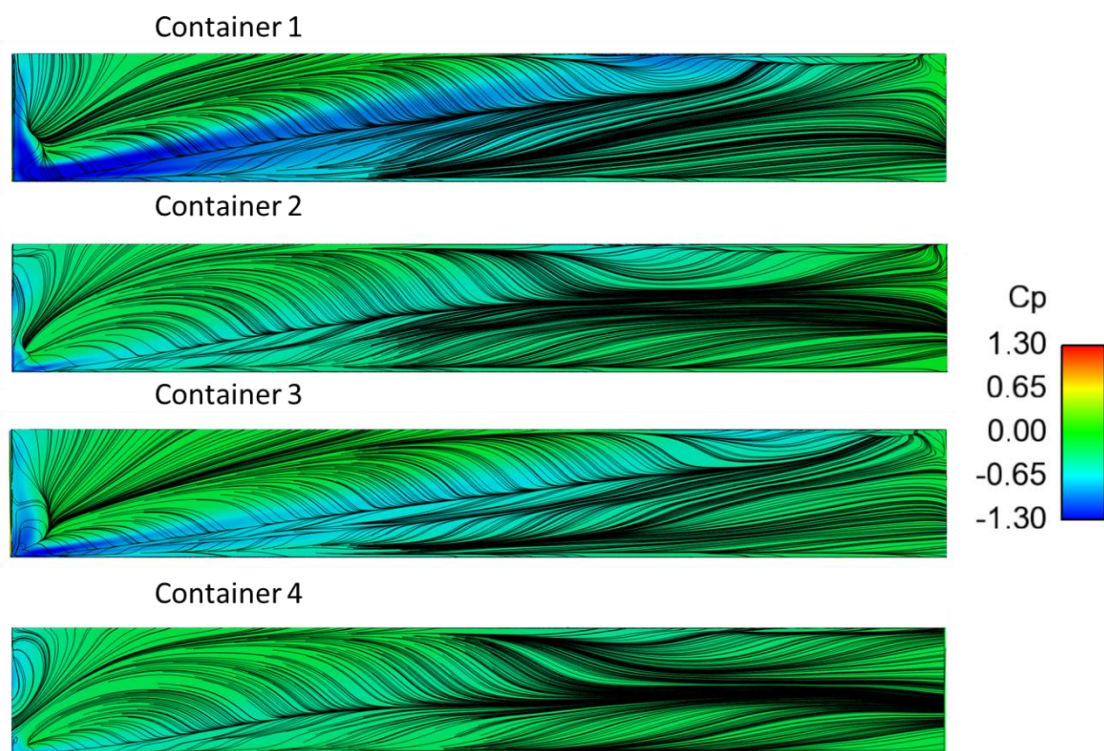


Figure 111 Surface streamlines on the roof of containers, coloured by  $C_p$

Figure 112 shows pressure isosurfaces ( $C_p = -0.6$ ) on the roofs of the four containers which are observed to correspond well to the streamlines shown in Figure 111. The isosurfaces on containers one and three are larger than those on containers two and four which suggests that larger preceding inter-wagon spacings are conducive to lower-pressure regions on the roofs of the containers which has been shown in force coefficients by Soper (2014).

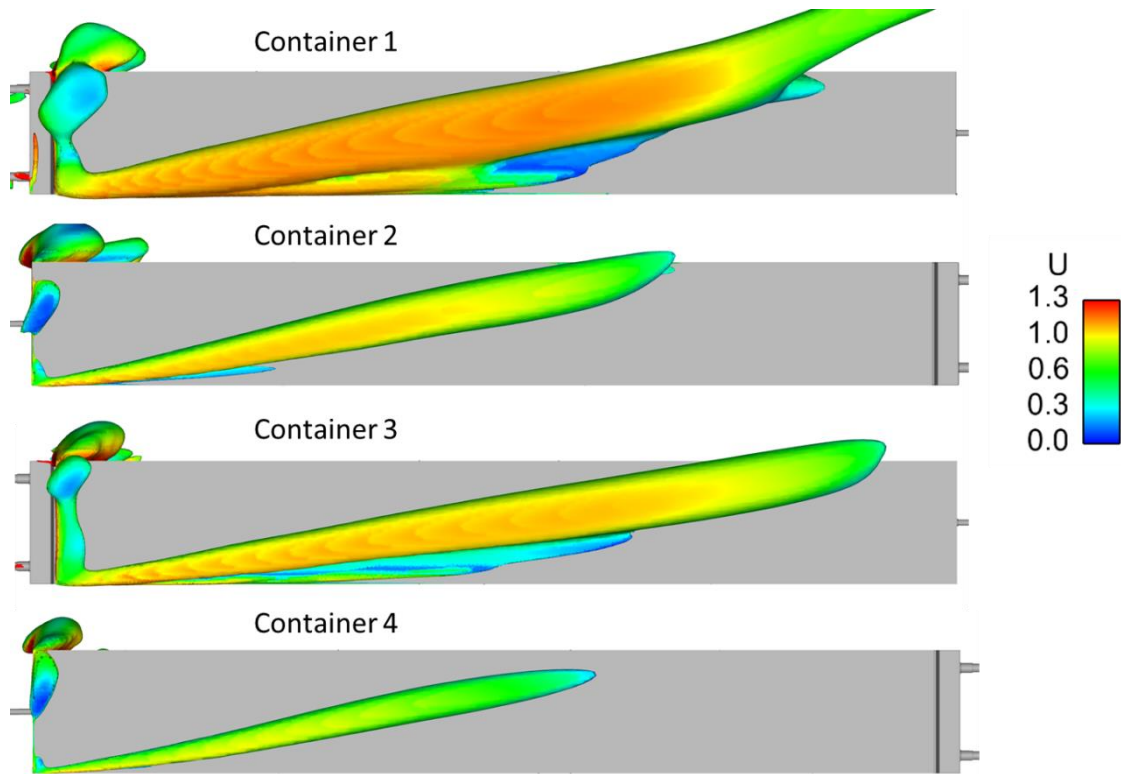


Figure 112 Isosurfaces of pressure ( $C_p = -0.6$ ), coloured by velocity magnitude

On the leeward side of the train a large trailing vortex is visualised by using a negative pressure isosurface (Figure 113). The vortex originates at the front of the locomotive due to the abrupt flow separation which occurs there, and continues to develop along the train length. The isosurface is approximately 70 m long and extends up to  $y=10$  m. The isosurface is observed to disappear after  $x \approx 70$  m although this is not the end of the vortex, it merely the equalisation of the negative pressure as a result of the flow through the largest inter-wagon spacing.

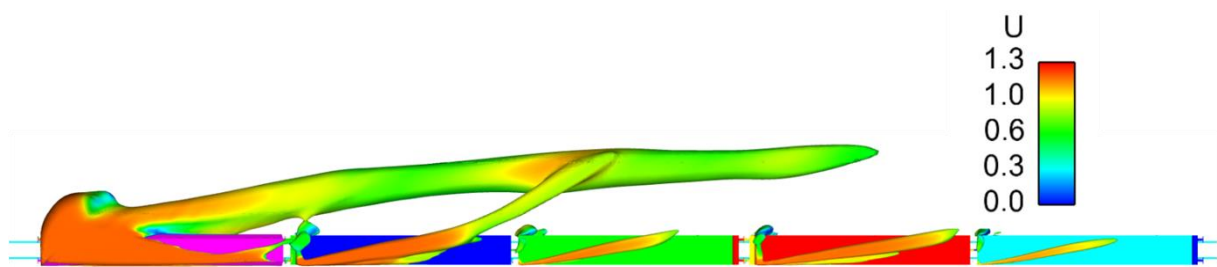


Figure 113 Pressure isosurface ( $C_p = -0.6$ ) coloured by velocity magnitude

Figure 114 shows the vortex on the leeward side of the freight train and also a similar flow structure that occurs on the leeward side of the ICE2 when subjected to a 30° crosswind (Diedrichs, 2003). The streamlines around the freight train in the present case show greater variability on the leeward side of the locomotive near the ground because the underbody geometry of the freight train is more complicated than for the ICE2. The streamlines released in Diedrichs (2003) often remain close to the train side, whereas on the leeward side of the freight train the vortex structure is observed to convect away from train side along the first container wagon.

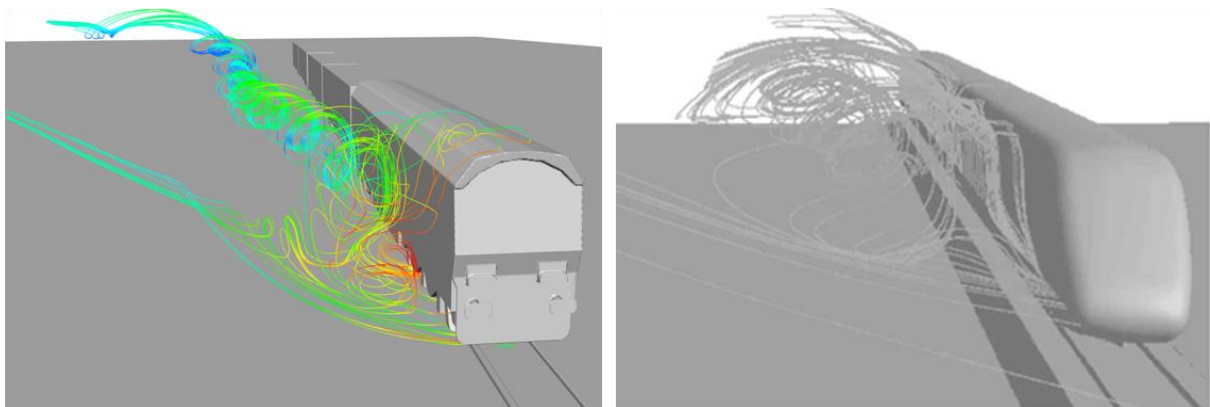


Figure 114 Time-averaged velocity streamlines showing leeward vortices for present case (left) and ICE2 at 30° (right) (Diedrichs, 2003)

### ***5.3.9 Surface pressure coefficients***

Surface pressure coefficients are sampled from loops around the longitudinal axis of each container and are shown in Figure 115. The loops are at 25%, 50% and 75% along the length of the containers and the pressure coefficients are shown on the windward, roof and leeward sides. The locations of flow separation are visible on the surface of each container and are distinguishable by negative pressure peaks. Towards the rear of each container the peak  $C_p$  in each loop shifts towards the leeward side in accordance with the angle that the roll vortices are inclined at (Figure 112).

The magnitudes of the surface pressure coefficients on the roofs of the containers show a general trend of decreasing with loading position. There is also correlation between the size of the vortices in Figure 112 and the magnitude of the pressures shown in Figure 115, with the first and third containers having lower surface pressures than containers two and four.

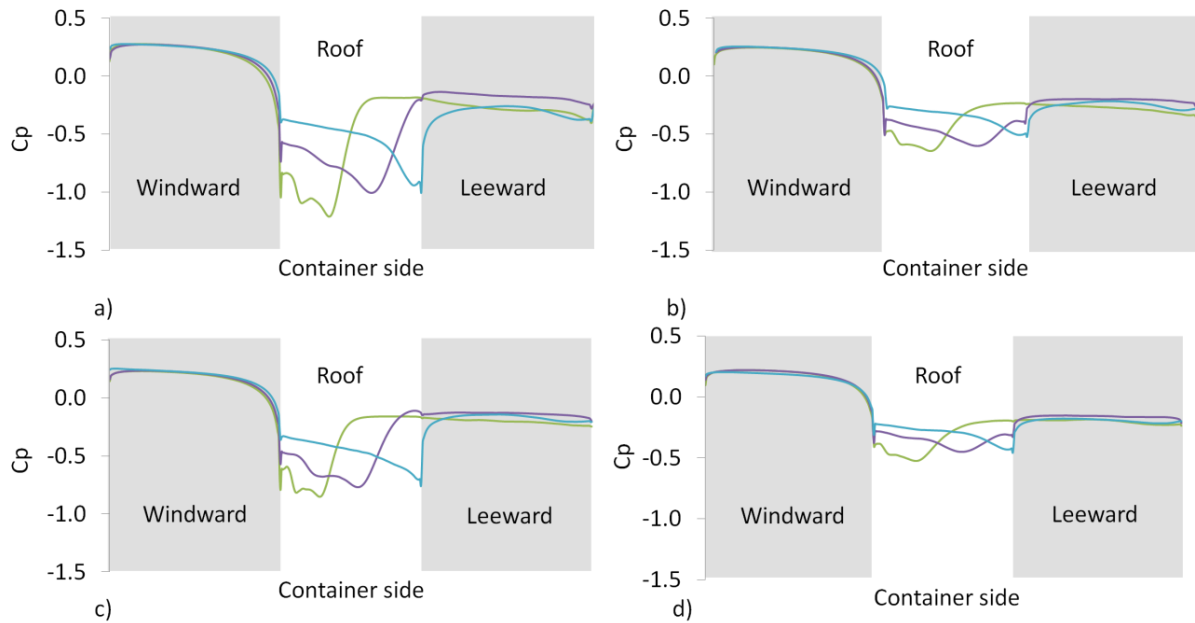


Figure 115 Surface-pressure coefficients on windward, roof and lee-sides for containers a) 1, b) 2, c) 3 and d) 4 at 25% (green), 50% (purple) and 75% (blue) along each container

### 5.3.10 Flow structures in the inter-wagon spacings

Mean velocity streamlines projected onto a plane at half-height and show flow structures in the inter-wagon spacings, are shown in Figure 116. The two larger spacings (Figure 116 a & c) each contain two mean-flow vortices, where one is five times the lateral diameter of the other. The two smaller spacings (Figure 116 b & d) appear to only contain a single mean-flow vortex at half-height.

On the leeward side of the train, outside of all of the inter-wagon spacings, a small region of recirculation exists where the flow separates around the leeward front corners of the containers.

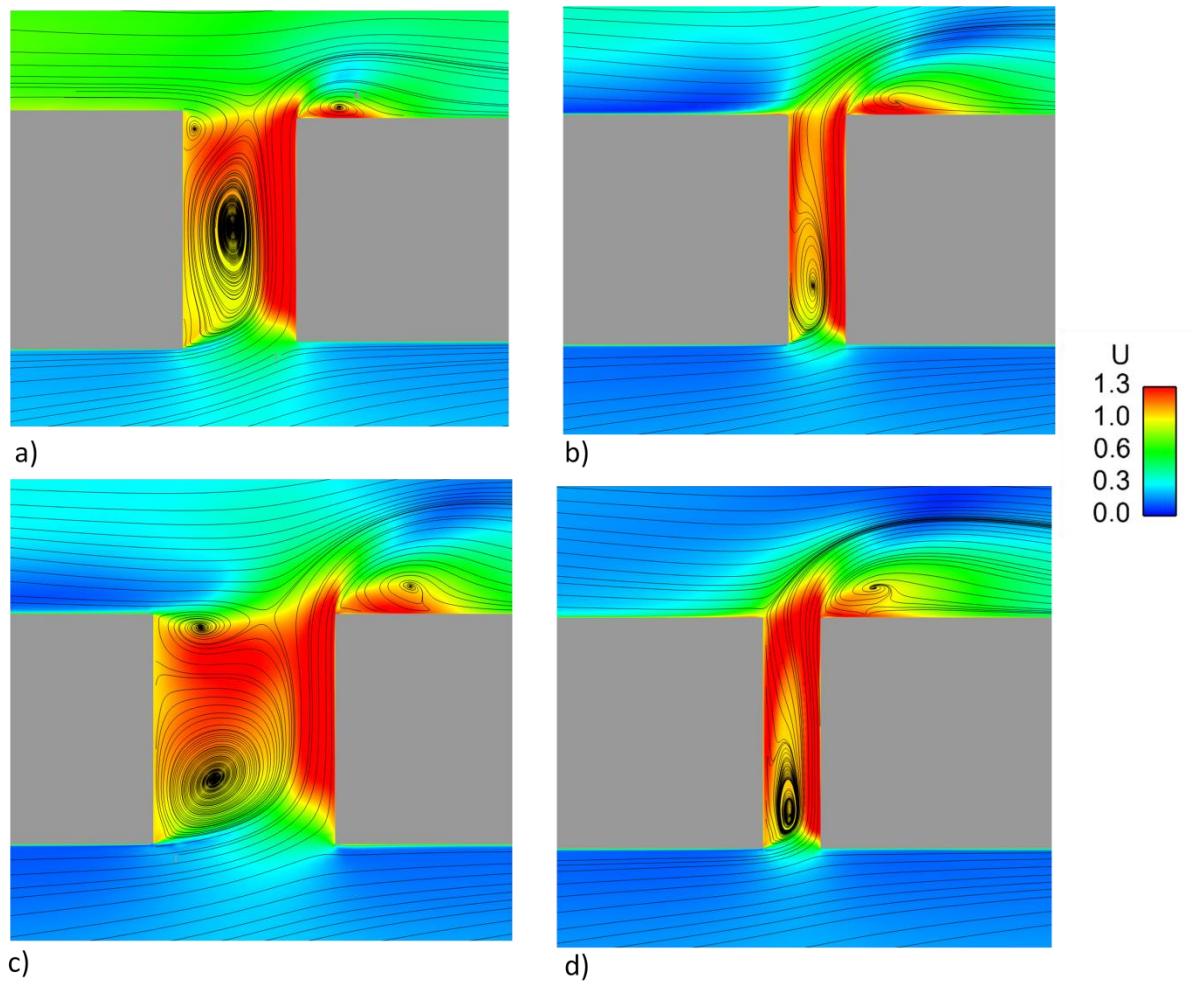


Figure 116 Time-averaged streamlines projected on a plane at half train height coloured by velocity magnitude

Figure 117 shows mean velocity streamlines projected onto a plane at  $y=0$  m. The smaller inter-wagon spacings (Figure 117 b & d) contain a single high aspect ratio mean-flow structures but also a single low aspect ratio flow structure at the top and bottom of the spacing. The larger spacings (Figure 117 a & c) contain large, low aspect ratio flow structures as well as a number of much smaller ones. The velocity magnitude is generally greater closer towards the most rear of the two containers which are adjacent to the spacing.

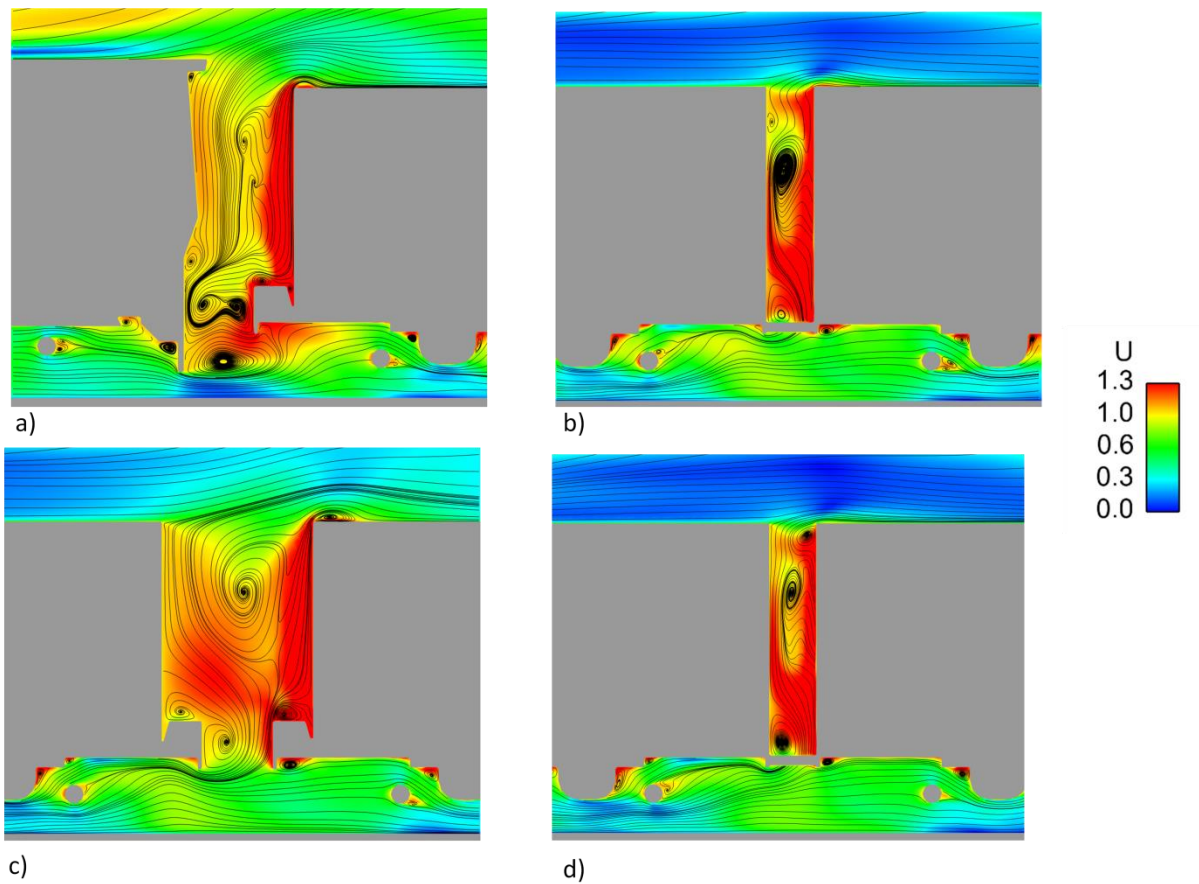


Figure 117 Time-averaged streamlines projected on a plane at  $y=0$  m coloured by velocity magnitude

### ***5.3.11 Forces experienced by locomotive and containers***

The mean force coefficients experienced by the locomotive, containers and container-flats are given in Table 6, Table 7 and Table 8 and the contributions of pressure and friction to the mean force coefficients are also provided.

Pressure is dominant in the contribution to the drag force,  $C_d$ , experienced by the containers, with pressure forces often an order of magnitude higher than the frictional contributions. The increased contribution of pressure to the drag force, in comparison to the no-crosswind case, is due to the yaw angle exposes the front faces of the containers and allows for more

stagnation to occur. The contributions of pressure and friction to the  $C_d$  experienced by container 1 are approximately equal with the small pressure contribution due to the shielding effect of the locomotive which precedes the container wagon.

Container 2 experiences negative pressure drag which is a result of the lower pressure in the preceding inter-wagon spacing (Figure 118) causing suction and thus causing the negative drag force. This phenomenon has been observed in the wind engineering field for tall buildings and is known as upwind-acting force (Lam et al., 2008). In the no crosswind case it was the first container which experienced negative pressure drag however, the larger spacing between the locomotive and first container allow for stagnation at  $30^\circ$ .

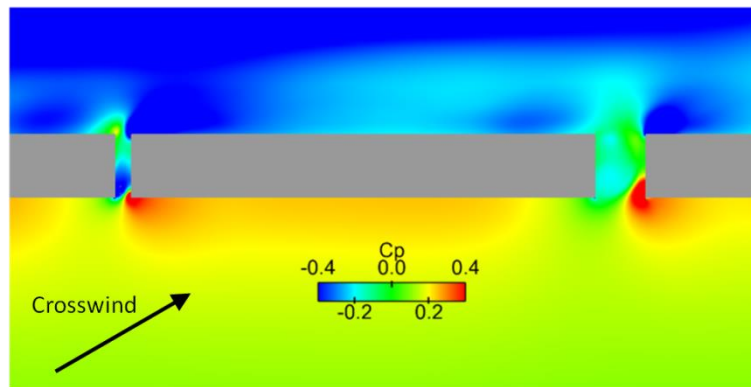


Figure 118 Plane at  $z=2$  m coloured by pressure coefficient showing the pressure around the second container

The flat-bed wagons experience greater drag than the containers for the first, second and fourth wagons. The third wagon is an exception to the rule because the exposed front face of the container allows for stagnation from the freestream flow. Furthermore the smaller inter-wagon spacing behind the third container is dominated by low pressure which thus results in a larger drag force than is experienced by other containers.

Table 6 Drag force coefficients

	Total	Pressure	Friction	Whole wagon
<b>Class 66</b>	1.47	1.40	0.07	1.47
<b>Container 1</b>	0.10	0.05	0.05	
<b>Flatbed wagon 1</b>	0.21	0.18	0.03	0.31
<b>Container 2</b>	0.02	-0.02	0.04	
<b>Flatbed wagon 2</b>	0.26	0.23	0.03	0.28
<b>Container 3</b>	0.35	0.30	0.05	
<b>Flatbed wagon 3</b>	0.26	0.23	0.03	0.61
<b>Container 4</b>	0.11	0.07	0.04	
<b>Flatbed wagon 4</b>	0.25	0.22	0.03	0.36

The contribution of viscous forces to the side force coefficients,  $C_s$ , are much lower than for  $C_d$  due to the shorter lateral distance that the flow travels along the surface of the containers. The locomotive experiences the highest force coefficient and the general trend of side-force coefficient decreasing with loading position.

As occurred for the drag force, the side force coefficients experienced by the flat bed wagons are greater than those experienced by the containers for the first, second and fourth wagons. The first container experiences the greatest side force due to blockage effect of the

locomotive causing the low-pressure region on the leeward side of the wagon to be maintained thus causing greater side-force. The equalisation of the leeward low-pressure field occurs along train length due to the inter-wagon spacings and underbody region.

Table 7 Side force coefficients

	<b>Total</b>	<b>Pressure</b>	<b>Friction</b>	<b>Whole wagon</b>
<b>Class 66</b>	6.64	6.62	0.02	6.64
<b>Container 1</b>	3.21	3.21	0.00	3.97
<b>Flatbed wagon 1</b>	0.76	0.75	0.01	
<b>Container 2</b>	3.16	3.16	0.00	3.92
<b>Flatbed wagon 2</b>	0.76	0.75	0.01	
<b>Container 3</b>	2.49	2.49	0.00	3.16
<b>Flatbed wagon 3</b>	0.67	0.66	0.01	
<b>Container 4</b>	2.50	2.50	0.00	3.14
<b>Flatbed wagon 4</b>	0.64	0.63	0.01	

The lift force coefficients,  $C_l$ , experienced by flat-bed wagons are negative as a result of the low pressure that that exists beneath them. The  $C_l$  experienced by the containers decreases along train length until the third container where an increase happens as a result of the larger preceding inter-wagon spacing.

The first container experiences a lift coefficient 30% greater than the third wagon. It is hypothesised that the relatively high lift force coefficient experienced by the first wagon is due to the taller locomotive shielding the roof flow causing a low pressure region.

Table 8 Lift force coefficients

	<b>Total</b>	<b>Pressure</b>	<b>Friction</b>	<b>Whole wagon</b>
<b>Class 66</b>	3.96	3.93	0.03	3.96
<b>Container 1</b>	3.09	3.08	0.01	
<b>Wagon 1</b>	-0.68	-0.68	0.00	2.41
<b>Container 2</b>	1.96	1.95	0.01	
<b>Wagon 2</b>	-0.70	-0.70	0.00	1.26
<b>Container 3</b>	2.31	2.30	0.01	
<b>Wagon 3</b>	-0.50	-0.50	0.00	1.81
<b>Container 4</b>	1.66	1.65	0.01	
<b>Wagon 4</b>	-0.60	-0.60	0.00	1.06

Table 9 shows the rolling moment coefficient about the centre of track for the locomotive, each container and flatbed wagon. The rolling moment coefficient,  $C_M$ , is defined as

$$C_M = \frac{M_x}{\frac{1}{2}\rho u_r^2 AH}, \quad (5.1)$$

where

$M_x$  – rolling moment about centre of track.

Table 9 Rolling moment for the locomotive, containers and flatbed wagons about the centre of track

	Moment	Total
<b>Class 66</b>	-3.36	-3.36
<b>Container 1</b>	-1.92	-1.98
<b>Flatbed Wagon 1</b>	-0.06	
<b>Container 2</b>	-1.74	-1.80
<b>Flatbed Wagon 2</b>	-0.06	
<b>Container 3</b>	-1.45	-1.51
<b>Flatbed Wagon 3</b>	-0.06	
<b>Container 4</b>	-1.41	-1.45
<b>Flatbed Wagon 4</b>	-0.04	

The drag, side & lift force coefficients experienced by each container and the rolling moment experienced by each entire wagon are shown against loading position in Figure 119. It is observed that the locomotive experiences the largest side, lift and drag force coefficients as well as the greatest rolling moment. The drag and side forces experienced by the locomotive are approximately double those experienced by the subsequent containers. The third container

experiences the greatest drag coefficient as a result of the relatively large preceding inter-wagon spacing which allows for stagnation on its front face. The lift force coefficient also increases at the third container because the development of a roll vortex on the roof is less inhibited due to the larger adjacent inter-wagon spacing (Figure 112).

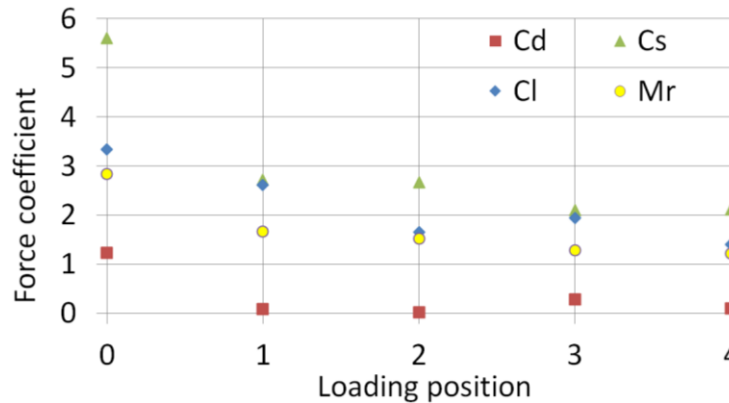


Figure 119 Force coefficients experienced by each container and rolling moment experienced by each entire wagon against loading position

Figure 119 highlights the difference in magnitude between the drag, side and lift forces experienced by each container. The drag, side and lift forces show a general trend of decreasing with loading position. Due to variability of the experienced forces with loading position it is difficult to accurately approximate at what train length the variability will diminish thus a longer train would help to identify this. It was mentioned in Section 5.3.5 that the velocity components on the leeward side of the train did not stabilise along train length: the same is true in the present chapter for the force coefficients. Golovanevskiy et al. (2012) showed that the force coefficients experienced by wagons in a train subjected to a crosswinds, between 0° and 20°, required approximately five wagons before the force coefficient becomes stabilised, after which the force coefficients remain very similar between wagons until the final wagon in the train.

The force coefficients obtained from ambient conditions and the crosswind case in Soper (2014) are discussed below and are converted to 10 m<sup>2</sup> area normalising values to aid

consistency. The drag force coefficient the third container in the no-crosswind case is  $C_d=0.097$ , whereas the values obtained from Soper (2014) is  $C_d=0.063$  which is 35% lower than in the CFD model. The side and lift force coefficients on the third container are  $C_s=2.10$  and  $C_l=1.94$ , respectively whereas Soper (2014) calculates values of  $C_s=1.71$  and  $C_l=2.32$  for the side and lift force coefficients, respectively. The relatively large discrepancy between the experimental and numerical force coefficients is anticipated considering the relatively large discrete areas which the experimental surface pressures were integrated over but also the effect of the turbulent CWG.

## **5.4**      *Instantaneous flow*

### **5.4.1**   *Vortex generation*

Figure 120 shows isosurfaces of the second invariant of the velocity gradient tensor,  $Q$ , as a means of visualising vortex generation. Figure 120a is a plan view of the flow separation around the locomotive. For the first half of the locomotive, the flow remains attached and only begins to separate on the windward side towards the rear of the vehicle. Figure 120b shows the rooftop vortices generated at the windward corners of the container wagons. The height of vortices above the container roof shows the level of influence that bluff geometries cause on the local flow field in comparison to more streamlined trains (Hemida and Krajnovic, 2005).

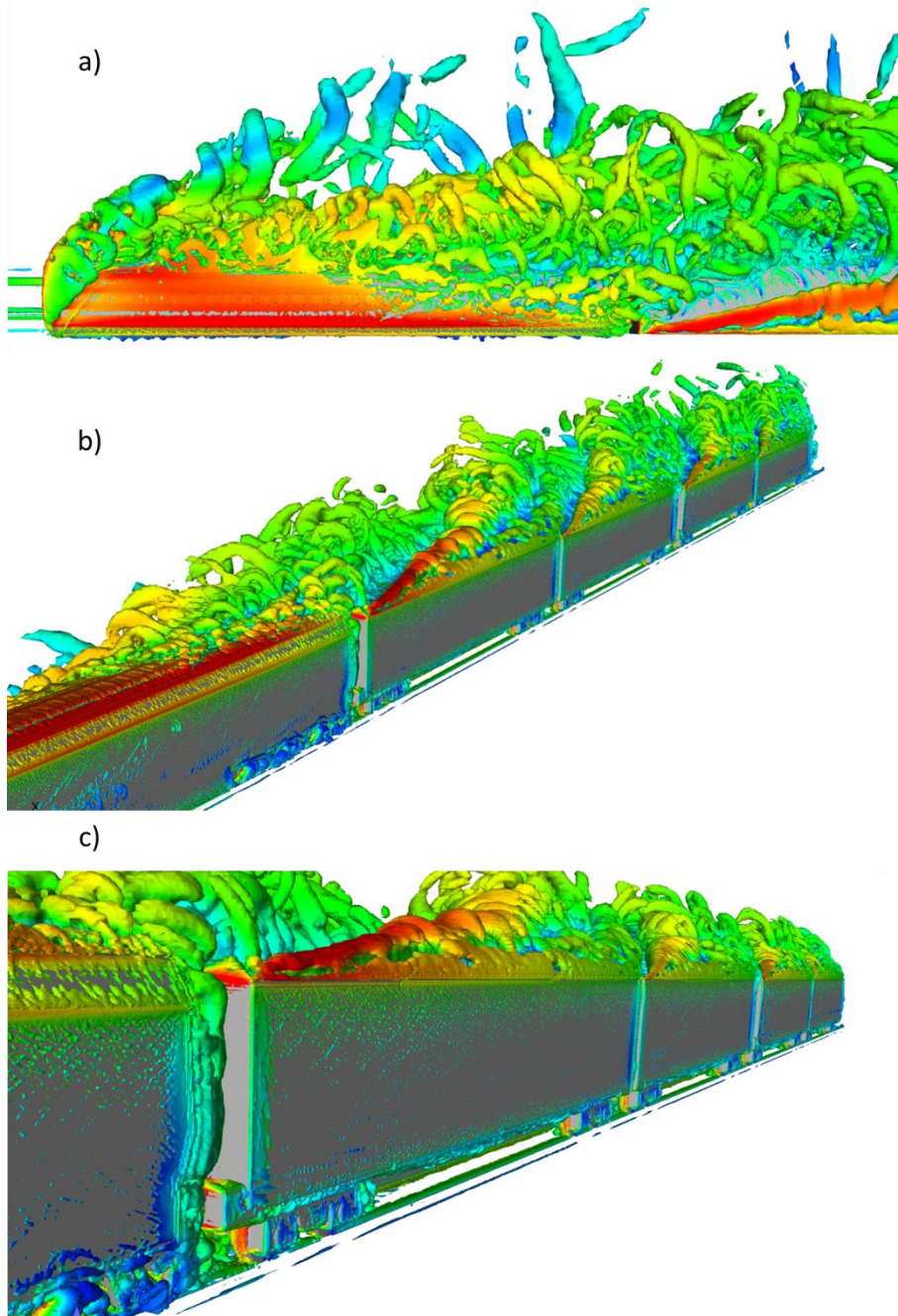


Figure 120 Isosurfaces of the second invariant of the velocity gradient tensor,  $Q=50,000$ , coloured by velocity magnitude

#### 5.4.2 Time-varying force coefficients

The force and rolling moment coefficients shown in Figure 121 fluctuate about mean values as would be expected from a vehicle subjected to a steady crosswind. The magnitude of fluctuations of  $C_l$  and  $C_s$  are large in comparison to  $C_d$  due to the fact that the areas normal to

the roof and leeward sides are unconfined. In confined flow regions shown here, the scale of the turbulent flow structures is limited by the size of the inter-wagon spacing and thus smaller, higher-frequency modes are present and observed in the drag force signal. The flow above, and at the side of the containers is unconfined, thus the length-scales are allowed to develop and are consequently larger causing larger, lower frequency fluctuations in the force signal.

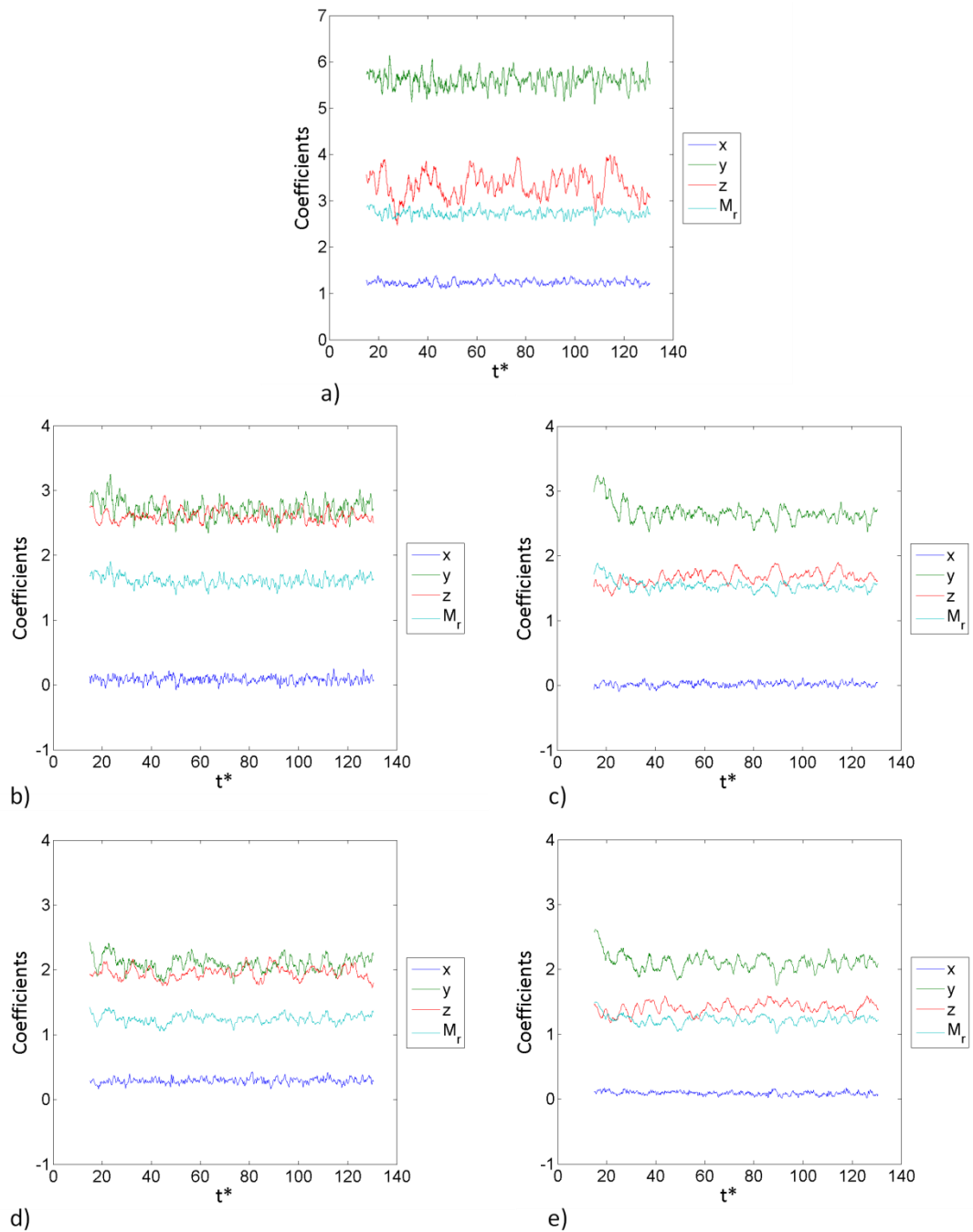


Figure 121 Force coefficients on a) class 66 locomotive, b) container 1, c) container 2, d) container 3 and e) container 4

### 5.4.3 Turbulence intensity on the windward side of the train

Figure 122 shows the turbulence intensity,  $I$ , on the windward side of the freight train. The turbulence intensities are generally between  $I=5-20\%$  in the boundary layer region which is comparable to the no-crosswind case. The significant feature in the majority of the samples is the large peak in the near wake of the train which is due to a combination of lower-than-

crosswind velocity and unsteadiness due to flow separation around the end of the last container.

Turbulence intensity is lowest in the near wake at  $z=4$  m as a result of the highest velocities occurring above  $z=3$  m as shown in Figure 90. The turbulence intensity is lowest in the boundary layer region at  $z=2$  m and  $z=3$  m, and higher values can be observed closer to TOR where the bogies have an effect on the flow. The peak value of turbulence intensity in the near wake of the train at  $z=2$  m is greater than 100% for  $y=1.59$  m and is thus not accommodated on the graph due to the unphysical value.

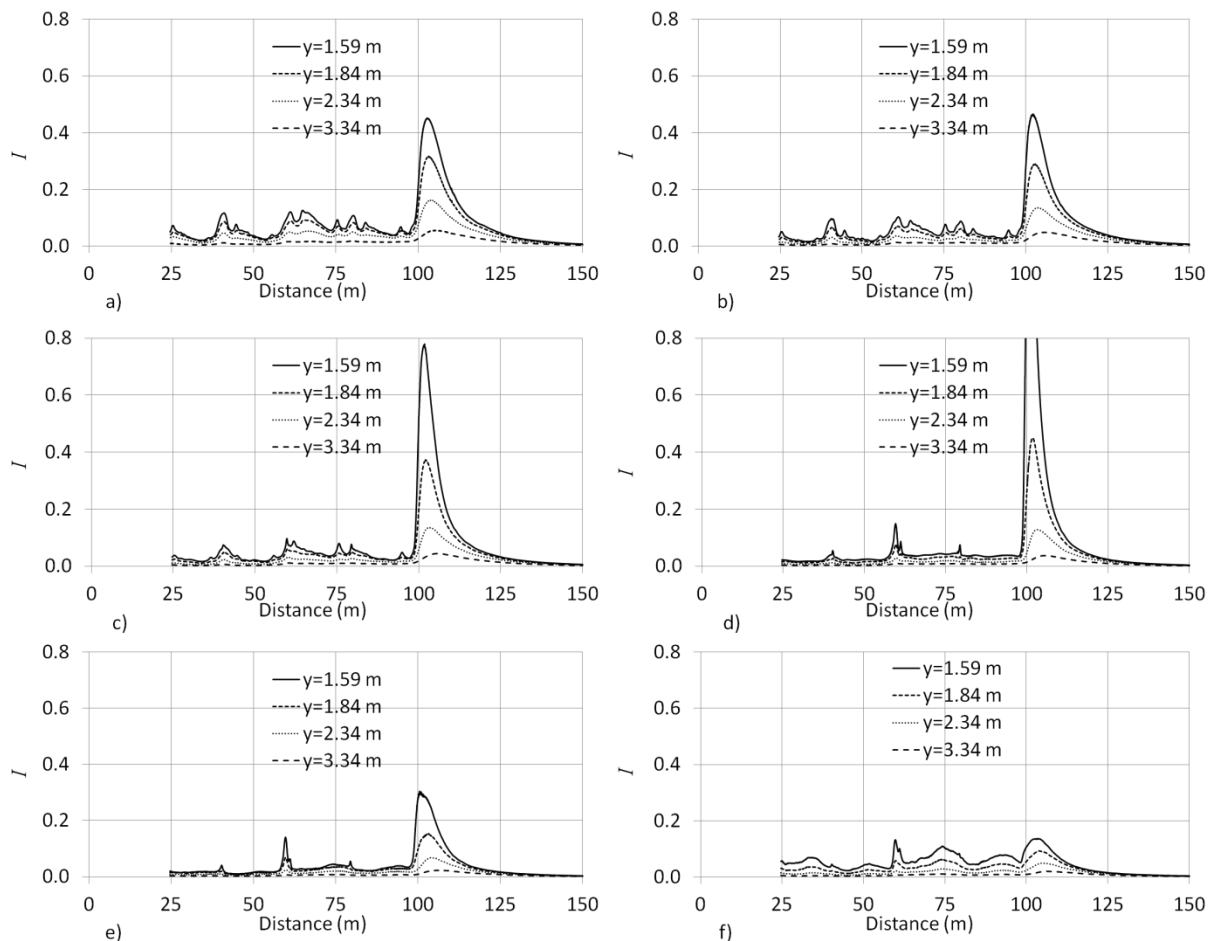


Figure 122 Turbulence intensity on the windward side of the freight train at a)  $z=0.25$  m, b)  $z=0.5$  m, c)  $z=1.0$  m, d)  $z=2.0$  m, e)  $z=3.0$  m and f)  $z=4.0$  m

The turbulence intensity on the leeward side of the train is not considered in the present work because the region contains massively-separated flow and the definition of turbulence intensity is not strictly valid for such flow regions.

#### 5.4.4 Integral length-scale

Numerical integration was performed under the autocorrelation curve of the longitudinal velocity in order to obtain integral time- and length-scales at the probe positions close to inter-wagon spacings on the leeward side of the train. The integral time- and length-scales, at static probe positions in the close to the inter-wagon spacings are shown in Table 14. The length-scales exhibit a trend of decreasing monotonically which is a result of the destruction of the flow structures along train length.

In all cases the time-scales are less than 1/3rd of the human reaction time discussed in Jordan et al. (2008) although the velocities shown in Section 5.3.3 are of sufficient magnitude to cause person instability. The integral time- and length-scales are much greater in the present chapter than they were in the no-crosswind case due to the massively separated flow on the leeward side of the train.

Table 10 Integral values at probe positions relative to train

Probe position	$x$	$y$	$z$	Time-scale (s)	Length-scale (m)
1	21	1.84	2.1	0.145	4.79
2	40	1.84	2.1	0.12	3.97
3	60	1.84	2.1	0.086	2.85
4	80	1.84	2.1	0.069	2.28

### 5.5 Concluding remarks

The current chapter presented results obtained from numerical simulations of the slipstream around the Class 66 locomotive-hauled freight train subjected to a 30° crosswind. The results

show two distinctive flow regimes on the windward and leeward sides of the train. The windward region is characterised by stagnation and, due to the steady uniform inlet, is generally quiescent. The flow on the leeward side is highly-turbulent, and is dominated by large-scale recirculation which exists for the entire train length.

The results from the 30° crosswind simulation were validated against experimental data (Soper, 2014) and good agreement was shown. The validity of the solution was further confirmed following a mesh sensitivity test and an inspection of the level of sub-grid velocity present in the solution. The results of the simulations were shown not a function of mesh density and the  $v_{sgs}$  levels were deemed to be adequately low so as not to affect the solution.

The windward velocity magnitude rapidly-decreases after the passing of the locomotive and remains low until the near-wake region where a rapid increase towards crosswind velocity occurs. On the leeward of the train, flow separation around the locomotive is responsible for velocity peaks which are in excess of train speed and are double the crosswind speed.

The locomotive experiences larger force and moment coefficients than the subsequent container wagons because it experiences the unimpeded freestream flow. The results from the present chapter show that there is a strong case for simulating locomotives in slipstream and crosswind aerodynamics experiments because the effect on subsequent wagons can be significant.

The results from the present chapter can be used to assess whether there is a risk to person stability due to amplified slipstream velocities. In order for the train used in the present work to experience a 30° resultant wind during operation (assuming an operational speed of 33 m/s), the wind speed perpendicular to the track would need to be 18 m/s. There are two points that must be considered about a wind speed that high. Firstly, the crosswind speed alone would be between the ranges of affecting ease of walking to causing difficulty of walking, for

mean steady winds (Hunt et al., 1976) . Secondly, the wind-loading on the freight train and surrounding structures could cause the line to be closed due to fallen trees or container-shedding risk, thus removing any risk of slipstream amplification effects due to the lack of trains that would be running.

A further consideration is the likelihood of an 18 m/s gust occurring. From the Weibull distribution, it is known that the greater a mean velocity is the less likely it is to occur (Weibull, 1951). It is hypothesised that a 30° is less likely to occur than a much lower crosswind, thus the next chapter considers the effect of a 10°crosswind on the slipstream of the freight train.

# Chapter 6 Freight train subjected to a 10° Crosswind

## 6.1 *Introduction*

The present chapter presents data obtained from DDESs of the slipstream of the model-scale freight train when subjected to a steady 10° crosswind. The 10° yaw angle was chosen because there are existing model-scale (Baker et al., 2001) and full-scale (Figura-Hardy, 2005) experimental data at approximately that angle. Furthermore, the 10° case is also on the border between fully-attached flow and slender body flow for high speed trains (Chiu and Squire, 1992) and will thus provide a useful comparison between freight and passenger train slipstream behaviour.

## 6.2 *Solution verification*

### 6.2.1 *Mesh sensitivity*

The comparison between the time-averaged surface pressure around the middle of each container, for the coarse and fine meshes is shown in Figure 123. The surface pressure on the windward faces of each container show very good agreement with differing only slightly between fine and coarse meshes. The pressures on the roofs generally show the worst agreement with the greatest discrepancy being 8% on container 1. Generally good agreement is observed between the  $C_p$  from the coarse and fine meshes indicating that the energy-containing motions that will affect the solution have been resolved and therefore a finer mesh is not required for the level of accuracy considered here.

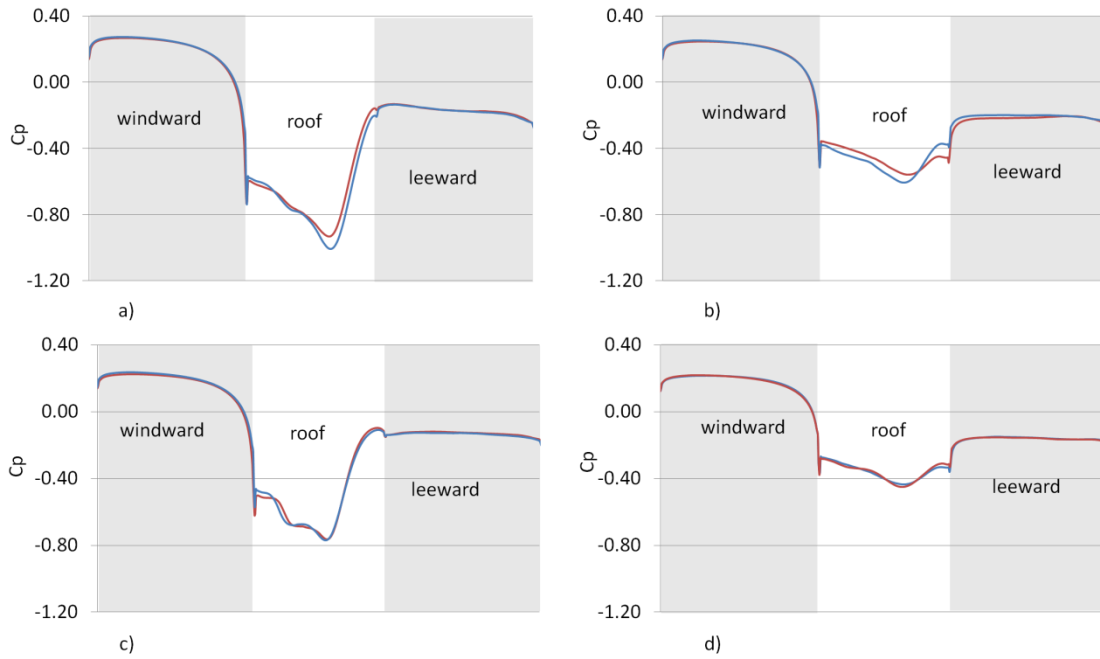


Figure 123 Pressure coefficients on each a) container 1, b) container 2, c) container 3 and d) container 4 at mid-length for fine and coarse meshes

### 6.2.2 Verification of sub-grid viscosity levels

The ratio of sub-grid to kinematic viscosity,  $\nu_{SGS}/\nu$ , along the leeward side of the train is shown in Figure 124. The values of  $\nu_{SGS}/\nu$  are greatest along the length of the locomotive due to the high strain-rates which exist there as a result of flow separation and recirculation. The mean value of  $\nu_{SGS}/\nu$  should theoretically be higher in all regions for the coarse mesh although the  $\nu_{SGS}/\nu$  shown in Figure 124 are instantaneous and are thus dependent on the strain-rate at a specific instance in time. Overall, the peak values of approximately  $\nu_{SGS}/\nu=70$  for the first 15 m of the slipstream and decays significantly thereafter, with peak values of  $\nu_{SGS}/\nu=15$  in the boundary layer region. From the present examination it is determined that the solution should not be greatly affected by the  $\nu_{SGS}/\nu$  levels.

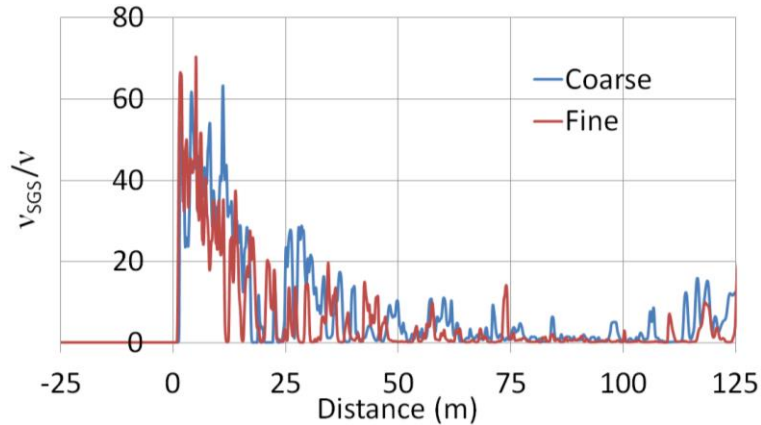


Figure 124 Ratio of sub-grid to kinematic viscosity on the leeward side of the train at  $y=2.35$  m and  $z=2$  m

### 6.3 Time-averaged flow

#### 6.3.1 Velocity magnitude on the windward side of the train

Figure 125 shows the velocity magnitude on the windward side of the train relative to a static observer. Ahead of the train ( $x < 0$  m) the crosswind of approximately 6 m/s can be seen which would be what a static observer would experience. Velocity peaks occur in the nose region at  $y=1.59$  m and  $y=1.84$  m for all heights above TOR as a result of flow separating around the windward corner of the locomotive. The peak velocity at in the nose region is  $U=1.05$  and occurs at  $y=1.59$  m and  $z=1$  m. In the boundary layer region the highest velocity magnitude is  $U=0.4$  and occurs at  $x=22$  m for  $y=1.59$  m and  $z=1$  m. This peak on the windward side of the train is a consequence of the flow separating around the windward corner of the first container. Velocity magnitude at  $y=3.34$  m and at all heights above TOR exhibits a gradual decrease in the boundary layer region with no transients occurring.

At  $z=4$  m the velocities are highest in the latter half of the boundary layer region than at any other height above TOR as a result of flow separation around the roofs of the containers causing the flow to accelerate. The magnitude of the wake transient decreases with distance above TOR and is observed to be negligible at  $z=4$  m.

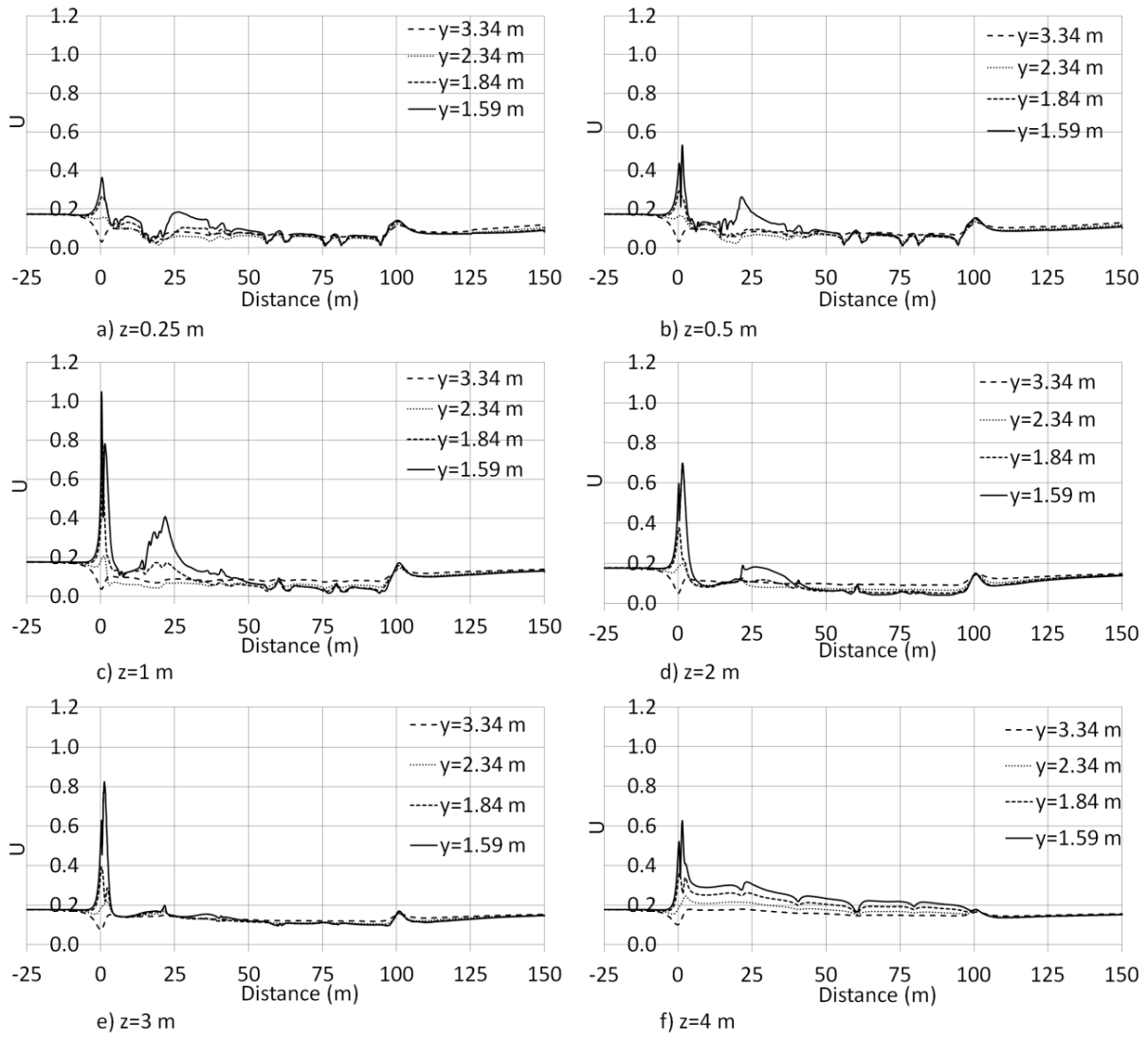


Figure 125 Normalised velocity magnitude relative to a static observer at a)  $z=0.25$  m, b)  $z=0.5$  m, c)  $z=1.0$  m, d)  $z=2.0$  m, e)  $z=3.0$  m and f)  $z=4.0$  m

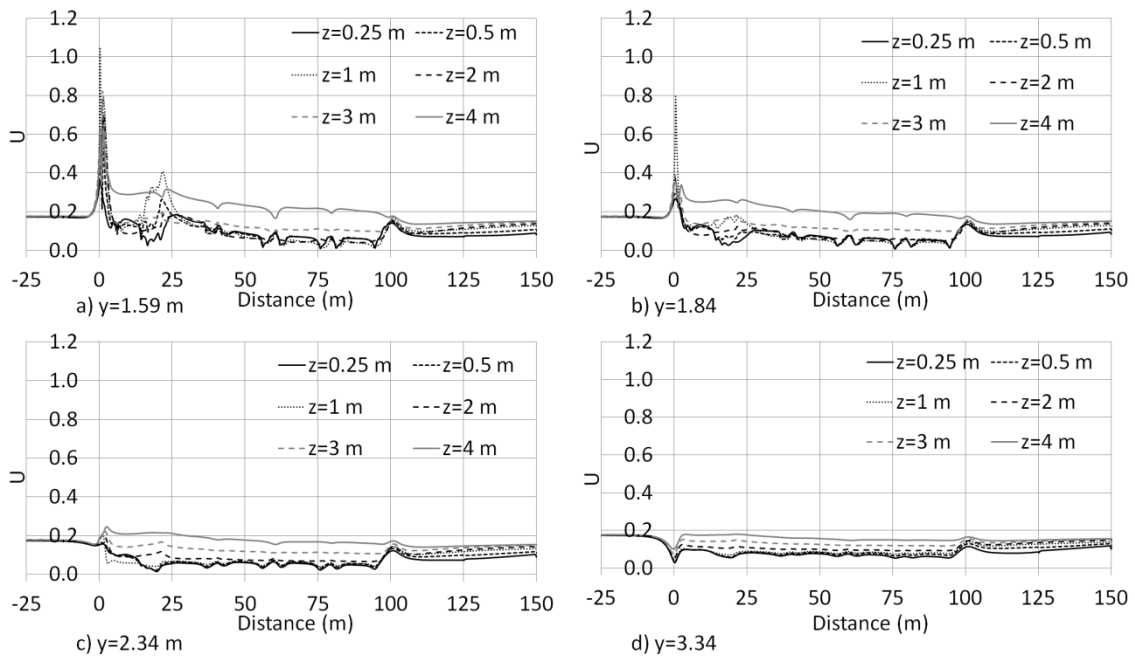


Figure 126 Normalised velocity magnitude relative to a static observer varying with height at a)  $y=1.59$  m, b)  $y=1.84$  m, c)  $y=2.34$  m and d)  $y=3.34$  m

Figure 126 shows the data from Figure 125 re-plotted with respect to height. The data show that the greatest nose peaks occur  $z=1$  m above TOR and that the highest  $U$  after  $x=25$  m are always at  $z=4$  m as a result of the additional vertical component due to the flow separating around the roofs of the containers.

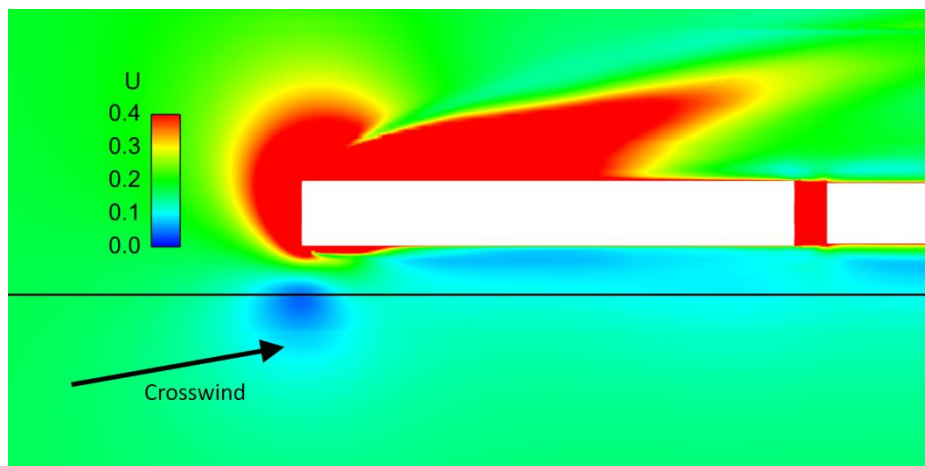


Figure 127 Colour plot of normalised velocity magnitude around the train at  $z=2$  m. The black line represents the  $y=3.34$  m sampling location

Figure 127 shows velocity magnitude on a plane at  $z=2$  m. On the windward side of the train a low velocity region is observed at  $x \approx 0$  m. This observation is congruent with the velocities in Figure 125d at  $y=3.34$  m and the phenomenon is a result of flow acceleration towards the rear of the train thus appearing as a low velocity to a static observer.

### 6.3.2 Velocity magnitude on the leeward side of the train

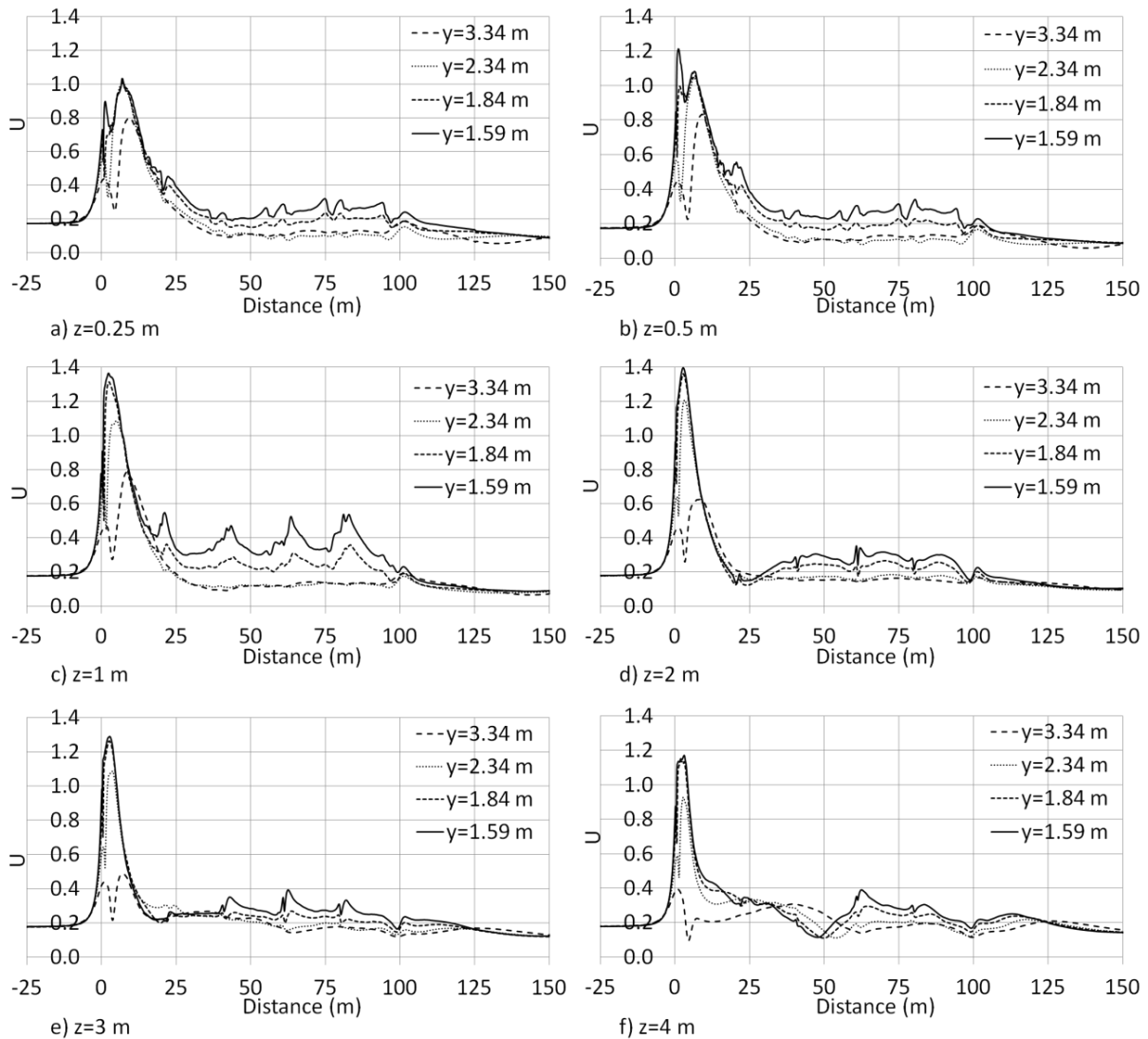


Figure 128 Normalised velocity magnitude relative to a static observer at a)  $z=0.25$  m, b)  $z=0.5$  m, c)  $z=1.0$  m, d)  $z=2.0$  m, e)  $z=3.0$  m and f)  $z=4.0$  m

Figure 128 shows the velocity magnitude on the leeward side of the train. The flow on the leeward side of the train is characterised by a velocity peak in the nose region, followed by a

decrease in the boundary layer region which is then punctuated by transients at inter-wagon spacings. The peak velocity magnitude occurs at  $y=1.59$  m and  $z=2$  m and has a value of  $U=1.4$  which is over 7 times greater than the crosswind value. The peak velocity for  $y=1.84$  m is approximately 5% lower than the peak value at  $y=1.59$  m, suggesting that even a low yaw angle crosswind can not only increase velocity samples on the leeward side, but also increase the distance it occurs from COT in comparison to the no-crosswind case

Velocity in the boundary layer region reaches maximum values of  $U=0.55$  and the greatest transients occur as a result of inter-wagon spacings at  $z=1$  m. The velocity in the boundary layer region at  $z=2$  m exhibits rapid growth along the first and second container wagons whereas at other heights above TOR the boundary layer region stabilises immediately after the nose peak.

At  $z=0.25$  m and  $z=0.5$  m, two peaks are observed between  $x=0$  m and  $x=15$  m. At  $z=0.25$  m the first peak is lowest whereas at  $z=0.5$  m the second peak is lowest. Figure 129 shows the velocity magnitude on planes at  $z=0.25$  m and  $z=0.5$  m. The exact locations of the first and second peaks are not discernible from the colour plots although the origins of the peaks are visible. The limits of the colour plots are taken from the approximate peak values at each height.

The slipstream amplification and distances from train side at which they occur have inherent implications for person safety but also with codification. It was shown in Chapter 4 that slipstream velocities become very low at 2 m from train side and are of little risk to a person's safety considering results from person stability in wind gust studies (Hunt et al., 1976, Jordan, 2008, Penwarden et al., 1978).

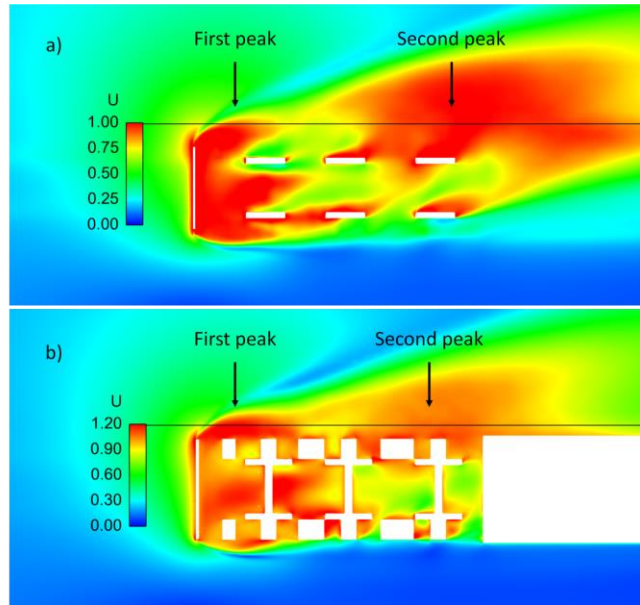


Figure 129 Colour plots of normalised velocity magnitude at a)  $z=0.25$  m and b)  $z=0.5$  m.  
The black line is  $y=1.59$  m from COT

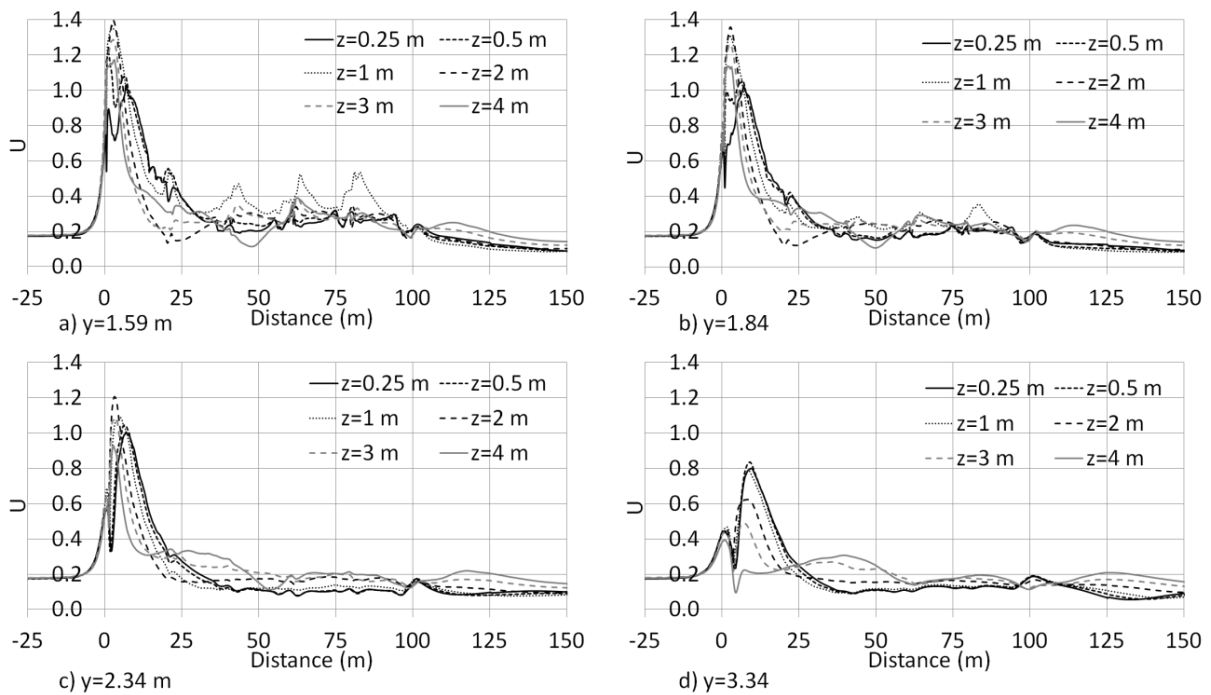


Figure 130 Normalised velocity magnitude relative to a static observer varying with height at  
a)  $y=1.59$  m, b)  $y=1.84$  m, c)  $y=2.34$  m and d)  $y=3.34$  m

Figure 130 shows the data from Figure 128 plotted with respect to height. In comparison to the windward samples, the leeward data show a greater variability with height and distance

from COT. The peak velocities for all heights above TOR occur at  $z=2$  m. At  $y=1.59$  m the velocity magnitude at  $z=1$  m has the greatest peaks in the boundary layer region with values of  $U=0.47$ ,  $U=0.52$  and  $U=0.54$ , at  $x=43$  m,  $x=64$  m and  $x=81$  m, respectively. At further distances from train side the variation in velocity with respect to height decreases from peak boundary layer region values of 0.55 at  $z=1$  m to 0.4 at  $z=4$  m for  $y=1.59$  m.

### 6.3.3 Velocity components on the windward side of the train

In this section the velocity components on the windward side of the train are considered at each distance from COT and TOR.

**$z=0.25$  m**

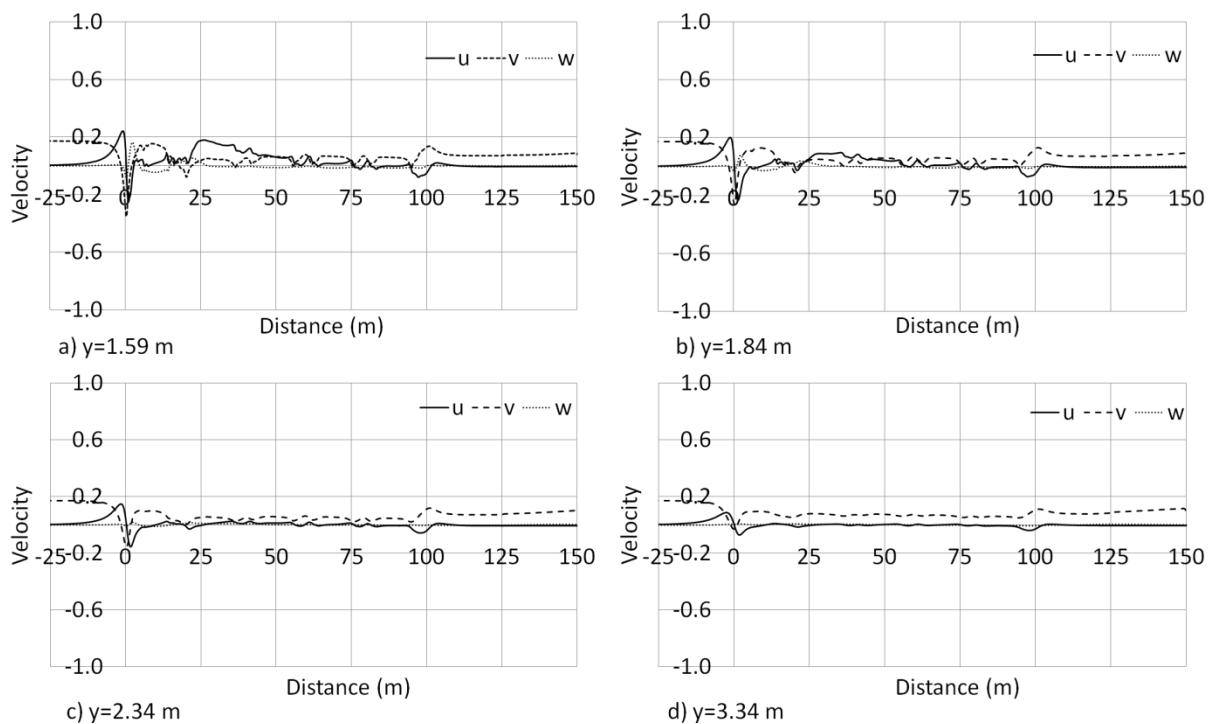


Figure 131 Normalised velocity components at a)  $y=1.59$  m, b)  $y=1.84$  m, c)  $y=2.34$  m and d)  $y=3.34$  m

Figure 131 shows the normalised velocity components at  $z=0.25$  m for four distances from COT. The maximum positive and negative longitudinal velocities are  $u=0.24$  and  $u=-0.24$ , and occur at  $x=-1$  m and  $x=1$  m, respectively. The spacing between the locomotive and the

first container wagon causes a disturbance in the longitudinal velocity at  $x=21$  m which results in a peak at  $x=25$  m which is approximately 75% of the nose peak. The lateral velocity reaches a peak value of  $v=-0.3$  at  $y=1.59$  m and remains lower than the crosswind value for all other distances from COT. The vertical component is negligible apart from  $y=1.59$  m where a peak of  $w=0.16$  is reached at  $x=0$  m. The lateral velocity transients at inter-wagon spacings occur before the longitudinal transients.

**$z=0.5$  m**

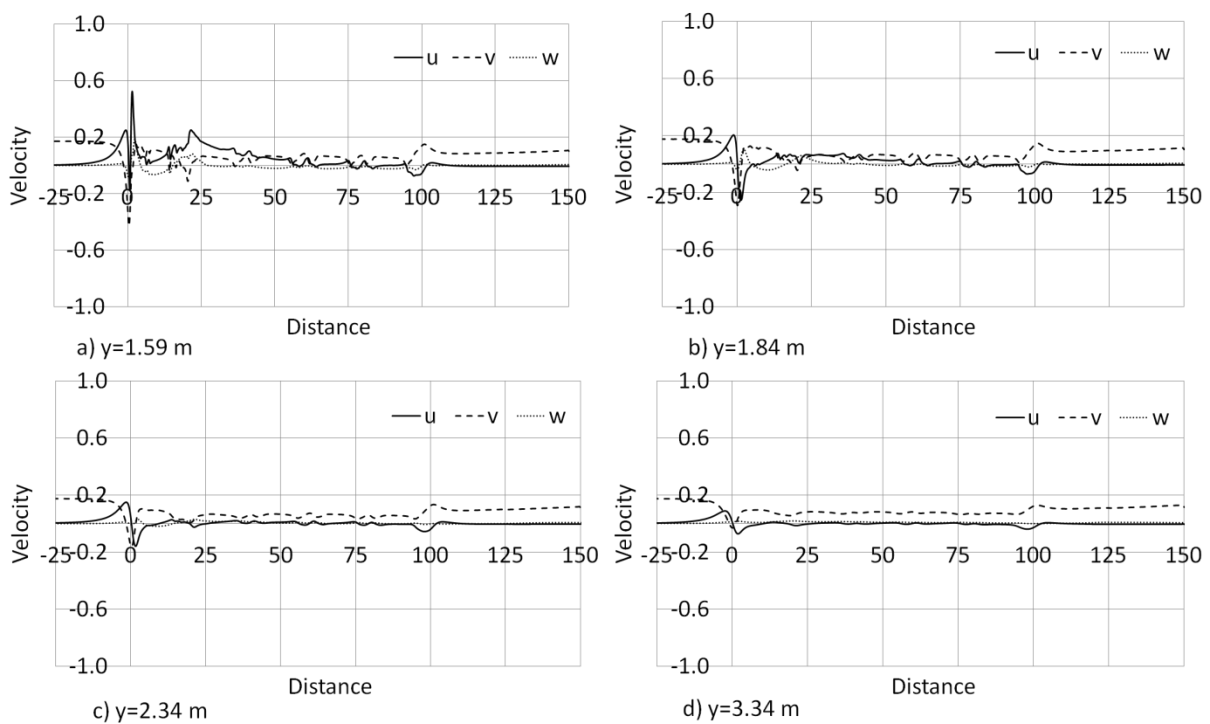


Figure 132 Normalised velocity components at a)  $y=1.59$  m, b)  $y=1.84$  m, c)  $y=2.34$  m and d)  $y=3.34$  m

The longitudinal velocity at  $y=1.59$  m reaches a peak value of  $u=0.52$  at  $x=1$  m, where a second positive velocity peak occurs (Figure 132). The lateral velocity reaches a peak of  $v=-0.43$  from the crosswind value of  $v=0.17$ . In the near wake, the lateral velocity has a minor positive peak which is a result of the flow separating around the fourth container wagon and is visible for all distances from COT. For all positions from COT the vertical velocity remains negligible relative to the longitudinal and lateral components.

**z=1 m**

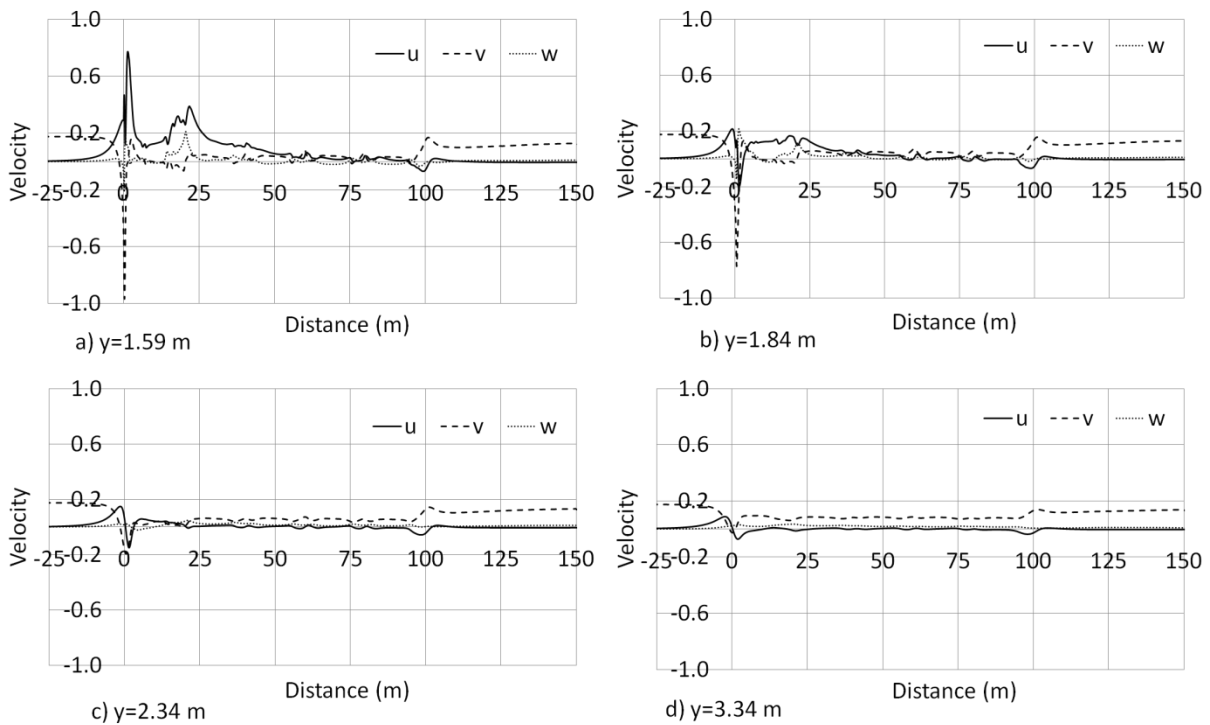


Figure 133 Normalised velocity components at a)  $y=1.59$  m, b)  $y=1.84$  m, c)  $y=2.34$  m and d)  $y=3.34$  m

The peak longitudinal velocity is 0.75 and occurs at  $y=1.59$  m (Figure 133). The greatest overall peak component is lateral velocity is  $v=-0.97$  and also occurs at  $y=1.59$  m. At  $y=1.84$  m the peak longitudinal velocity is less than 33% of the peak value observed at  $y=1.59$  m. The spacing between the locomotive and first container wagon produces longitudinal and vertical velocities at  $y=1.59$  m of  $u=0.375$  and  $w=0.165$ , respectively. In the nose region at  $y=1.59$  m the longitudinal and vertical peak velocities are comparable with values of  $u=0.22$  and  $w=0.21$ , respectively.

**z=2 m**

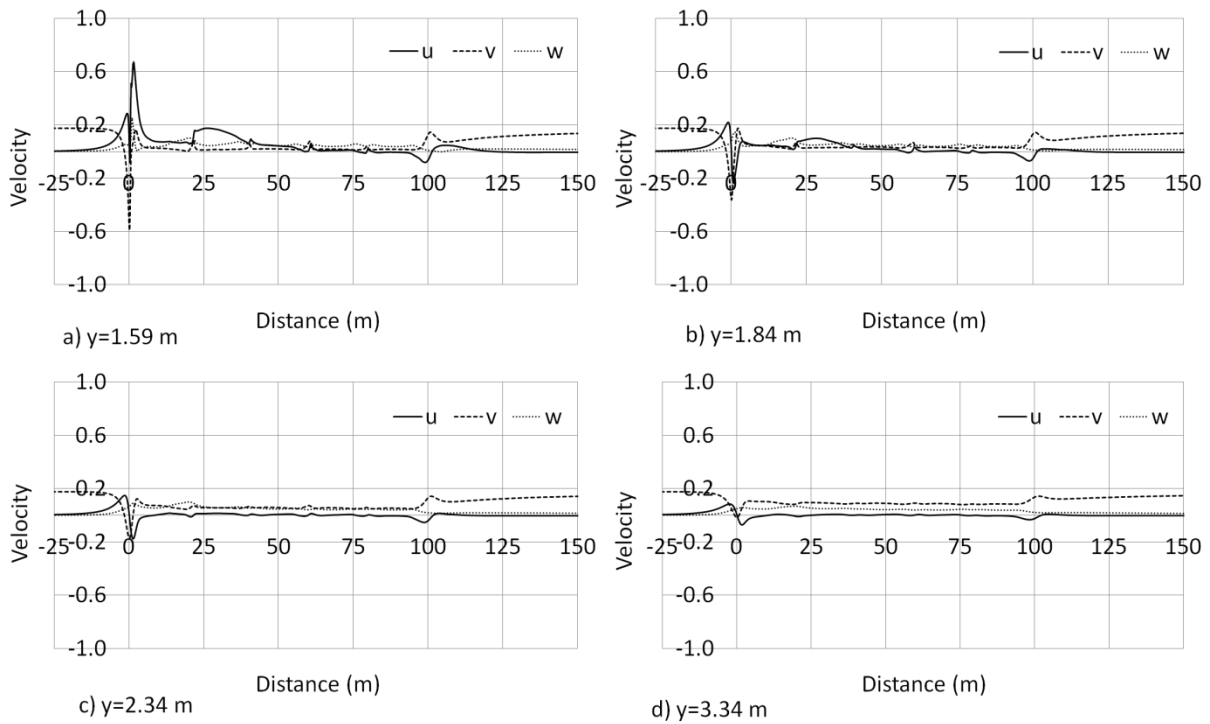


Figure 134 Normalised velocity components at a)  $y=1.59$  m, b)  $y=1.84$  m, c)  $y=2.34$  m and d)  $y=3.34$  m

At  $z=2$  m the peak longitudinal and lateral velocities in the nose region are  $u=0.68$  and  $v=-0.57$ , respectively at  $y=1.59$  m (Figure 134). Between  $x=22$  m and  $x=40$  m a rapid increase in longitudinal velocity is observed which is followed by a gradual decline along the first container. Figure 135 shows the higher velocity around the windward corner of the first container which is a consequence of the spacing between the container and the locomotive, but also due to the difference in width.

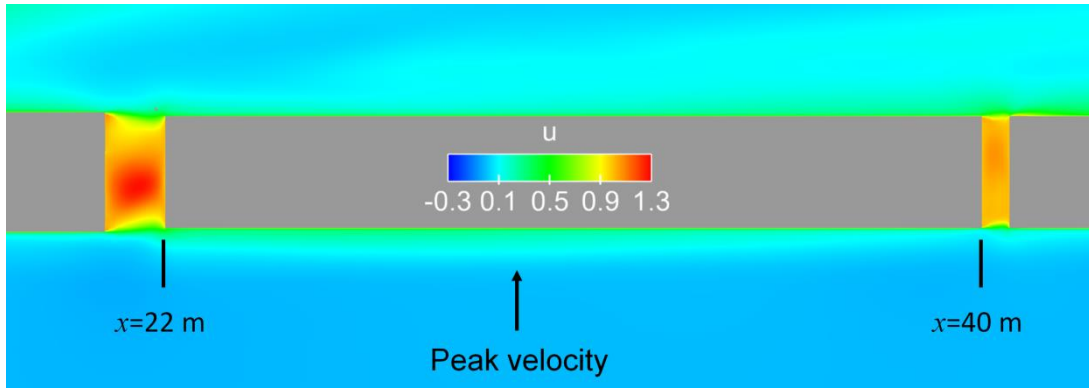


Figure 135 Colour plot of longitudinal velocity component around first container wagon on a plane at  $z=2$  m

**$z=3$  m**

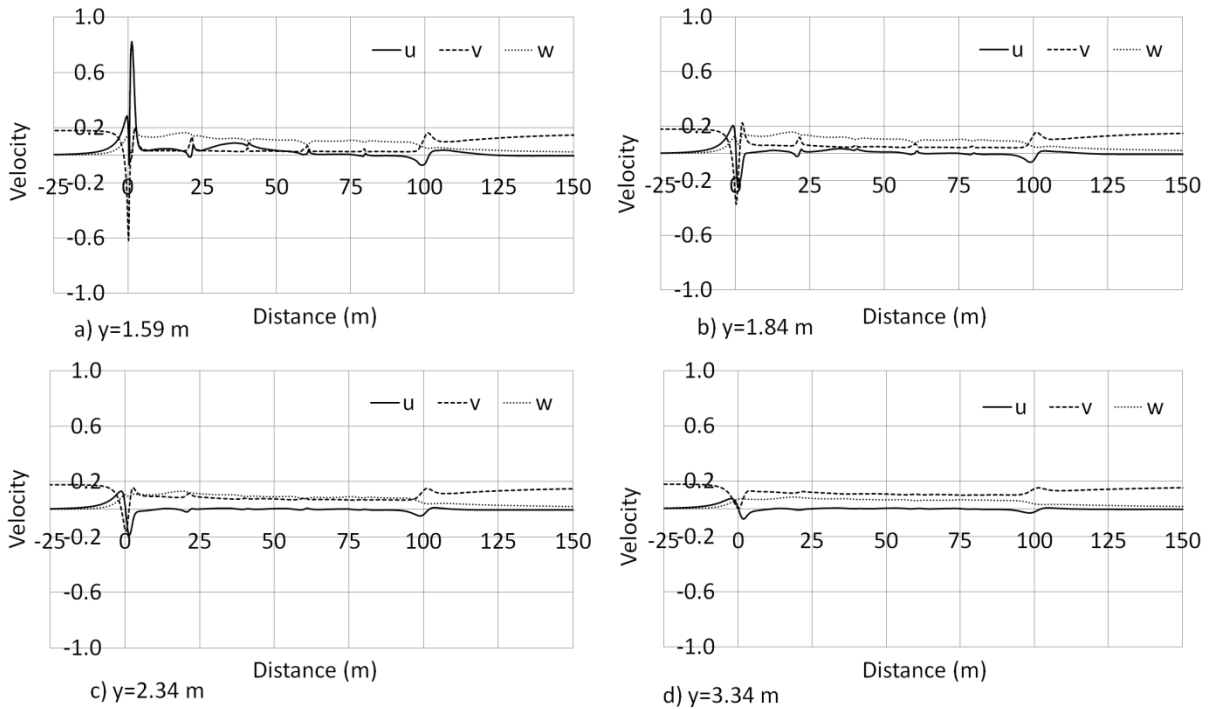


Figure 136 Normalised velocity components at a)  $y=1.59$  m, b)  $y=1.84$  m, c)  $y=2.34$  m and d)  $y=3.34$  m

Similarly to lower heights above TOR, at  $z=3$  m the longitudinal and lateral velocity components reach peak values in the nose region of  $u=0.82$  and  $v=0.62$ , respectively (Figure 136). The influence of the inter-wagon spacings on the velocity components are negligible at  $y=3.34$  m and  $y=2.34$  m. At  $y=1.59$  m and  $y=1.84$  m the vertical velocity component

becomes significant in the boundary layer region with wind speeds either matching or exceeding crosswind values. This observation is a result of flow separation over the roof of the containers causing a low-pressure region and thus entrainment which increases the magnitude of the vertical component.

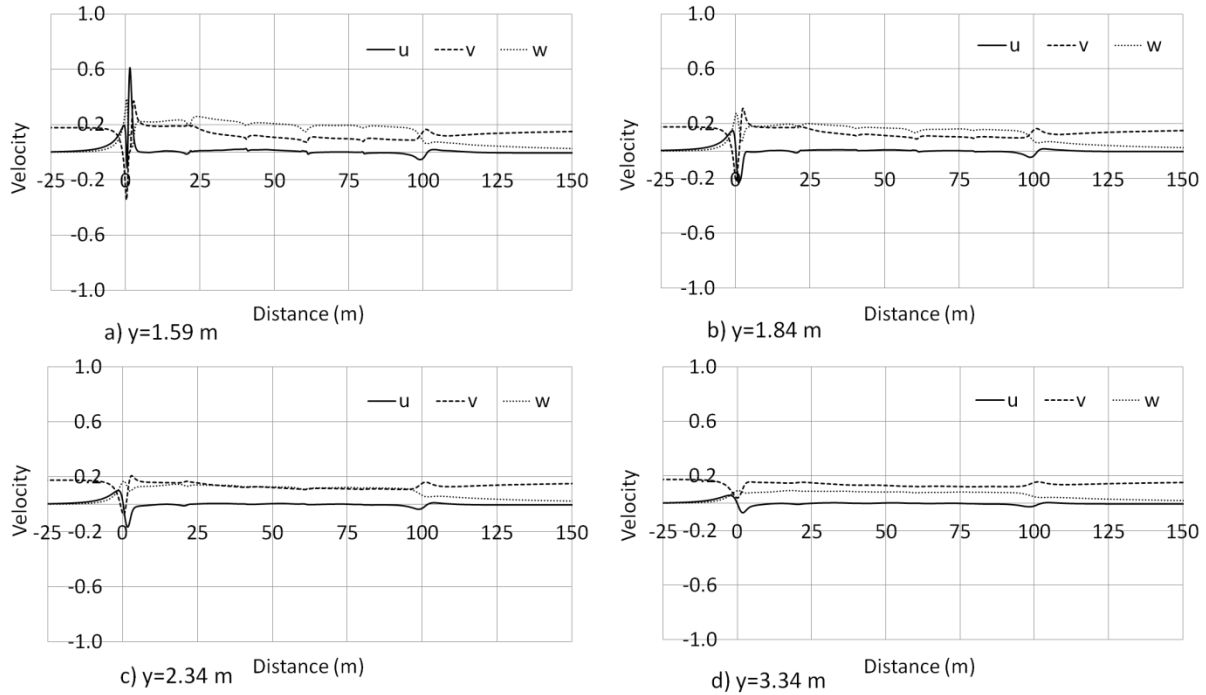


Figure 137 Normalised velocity components at a)  $y=1.59$  m, b)  $y=1.84$  m, c)  $y=2.34$  m and d)  $y=3.34$  m

The longitudinal, lateral and vertical velocity peaks which occur at  $x \approx 0$  m are  $u=0.6$  and  $v=-0.32$ ,  $w=0.36$ , respectively: this is the greatest vertical velocity component along train length (Figure 137). In the boundary layer region the lateral and vertical components are dominant whereas the longitudinal component is approximately  $u=0$  and only changes from this value in the near wake.

### Windward component summary

At  $z=3$  m &  $z=4$  m the vertical velocity component becomes dominant close to the train. Longitudinal and lateral velocity peaks are greatest at  $z=3$  m and the greatest vertical velocity

peak occurs at  $z=4$  m. The effect of inter-wagon spacings on velocity components is negligible at furthest measurement position from the train.

### 6.3.4 Velocity components - leeward

$z=0.25$  m

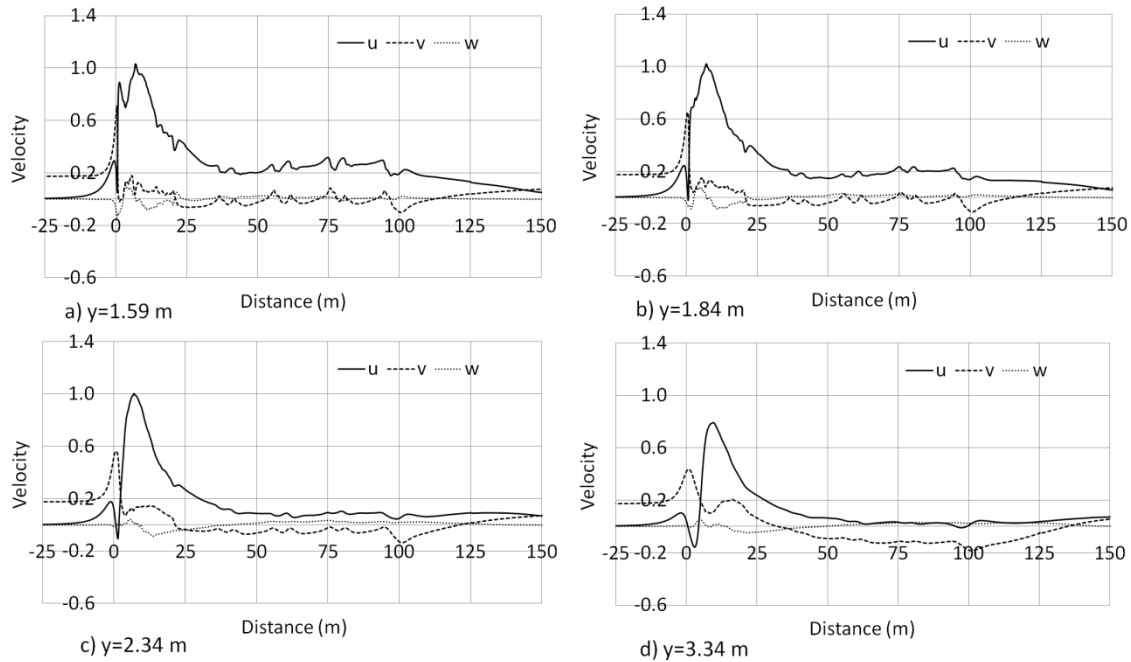


Figure 138 Normalised velocity components at a)  $y=1.59$  m, b)  $y=1.84$  m, c)  $y=2.34$  m and d)  $y=3.34$  m

The velocity components on the leeward side of the train at  $z=0.25$  m are shown in Figure 138. The peak longitudinal velocities for  $y=1.59$ ,  $1.84$  and  $2.34$  m are all within 5% of train speed. The longitudinal velocity shows the influence of the air dam on the flow at  $x=0$  m at  $y=1.59$  m, as was observed at  $30^\circ$  which comes in the form of the initial velocity peak. The lateral velocity is negative, and hence towards the train, for the majority of the train length as a result of the low-pressure region forming under the train. The influence of the inter-wagon spacings on the velocity components is evident for the  $y=1.59$ ,  $1.84$  and  $2.34$  m. In the near wake minor transients are observed which have similar magnitude to those on the windward side of the train.

**z= 0.5 m**

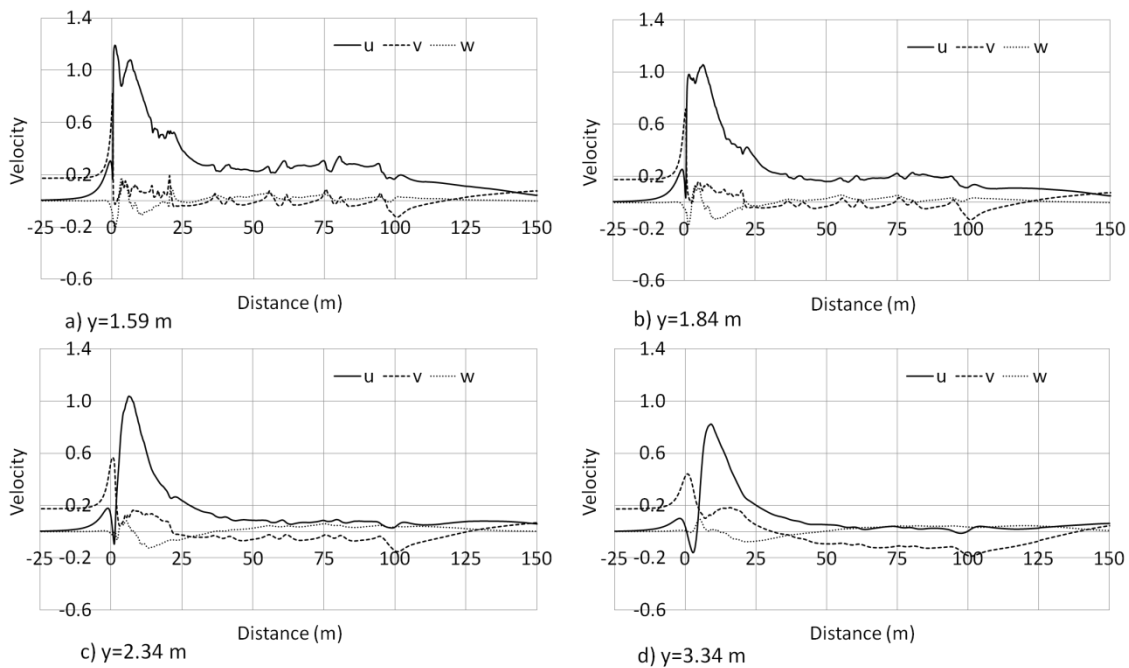


Figure 139 Normalised velocity components at a)  $y=1.59$  m, b)  $y=1.84$  m, c)  $y=2.34$  m and d)  $y=3.34$  m

Figure 139 shows the velocity components along train length at  $z=0.5$  m. The longitudinal velocity exhibits a double-peak behaviour at  $y=1.59$  m. The greatest value occurs at the first of the two peaks rather than the second as was observed at  $z=0.25$  m (Figure 138). At  $y=3.34$  m the longitudinal velocity is  $u=0.83$ , this is the greatest value for that distance from train side for all heights above TOR. Approximately half-way along the locomotive ( $x=12$  m) the vertical velocity tends towards the ground for all distances from COT as a result of the recirculation on the leeward side as is shown in Figure 140.

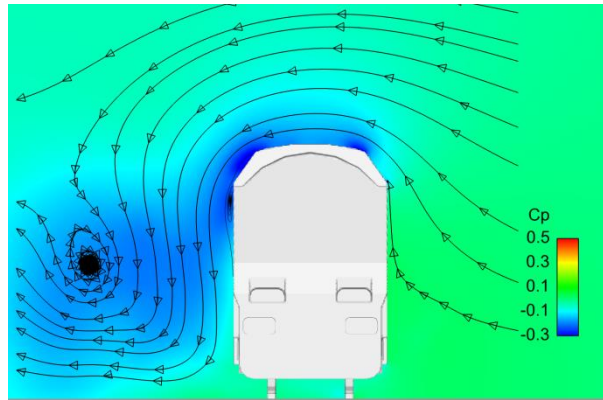


Figure 140 Mean velocity streamlines projected onto a colour plot of pressure coefficient,  $C_p$ , at  $x=12$  m

**$z=1$  m**

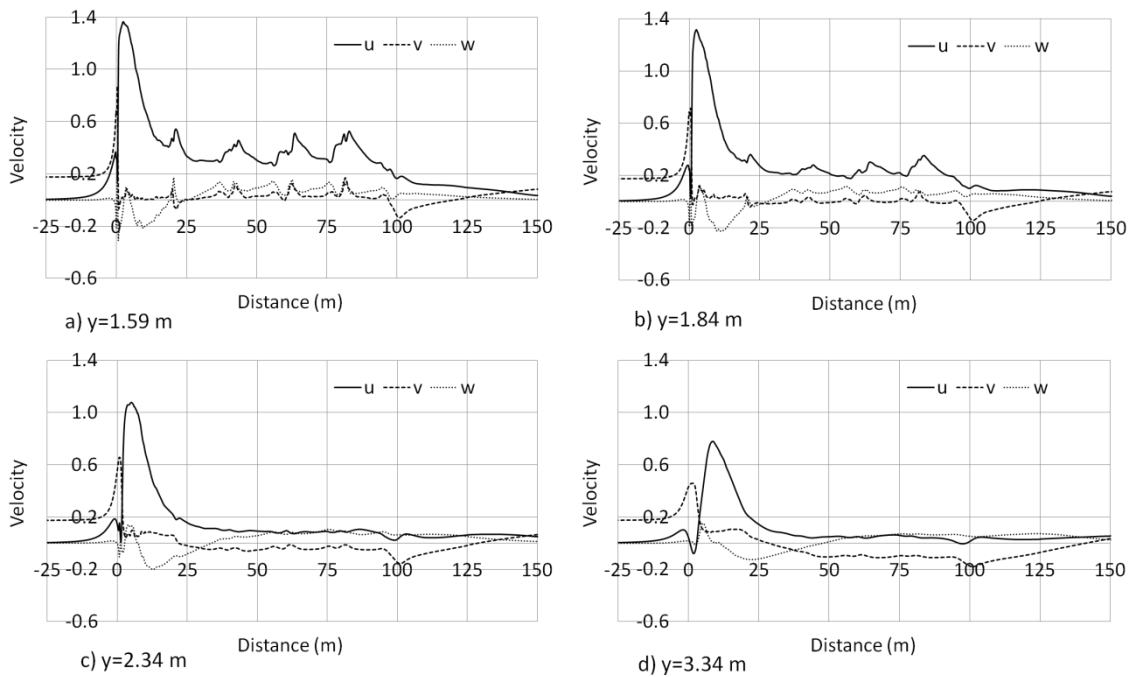


Figure 141 Normalised velocity components at a)  $y=1.59$  m, b)  $y=1.84$  m, c)  $y=2.34$  m and d)  $y=3.34$  m

Figure 141 shows the velocity components along train length at  $z=1$  m. The peak longitudinal velocity in the nose region at  $y=1.59$  m is  $u=1.36$ . For  $y=1.59$  m and  $y=1.84$  m, the longitudinal velocity component is greatest along train length, followed by the lateral and then the vertical component. The longitudinal velocity remains the greatest component at

$y=2.34$  m and  $y=3.34$  m until  $x\approx 60$  m where the vertical component becomes approximately equal to the longitudinal component. The lateral velocity reaches a maximum value of four times greater than the crosswind velocity. Vertical velocity tends towards the ground at  $x\approx 0$  m and along the locomotive where a peak value of  $w=0.31$  at  $x=1$  m and  $y=1.59$  m.

**$z=2$  m**

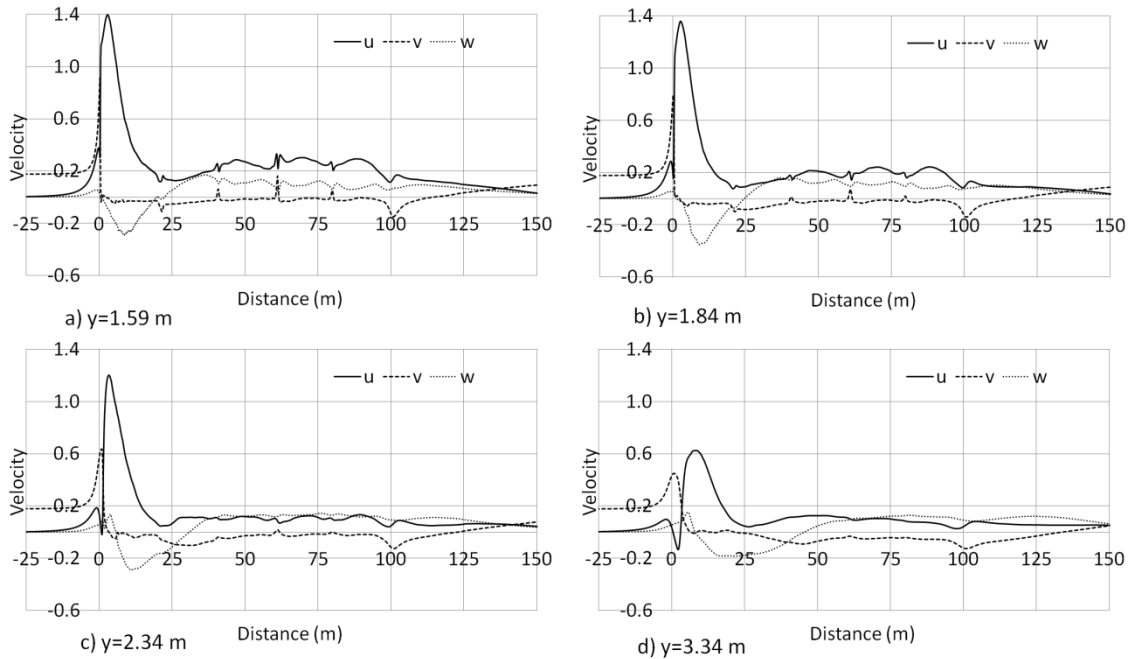


Figure 142 Normalised velocity components at a)  $y=1.59$  m, b)  $y=1.84$  m, c)  $y=2.34$  m and d)  $y=3.34$  m

Figure 142 shows the velocity components along train length at  $z=2$  m. The peak longitudinal velocity is  $u=1.4$  and occurs  $x=3$  m and  $y=1.59$  m. The longitudinal velocity shows a gradual increase along train length for  $y=1.59$  m and  $y=1.84$  m whereas at  $y=2.34$  m and  $y=3.34$  m stabilisation or a gradual decrease is observed. The peak lateral velocity at  $x=0$  m and  $y=1.59$  m is  $v=0.91$ . Although the lateral velocity has such a large peak in the nose region the component is lower than the vertical and longitudinal velocities for the majority of train length except at  $y=3.34$  m. Between the locomotive and the first container wagon the lateral

velocity undergoes a change of being towards the train and then away from the train, respectively.

**z= 3 m**

Figure 143 shows the velocity components along train length at z=3 m. The lateral component is negligible in the boundary layer region for all distances from COT. The lateral component is greater than at z=3 m than it is at z=2 m, for y=1.59 m and y=1.84 m. The peak longitudinal velocity is 8% lower than at z=2 m and reaches a maximum value of u=1.29. A similar decrease is observed for the longitudinal velocity at y=1.84 m. At y=3.34 m, the longitudinal velocity exceeds the crosswind velocity for the first time at that distance from COT. The vertical velocity reaches a peak value of w=-0.46 at y=1.84 m and the remains negative at y=3.34 m for 38 m.

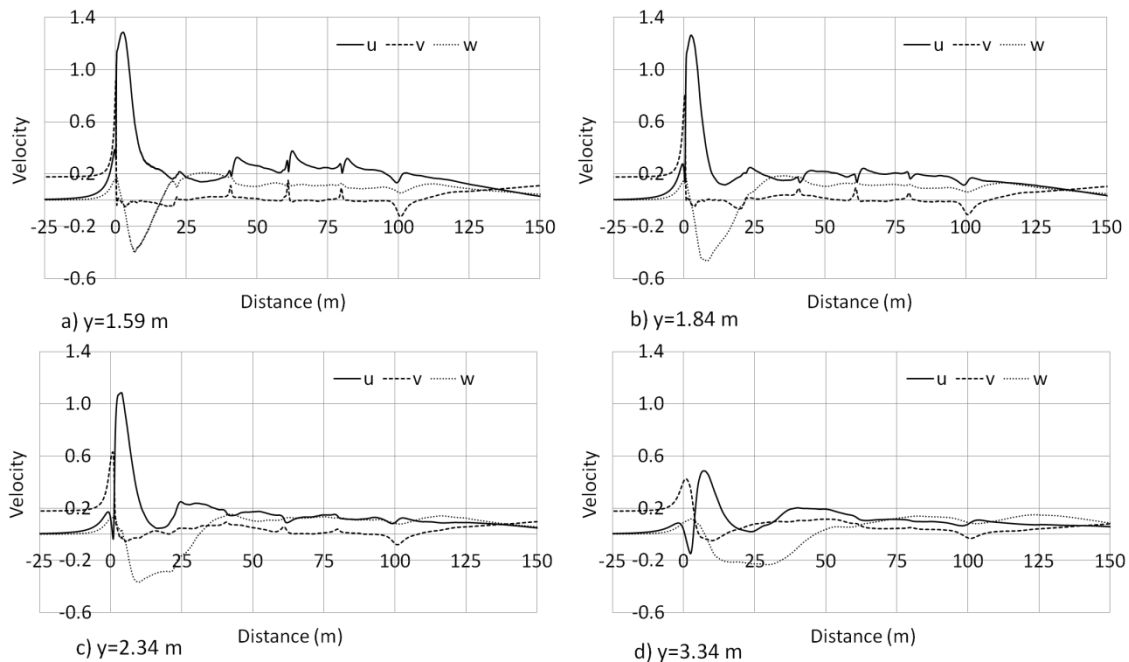


Figure 143 Normalised velocity components at a) y=1.59 m, b) y=1.84 m, c) y=2.34 m and d) y=3.34 m

**z= 4 m**

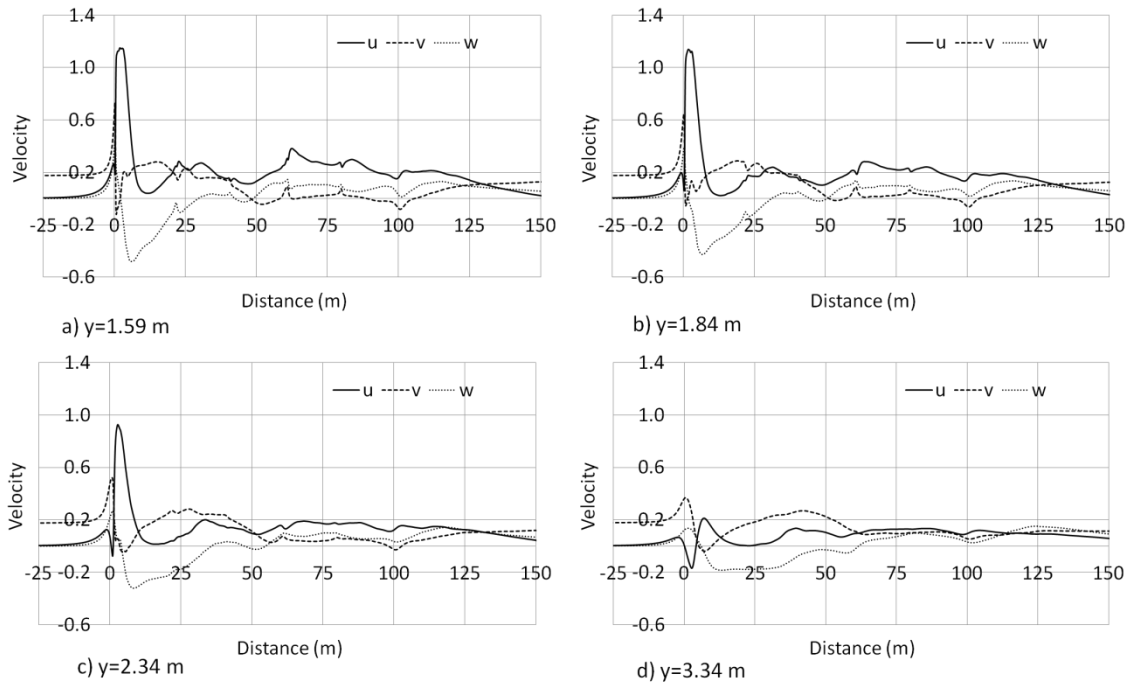


Figure 144 Normalised velocity components at a)  $y=1.59$  m, b)  $y=1.84$  m, c)  $y=2.34$  m and d)  $y=3.34$  m

Figure 144 shows the velocity components along train length at  $z=4$  m. The peak values of longitudinal velocity at  $y=1.59$  m and  $y=1.84$  m are  $u=1.15$  and  $u=1.14$ , respectively. The peak vertical velocity occurs along the locomotive at  $y=1.59$  m with a value of  $w=0.48$ . The longitudinal, lateral and vertical velocities converge to similar values at  $y=3.34$  m after  $x=70$  m.

### Leeward component summary

Greater longitudinal velocity components were observed on the leeward side of the train than on the windward side. Vertical velocities were negative along the locomotive for the majority of heights above TOR which then became positive further along train length.

### 6.3.5 Pressure on the windward side of the train

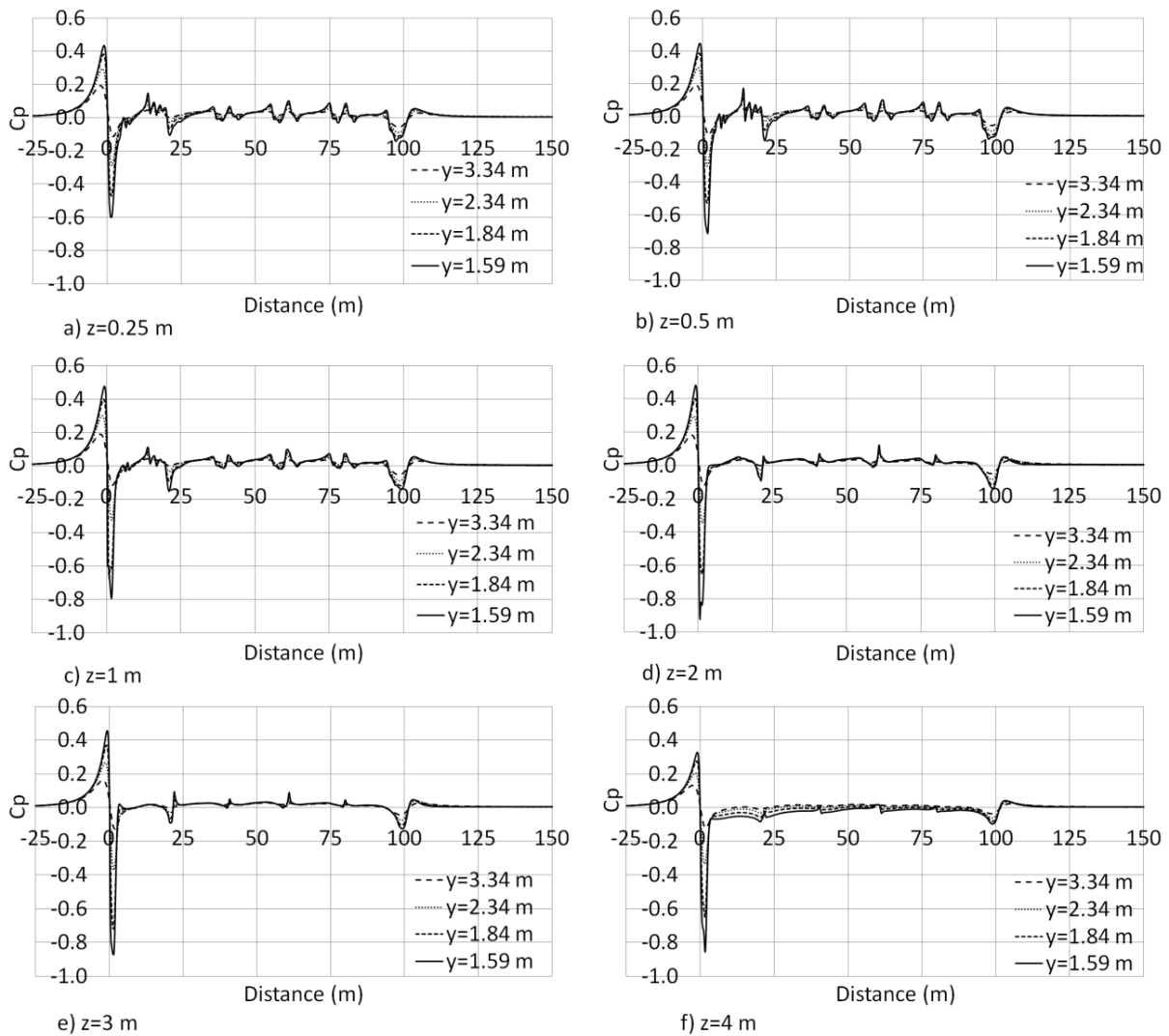


Figure 145 Pressure coefficients relative to a static observer at a)  $z=0.25$  m, b)  $z=0.5$  m, c)  $z=1.0$  m, d)  $z=2.0$  m, e)  $z=3.0$  m and f)  $z=4.0$  m

Figure 145 shows  $C_p$  on the windward side of the train. The general trend in  $C_p$  is a positive-negative pressure pulse at  $x \approx 0$  m followed by transients along train length that are at most 10% of the nose transient magnitude. In the near wake a negative-positive pressure pulse is observed for all heights above TOR. The maximum peak-to-peak pressure pulse is  $\Delta C_p = 1.41$  and occurs at  $y = 1.59$  m and  $z = 2$  m. The pressure signals between  $z = 0.25$  m and  $z = 1$  m appear jagged and reflect the relatively rough geometry of the bogies. In contrast, for  $z \geq 2$  m, the  $C_p$  signals are smoother than those at  $z \leq 1$  m as a result of the relatively smooth geometry of the

container sides. At  $x=21$  m the influence of the spacing between the locomotive and the first container wagon is observed at  $y=1.59$  m as a negative peak.

At  $y=1.59$  m for  $z=2$  m and  $z=4$  m the negative pressure pulse is not rounded as can be seen for all other distances from train side. This shape is a result of the complex flow topology in close proximity to the Class 66 locomotive when subjected to a crosswind.

The magnitude of the nose region pressure transient decreases with distance from train side.

At  $z=2$  m the nose transient magnitude is seen to be  $\Delta C_p=1.41$  for  $y=1.59$  m although this value decreases to  $\Delta C_p=0.3$  at  $y=3.34$  m.

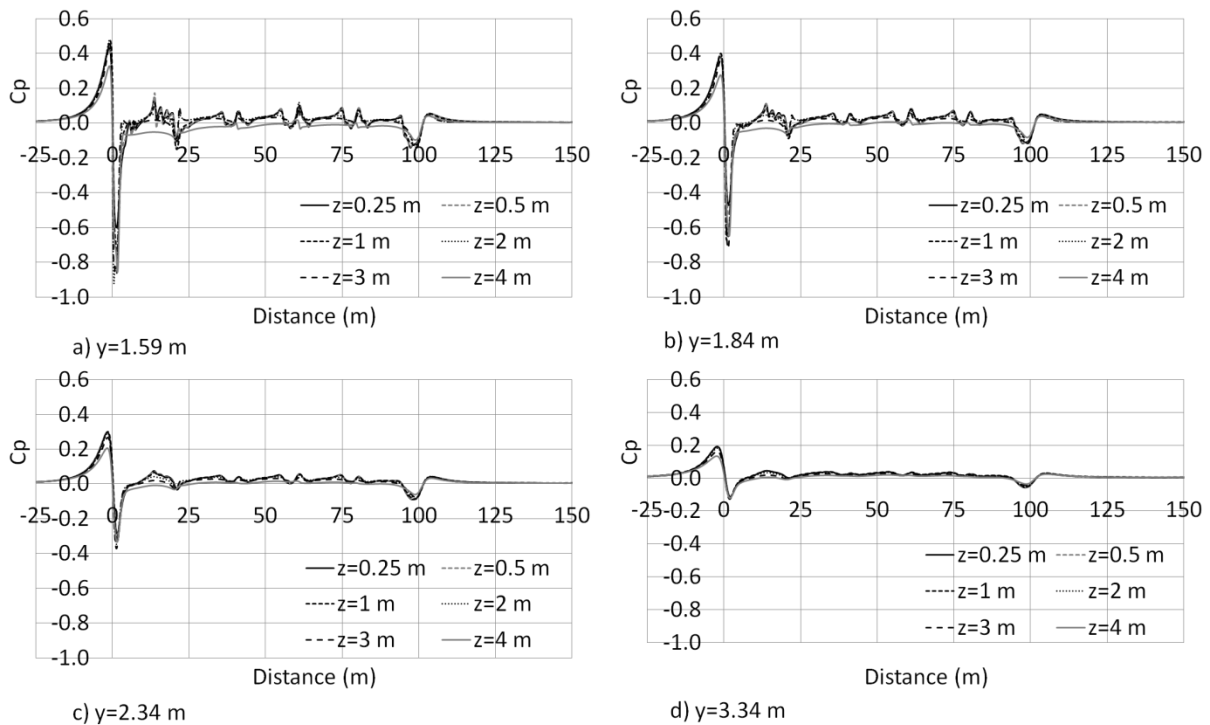


Figure 146 Pressure coefficients relative to a static observer varying with height at a)  $y=1.59$  m, b)  $y=1.84$  m, c)  $y=2.34$  m and d)  $y=3.34$  m

Figure 146 shows the data from Figure 145 plotted for each lateral position with respect to height. It can be seen that  $C_p$  in the boundary layer region is positive for most of the train length after the locomotive due to flow stagnating on the container sides. At  $z=4$  m the  $C_p$  are

mostly negative as a result of the flow separation occurring around the roofs of the containers although this effect is minimal in comparison to the 30° crosswind case.

### 6.3.6 Pressure on the leeward side of the train

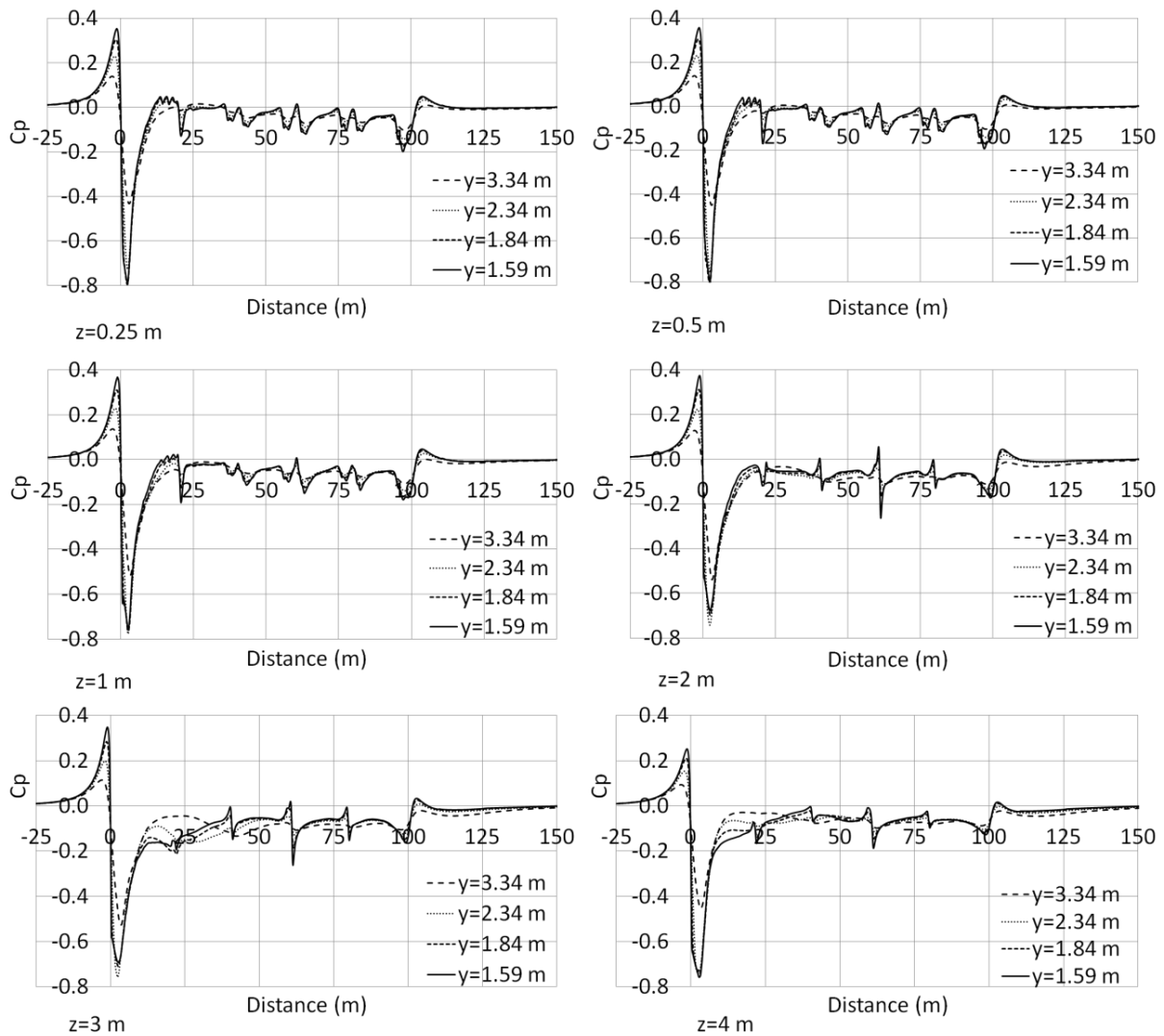


Figure 147 Pressure coefficients relative to a static observer at a)  $z=0.25$  m, b)  $z=0.5$  m, c)  $z=1.0$  m, d)  $z=2.0$  m, e)  $z=3.0$  m and f)  $z=4.0$  m

Figure 147 shows the  $C_p$  on the leeward side of the train. A positive-negative pressure pulse is observed at  $x \approx 0$  m which has peak positive and negative pressures of  $C_p = 0.36$  and  $C_p = -0.81$ , respectively at  $y = 1.59$  m and  $z = 0.5$  m. At  $z = 1, 2$  and  $3$  m the greatest negative  $C_p$  is observed at  $y = 2.34$  m rather than at the closest measurement position to the train ( $y = 1.59$  m) and is explained by the isosurface in Figure 148. The pressure region below  $C_p = -0.7$  is

observed to be further than 0.4 m from train side at  $z=2$  m as opposed to the windward side where the lowest pressure is closer to train side.

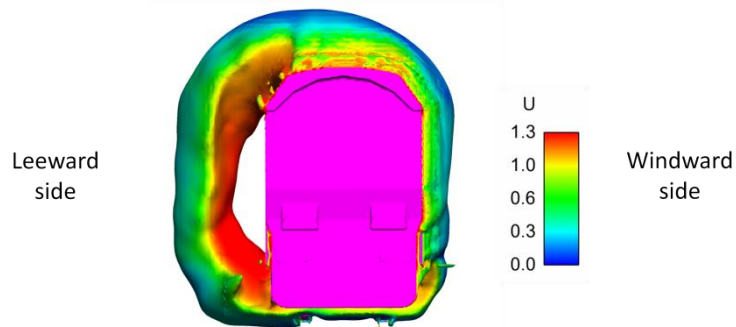


Figure 148 Pressure isosurface ( $C_p=-0.7$ ) coloured by mean velocity magnitude

The transients at the inter-wagon spacings are greater in magnitude on the leeward side of the train than on the windward side. The greatest transients in the boundary layer region occur at the largest inter-wagon spacing between  $z=1$  m and  $z=4$  m where there are no blockages in the spacings such as container-flat buffers.

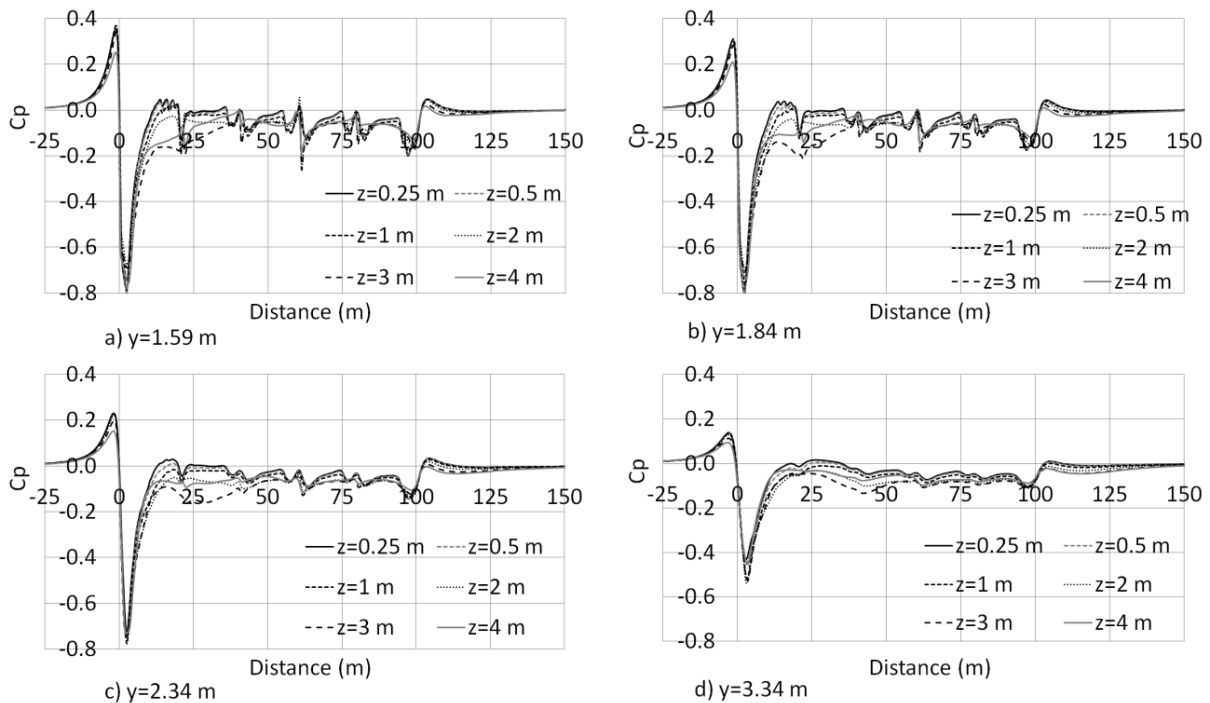


Figure 149 Pressure coefficients relative to a static observer varying with height at a)  $y=1.59$  m, b)  $y=1.84$  m, c)  $y=2.34$  m and d)  $y=3.34$  m

Figure 149 shows the data from Figure 147 plotted with respect to height. It can be seen that the variation in  $C_p$  in the boundary layer region decreases with distance from COT. Furthermore there is a general trend of increasing negative pressure towards the rear of the train although this is less than 10% of the nose region pressure transient. Pressure transients occur at the spacing between the locomotive and the first container wagon and are approximately 60% of the magnitude of those at the largest inter-wagon spacing.

The nose region pressure transient is observed to be longer in duration for the leeward flow than for the windward flow. Figure 150 shows a pressure isosurface ( $C_p=-0.3$ ) around the locomotive and it is apparent that the negative pressure field extends not only further from the train on the leeward side, but also further along the length of the locomotive. This observation explains the greater duration in the nose pressure transient on the leeward side of the train.

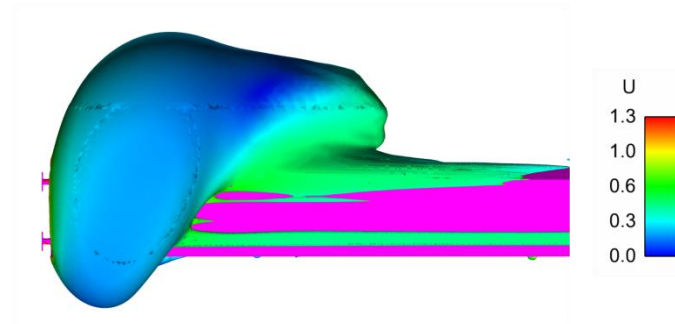


Figure 150 Isosurface of pressure coefficient ( $C_p=-0.3$ ) around the locomotive, coloured by velocity magnitude.

### **6.3.7 Flow visualisation**

Figure 151 shows mean velocity streamlines at longitudinal positions along the train length. It can be seen that a longitudinal vortex structure exists on the leeward side of the train and increases in diameter along train length. The leeward vortex finishes with the approximately twice the diameter of train width which is approximately  $1/3^{\text{rd}}$  of the diameter of the vortex

generated on the leeward side of the train in the 30° crosswind case. The large-scale recirculation region on the leeward side of the train explains the variability in velocity components observed previously.

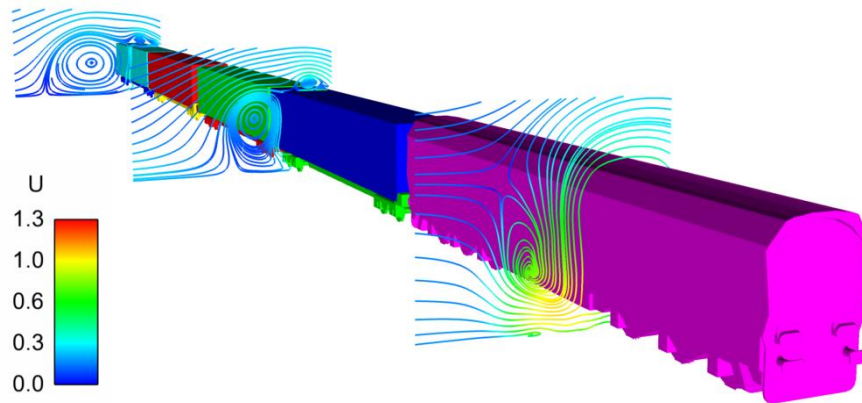


Figure 151 Longitudinal vortices on the leeward side of the train

Figure 152 shows the mean flow separation regions around the windward and leeward corners of the locomotive at mid-height. The reattachment of the flow on the windward side occurs 2.5 m from the front face of the locomotive, 40% of the reattachment distance for the leeward side, which occurs at  $x=6.3$  m. The recirculation regions extend 0.4 m and 2.2 m from the side of the train, for the windward and leeward sides, respectively.

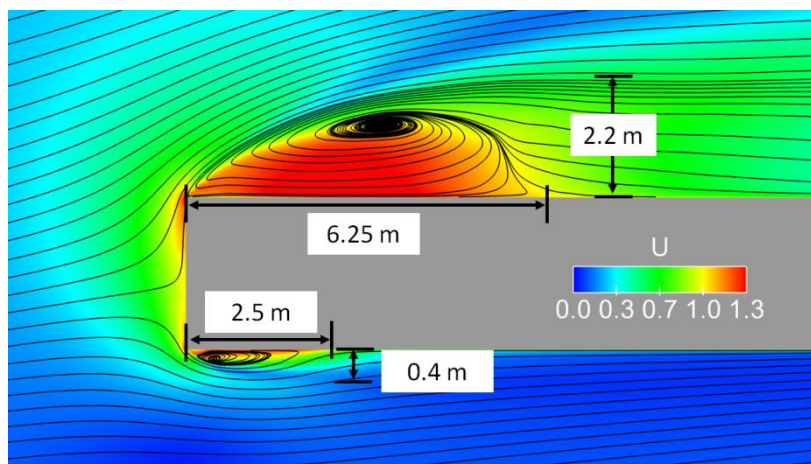


Figure 152 Streamlines projected onto a plane at mid-height showing regions of flow reattachment, coloured by velocity magnitude

### 6.3.8 Surface pressure coefficients

Figure 153 shows the surface pressures in loops around the longitudinal axis of each container, beginning at the lower windward side. The location of the roll vortex on the roof of the first container can be seen as the lowest pressure peak on each sampling ring. The low pressure peaks move towards the leeward side of the roof with increasing distance along the container which corresponds to a similar yaw angle as the angle the resultant wind. The peak pressures on the roof of the first container are greater than twice the value of the peak pressures on subsequent container. It was shown in Figure 160 that the roll vortex on the roof of the first container is the only coherent one due to the relatively unimpeded flow which it experiences; this effect is shown in Figure 153 quantitatively in the form of  $C_{p_s}$ . It is hypothesised that the locomotive provides significant shielding due to its greater height thus causing lower pressures in its wake and aiding the low pressure on the first container's roof.

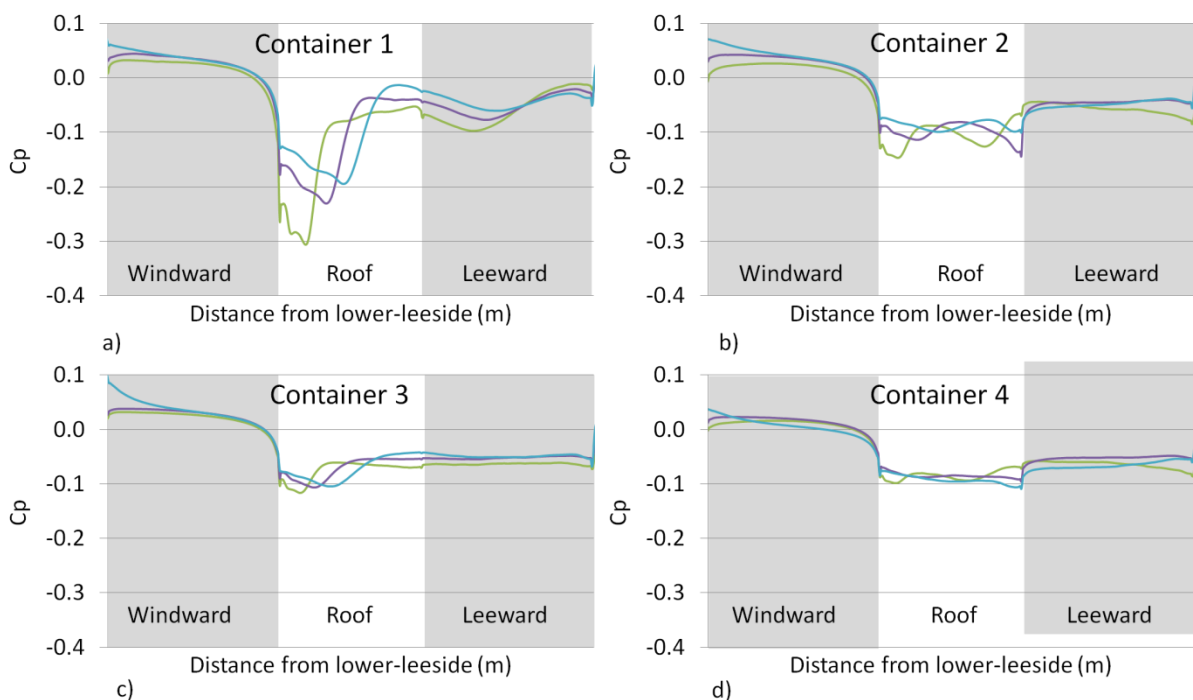


Figure 153 Surface-pressure coefficients on windward, roof and lee-sides for containers a) 1, b) 2, c) 3 and d) 4 at 25% (green), 50% (purple) and 75% (blue) along each container

There is a large contrast between the surface pressures on the roofs of containers 1 and 2. The peak pressure 25% along the roof of container 2 is less than half of the peak pressure on container 1 at the same location and the minor vortex that forms at the windward corner can be seen in Figure 154. The lowest pressure half-way along container 2 occurs at the leeward edge of the roof as a result of the continuation of a roll vortex that originated on container 1 (Figure 154). As discussed previously, the relatively minor negative pressures on the roof of container 2 and subsequent containers is a result of the wake of the previous wagon.

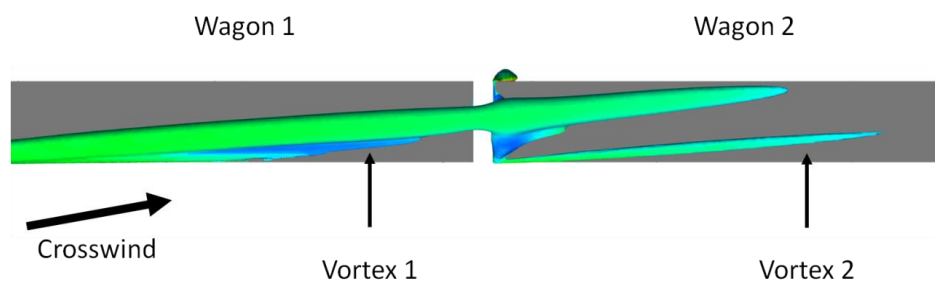


Figure 154 Pressure isosurfaces ( $C_p=-0.15$ ) showing roll vortices on the roofs of containers 1 and 2

Pressures on the roofs of containers 3 and 4 do not exceed  $C_p=-0.12$ . Container 3 experiences lower pressure on the roof than container 4 as a result of the larger inter-wagon spacing that precedes it. The effect of spacings between containers on surface pressures and force coefficients was discussed further in Soper (2014).

### ***6.3.9 Flow structures in the inter-wagon spacings***

Mean streamlines were projected onto a horizontal colour plane at mid-height are shown in Figure 155. The two larger inter-wagon spacings (Figure 155a & c) each contain two large-scale vortices. In Figure 155a, the first inter-wagon spacing contains vortices with aspect ratios of the vortices is approximately 1 whereas in Figure 155c the windward vortex dominates the inter-wagon spacing. The difference between the vortices in the first and third inter-wagon spacings is likely to be a result of the pressure gradient between the windward

and leeward sides of the train. The two smaller inter-wagon spacings (b & d) contain a single vortex each, centred at the windward side of the spacing. Although the flow structures exhibit some asymmetry, there is little evidence of the mean flow escaping the inter-wagon spacings at mid-height.

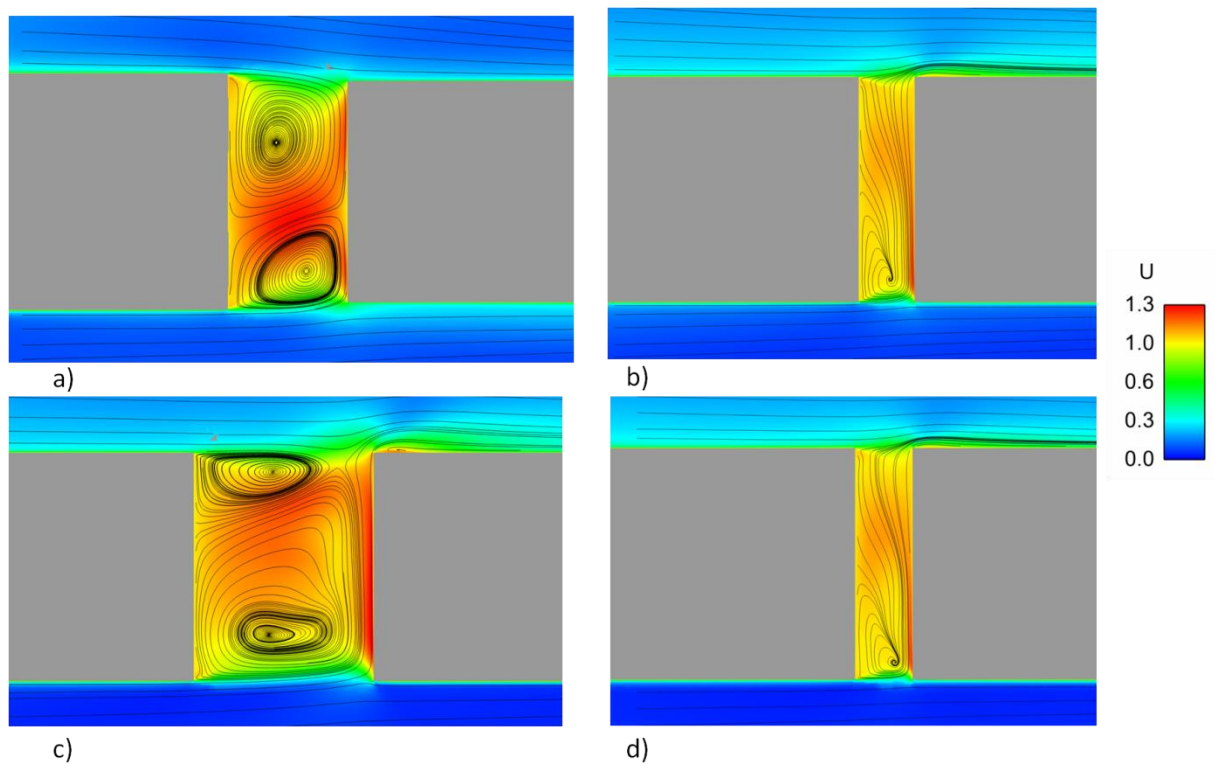


Figure 155 Mean streamlines projected on colour plot of velocity magnitude at mid-height for inter-wagon spacings a) 1, b) 2, c) 3 and d) 4

Figure 156 shows the mean streamlines in inter-wagon spacings projected onto a colour plane at COT. The first inter-wagon spacing (Figure 156a) contains a vortex of approximately 10% of locomotive height at  $z \approx 3.9$  m, further vortices exist between the buffers and underneath the train. The second inter-wagon spacing (Figure 156b) contains no vortices between the containers however a small amount of recirculation is visible at the join between the flat-bed wagons. The third spacing (Figure 156c) contains a large-scale vortex with its centre at  $z \approx 3$  m on the leeward-side of the spacing. The final spacing (Figure 156d) contains a large-scale vortex structure with a high aspect ratio.

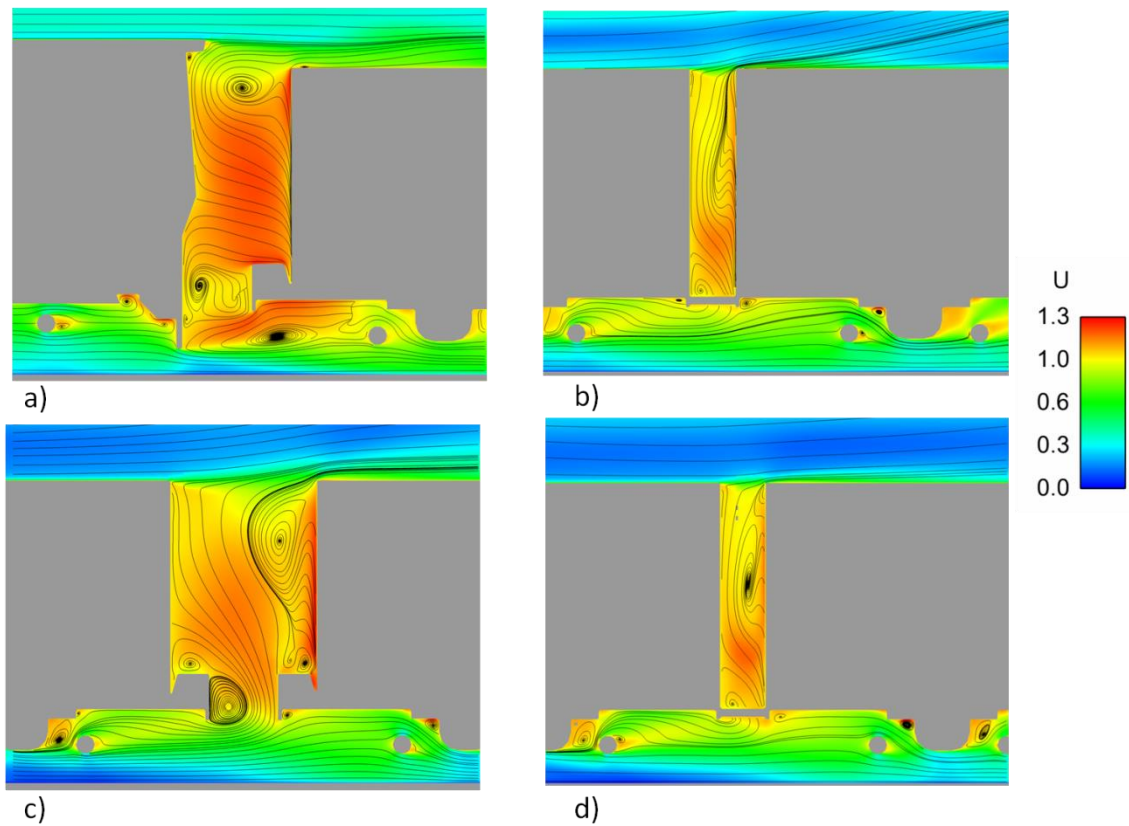


Figure 156 Mean streamlines projected on colour plot of velocity magnitude at COT for inter-wagon spacings a) 1, b) 2, c) 3 and d) 4

### **6.3.10 Slipstream comparison to ICE 2**

The slipstream of a model-scale ICE2 was investigated using the University of Birmingham's TRAIN rig (Baker et al., 2001). As well as measuring the slipstream velocities of the train in ambient conditions, the vehicle was also passed through a crosswind and the slipstream velocity on the leeward side was measured. Comparison between the present work and Baker et al.(2001) is made in order to indicate how differently crosswinds affect the slipstreams of freight and passenger trains. It should be noted that the yaw angle considered by Baker et al.(2001) was  $\theta \approx 11^\circ$  although due to unsteadiness in the crosswind generator and variation of train speeds between runs some variability will arise in the ensemble average. Baker et al.(2001) only measured the longitudinal and lateral velocity components hence Figure 157 shows the normalised horizontal velocities,  $U_h$ , for  $y'=1\text{m}$  and  $y'=2\text{m}$ .

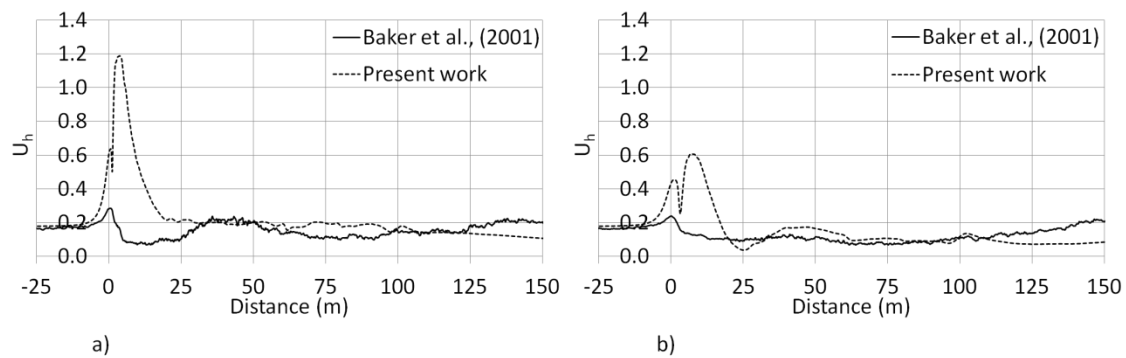


Figure 157 Time-averaged and ensemble-mean normalised horizontal slipstream velocities,  $U_h$ , on the leeward side of the freight train in the present work and the ICE2 (Baker et al., 2001) at a) 1 m and b) 2m from train side at  $z=2.25$  m

At  $y'=1$  m the greatest difference in velocities from the two cases occurs in the nose region of the trains. The peak velocity on the leeward side of the ICE2 is  $U_h=0.28$ , whereas it is  $U_h=1.19$  on the leeward side of the Class 66 locomotive. The relatively massive nose peak from the present work has been attributed to the flow shearing around the corners of the locomotive whereas the relatively low  $U_h$  on the leeward side of the ICE2 is due to the rounded shape which prevents such abrupt flow separation.

Further from train side, at  $y'=2$  m, the peak velocity generated by the Class 66 is  $U_h=0.6$  which is half the peak value at  $y'=1$  m. The peak velocity in the slipstream of the ICE2, at  $y'=2$  m, is  $U_h=0.24$ , 40% of the peak velocity on the leeward side of the Class 66.

The velocities presented in Figure 157 are normalised by train speed. It is known that freight trains in the UK, such as the one under investigation in the present work, travel at a maximum speed of 120 km/h (33 m/s) whereas an ICE2s have an operational speed of 280km/h (77 m/s). The units for the velocities have been re-introduced into Figure 158 to highlight the fact that  $10^\circ$  crosswinds are relative to the train speed.

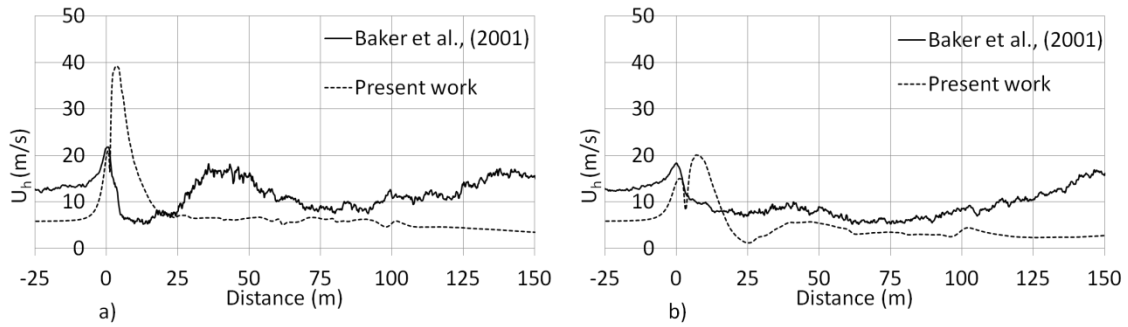


Figure 158 Time-averaged and ensemble-mean horizontal velocities,  $U_h$ , on the leeward side of the freight train in the present work and the ICE2 (Baker et al., 2001) at a) 1 m and b) 2m from train side at  $z=2.25$  m

At  $y'=1$  m, the peak velocities for the ICE2 and Class 66 are  $U_h=22$  m/s and  $U_h=39$  m/s, respectively. This difference in  $U_h$  is significantly reduced at  $y'=2$  m, where the ICE2 and Class 66 have peak  $U_h$  of 18m/s and 20 m/s, respectively: with increasing distance from train side, the  $U_h$  show increasing congruence in the nose region as well as in the boundary layer region.

It can be seen from Figure 158 that the track-normal wind speed necessary to make a  $\theta \approx 10^\circ$  resultant wind with the train is approximately twice as great for the ICE2 than for the freight train. Furthermore, the required wind speed to make the  $\theta \approx 10^\circ$  yaw angle with the ICE 2 is within the range specified by Jordan et al. (2008) that could cause person instability. Moreover, if crosswind speeds could cause person instability then the effects of slipstream amplification would be considered secondary to this effect. The peak velocity produced by the freight train is nearly twice as great as that for the ICE2, which suggests that there is a much greater risk to a person's safety on the leeward side of the freight train than the ICE2.

### **6.3.11 Forces experienced by locomotive and containers**

Table 11 shows the drag force coefficients,  $C_d$ , experienced by the Class 66 locomotive, each container and flat-bed wagon. The locomotive experiences the highest drag force, which is 23 times greater than that experienced by container 2. Due to the shielding effect of the

locomotive and the subsequent low pressure region in its wake, container 1 experiences a very minor negative drag force which is nearly offset by the frictional force on the container. The pressure contribution to the drag force is dominant for the 3<sup>rd</sup> and 4<sup>th</sup> containers and especially for the flat-bed wagons where the pressure force is often an order of magnitude greater than the frictional forces.

Table 11 Drag force coefficients

	<b>Total</b>	<b>Pressure</b>	<b>Friction</b>	<b>Whole wagon</b>
<b>Class 66</b>	1.04	1.01	0.03	1.04
<b>Container 1</b>	-0.01	-0.05	0.04	
<b>Flatbed wagon 1</b>	0.04	0.03	0.01	0.03
<b>Container 2</b>	0.05	0.02	0.03	
<b>Flatbed wagon 2</b>	0.10	0.09	0.01	0.15
<b>Container 3</b>	0.08	0.05	0.03	
<b>Flatbed wagon 3</b>	0.12	0.11	0.01	0.20
<b>Container 4</b>	0.15	0.12	0.03	
<b>Flatbed wagon 4</b>	0.15	0.14	0.01	0.30

Table 12 presents the side force coefficients,  $C_s$ , for the locomotive, containers and flat-bed wagons. Pressure is highly dominant in the contribution to the total side force experienced by each container and wagon flat-bed. The pressure force experienced by container 4 is 260 times greater than the frictional force due to the lack of tangential surface in the direction of the side force but also the magnitude of the pressure gradient between the windward and

leeward sides of the train. The locomotive experiences the highest side force which is twice as great as the force on the third container.

Table 12 Side force coefficients

	Total	Pressure	Friction	Whole wagon
<b>Class 66</b>	1.26	1.25	0.01	1.26
<b>Container 1</b>	0.38	0.38	0.00	
<b>Flatbed wagon 1</b>	0.02	0.02	0.00	0.40
<b>Container 2</b>	0.44	0.44	0.00	
<b>Flatbed wagon 2</b>	0.09	0.09	0.00	0.53
<b>Container 3</b>	0.50	0.50	0.00	
<b>Flatbed wagon 3</b>	0.11	0.11	0.00	0.61
<b>Container 4</b>	0.41	0.41	0.00	
<b>Flatbed wagon 4</b>	0.09	0.09	0.00	0.50

The lift force coefficients,  $C_l$ , for the locomotive, containers and wagons are shown in Table 13. All of the flatbed wagons experience a negative lift force except for the first wagon and is hypothesised to be a direct result of the presence of the locomotive. The third wagon experiences the greatest lift force and the fourth wagon experiences the greatest negative lift force.

Table 13 Lift force coefficients

	Total	Pressure	Friction	Whole wagon
<b>Class 66</b>	1.03	1.02	0.01	1.03
<b>Container 1</b>	0.58	0.57	0.01	0.61
<b>Flatbed wagon 1</b>	0.03	0.03	0.00	
<b>Container 2</b>	0.45	0.45	0.00	0.43
<b>Flatbed wagon 2</b>	-0.02	-0.02	0.00	
<b>Container 3</b>	0.37	0.37	0.00	0.35
<b>Flatbed wagon 3</b>	-0.02	-0.02	0.00	
<b>Container 4</b>	0.41	0.41	0.00	0.28
<b>Flatbed wagon 4</b>	-0.13	-0.13	0.00	

Figure 159 shows the force coefficients experienced by the locomotive and containers, as well as the rolling moment,  $M_r$ , on the locomotive and each container wagon about COT. The drag force coefficient varies substantially with loading position, falling from  $C_d=1$  on the locomotive to  $C_d=-0.01$  on the first container. The drag experienced by the last container,  $C_d=0.15$ , is due to the low pressure of the wake behind the exposed rear face of the container.

The side-force coefficient experienced by the locomotive is  $C_s=1.26$ . The third container experiences the greatest side-force coefficient at a value of  $C_s=0.5$  which is 66% lower than is experienced by the locomotive.

The lift force coefficient experienced by the locomotive is  $C_l=1.02$  which decreases by 43% to  $C_l=0.58$  on the first container. The lift force further decreases with loading position until the final container where it increases again from  $C_l=0.37$  to  $C_d=0.41$ .

The rolling moment,  $M_r$ , experienced by the locomotive is  $M_r=0.7$  whereas the fourth wagon experiences the lowest moment at  $M_r=0.26$ . The rolling moment experienced by the third container wagon is higher than the other container wagons due to the largest inter-wagon spacing preceding it.

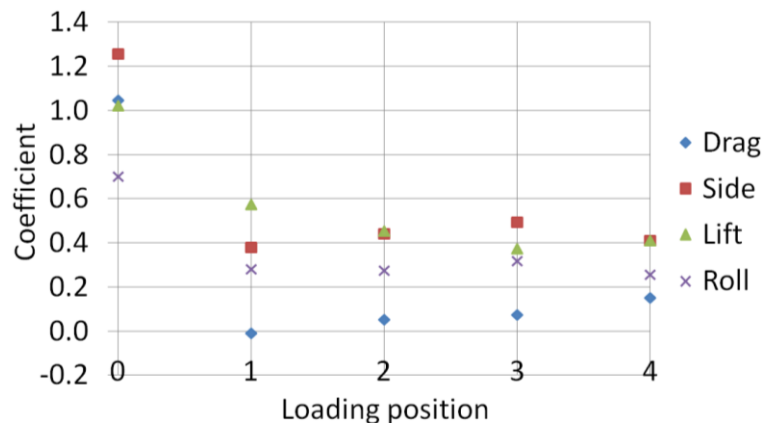


Figure 159 Force and moment coefficients experienced by the locomotive, containers and wagons against loading position

The force and moment coefficients experienced by the locomotive, containers and container wagons do not reach stable values along train length i.e. the forces experienced by container wagons differ with loading position. It was observed by Golovanevskiy et al.(2012) that the forces experienced by adjacent container wagons stopped varying significantly after the fourth wagon. Due the present wagons being paired, the differing geometry between adjacent wagons could cause the variation of experienced forces to continue for longer.

## 6.4 *Instantaneous flow*

### 6.4.1 *Vortex generation*

Figure 160 shows isosurfaces of the second invariant of the velocity gradient tensor,  $Q$ -criteria, to aid the visualisation of the vortices generated in the slipstream of the freight train. The flow separation region on the leeward side of the locomotive is similar to that observed when the train was subjected to a  $30^\circ$  crosswind (Figure 160a).

The vortices generated in the under-floor region of the locomotive are shown to travel along the windward side of the first container and upwards towards the roof (Figure 160c). This observation highlights the extent of the influence that the low pressure caused by the separated flow over the roof has on the flow at  $z=2$  m.

Roll vortices are observed on the roof of each container and originate at the windward corners (Figure 160b). The only flow structure which exists coherently (i.e. without any discontinuity) is on the roof of the first container. As has been previously discussed, the wake of each container wagon has an interference effect on the flow around subsequent wagons, thus the vortices on the roofs of the other containers are affected.

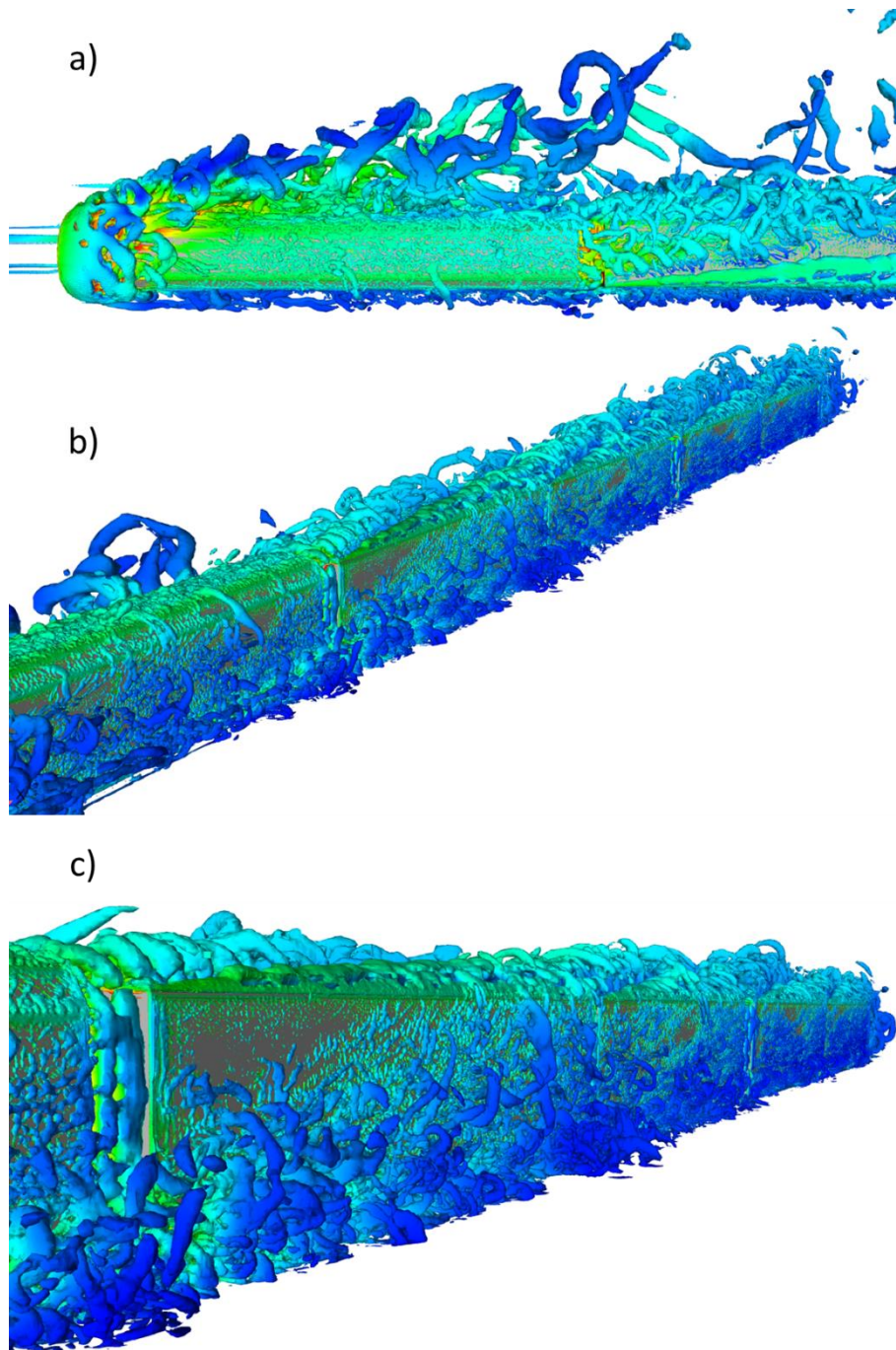


Figure 160 Isosurfaces of the second invariant of the velocity gradient tensor,  $Q=50,000$ , coloured by velocity magnitude

#### ***6.4.1 Turbulence intensity on the windward side of the train***

Figure 161 shows the turbulence intensity,  $I$ , on the windward side of the train. The turbulence intensity on the leeward side of the train is omitted for because the region is

dominated by the large-scale separation and recirculation and thus the definition of turbulence intensity is not strictly valid.

Peak values of  $I$ , for  $z \leq 1$  m, occur along the first container wagon as a result of the flow separating around its windward corner. The flow separation around the windward corner of the first container is also responsible for higher slipstream velocities shown in Figure 135. The greatest peak  $I$  occurs in the wake of the train at  $z=2$  m and is due to an unsteady shear layer that forms on the windward side of the train Figure 162. The vortices generated on the windward side of the train are a result of the faster-moving air behind the train interacting with the slower-moving air around it.

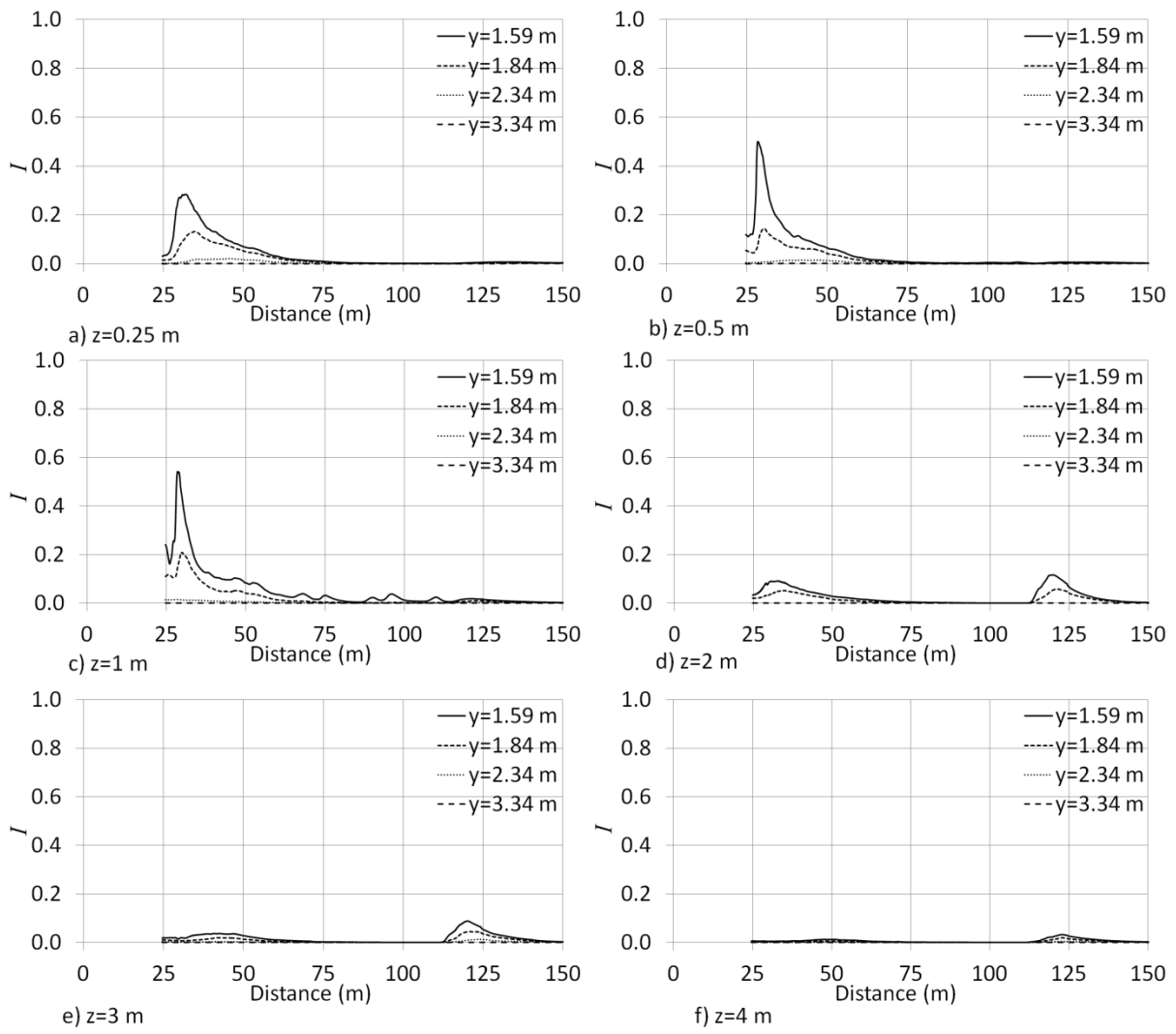


Figure 161 Turbulence intensity on the windward side of the freight train at a)  $z=0.25$  m, b)  $z=0.5$  m, c)  $z=1.0$  m, d)  $z=2.0$  m, e)  $z=3.0$  m and f)  $z=4.0$  m

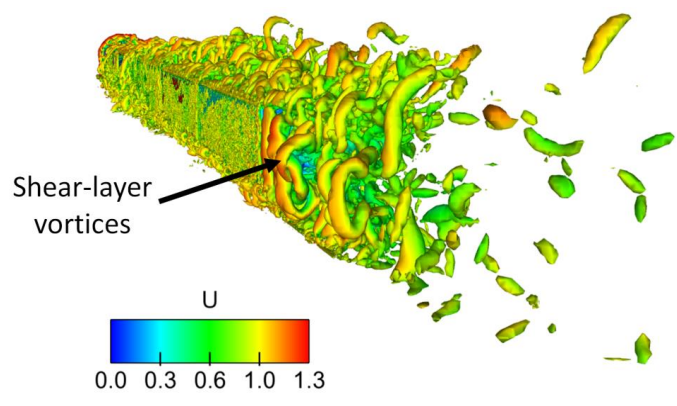


Figure 162 Vortices generated around the rear windward side of the last container wagon. Isosurfaces of  $Q=50,000$ , coloured by velocity magnitude.

### 6.4.2 Integral length scale

The integral time- and length-scales, at static probe positions in the slipstream, are shown in Table 14 . Autocorrelation was performed on the longitudinal velocity signal and the integral time-scale was then found by numerically integrating under the autocorrelation curve using the trapezium rule.

The length-scales are of similar magnitude to those from the no-crosswind case but the length-scales exhibit a trend of increasing monotonically which is a result of the growing leeward recirculation region shown in Figure 151.

In all cases the time-scales are less than  $1/3^{\text{rd}}$  of the human reaction time discussed in Jordan (2008) although the velocities shown in Section 6.3.2 could cause person instability.

Table 14 Auto correlation values

Probe	$x$ (m)	$y$ (m)	$z$ (m)	Time-scale (s)	Length-scale (m)
1	21	1.84	2.1	0.047	1.17
2	40	1.84	2.1	0.059	1.48
3	60	1.84	2.1	0.086	2.16
4	80	1.84	2.1	0.11	2.75

### 6.4.3 Force coefficients

Figure 163 shows the instantaneous force and rolling moment coefficients experienced by the locomotive and container wagons. The lift coefficient experienced by the locomotive has RMS fluctuations of 0.01, with the drag and side force coefficients having RMS values of 0.06 and 0.07, respectively.

The RMS drag, side and lift force coefficients on the first container 0.04, 0.02 and 0.004, respectively. The RMS lift force is 10% of the drag force's and 20% of the side force's. The

low vertical force fluctuation is a result of the shielding effect from the locomotive which precedes the container.

The second container experiences RMS drag, side and lift force coefficients of 0.023, 0.012 and 0.002, respectively. The fluctuations of the force coefficients are all approximately half of those experienced by the first container as a result of the interference caused by the first container.

The RMS drag, side and lift force coefficients experienced by the third container are 0.026, 0.013 and 0.003, respectively. The fluctuations are comparable to those experienced by the second container and again appear to be a result of the interference caused by the previous container.

The RMS force coefficients on the final container 0.020, 0.014 and 0.002, for the drag, side and lift forces, respectively. Between the first and fourth containers the variability of the drag force has halved as has the variability of the lift force. It has been shown that the interference effect of adjacent circular cylinders can drastically reduce or increase the RMS force coefficient on a body (Kareem et al., 1998). It is therefore hypothesised that closer container-spacing will increase the interference effect of adjacent wagons and reduce the RMS force coefficients.

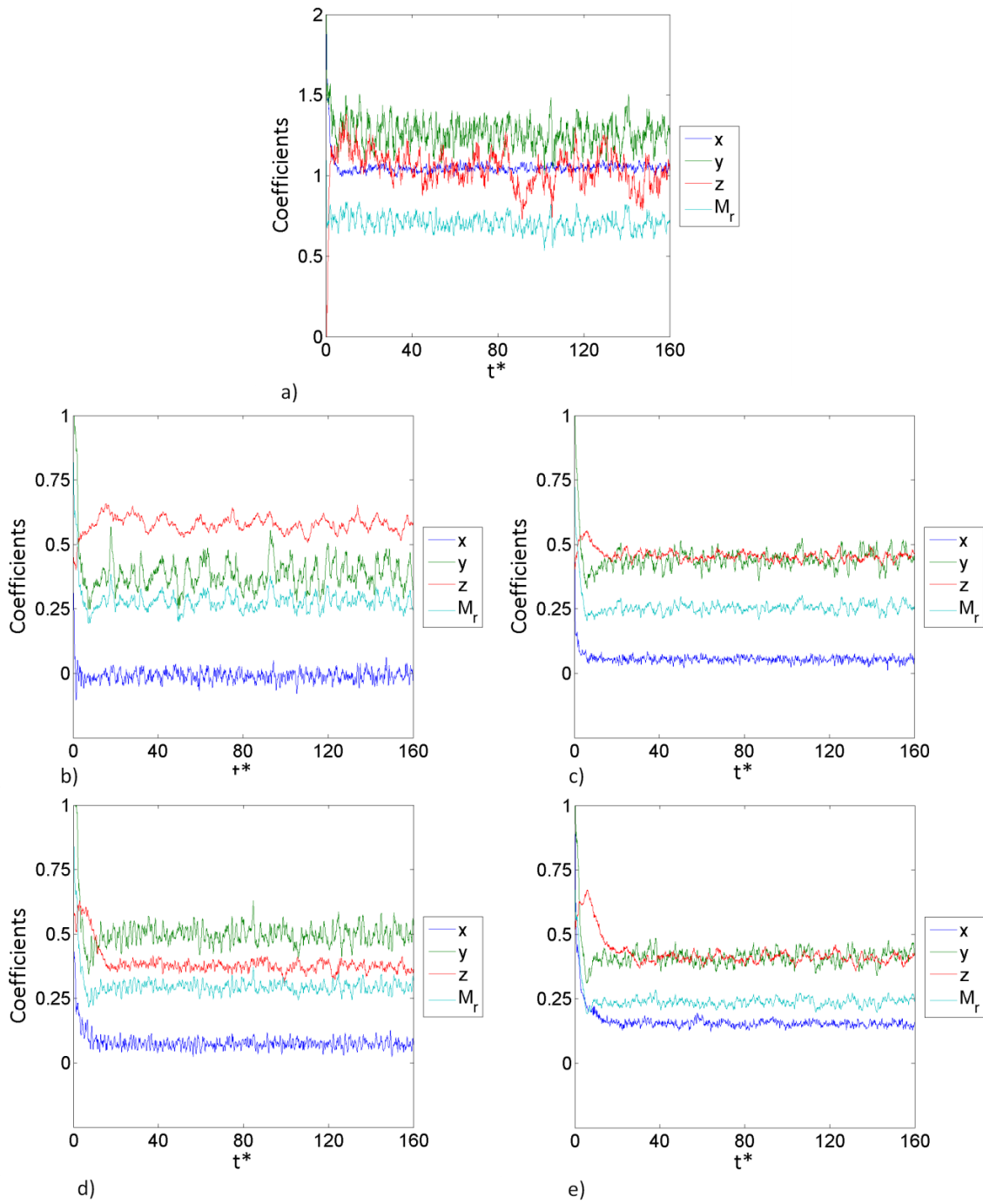


Figure 163 Instantaneous force coefficients for a) class 66 locomotive, b) container 1, c) container 2, d) container 3 and e) container 4

#### 6.4.4 TSI velocities

Twenty instantaneous horizontal velocities,  $U_h$ , at the TSI measurement position ( $y=3$  m and  $z=0.2$  m) are shown in Figure 164. The greatest horizontal velocity peak is  $U_h=44.7$  m/s and occurs at  $x=6$  m whereas the minimum horizontal velocity peak is  $U_h=31.4$  m/s and also occurs at  $x=6$  m. Ahead of the train ( $x<0$  m) the flow is to be inviscid as was observed for the no-crosswind case.

The maximum velocities, minimum velocities and the difference between them at given positions along the length of the train are shown in Figure 165. The greatest difference between the velocities occurs at  $x=10$  m and is  $\Delta U_h=37.5$  m/s. The smallest difference between the velocities along train length occurs at  $x=81$  m whereas the lowest value is in the near wake at  $x=118$  m.

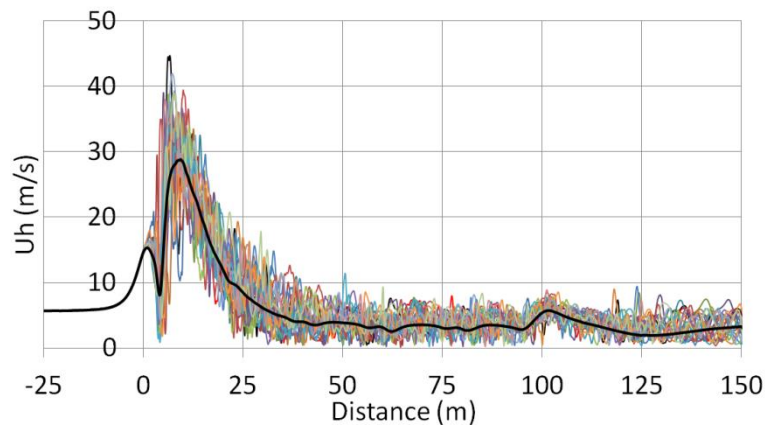


Figure 164 Horizontal velocity magnitudes at the TSI velocity measurement position ( $y=3$  m,  $z=0.2$  m) with time-averaged velocity (thick black line)

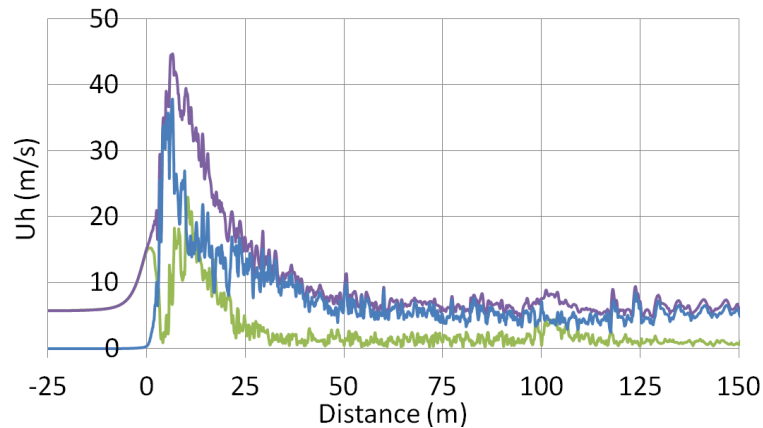


Figure 165 Maximum (purple), minimum (green) and the difference (blue) instantaneous horizontal velocities

By the application of the maximum one second moving average (MOSMA) technique the limiting value of velocity according to TSI and CEN is  $u_{2\sigma} = 20.1$  m/s. Although this technically breaches the limiting value for  $u_{2\sigma}$  according to CEN and TSI this analysis is not strictly valid because the crosswind is 2.9 times greater than the maximum crosswind allowed during the tests. However because the velocities produced are so large, some consideration for low speed crosswinds may need to be made.

#### 6.4.5 TSI pressures

The instantaneous pressures used to calculate TSI compliance at  $z=3.3$  m are shown in Figure 166. The position of  $z=3.3$  m was chosen to demonstrate the compliance test because it was shown in the no-crosswind case to cause the highest  $\Delta p_{2\sigma}$  and as such acts as a worst-case scenario.

The greatest instantaneous pressure is  $p = -1.28$  kPa however, the second lowest value is only  $p = -0.85$  kPa, which highlights the massively unsteady nature of flow separation around sharp-cornered bluff bodies. By applying the TSI methodology for pressure at  $z=3.3$  m, it is observed that the value of  $\Delta p_{2\sigma} = 1303$  which is 1.8 times the limiting value of  $\Delta p_{2\sigma} = 720$  Pa

for trains travelling between 160 km/h and 250 km/h and 1.6 times  $\Delta p_{2\sigma}=795$  Pa for trains travelling greater than 250 km/h.

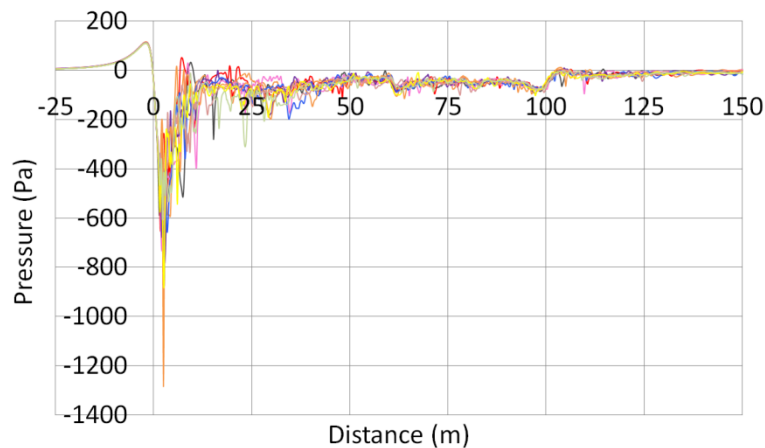


Figure 166 Instantaneous pressures at  $y=2.5$  m and  $z=3.3$  m

It has been shown that the addition of a 6 m/s crosswind causes the limiting values of pressure to be greatly exceeded. This being said, the aforementioned codes of practice are not designed to deal with slipstreams subjected to additional crosswinds or very bluff vehicles.

## 6.5 Concluding remarks

From an analysis of the slipstream of the class 66 locomotive-hauled container freight train subjected to a  $10^\circ$  crosswind, the following conclusions are drawn:

- The flow regimes on the windward and leeward sides of the train are distinctly different
- The greatest peak velocity magnitudes occur on the leeward side of the train
- Transients of velocity magnitude at inter-wagon spacings are greatest on the leeward side of the train
- The locomotive experiences higher force and rolling-moment coefficients than the containers or flat-bed wagons
- The drag-force coefficient on each container increases monotonically with loading position
- Greatest turbulence intensities on the windward side of the train occur along the first container wagon

- The addition of a 6 m/s crosswind caused the  $\Delta p_{2\sigma}$  to exceed the limiting value by 80% at  $z=3.3$  m
- $U_{2\sigma}$  was 5 % greater than the limiting value of 20 m/s with the addition of a 6 m/s crosswind
- The greatest difference between maximum and minimum instantaneous velocities at the TSI position on the leeward side of the train occurs at  $x=10$  m

# Chapter 7 A comparative analysis of the slipstream around the freight train from all crosswind conditions

## 7.1 *Introduction*

The aim of this thesis is to investigate the effect of crosswinds on the slipstream of a freight train and the associated implications. Thus far data have been presented from simulations of the slipstream when the train was in ambient conditions and when it was subjected to two different crosswinds. In isolation the data from each simulation elucidates the flow regime at a specific yaw angles, but by comparing the data from all the simulations directly, the effect of crosswinds on the slipstream of the freight train can be determined.

The present chapter compares mean and instantaneous velocities and pressures for each yaw angle case at varying distances from train side. Furthermore a brief analysis of the force coefficients on the locomotive and each container wagon is performed.

Time-averaged velocity magnitudes are presented in Section 7.2 and instantaneous velocity magnitudes are shown in Section 7.3. Time-averaged velocities and peak-to-peak velocity magnitudes are presented in 7.4 and 7.5, respectively. The force coefficients on each container are given in 7.6 and conclusions are drawn in Section 7.7.

## 7.2 *Time-averaged velocity magnitudes*

Time-averaged velocity magnitudes from samples at  $y=1.59$  m,  $y=1.84$  m,  $y=2.34$  m and  $y=3.34$  m are considered for the no-crosswind,  $10^\circ$  and  $30^\circ$  crosswind cases. It was shown in Chapters 4-6 that there are three distinct flow regimes on each side of the train at three different heights, namely  $z=0.5$  m,  $z=2$  m and  $z=4$  m; to this end the sampling locations above TOR are limited to three vertical positions. By using data from a reduced number of

sampling locations it is the author's intention that the salient features in the data will be more prominent and the impact of the results will not be diluted by the amount of data presented.

The velocity magnitudes on the windward side of the train for the no-crosswind, 10° and 30° crosswind cases at  $z=0.5$  are shown in Figure 167. For the two closest sampling positions to the train, the no-crosswind case produces the highest peak velocities which are  $U=0.95$  and  $U=0.76$  for  $y=1.59$  m and  $y=1.84$  m, respectively. At  $y=2.34$  m, the nose peak from the no-crosswind case is lower than the crosswind velocity in the 30° case. The velocity from the 30° case exhibits a rapid decrease in the nose region and a gradual decay along train length punctuated by the largest transients. The no-crosswind velocity in the boundary layer region is greater than the 10° and 30° cases from  $y=1.59$  m to  $y=2.34$  m however at  $y=3.34$  m the 30° crosswind has the highest velocity in the boundary layer region due to the reduced effect of stagnation at that distance from COT. The velocity in the 10° case exhibits nose peaks at  $y=1.59$  m and  $y=1.84$  m, which are greater than the crosswind value.

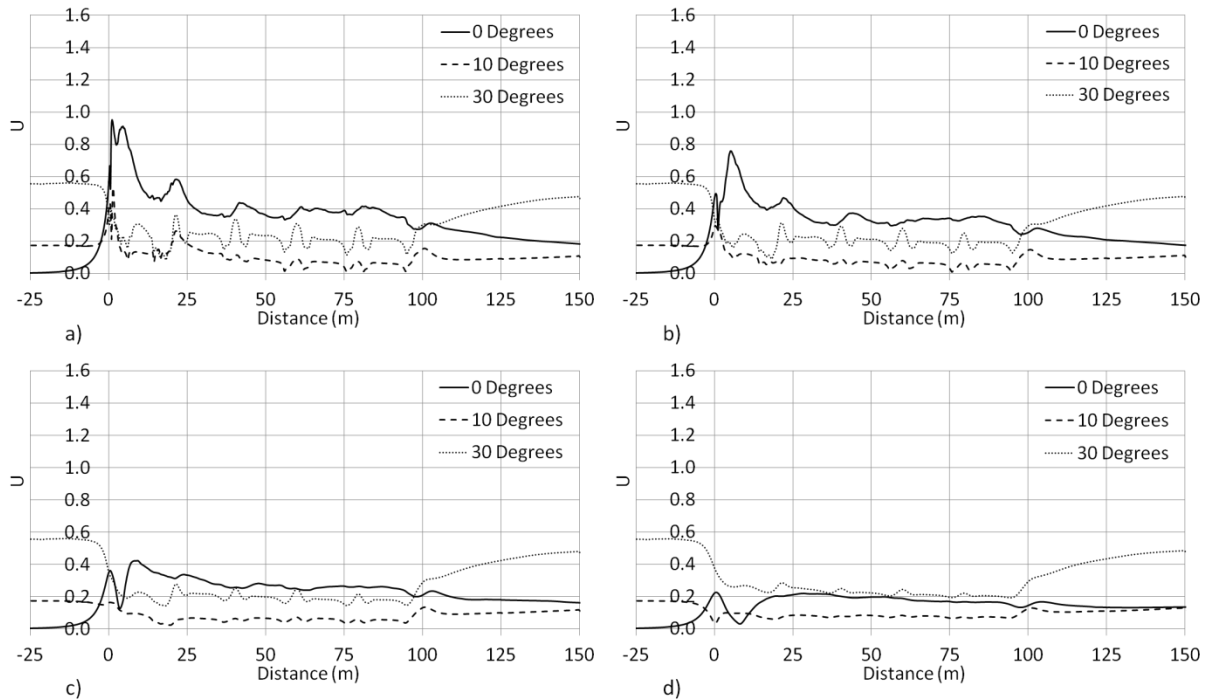


Figure 167 Slipstream velocity magnitudes relative to a static observer at  $z=0.5$  m at a)  $y=1.59$  m, b)  $y=1.84$  m, c)  $y=2.34$  m and d)  $y=3.34$  m for the no-crosswind,  $10^\circ$  and  $30^\circ$  crosswind cases on the windward side of the train

The velocity magnitudes at  $z=2$  m are shown in Figure 168. At  $y=1.59$  m, the velocity nose peak for the  $10^\circ$  case is greater than the crosswind velocity of the  $30^\circ$  case for the first time. It is also observed that the nose peak for the no-crosswind case is greater than twice the crosswind velocity of the  $30^\circ$  case at  $y=1.59$  m. In the boundary layer region the velocities of the  $10^\circ$  and  $30^\circ$  cases are comparable for  $y=1.59$  m, however only the  $30^\circ$  case exhibits transients of approximately  $\Delta U=0.2$ . At  $y=1.84$  m the velocity in the boundary-layer region of the  $30^\circ$  case is comparable to the no-crosswind velocity but increases to approximately double the no-crosswind value at  $y=3.34$  m due to the reduced influence of the stagnation region on the windward side of the train.

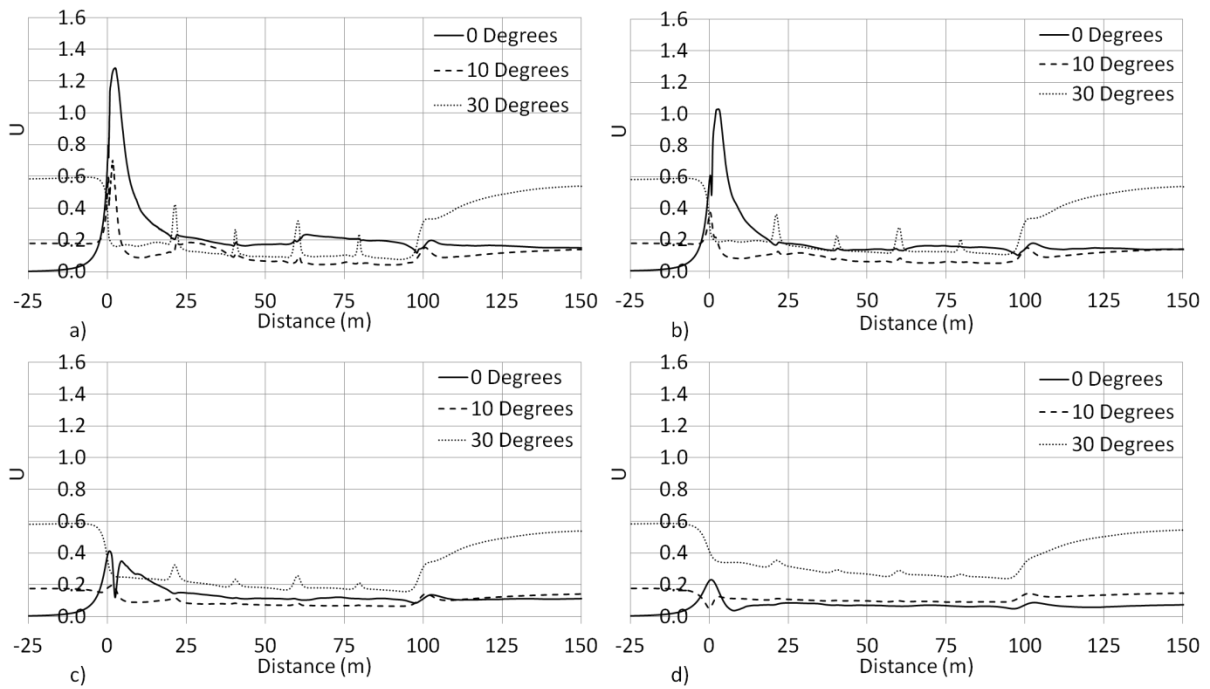


Figure 168 Slipstream velocity magnitudes relative to a static observer at  $z=2$  m at a)  $y=1.59$  m, b)  $y=1.84$  m, c)  $y=2.34$  m and d)  $y=3.34$  m for the no-crosswind,  $10^\circ$  and  $30^\circ$  crosswind cases on the windward side of the train

At  $z=4$  m the velocity in the boundary layer region of the  $30^\circ$  case is greater than its crosswind velocity for the first height above TOR (Figure 169). The velocity from the  $10^\circ$  case is greater in the first half of the boundary layer region than the no-crosswind case at  $y=1.59$  m, and for the entire boundary layer region at all other distances from COT. For  $y=1.59$  m and  $y=1.84$  m the velocity for the no-crosswind case is observed to increase along train length whereas for the  $10^\circ$  crosswind case the velocity either stabilises or decreases. Higher velocities occur for the  $30^\circ$  case because of the greater lateral component than in the  $10^\circ$  crosswind case, which causes greater separation.

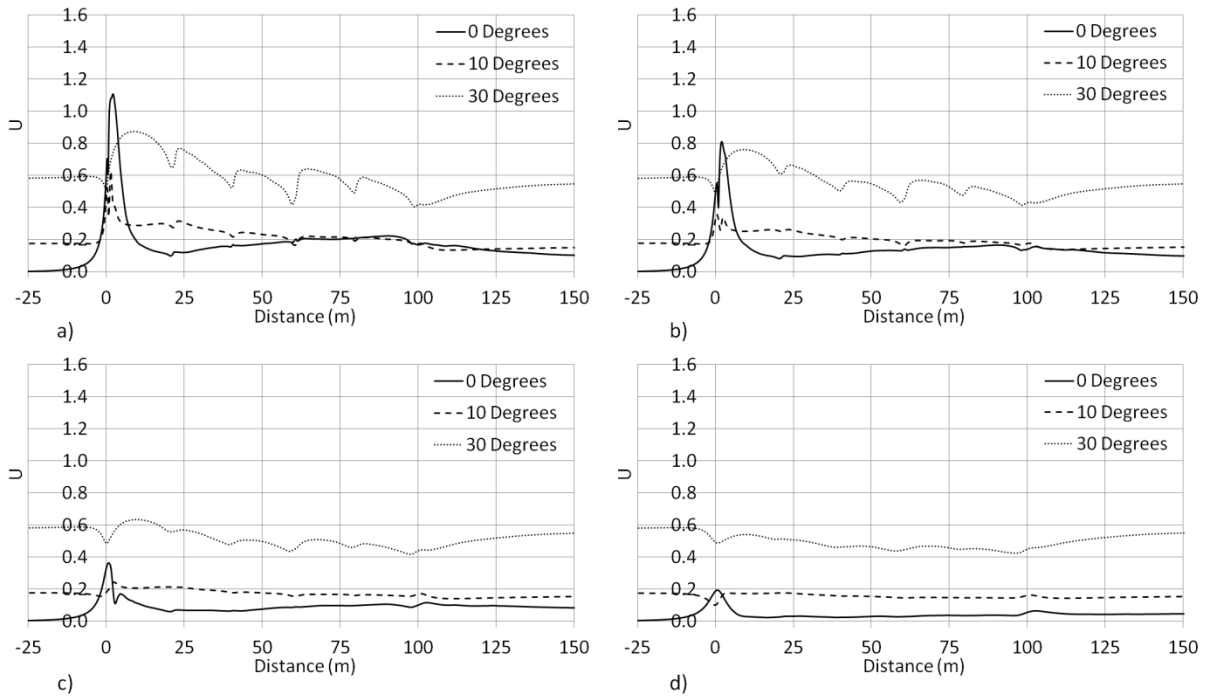


Figure 169 Slipstream velocity magnitudes relative to a static observer at  $z=4$  m at a)  $y=1.59$  m, b)  $y=1.84$  m, c)  $y=2.34$  m and d)  $y=3.34$  m for the no-crosswind,  $10^\circ$  and  $30^\circ$  crosswind cases on the windward side of the train

On the leeward side of the train, the nose region velocities at  $y=1.59$  m, for both crosswind cases, exhibit values within 30% of the no-crosswind peak (Figure 170). With increasing distance from train side the difference between the velocities in the nose region increases. The no-crosswind velocity is observed to decrease fastest with distance from train side, followed by the  $10^\circ$  case. The  $30^\circ$  crosswind velocity peaks remain almost constant with distance from train side and are thus the greatest velocities at  $y=1.84$  m,  $y=2.34$  m and  $y=3.34$  m. In the boundary layer region, at  $y=1.59$  m and  $y=1.84$  m, the no-crosswind case has the greatest velocity as a result of the shielding effect reducing the other two cases' velocities, followed by the  $10^\circ$  case and then the  $30^\circ$  case. The  $30^\circ$  case has the greatest velocity in the boundary layer region at  $y=3.34$  m.

The  $30^\circ$  case shows a double-peak phenomenon at all distances from train side with the highest velocity occurring at  $y=3.34$  m. The peak velocities on the leeward side of the  $30^\circ$

case which occur at  $y=2.34$  m and  $y=3.34$  m have values twice those of the crosswind velocity. At  $y=3.34$  m the peak velocity of the  $10^\circ$  case is greater than six times the value of its crosswind and approximately four times the peak of the no-crosswind case thus exhibiting significant slipstream amplification. The  $10^\circ$  crosswind case has the highest velocity peak at  $y=1.59$  m but decreases with distance from train side to  $U=0.83$  at  $y=3.34$  m.

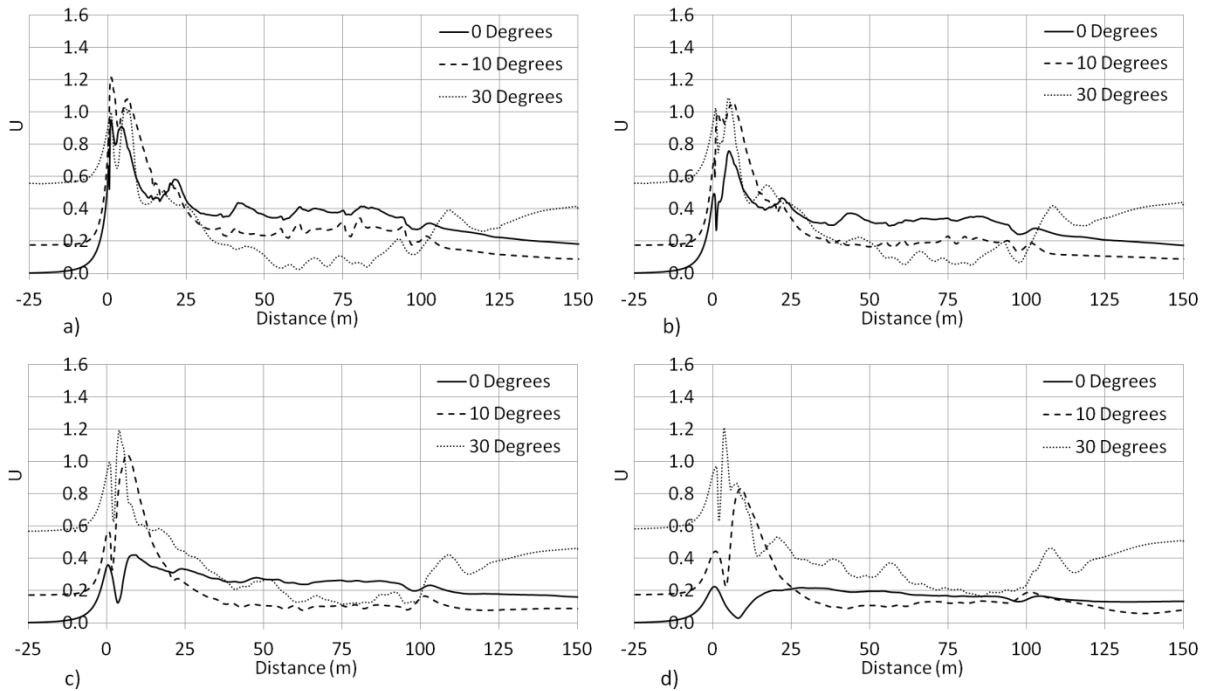


Figure 170 Slipstream velocity magnitudes relative to a static observer at  $z=0.5$  m at a)  $y=1.59$  m, b)  $y=1.84$  m, c)  $y=2.34$  m and d)  $y=3.34$  m for the no-crosswind,  $10^\circ$  and  $30^\circ$  crosswind cases on the leeward side of the train

As occurred at  $z=0.5$  m, the peak velocities in the nose region at  $y=1.59$  m and  $z=2$  m are comparable for all three cases (Figure 171). The velocity peak in the nose region of the  $30^\circ$  case differs by less than 13% between  $y=1.59$  m and  $y=3.34$  m. The reason for this behaviour is due to the shear layer extending further from train side due to the relatively high yaw angle.

The  $10^\circ$  crosswind case shows increasing velocity after the locomotive at  $y=1.59$  m and  $y=1.84$  m whereas at further distances from train side the velocity remains nearly constant

after  $x=30$  m. The increasing velocity near to train side is a result of some minor slipstream growth and will be discussed further later on in this chapter.

Overall, a greater variability in velocity is observed along train length for the  $30^\circ$  case in comparison to the no-crosswind and  $10^\circ$  crosswind cases. This result is due to the larger lateral velocity component which causes additional air to pass through the inter-wagon spacings which then accelerates around the leeward front corners of the container wagons.

In the near wake of the train in the  $30^\circ$  case, a velocity transient of approximately  $\Delta U=0.25$  is observed for all distances from train side between  $x=104$  m and  $x=108$  m. The velocity in the near wake of the  $30^\circ$  case is 100% greater than was observed for the no- and  $10^\circ$  crosswind cases and is a result of the flow shearing around the leeward corner of the last container.

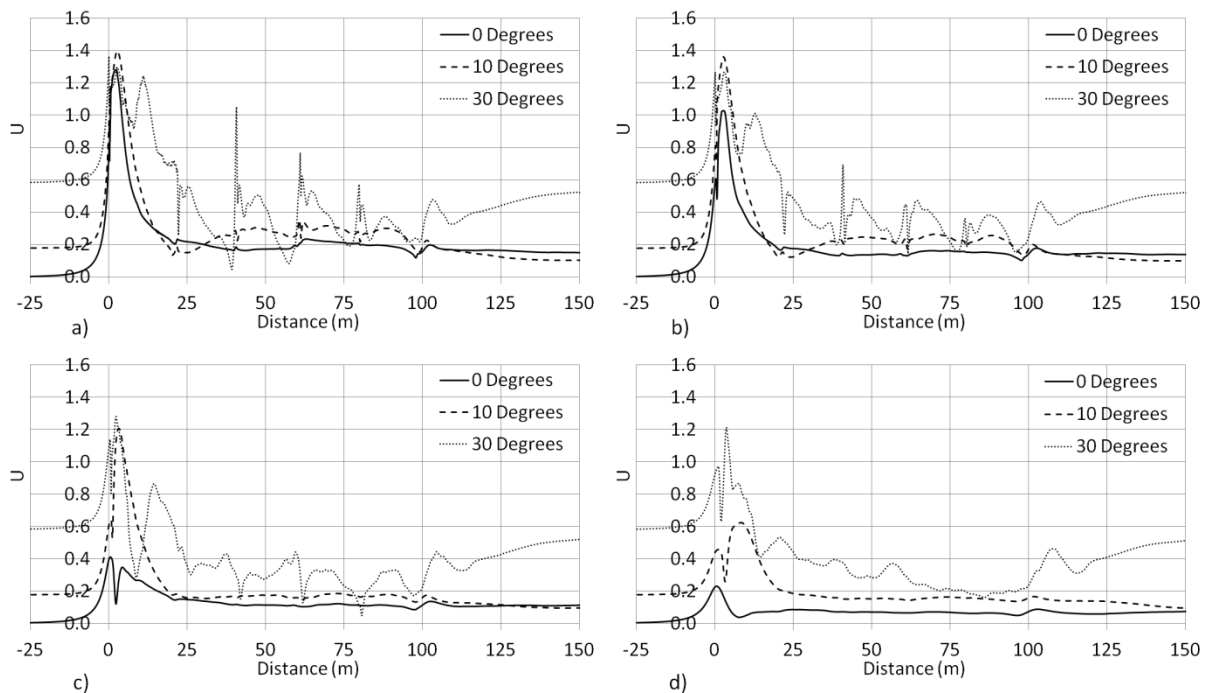


Figure 171 Slipstream velocity magnitudes relative to a static observer at  $z=2$  m at a)  $y=1.59$  m, b)  $y=1.84$  m, c)  $y=2.34$  m and d)  $y=3.34$  m for the no-crosswind,  $10^\circ$  and  $30^\circ$  crosswind cases on the leeward side of the train

On the leeward side of the train at  $z=4$  m, the mean velocity magnitudes from the  $10^\circ$  and  $30^\circ$  crosswind cases are greater than those obtained from the no-crosswind case for the majority

of train length and at all distances from COT (Figure 172). The higher velocities from the crosswind cases are a result of the flow around the leeward front corners of the containers and over the roofs causing higher lateral and vertical components in comparison to the no-crosswind case where the longitudinal component is dominant.

The velocity magnitude of the 10° case, at  $y=1.59$  m and  $y=1.84$  m, decreases along the first two container wagons as a result of the shielding effect of the locomotive and then increases due to an injection of higher-velocity air from the second inter-wagon spacing. A similar effect to this was noticed by Baker et al.(2007) where the velocity reached a very low value along the first two cars and then increased again to a similar value as the nose peak.

The peak velocity from the 10° crosswind was sampled at  $y=3.34$  m and is  $U=0.39$ , whereas the peak value from the 30° case is 2.7 times larger. Due to the higher yaw angle, the shear layer in the 30° case is at a higher incident angle to the train and thus extends further from train side than for the 10° crosswind case.

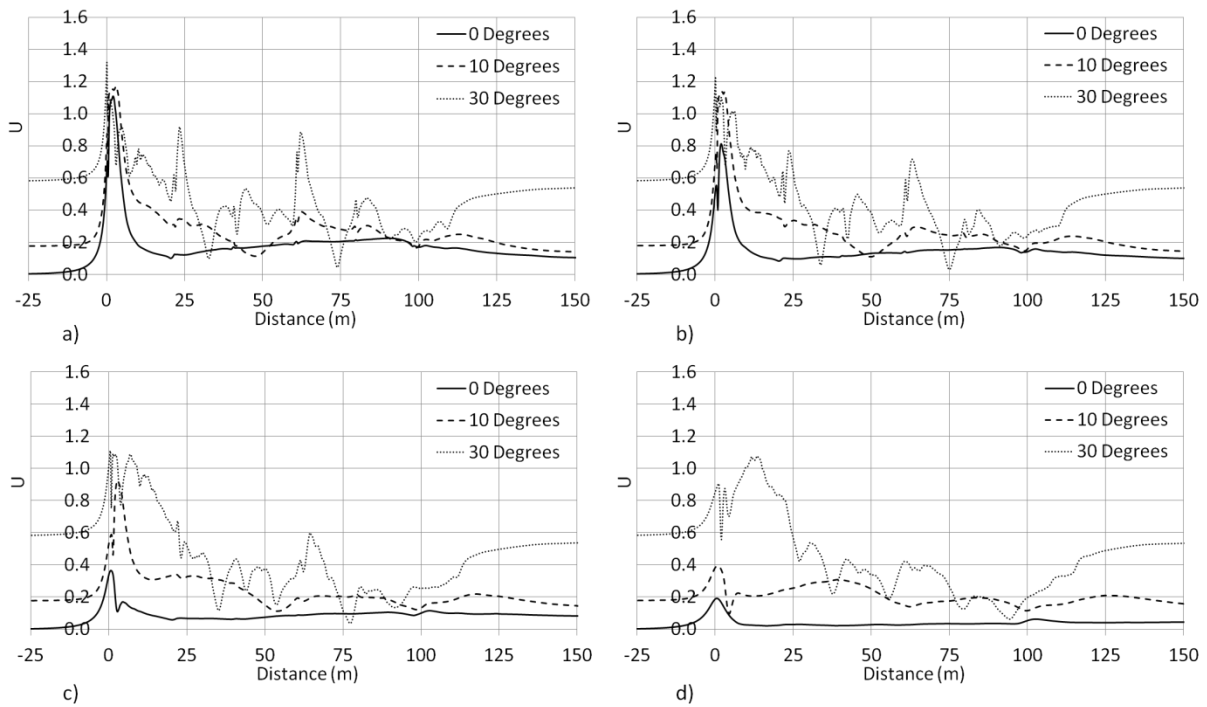


Figure 172 Slipstream velocity magnitudes relative to a static observer at  $z=4$  m at a)  $y=1.59$  m, b)  $y=1.84$  m, c)  $y=2.34$  m and d)  $y=3.34$  m for the no-crosswind,  $10^\circ$  and  $30^\circ$  crosswind cases on the leeward side of the train

Figure 173 shows a colour plot of the mean velocity magnitude at  $z=0.5$  m for all three cases. The no-crosswind case exhibits high velocities underneath the train which are most likely to be a result of separation around the air dam. Localised increases in velocity at the side of the train occur at the front of each flatbed wagon which then decreases further along each wagon due to an absence of roughness.

A region of high velocity extends up to  $y=10$  m from the leeward side of the train in the  $10^\circ$  case as a result of separation around the locomotive. Very close to the train, the flow reattaches at approximately  $x=25$  m and after which, lower velocities exist along train length. A region of higher-than-crosswind velocity is visible at  $x=60$  m and  $y=3$  m which is due to the presence of a recirculation region causing an increased lateral component.

The flow on the leeward side of the 30° case exhibits massive separation which manifests as velocity which is higher than train speed. The complexity of the under floor geometry causes the flow separation to be highly-variable with distance along the train. Moving out from the leeward side of the train there is a low velocity region, followed by a higher velocity region and then a second low velocity region. The low velocity region nearest to train side is what Baker et al.(2007) described as the ‘shielding effect’ i.e. where the presence of the train ‘blocks’ the crosswind. The higher velocity region is where the low pressure field in the core of the vortex entrains the air along with the train thus giving a higher velocity than the surrounding air.

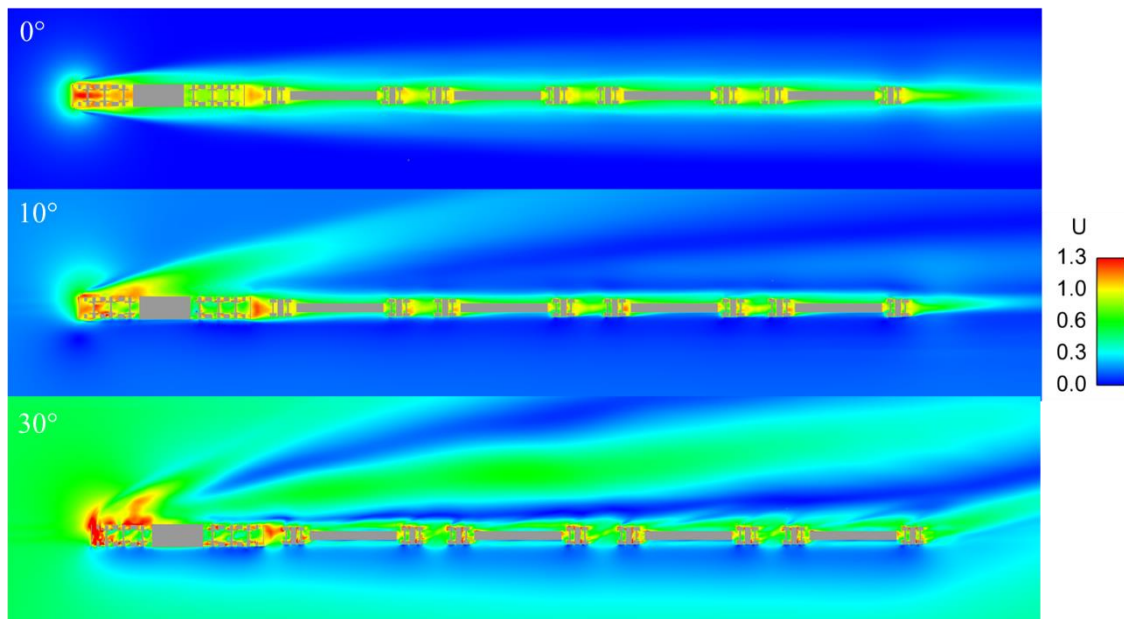


Figure 173 Time-averaged velocity magnitude at  $z=0.5$  m

Figure 174 shows the time-averaged velocity magnitude for each crosswind case on a plane at  $z=2$  m. For the no-crosswind case, the high velocity in the slipstream is localised to the nose region and once reattachment occurs the velocity remains fairly constant along train length due to a lack of local relative roughness.

The 10° crosswind case shows a similar higher velocity region on the leeward side of the locomotive to that observed at  $z=0.5$  m. Some higher velocities are observed on the leeward side of the containers, however it is unclear whether this should be defined as boundary layer region growth.

On the leeward sides of the second, third and fourth containers, regions of velocity which are higher than the surrounding air exist in the 30° case. These pockets of air are hypothesised to be a result of the result of separation around the front leeward corners of the containers.

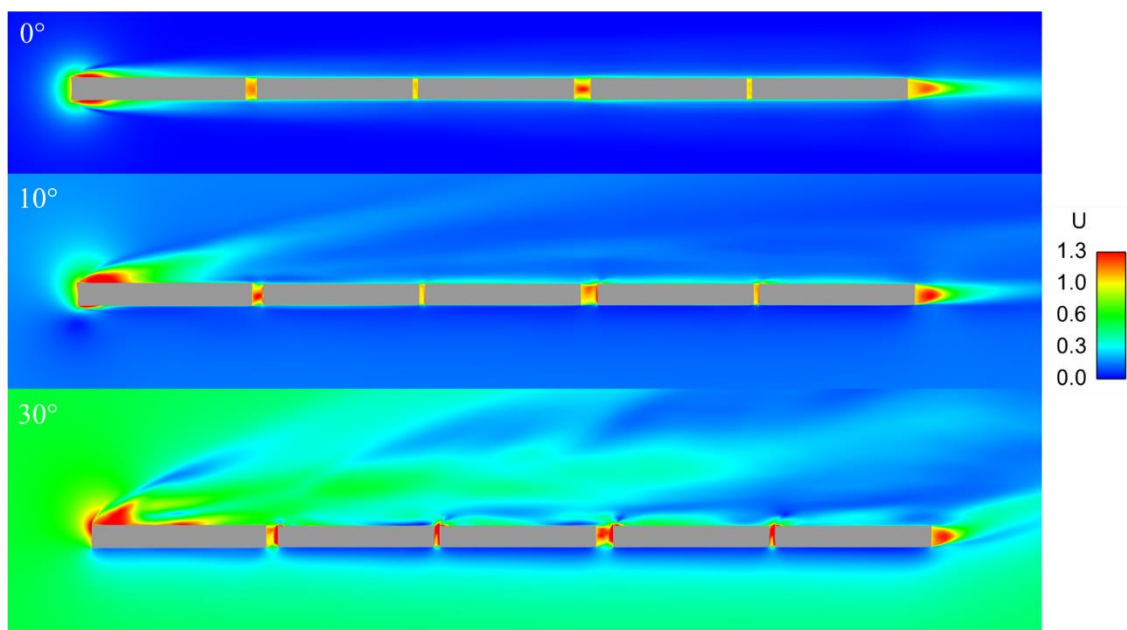


Figure 174 Time-averaged velocity profiles at  $z=2$  m

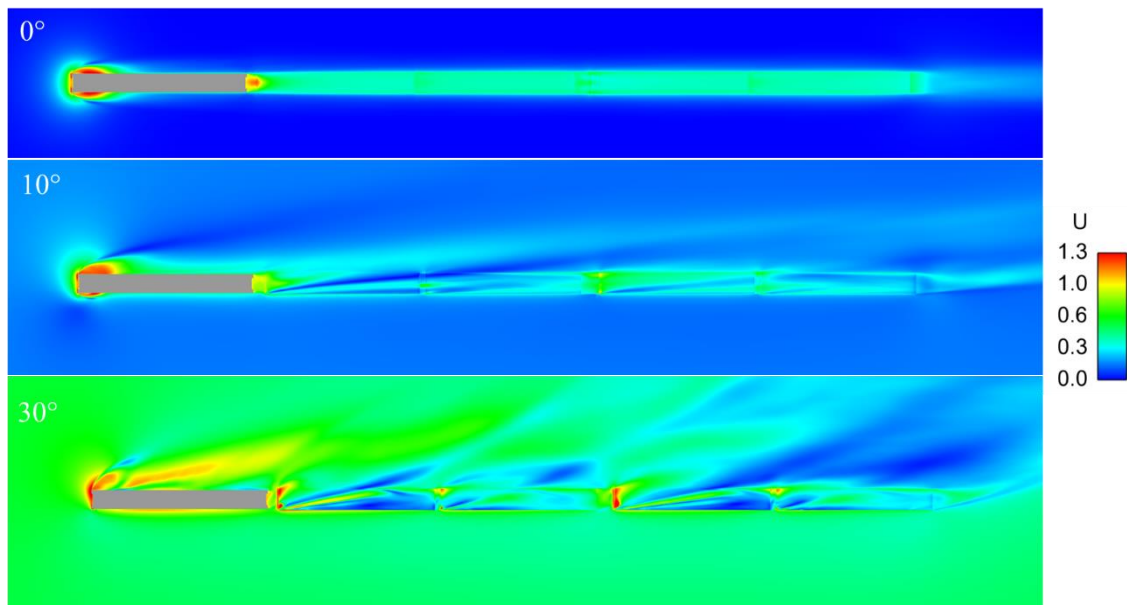


Figure 175 Time-averaged velocity profiles at  $z=4$  m

Figure 175 shows the time-averaged velocity for each case on a plane at  $z=4$  m. The no-crosswind flow separation region extends further from train side but is shorter along train length. This observation is likely to be due to effect of the slanted portion of the roof on the flow separation.

Higher velocities exist further from train side for the  $10^\circ$  crosswind case than they did for lower heights above TOR. The flow in the  $30^\circ$  case exhibits great complexity as a result of separation from the container roofs causing large velocity gradients.

### 7.3 *Instantaneous peak velocity magnitudes*

It was observed in Section 7.2 that the highest velocities are produced for all crosswinds at  $z=2$  m therefore only the velocities at this height will be presented in the current section to maintain succinctness in the presentation of the data.

To perform a peak value analysis the maxima of the velocity magnitudes from 20 time-steps in the simulations are used and the instantaneous ‘snapshot’ of the flow is considered to be the same as the flow experienced by a static observer relative to a passing train.

Figure 176 shows the peak velocity magnitudes at  $y=1.59$  m and  $z=2$  m for the no-crosswind,  $10^\circ$  and  $30^\circ$  crosswind cases. The greatest peak velocity occurs for the no-crosswind case, followed by the  $30^\circ$  and then the  $10^\circ$  case with values of  $U=1.85$ ,  $1.74$  and  $1.68$ , respectively. The mean of the peak velocities for each case are  $U_{\text{Mean}}=1.48$ ,  $1.53$  and  $1.52$  for the no-crosswind,  $10^\circ$  and  $30^\circ$  crosswind cases, respectively. The lack of distinctive trend of peak velocity against yaw angle is likely to be due to the distance at which the samples are taken from train side. All cases experience some flow separation and as such generate higher than train speed velocities. As shown in the previous section, an increase in the difference between the velocities produced in each crosswind case occurs with increasing distance from train side. The standard deviations of the instantaneous peaks are  $\sigma_U=0.16$ ,  $0.09$  and  $0.11$  for the no-crosswind,  $10^\circ$  and  $30^\circ$  crosswind cases, respectively. The greatest variation of peak velocities occurs for the no-crosswind case. A larger variation in the relative velocity was also observed at full-scale, in the slipstream of a freight train with no crosswind present (Baker et al., 2007), although a scarcity in the data prevent a full validation of the observation in the present chapter.

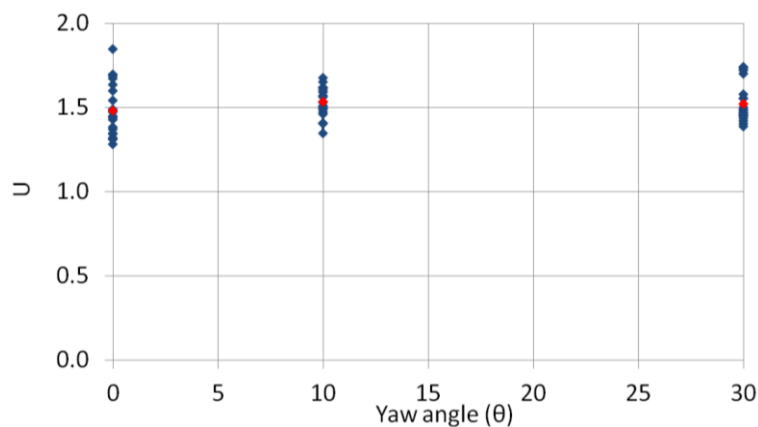


Figure 176 Instantaneous velocity magnitudes relative to a static observer at  $z=2$  m and  $y=1.59$  m for the no-crosswind,  $10^\circ$  and  $30^\circ$  crosswind cases on the leeward side of the train

Figure 177 shows the peak velocity magnitudes at  $y=1.84$  m and  $z=2$  m. The maximum velocities for each yaw angle are  $U=1.62$ ,  $1.65$  and  $1.68$  for the no-crosswind,  $10^\circ$  and  $30^\circ$

crosswind cases, respectively and the means of the peak velocities are  $U_{\text{Mean}}=1.25$ , 1.52 and 1.47 for the no-crosswind, 10° and 30° crosswind cases, respectively.

The relatively small difference between the maximum peak velocity magnitudes and the larger difference in the mean values at  $y=1.84$  m is a result of the decreasing variability of the peak velocities yaw angle. The no-crosswind case has the smallest mean and the largest standard deviation whereas the velocities from the 30° case have a larger mean but a smaller standard deviation. The standard deviations for the no-crosswind, 10° and 30° crosswind cases are  $\sigma_U=0.18$ , 0.08 and 0.10, respectively.

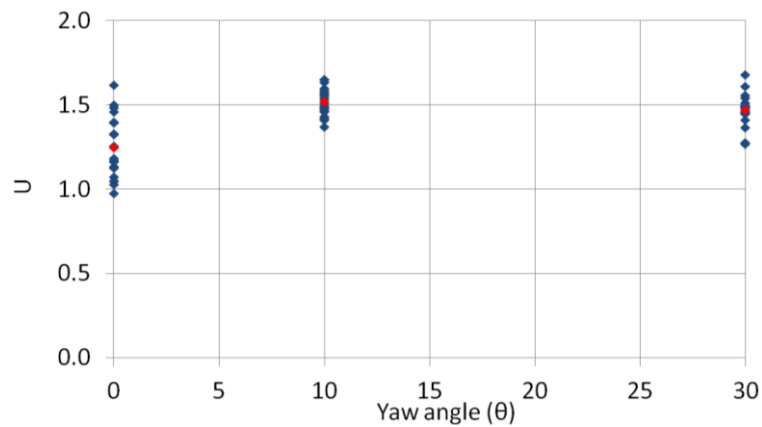


Figure 177 Instantaneous velocity magnitudes relative to a static observer at  $z=2$  m and  $y=1.84$  m for the no-crosswind, 10° and 30° crosswind cases on the leeward side of the train

Figure 178 shows the peak velocity magnitudes at  $y=2.34$  m and  $z=2$  m. The maximum velocity for each yaw angle is  $U=1.07$ , 1.62 and 1.63 for the no-crosswind, 10° and 30° crosswind cases, respectively. The peak velocity from the no-crosswind is 34 % lower than from the 10° case and the no-crosswind case at  $y=1.84$  m. The means of the peak instantaneous velocities are  $U_{\text{Mean}}=0.67$ , 1.35 and 1.49 for the no-crosswind, 10° and 30° crosswind cases, respectively. The standard deviations are  $\sigma_U=0.16$ , 0.15 and 0.10 for the no-crosswind, 10° and 30° crosswind cases, respectively. The 88 % increase in the standard

deviation in the 10° case over that observed at y=1.84 m suggests that y=2.34 m is in close proximity to the unsteady portion of the flapping shear layer around the locomotive.

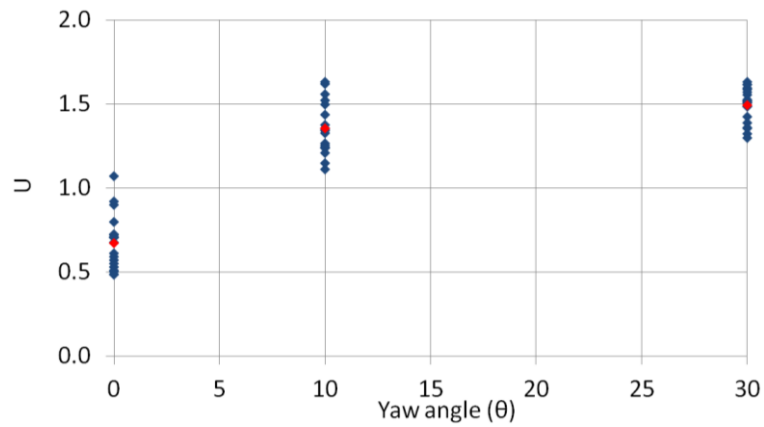


Figure 178 Instantaneous velocity magnitudes relative to a static observer at  $z=2$  m and  $y=2.34$  m for the no-crosswind, 10° and 30° crosswind cases on the leeward side of the train

Figure 179 shows the peak velocity magnitudes at  $y=3.34$  m and  $z=2$  m. The maximum velocities for each yaw angle are  $U=0.66$ , 1.16 and 1.66 for the no-crosswind, 10° and 30° crosswind cases, respectively and the means of the peak instantaneous velocities are  $U_{\text{Mean}}=0.41$ , 0.93 and 1.47 for the no-crosswind, 10° and 30° crosswind cases, respectively. The mean and maximum peak velocities show the most distinctive variation with yaw angle yet to be witnessed at train side.

The standard deviations are  $\sigma_U=0.13$ , 0.11 and 0.08 for the no-crosswind, 10° and 30° crosswind cases, respectively. The 28 % decrease in both the maximum velocity and standard deviation for the 10° case is hypothesised to be due to the sampling locating being further away from train side than the shear layer.

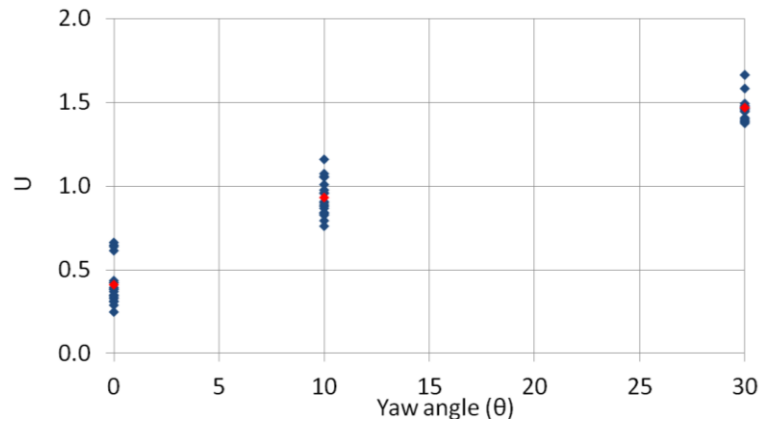


Figure 179 Instantaneous velocity magnitudes relative to a static observer at  $z=2$  m and  $y=3.34$  m for the no-crosswind,  $10^\circ$  and  $30^\circ$  crosswind cases on the leeward side of the train

#### 7.4 Time-averaged pressure

Figure 180 shows mean pressures in the slipstream on the windward side of the train at  $z=0.5$  m. For all distances from train side it can be seen that the  $30^\circ$  case produces the greatest positive nose pressure peak whereas the no-crosswind case has the greatest negative peak with values of  $C_p=0.55$  and  $C_p=-0.90$ , respectively. The  $30^\circ$  crosswind case does not exhibit the positive-negative pressure pulse such as those generated in the no-crosswind and  $10^\circ$  crosswind cases. The pressure on the windward side of the train subjected to the  $30^\circ$  crosswind is positive for the entire train length due to stagnation however, an instance of negative pressure occurs at  $x=20$  m due to the spacing between the locomotive and first container wagon.

For the majority of train length the pressure in the  $10^\circ$  case lies between the no-crosswind and  $30^\circ$  crosswind data due the lateral component causing some stagnation although only producing pressures approximately 25 % of those generated by the  $30^\circ$  crosswind.

The greatest peak-to-peak pressure transient,  $\Delta C_p$ , occurs around the locomotive for the no-crosswind case and is  $\Delta C_p=1.27$ , followed by  $\Delta C_p=1.16$  in the  $10^\circ$  case. The greatest peak-to-

peak pressure transient on the windward side of the freight train for the 30° crosswind is  $\Delta C_p=0.65$  and occurs at  $y=1.59$  m.

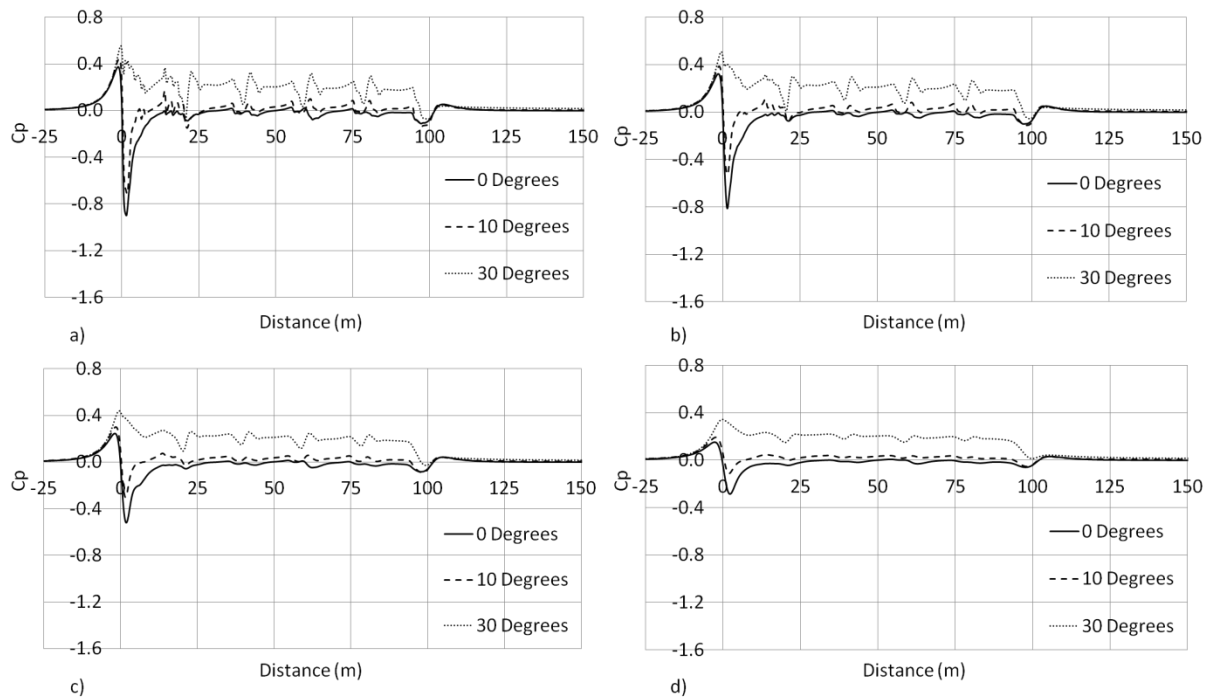


Figure 180 Slipstream pressure coefficients relative to a static observer at  $z=0.5$  m at a)  $y=1.59$  m, b)  $y=1.84$  m, c)  $y=2.34$  m and d)  $y=3.34$  m for the no-crosswind, 10° and 30° crosswind cases on the windward side of the train

The largest positive nose pressure-pulse at  $z=2$  m is obtained from the 30° crosswind case with a value of  $C_p=0.70$  (Figure 181). The greatest negative peak is from the no-crosswind case for all distances from COT except  $y=1.59$  m where the 10° case produces the lowest pressure of  $C_p=-0.92$ . The transients at the inter-wagon spacings are most significant for the 30° case where the greatest transient in the boundary layer region is  $\Delta C_p=0.45$ , at  $y=1.59$  m. The wake transients are comparable for all cases at  $y=1.59$  m and  $y=1.84$  m, although the 30° crosswind exhibits a different behaviour at  $y=2.34$  m and  $y=3.34$  m.

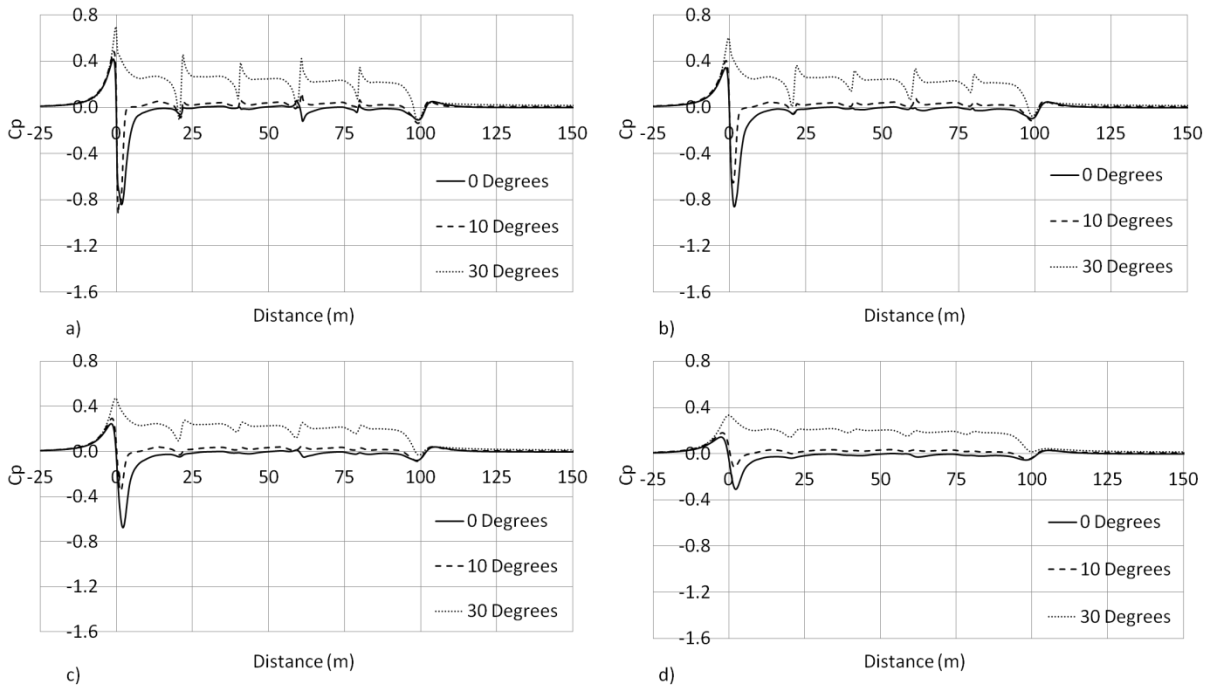


Figure 181 Slipstream pressure coefficients relative to a static observer at  $z=2$  m at a)  $y=1.59$  m, b)  $y=1.84$  m, c)  $y=2.34$  m and d)  $y=3.34$  m for the no-crosswind,  $10^\circ$  and  $30^\circ$  crosswind cases on the windward side of the train

Figure 182 shows mean pressure in the slipstream on the windward side of the train at  $z=4$  m. The greatest positive and negative peak pressures occur in the slipstreams of the  $30^\circ$  and  $10^\circ$  cases and are  $C_p=0.38$  and  $C_p=-0.86$ , respectively. The  $30^\circ$  case exhibits negative pressure along the length of the locomotive at  $y=1.59$  m and  $y=1.84$  m as a result of the flow separating over its roof. The pressure from the no- and  $10^\circ$  crosswind cases remains relatively constant along train length whereas the pressure from the  $30^\circ$  case increases with distance from train side due to the reducing effect of the roof flow separation. The greatest mean peak-to-peak pressure transient is  $\Delta C_p=1.19$  and occurs at  $y=1.59$  m for the  $10^\circ$  crosswind case.

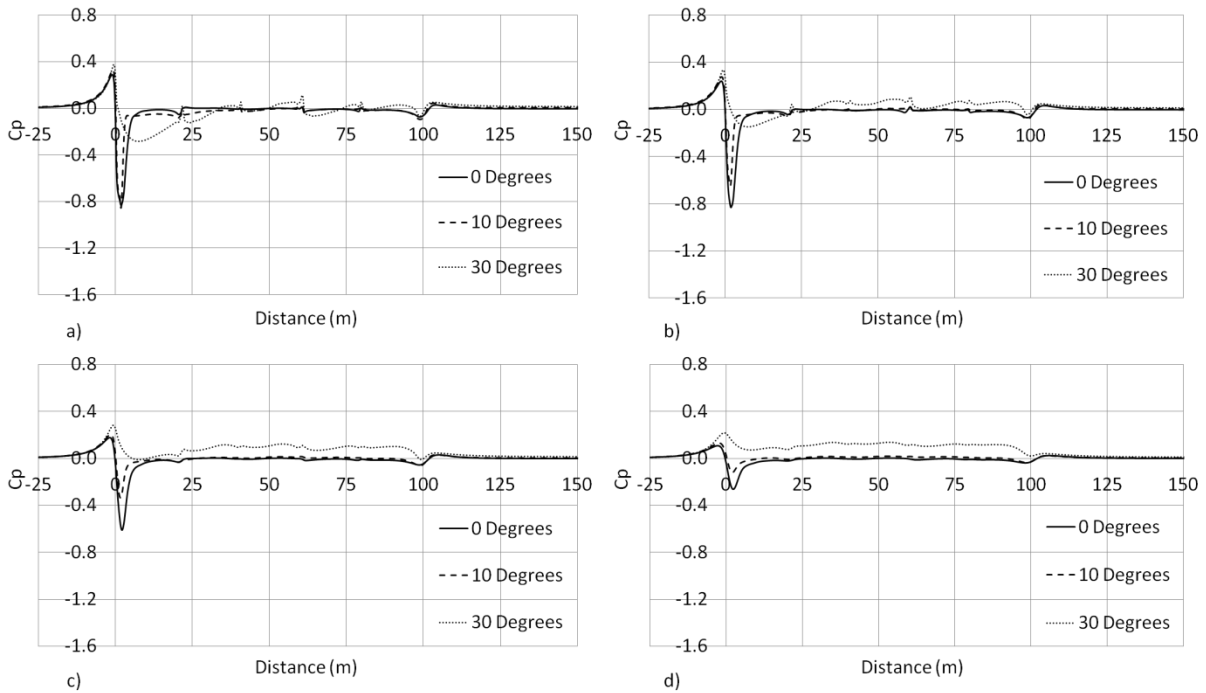


Figure 182 Slipstream pressure coefficients relative to a static observer at  $z=4$  m at a)  $y=1.59$  m, b)  $y=1.84$  m, c)  $y=2.34$  m and d)  $y=3.34$  m for the no-crosswind,  $10^\circ$  and  $30^\circ$  crosswind cases on the windward side of the train

The negative pressure on the leeward side of the train at  $z=0.5$  m is greatest for the  $30^\circ$  case at all distances from COT with the lowest value being  $C_p=-0.95$  (Figure 183). The positive nose peak pressures for the no- and  $10^\circ$  crosswinds remain within 10 % of each other for all distances from COT. The negative pressure from the no-crosswind case is greater than the  $10^\circ$  case for  $y=1.59$  m, however at  $y=1.84$  m,  $y=2.34$  m and  $y=3.34$  m the  $10^\circ$  case's pressure is either equal or greater.

The behaviour of the  $30^\circ$  crosswind nose transient is significantly different in comparison to those from the no- and  $10^\circ$  crosswinds. The peak-to-peak pressure transients for the no- and  $10^\circ$  crosswind cases produce values of  $\Delta C_p=1.27$  and  $\Delta C_p=1.16$ , respectively. After the no-crosswind and  $10^\circ$  transients reach their negative maxima, the pressures then return to approximately 0 along train length whereas the  $30^\circ$  crosswind reaches a negative peak and then fluctuates about  $C_p=-0.25$ .

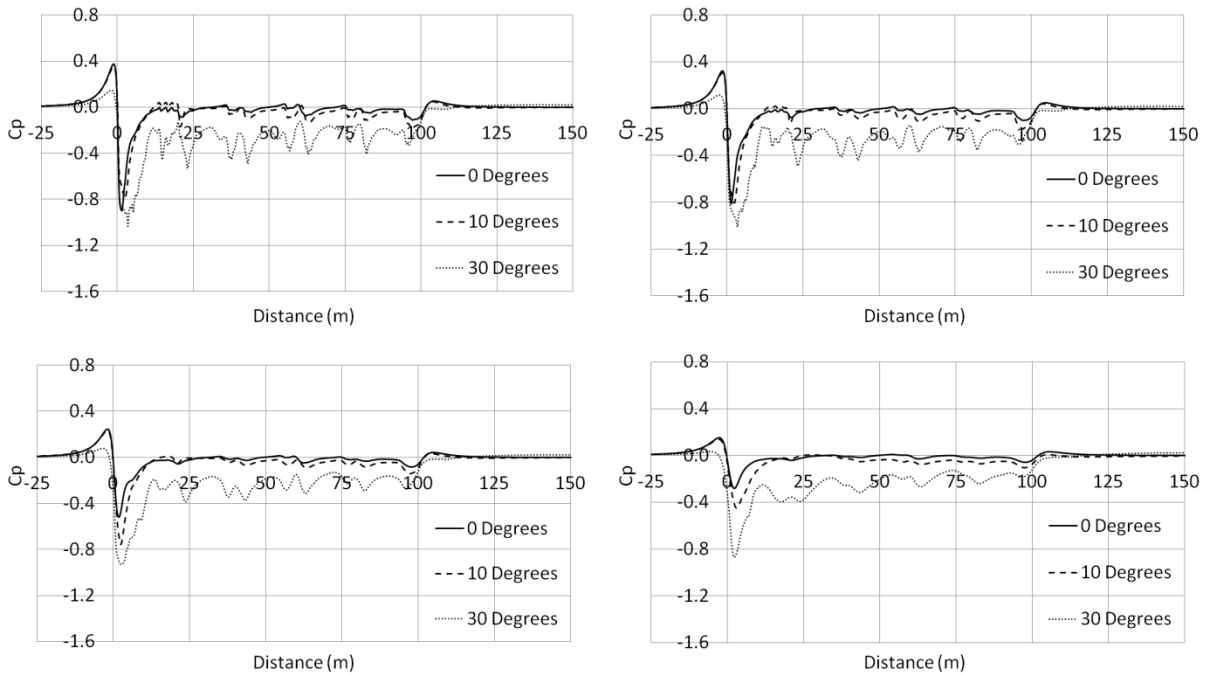


Figure 183 Slipstream pressure coefficients relative to a static observer at  $z=0.5$  m at a)  $y=1.59$  m, b)  $y=1.84$  m, c)  $y=2.34$  m and d)  $y=3.34$  m for the no-crosswind,  $10^\circ$  and  $30^\circ$  crosswind cases on the leeward side of the train

Figure 184 shows the pressure isosurfaces ( $C_p=-0.3$ ) around the locomotive for the no-crosswind,  $10^\circ$  and  $30^\circ$  crosswind cases. For the no-crosswind case, the pressure isosurface is symmetrical and is seen to extend further along the length of the locomotive at positions closer to the ground as a result of separation around the air dam and bogies. The pressure isosurface around the locomotive in the presence of a  $10^\circ$  crosswind extends half as far from the windward side of the train than is observed in the no-crosswind case. On the leeward side of the train, the isosurface extends 40 % further from train side and more than 50 % further along the locomotive than occurs in the no-crosswind case.

The negative pressure region around the locomotive for the  $30^\circ$  crosswind is significantly larger than for the other two cases due to the greater degree of flow separation. In Figure 183 it was observed that the pressure in the  $30^\circ$  case does not return to 0 after the transient, but to

a value of approximately  $C_p=-0.25$ . The characteristics of the pressure in the 30° case (Figure 183) are illustrated by the topology isosurface in Figure 184c.

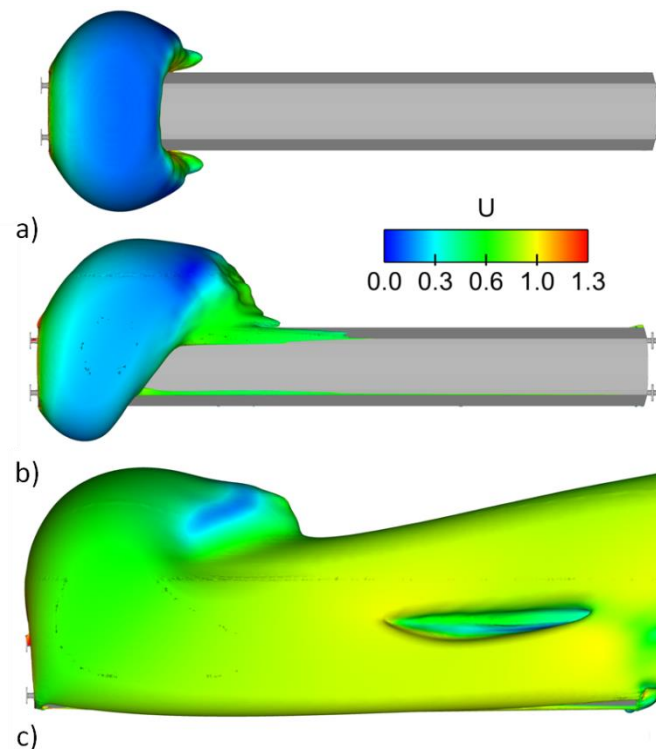


Figure 184 Time-averaged pressure isosurfaces ( $C_p=-0.3$ ) around the locomotive, coloured by velocity magnitude for the a) no-crosswind, b) 10° crosswind and c) 30° crosswind cases

The significant difference between the flow regimes around the train for the no-crosswind, 10° and 30° cases is highlighted by pressure coefficient as seen in Figure 185. In the 30° case the nose transient has the most pronounced double-peak behaviour at  $y=2.34$  m and  $y=3.34$  m whereas in the 10° and no-crosswind cases only a single nose peak is observed. At  $y=2.34$  m and  $y=3.34$  m the peak-to-peak pressure transients for the 10° and 30° cases are  $\Delta C_p=1.05$  and  $\Delta C_p=1.28$ , respectively.

As was observed at  $z=0.5$  m, the no-crosswind case has a greater negative nose pressure pulse than the 10° crosswind at  $y=1.59$  m and  $y=1.84$  m, although at  $y=2.34$  m and  $y=3.34$  m the contrary is true. The duration of the negative portion of the 10° nose pressure transient is

longer than occurs for the no-crosswind case as illustrated by the longer pressure isosurface at mid-height in Figure 184.

The pressure transients at the inter-wagon spacings for the 30° crosswind case are greater than, or close to the magnitude of the nose transient for the 10° crosswind case, at  $y=1.59$  m. The greatest transient in the boundary layer region is from the 30° crosswind case and is  $\Delta C_p=1.15$ .

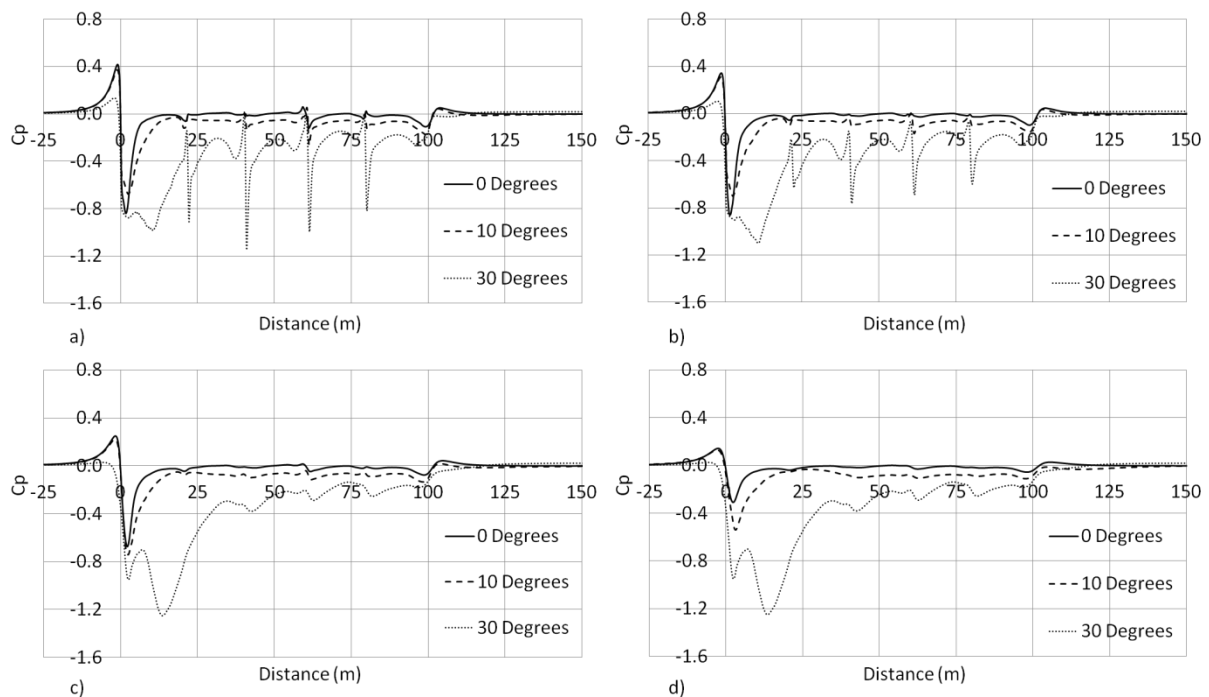


Figure 185 Slipstream pressure coefficients relative to a static observer at  $z=2$  m at a)  $y=1.59$  m, b)  $y=1.84$  m, c)  $y=2.34$  m and d)  $y=3.34$  m for the no-crosswind, 10° and 30° crosswind cases on the leeward side of the train

Figure 186 shows the pressure coefficients at  $z=4$  m on the leeward side of the train. Between  $x=0$  m and  $x=100$  m the pressure in the slipstream of the 30° case remains negative, the same is true in the 10° case however lesser magnitudes occur. The 30° crosswind exhibits smaller transients at the inter-wagon spacings than occurred at  $z=2$  m, and the presence of the double nose peak along the locomotive only exists at  $y=3.34$  m.

The peak negative pressure for the 30° case is  $C_p=-0.95$  and the pressure remains relatively constant with increasing distance from train side with negative pressure falling to  $C_p=-0.94$  at  $y=3.34$  m whereas the pressures from the no- and 10° crosswind cases decrease more rapidly over the same distance from train side. Peak negative values for the no- and 10° cases at  $y=1.59$  m are  $C_p=-0.83$  and  $C_p=-0.76$ , respectively, but at  $y=3.34$  m, peak negative pressures for the no- and 10° cases fall to  $C_p=-0.26$  and  $C_p=-0.45$ , respectively.

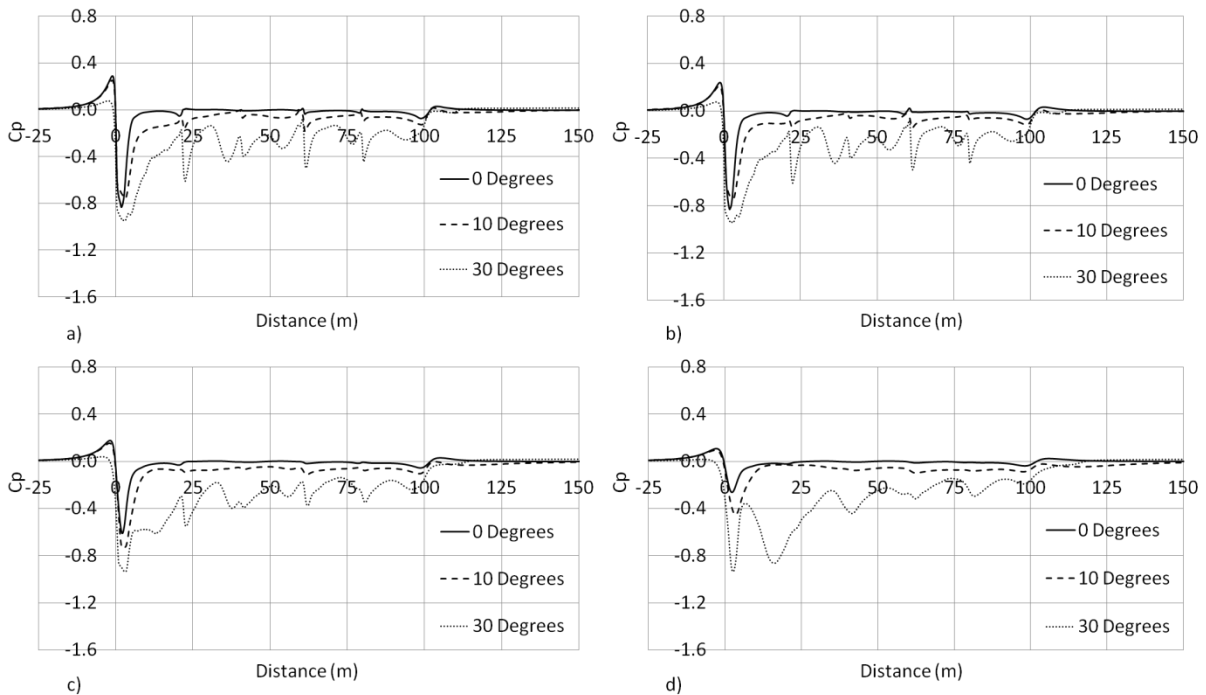


Figure 186 Slipstream pressure coefficients relative to a static observer at  $z=4$  m at a)  $y=1.59$  m, b)  $y=1.84$  m, c)  $y=2.34$  m and d)  $y=3.34$  m for the no-crosswind, 10° and 30° crosswind cases on the leeward side of the train

Figure 187 shows the time-averaged pressure on a plane at  $z=0.5$  m for all cases. The pressure field in the no-crosswind case, is highest in ahead of the train and lowest underneath and around the front of the locomotive. A small region of low pressure is observed in the wake of the train but at a lower magnitude than in the nose region.

The 10° case shows an asymmetrical pressure field around the locomotive as was initially observed in Figure 184. The positive pressure field on the front face of the locomotive

remains largely indifferent to the effect of the crosswind insomuch as it is superficially comparable to the pressure field in the no-crosswind case. Greater positive pressures are observed beneath the 10° case due to relatively unimpeded flow in comparison to the no-crosswind case where any flow reaching the underbody of a flat-liner will already have stagnated or been otherwise affected by a previous wagon.

The leeward region of the 30° case is dominated by a pressure field below  $C_p = -0.3$ . The low pressure region is observed to convect away from train side, at a yaw angle of approximately  $\theta \approx 7^\circ$ . The positive pressure field on the windward side of the train exhibits a trend of decreasing along train length, which is hypothesised to be due to the frictional effects of the inter-wagon spacings allowing the pressure to diffuse through them.

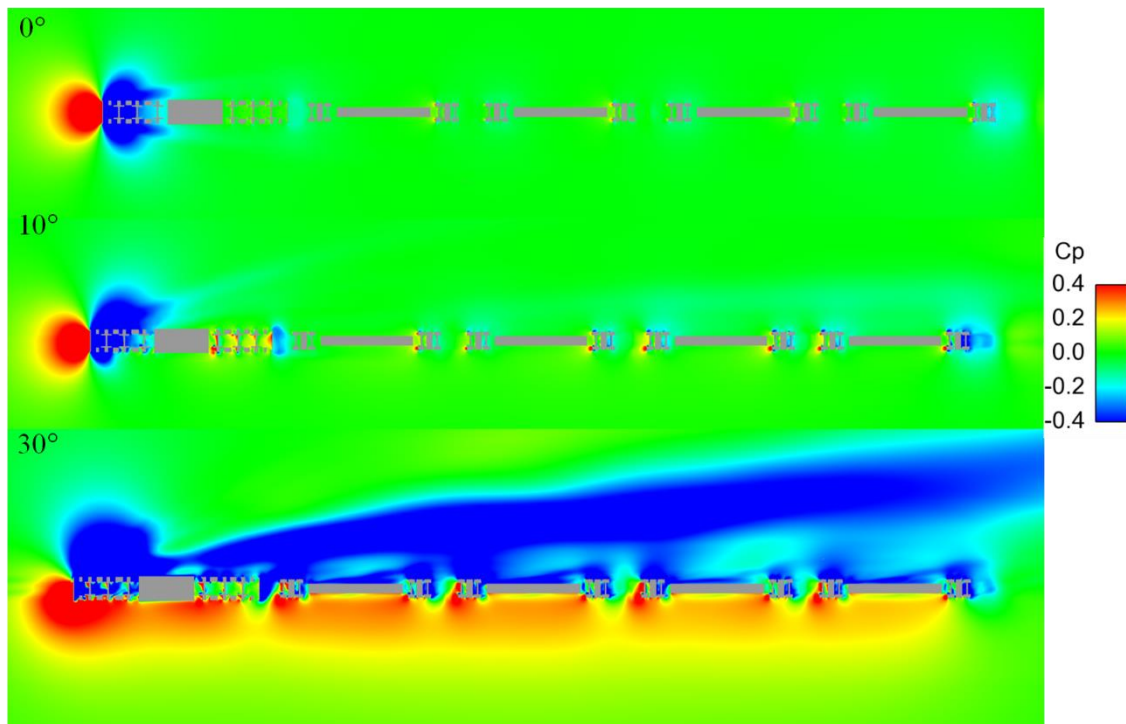


Figure 187 Colour plot of time-averaged pressure at  $z=0.5$  m

Figure 188 shows the pressure around the train at  $z=2$  m for all three cases. The pressure field around front of the locomotive in the no-crosswind case does not extend as far from train side as it does at  $z=0.5$  m and the 10° case exhibits negative pressure on the windward side of the

locomotive. On the leeward side of the third wagon in the 30° case, a reduced low pressure region exists between the lower-pressure vortex and the train. After this point, the leeward vortex is observed to move further from train side and this movement is hypothesised to be a result of the larger inter-wagon spacing causing an equalisation of the negative pressure field.

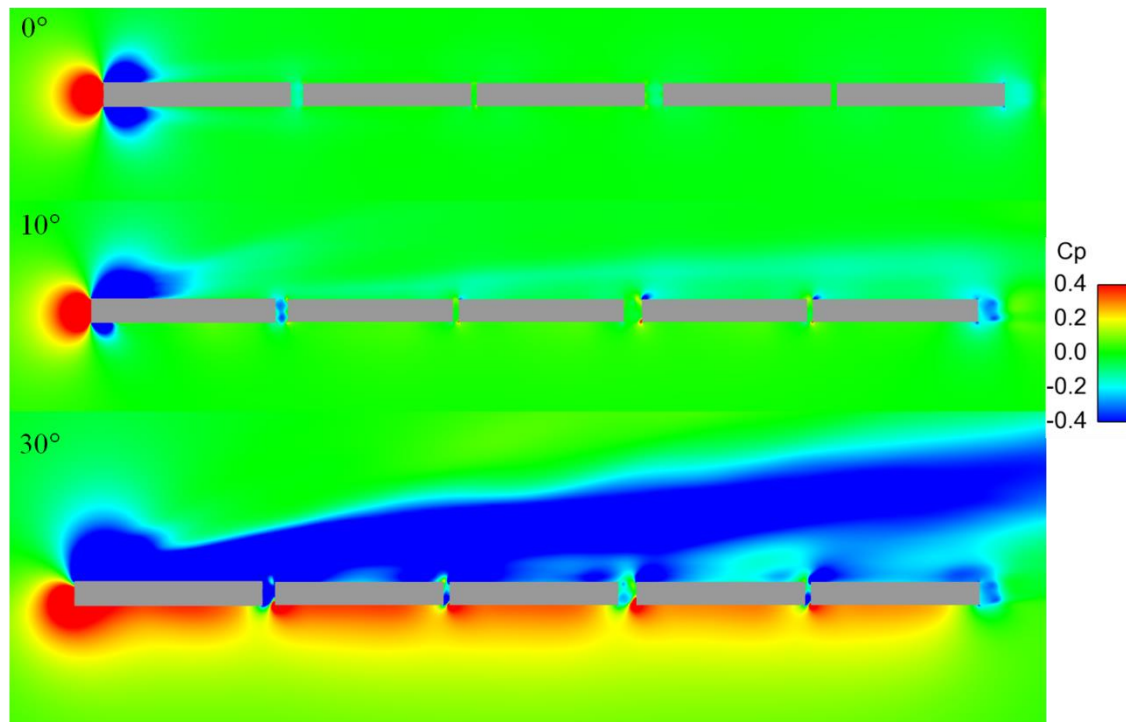


Figure 188 Colour plot of time-averaged pressure at  $z=2$  m

The pressure field around the train at  $z=4$  m is shown in Figure 189. The pressure above the largest inter-wagon spacing for the no-crosswind case is observed to be negative and positive for the rear end of the second and front end of the third containers, respectively. The pressure above the roof of the containers is lower for the 30° case than for the 10° case as a result of the enhanced flow separation due to the higher lateral component.

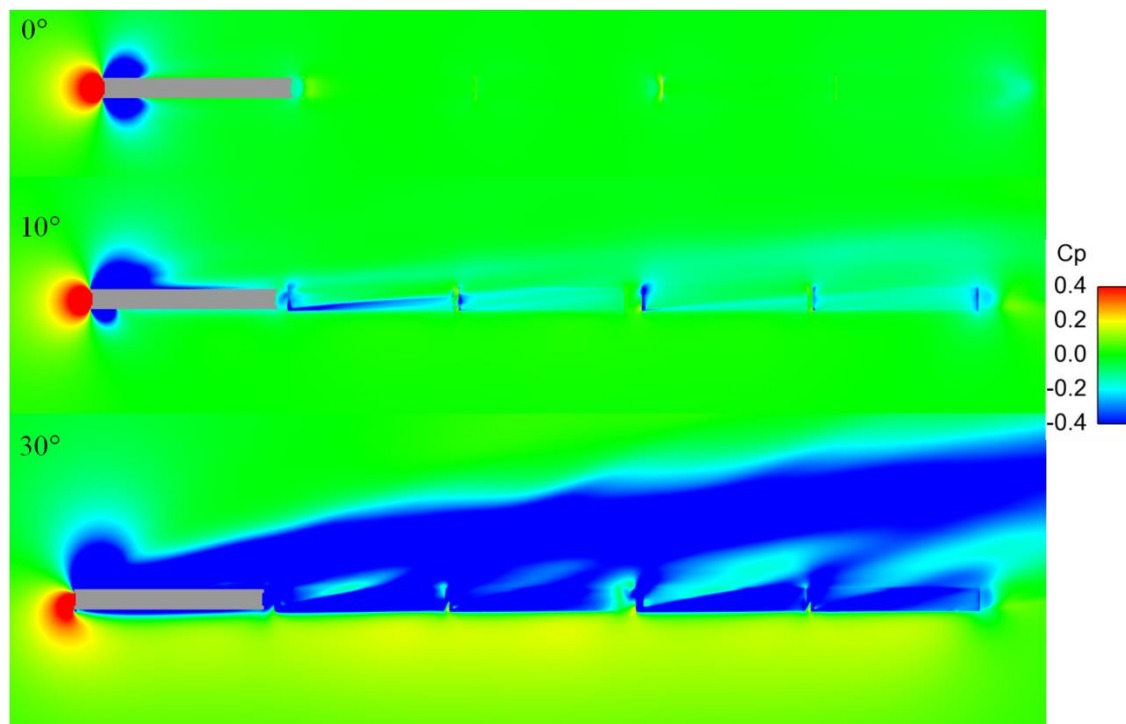


Figure 189 Colour plot of time-averaged pressure at  $z=4$  m

### 7.5 *Instantaneous peak-to-peak pressure transients*

The current section shows the value of 20 instantaneous peak-to-peak pressure transients for each yaw angle at  $z=2$  m. The benefit of using instantaneous instead of time-averaged transients, is that a person will experience an instantaneous transient and not a time-averaged one. Furthermore, using instantaneous data allows for the range of pressures which occur around the locomotive to be highlighted.

Figure 190 shows instantaneous peak-to-peak pressure transients obtained at  $y=1.59$  m from the no-crosswind,  $10^\circ$  and  $30^\circ$  crosswinds. The maximum peak-to-peak pressure transients are  $\Delta C_p=1.78$ ,  $1.44$  and  $1.81$  for the no-crosswind,  $10^\circ$  and  $30^\circ$  crosswinds, respectively. Mean values of the peak-to-peak pressure transients are  $\Delta C_{p\text{Mean}}=1.51$ ,  $1.17$  and  $1.60$  for the no-crosswind,  $10^\circ$  and  $30^\circ$  crosswinds, respectively. The data in Figure 190 exhibit the decreasing and then increasing trend which occurred for the instantaneous peak velocity data in Figure 176. Although the maximum and mean of the peak-to-peak pressure transients show

a variable trend with increasing yaw angle, the standard deviations show a trend of decreasing with yaw angle with values of  $\Delta C_{p\sigma}=0.15, 0.12$  and  $0.10$  for the no-crosswind,  $10^\circ$  and  $30^\circ$  crosswinds, respectively.

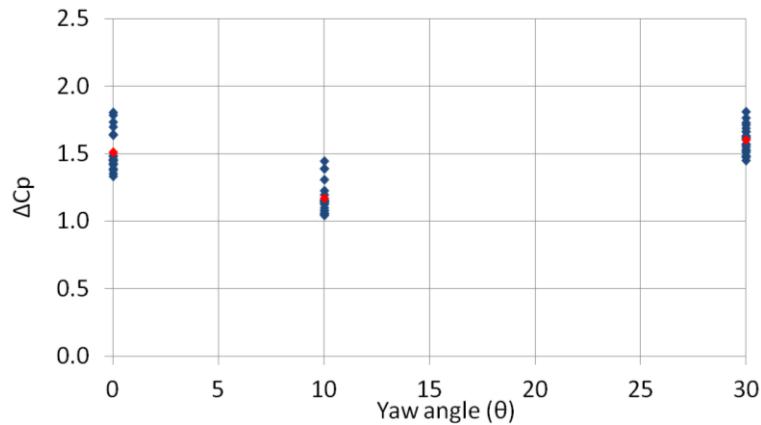


Figure 190 Instantaneous pressure transient magnitudes (blue) for  $y=1.59$  m and  $z=2$  m with mean values (red)

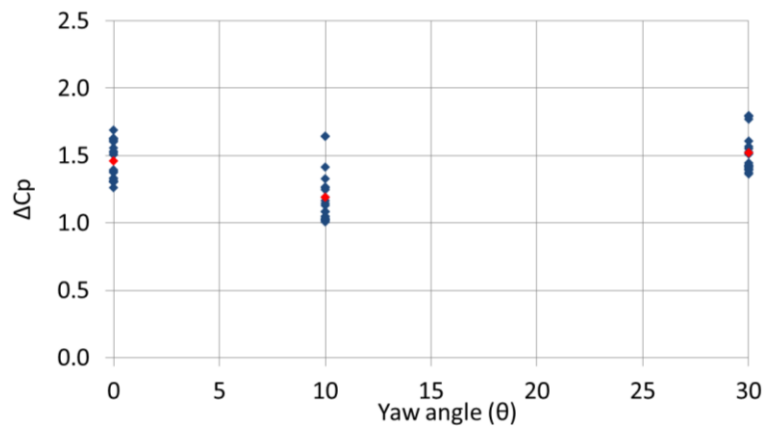


Figure 191 Instantaneous pressure transient magnitudes (blue) for  $y=1.84$  m and  $z=2$  m with mean values (red)

The instantaneous peak-to-peak pressure transients at  $y=1.84$  m for the three cases are shown in Figure 191. The maximum values for the instantaneous peak-to-peak pressures transients are  $\Delta C_p=1.69, 1.64$  and  $1.79$  for the no-crosswind,  $10^\circ$  and  $30^\circ$  crosswinds, respectively. The trend of decreasing and the increasing maximum velocities with increasing yaw angle also occurs at  $y=1.84$  m. Furthermore, the mean values exhibit a similar trend with values of  $\Delta C_{pMean} = 1.46, 1.19$  and  $1.52$  for the no-crosswind,  $10^\circ$  and  $30^\circ$  crosswinds, respectively. The

standard deviation of the instantaneous peak-to-peak pressure transients are  $\Delta C_{p\sigma}=0.14$ , 0.19 and 0.15 for the no-crosswind, 10° and 30° crosswinds, respectively.

The peak-to-peak pressure transients at  $y=2.34$  m are shown in Figure 192. The maxima of the peak-to-peak pressure transients exhibit a decrease and then an increase with increasing yaw angle, whereas the mean and minima both show monotonic increases. The maxima are  $\Delta C_p=1.88$  1.75 and 2.07 for the no-crosswind, 10° and 30° crosswinds, respectively. The mean values on the other hand are  $\Delta C_{pMean}=1.19$  1.34 and 1.73 for the no-crosswind, 10° and 30° crosswind cases, respectively. The standard deviation of the instantaneous peak-to-peak pressure transients are  $\Delta C_{p\sigma}=0.22$ , 0.21 and 0.17 for the no-crosswind, 10° and 30° crosswinds, respectively. The overall increase in the variability in  $\Delta C_p$  values with distance from train side is in line with observations for peak velocity magnitudes (Figure 178).

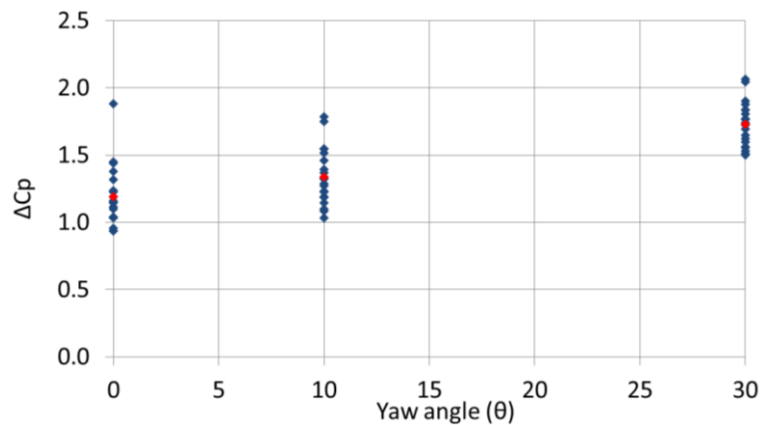


Figure 192 Instantaneous pressure transient magnitudes (blue) for  $y=2.34$  m and  $z=2$  m with mean values (red)

The maximum, mean and minimum peak-to-peak pressure transients show an increase with increasing yaw angle in the slipstream for the first time at train side (Figure 193). The maximum peak-to-peak pressure transient for each yaw angle is  $\Delta C_p=0.60$ , 1.47 and 1.91 for the no-crosswind, 10° and 30° cases, respectively. The mean of the peak-to-peak pressure transients for each yaw angle is  $\Delta C_{pMean}=0.49$ , 0.93 and 1.56 for the no-crosswind, 10° and 30° crosswinds, respectively. The variation of the peak-to-peak pressure is seen to be greatest

at  $10^\circ$  where the standard deviation is  $\Delta C_{p\sigma}=0.24$ , in comparison to  $\Delta C_{p\sigma}=0.03$  and  $0.11$ , for the no- and  $30^\circ$  crosswind cases, respectively. The standard deviation of the peak-to-peak pressure transients at  $10^\circ$  is the greatest for any crosswind case or position from COT, highlighting the massive unsteadiness which exists there.

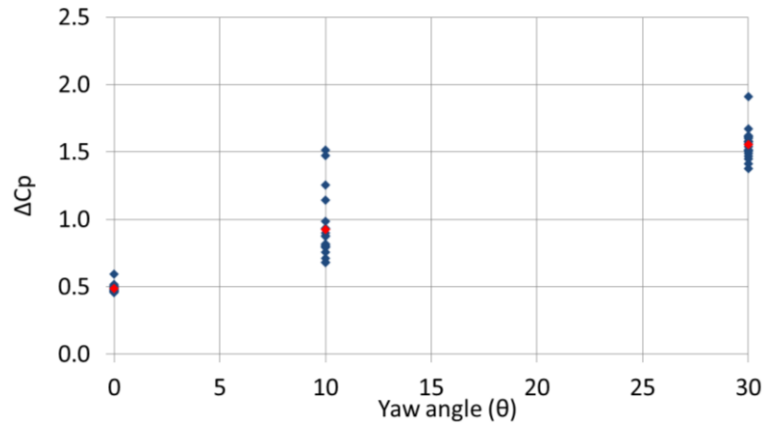


Figure 193 Instantaneous pressure transient magnitudes (blue) for  $y=3.34$  m and  $z=2$  m with mean values (red)

## 7.6 Force coefficients

Figure 194 shows the drag forces experienced by the locomotive and each container for the no-crosswind,  $10^\circ$  and  $30^\circ$  crosswind cases. It is observed that the locomotive and containers experienced the highest drag coefficient,  $C_d$ , in the  $10^\circ$  crosswind case. The higher  $C_d$  experienced by the containers are a result of the additional lateral component of the crosswind causing stagnation on the front faces which are not be exposed to direct flow in the no-crosswind case. The drag forces experienced by the locomotive in the  $10^\circ$  and  $30^\circ$  cases are  $C_d=1.26$  and  $C_d=1.24$ , respectively. The drag forces experienced by the containers in the no-crosswind case monotonically increase in with loading position although this is not the case for the  $10^\circ$  and  $30^\circ$  cases where massive variability occurs. Golovanevskiy et al.(2012) showed that for their train the increase in drag force for a given wagon was monotonic with yaw angle. Furthermore, they used regularly-spaced container wagons thus a slightly different force against loading position profile is anticipated.

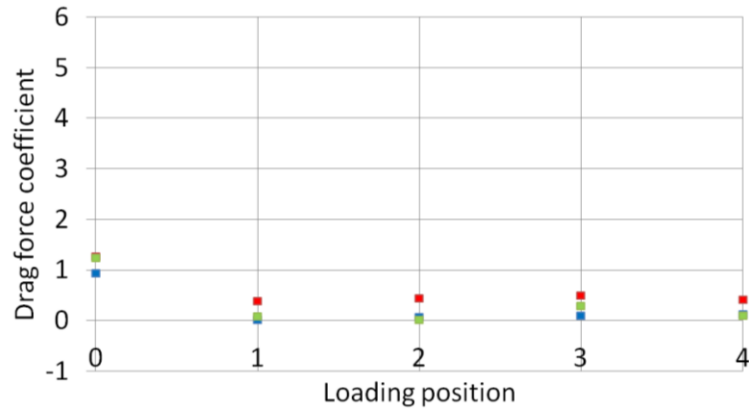


Figure 194 Drag force coefficient against loading position for the no-crosswind (blue), 10° crosswind (red) and 30° crosswind (green) cases

Figure 195 shows the side force coefficients,  $C_s$ , on the locomotive and each container for the no-crosswind, 10° and 30° crosswind cases. The side force on the locomotive and containers is greatest in the 30° crosswind case and the relatively large aerodynamic load is due to the greater track-normal velocity component which induces massive flow separation on the leeward side of the train. The side force coefficient on the locomotive in the 30° case is five times greater than the next closest value which is obtained from the 10° crosswind case. The side force coefficient on the third container is lower than on the second for the 30° case which is hypothesised to be due to an equalisation of pressure between the windward and leeward sides of the container as shown in Figure 188.

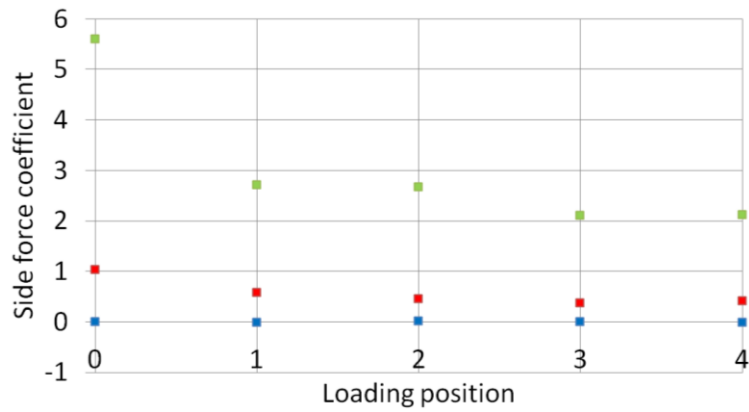


Figure 195 Side force coefficient against loading position for the no-crosswind (blue), 10° crosswind (red) and 30° crosswind (green) cases

Figure 196 shows the lift force coefficients,  $C_l$ , on the locomotive and each container for the no-crosswind, 10° and 30° crosswind cases. The lift forces experienced by the locomotive and containers in no-crosswind and 10° cases are dwarfed by those in the 30° case. The data in Figure 196 are a reflection of the low-pressure region above the container roofs initially presented in Figure 189. Although the 10° crosswind has a lateral component, it is only 32 % of the lateral component in the 30° case and therefore the separation over the roof is greatly reduced and thus significantly lower force coefficients occur.

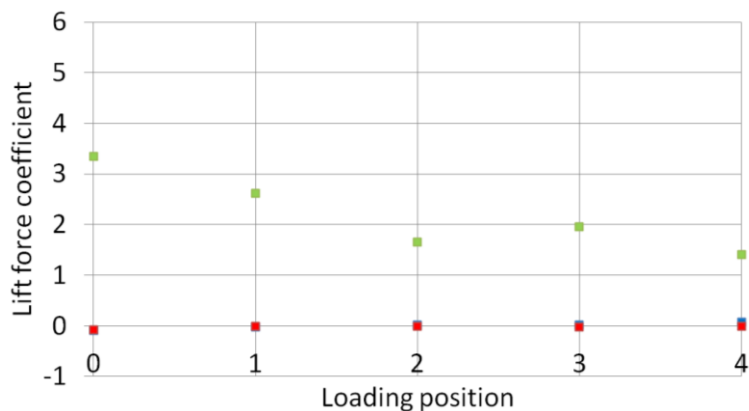


Figure 196 Lift force coefficient against loading position for the no-crosswind (blue), 10° crosswind (red) and 30° crosswind (green) cases

The general trend with each force coefficient in the current section is a decrease with loading position except for the drag force in the no-crosswind case which exhibits a very gradual increase. From this trend of decreasing force coefficients it becomes more evident that the use of an isolated container or small number of containers to reproduce force coefficients experienced by containers in a freight train is bad practice, especially considering the length of operational freight trains (Alam and Watkins, 2007). There may be some advantage to using a small number of wagons when considering worst-case scenarios for overturning, although that is out of the scope of this thesis. The locomotive used in the analysis is especially bluff when compared to other locomotive types and it may be the case that the Class 66 locomotive would have a greater effect on the force coefficients on subsequent wagons than other locomotive designs. To this end, it is recommended that locomotives are included in crosswind force assessments on container wagons, especially at lower yaw angles where a locomotive's influence is greatest.

## 7.7 *Concluding remarks*

This chapter presented a comparison between mean and instantaneous velocity and pressure data on the windward and leeward sides on the train at different measurement positions for each crosswind case. Force coefficients were also considered for the locomotive and containers for each yaw angle case.

From the data presented in the current chapter the following conclusions are drawn:

- Lower pressures and higher velocities were observed on the leeward side of the train than on the windward side for higher yaw angles
- At the two furthest positions from train side, the peak instantaneous velocities and peak-to-peak pressure transients show a general trend of increasing with yaw angle
- The maximum instantaneous pressure transient is  $\Delta C_p=1.91$  and occurs for 30° case at  $y=3.34$  m

- The highest standard deviation of the instantaneous pressure transient is  $\Delta C_p=0.24$  and occurs for the  $10^\circ$  case at  $y=2.34$  m
- The maximum instantaneous velocity magnitude is  $U=1.85$  and occurs for no-crosswind case at  $y=1.59$  m
- The highest standard deviation of the instantaneous velocity magnitude is  $\sigma_U=0.18$  and occurs for the no-crosswind case at  $y=1.59$  m
- Force coefficients showed a general trend of decreasing along train length except for the no-crosswind drag
- The  $10^\circ$  case produced the highest drag forces on the locomotive and containers for all loading positions
- The  $30^\circ$  case produced the highest side and lift force coefficients for all loading positions

# Chapter 8 Human stability of a person subjected to a slipstream-generated wind gust

## 8.1 *Introduction*

The current chapter presents human instability and pushchair movement probabilities obtained from a previously-developed mathematical model (Jordan, 2008) when subjected to wind gusts obtained from the numerical simulations.

Models such as those developed by (Jordan, 2008) allow for an approximation of the likelihood of a given person becoming unsteady when subjected to wind gusts. Furthermore, by randomly-generating a relatively large number of people, with height and weight characteristics in line with national trends, the effect of the slipstream gusts on a representative portion of the population can be evaluated. Once obtained, this information can be utilised as an input to a risk-analysis framework thereby enabling the total risk of an incident to be calculated.

Following the pushchair movement tests at Apsley and reports of incidents on platforms (Temple and Howlett, 1994), pushchairs were also considered to be at risk from slipstream gusts and as such were considered in the mathematical model (Jordan, 2008). As was done with the person generation, the key factors in pushchair movement such as loading, weight, height, centre of gravity, rolling friction coefficient, wheel base width and projected area were all randomised.

## 8.2 Stability of people subjected to winds

The wind-induced force experienced by a standing person (Penwarden et al., 1978) can be calculated by

$$F(t) = \frac{1}{2} \rho u^2 A_p C_d \quad (8.1)$$

where

$A_p$  – projected area to the wind ( $m^2$ ).

Estimating the projected area of a given person to the wind can be performed using the Dubois area,  $A_{DU}$ , (Du Bois and Du Bois, 1916) which is calculated as

$$A_{DU} = 0.0769 W_p^{0.425} h_p^{0.725} \quad (8.2)$$

where

$W_p$  – weight of a person (N)

$h_p$  – height of a person (m).

The Dubois area is a convenient parameter for approximating the projected area of a person based upon easily obtainable parameters such as height and weight. The validity of the exponents were verified by Penwarden et al.(1978) for a sample size of 331 and were found to be suitable.

Penwarden et al.(1978) used wind tunnel testing to evaluate the drag force experienced by persons standing in a wind tunnel. Clothing was found to have a significant effect of forces on persons, as a result of the projected area. The orientation of a person to an oncoming wind also has a strong effect on the force on a person due to the difference in projected area. The

drag coefficients for a person facing the wind and a person side-on to the wind are  $C_d=1.17$  and  $C_d=1.01$ , respectively.

### 8.2.1 Cuboid model

It was noted by Fukuchi (1961) that a person subjected to a gust has a response time of approximately 0.375 s in which they behave as a solid object due to the speed at which the muscles react. The response of a human to a wind-induced force during the first 0.375 s can be crudely approximated as a cuboid (Figure 197) (Johnson and Prevezer, 2005). The cuboid is a very simplistic method of modelling human response to wind-loads because it can only pivot about one edge whereas a person can pivot about their toes, heels or sides of feet which all have different stability criteria (Jordan, 2008).

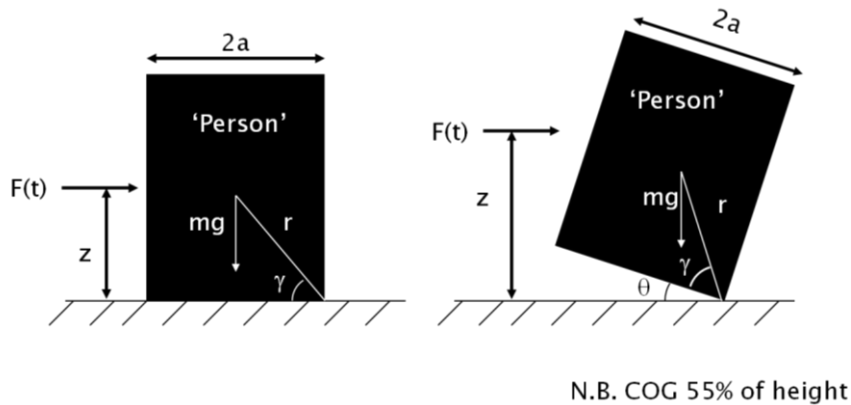


Figure 197 Cuboid subjected to a wind-induced load in original and displaced positions

Instability of the cuboid model is considered to occur when the overturning moment due to the wind force is greater than the restoring moment of the cuboid. The overturning moment due to the wind-induced force,  $M_F$ , is given as

$$M_F = F(t)[r\sin(\theta + \gamma) + a\sin(\theta)] \quad (8.3)$$

and the restoring moment,  $M_M$ , is given as

$$M_M = mgbcos(\theta + \gamma) + asin(\theta) \quad (8.4)$$

where

a – cuboid half-width (m)

b – distance from leeward corner to centre of mass (m)

m – mass of cuboid (kg)

g – gravitational acceleration ( $m/s^2$ ).

The cuboid model has the advantage of being very simple to implement although it is a gross simplification of human reaction to gusts. Furthermore, the cuboid model is only considered to be valid for 0.375 s after a young or middle-aged person is exposed to a gust, this value is 0.476 s for elderly people (Mackey and Robinovitch, 2006).

### **8.2.2 Three-mass system**

Perhaps a more realistic method of approximating the dynamic behaviour of the human body in its reaction gusts is the mass-spring-damper system developed by Jordan (2008); the schematic is shown in Figure 198. The human body is considered to consist of three masses moving relative to one another which represent the motion of the legs, torso and head, of a person with springs and dampers to represent the elastic behaviour of the muscles (Wexler et al., 1997). The displacement of the cuboid model at 0.375 s is used for the initial displacement of the mass-spring-damper model.

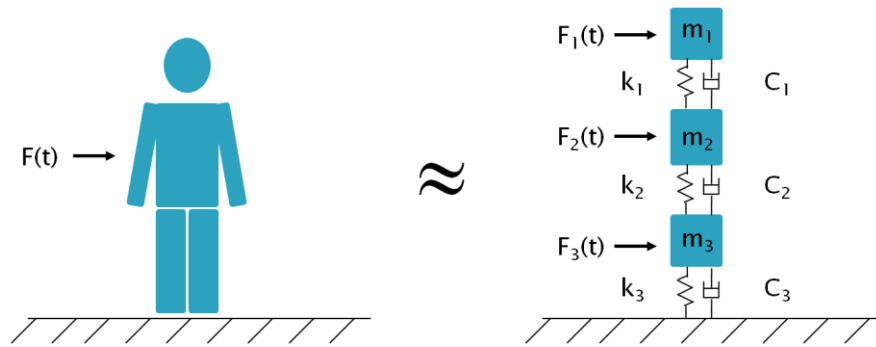


Figure 198 Mass-spring-damper stability model of person

### 8.2.3 Wind tunnel tests and model calibration

The mass-spring-damper model relies on constants in order to calibrate its behaviour to something akin to the response of a person subjected to a wind-induced force. In order to calibrate the modal constants, Jordan et al.(2008) placed 29 volunteers in a wind tunnel and measured their response to different step change gusts (Figure 199). Of the experiment participants, 12 were female and 17 were male. The volunteers were aged between 18 and 50 and the percentage weighting was 69 %, 14 %, 7 % and 10% for the 18-24, 25-30, 31-40 and 41-50 ranges, respectively. The average weight of the male and female participants was 72.2 and 53.4 kg, respectively.

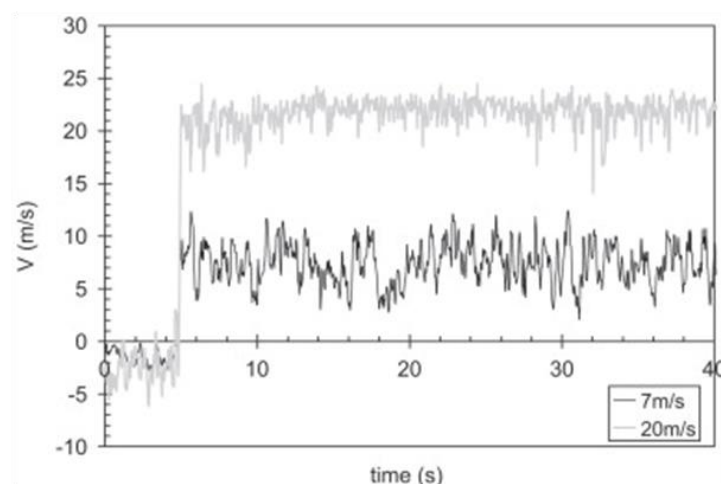


Figure 199 Wind speed profiles generated in the wind tunnel (Jordan et al., 2008)

All of the test subjects were exposed to step changes in wind at freestream velocities of 7, 10, 12 and 15 m/s, although males were subjected to a further 20 m/s gust. Females were excluded from the additional gust because of safety concerns based on previous displacement behaviour.

The wind speed step-changes were generated by using a 'fence panel' attached to a forklift truck which was reversed from in front of the participants, thus exposing them to the free-stream wind. Each group of volunteers were subjected to the gusts while standing at different orientations to the wind, allowing for the stability of each stance to be approximated.

The displacements of the volunteers were measured by a digital camera and the distances were estimated using 2x2 m squares on the wind tunnel's floor. The displacements of the test subjects could be approximated within an accuracy of 0.05 m.

Figure 200 shows instantaneous slipstream velocities from Chapter 4 compared to the gust generated by Jordan et al.(2008). Numerous instantaneous slipstream velocities are included to demonstrate the run-to-run variability of the slipstream in comparison to the single instantaneous velocity from the wind tunnel. The step change in wind speed from the wind tunnel takes approximately 0.8 s to reach the first peak, whereas the time-scale of the nose peak observed from the freight train is closer to 0.2 s. It has already been stated numerous times that gust duration is a significant factor in person instability.

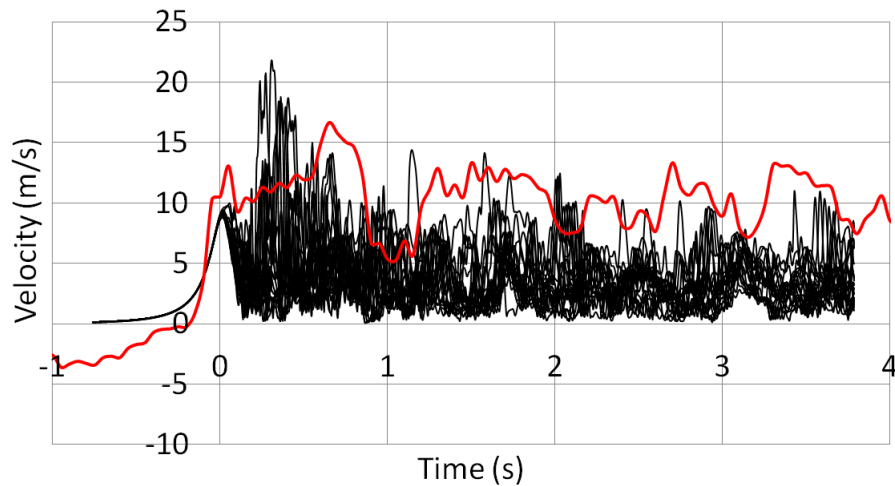


Figure 200 Instantaneous velocities from Chapter 4 at  $y=3$  m and  $z=2$  m (black) and Jordan (2008) (red)

The freight train slipstream velocities exhibit impulse gusts in the form of a dominant peak whereas the wind tunnel velocities show a step function increase and then fluctuate about the free stream mean for the wind tunnel. This difference is not likely to be significant because it is the initial gust which is responsible for person unsteadiness and once the wind stabilises about the free stream then the person has already reacted to the gust and is braced.

The three masses of the mass-spring-damper system were intended to approximate the legs, torso and head of a person with each mass given as 30, 64 and 6% of the total mass based upon data from the National Highway Traffic Safety Administration (2002).

The difference between the spring,  $k$ , and damping constants,  $C$ , connecting the torso and legs as well as torso and head are unavailable in the literature, thus the values of the spring and damping constants were kept the same i.e.  $k_1=k_2=k_3$  and  $C_1=C_2=C_3$ .

The values of total damping,  $C_{tot}$ , and frequency,  $f$ , were determined from the wind tunnel tests. Jordan (2008) investigated the effect of model sensitivity coefficients such as  $C_{tot}$ ,  $f$ ,  $C_d$  and  $A_p/A_{DU}$  on the percentage of people destabilised. It was found that setting  $C_{tot}=0$  caused 78% of people to become displaced whereas setting  $f=0.5$  Hz increased the displaced people

to 97.5 %. Increasing  $C_d$  and  $A_p/A_{DU}$  to 1.33 and 0.34, respectively caused an 87% chance of person unsteadiness. It is evident that the model has a large degree of sensitivity to input parameters but due to a scarcity of data in the literature the current parameters are the best available.

#### ***8.2.4 Pushchairs***

Pushchairs can be affected by winds in two ways: toppling and rolling. The movement of a pushchair subjected to a force is dependent on frictional coefficients which were obtained from static loading experiments. The toppling moments were also obtained from static loading tests. The orientation of the wheels and pushchairs were considered separately and a range of coefficients for each configuration were obtained. As was done with people, the key factors such as loaded pushchair weight, height, centre of gravity, wheel base width and projected area were all randomised. The force required to move or topple a pushchair was also calculated in the same way as a person from the cuboid method.

### ***8.3 Velocity inputs for person and pushchair models***

In order to simulate a wind-induced force on the person and pushchair models, input velocities were required. Each person or pushchair generated was subjected to one of 20 instantaneous velocities sampled from the CFD simulations, those from the no-crosswind case are shown in Figure 201. Unlike the velocities from Jordan (2008) only one of 20 instantaneous velocities are used for each person in the present work, so rather than a completely unique, randomly-generated velocity for each person, the randomly-generated people or pushchairs will instead be subjected to one of 20 randomly-selected velocities. It is assumed that applying the velocities from the CFD simulations to a randomly-generated person produces similar results as applying a unique randomly-generated velocity to randomly-generated people or pushchairs. The basis of this assumption is that the velocities

obtained from the simulations are numerous enough to provide a representative sample of the range of velocities which occur in a slipstream during operation.

The velocities sampled from the numerical simulations have the main advantage of possessing some physical basis, however the assumption is made that the velocities next to a static vehicle at a single instant in time are the same as those measured by a static probe when a train passes.

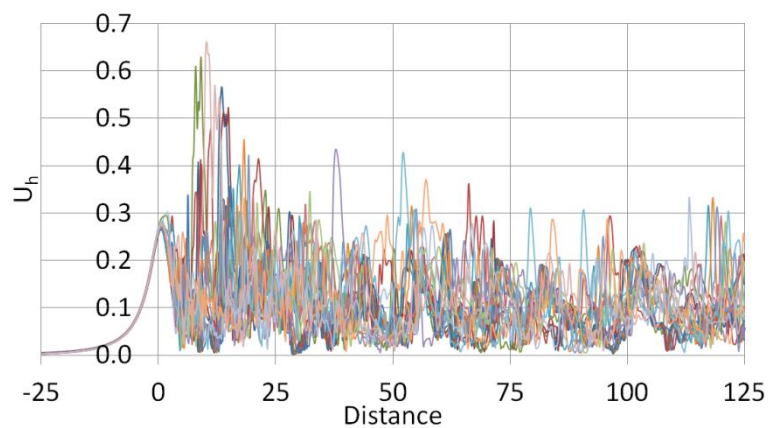


Figure 201 Instantaneous velocities at  $y=3$  m and  $z=2$  m

The person stability and pushchair models were run using velocities at five distances from COT with data from the no-crosswind,  $10^\circ$  and  $30^\circ$  crosswind cases. The sampling locations used in the previous chapters were at  $y'=0.25, 0.5, 1$  and  $2$  m and suit the purpose of showing slipstream property variation however the sampling locations used in the present chapter are chosen to show the variation in person stability at evenly-spaced positions from COT. Samples were made at  $y \geq 2$  m and  $y \leq 4$  m, with  $0.5$  m intervals.

The slipstream velocities were sampled at  $z=2$  m which, taking a standard UK platform height to be  $z=1$  m, gives velocities at approximately mid-height of a person although it is also assumed that the presence of the platform has a negligible effect on the slipstream velocity.

Velocities closer than  $y=2$  m have been neglected due to potentially misleading results because it is considered highly unlikely that a person would stand or leave their pushchair that close to the train especially considering the audible warnings and platform attendants present. Furthermore,  $y=2$  m, is 1m closer to the train than the yellow safety line position and it is considered very unlikely that any person would stand much closer to the edge of the platform than this. The furthest position of slipstream sampling was chosen as  $y=4$  m because this was at the outer portion of the high-resolution mesh region and solution quality of samples at further distances from train side cannot be assured.

#### *8.4 Randomly-generated people*

The people considered in the current model fall into six categories: boy, girl, man, woman, elderly man and elderly woman. These categories are chosen because each group has different height and weight distribution with age. When calibrating the model, Jordan (2008) did not subject children or the elderly to the wind tunnel test. However the elderly peoples' reaction times are approximated based upon observations made by Mackey and Robinovitch (2006) and children were assumed to have the same reaction times as adults.

The heights, weights and standard deviations of the people generated in the model are normally distributed about a mean value which was based upon data from the United States (National Center for Health Statistics, 2007); it was however ensured that the data were applicable to the United Kingdom. Figure 202 shows a distribution of the heights and weights of 1000 randomly-generated people from the model. The distribution is superficially comparable to that obtained by Penwarden et al.(1978) for the heights and weights of 331 test subjects which is shown for comparison in Figure 203. In the present case, the maximum height and weight is  $h_p=1.93$  m and  $W_p=118$  kg, respectively whereas the minimum height and weight is  $h_p=1.21$  m and  $W_p=18.8$  kg, respectively. The maximum height and weight of

the people used in Penwarden et al.(1978) were  $h_p=1.96$  m and  $W_p=127$  kg, respectively and the minimum height and weight were  $h_p=1.23$  m and  $W_p=24.3$  kg, respectively. It is thus shown that the heights and weights of the people used in the model are reasonable and thus sufficient for the purposes of the present work.

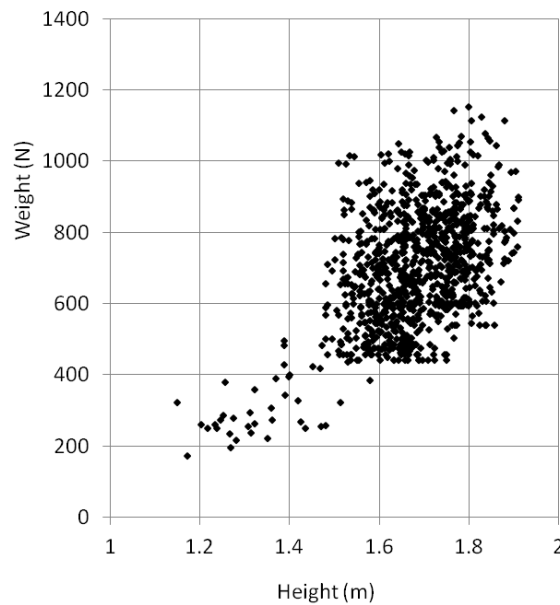


Figure 202 Height and weight of randomly-generated people in the mathematical model

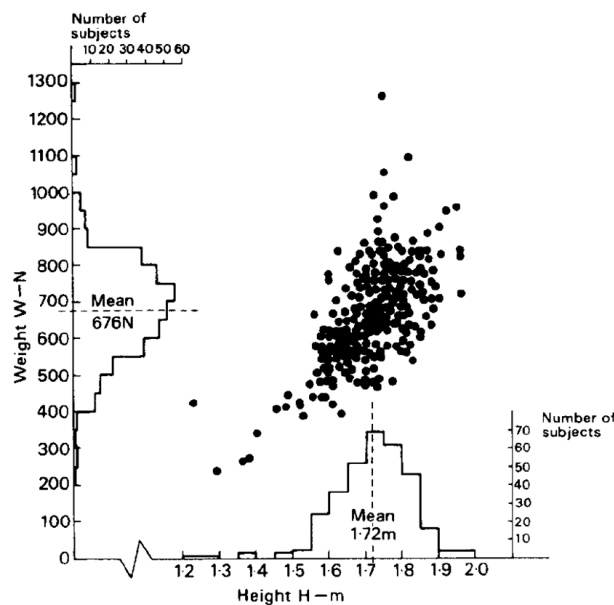


Figure 203 Distribution of heights and weights for persons used in wind tunnel experiments (Penwarden et al., 1978)

Table 15 Constants used in the mathematical model

	Young	Middle-aged	Elderly
<b>Response time (s)</b>	0.375	0.375	0.495
<b>Spring constant, <math>k_3</math> (N/m)</b>	$k_3$	$k_3$	$0.7k_3$
<b>Damping constant, <math>C_{tot}</math> (Ns/m)</b>	215	215	215
<b>F (/s)</b>	0.9	0.9	0.9

## 8.5 Results

In the data presented below, the likelihood of person instability or pushchair movement is given in percentage form. The model was run three times at each position from train side for each crosswind case in order to ensure that data from a single run did not provide erroneous data. The results from the spring-mass-damper and pushchair models were highly-repeatable and for three runs produced unsteadiness values within 3 % of each other run.

The probability of person instability caused by velocities sampled at  $y=4$  m for the no-crosswind,  $10^\circ$  and  $30^\circ$  crosswind cases is shown in Table 16. The no-crosswind case produces no person instability at  $y=4$  m whereas the  $10^\circ$  and  $30^\circ$  crosswinds cause instabilities rates of 35 and 54 %, respectively. The probability of pushchair instability is 0, 5 and 85 % for the no-crosswind,  $10^\circ$  and  $30^\circ$  crosswinds, respectively (Table 17). Between the  $10^\circ$  and  $30^\circ$  cases, the likelihood of person unsteadiness increases by 54 % which is

consistent with the trend of the peak slipstream velocities as shown in Chapter 7. The pushchair instability between the 10° and 30° cases is shown to increase by 16 times which is likely to be due to a threshold value being reached.

Table 16 Person instability results for velocities obtained between y=4 m and y=2 m at z=2 m

<b>Percentage person unsteadiness caused by slipstream velocities</b>			
<b>Distance from COT (m)</b>	<b>No crosswind</b>	<b>10 crosswind</b>	<b>30 crosswind</b>
<b>4.0</b>	0	35	54
<b>3.5</b>	0	46	79
<b>3.0</b>	0	64	97
<b>2.5</b>	7	85	84
<b>2.0</b>	34	96	97

The likelihoods of person instability at y=3.5 m are 0, 35 and 54 % for the no-crosswind, 10° and 30° crosswinds, respectively whereas pushchair movement is 0, 5 and 85 %. Person unsteadiness increases by 61 % between the 10° and 30° cases and the increase in probability of pushchair movement is 1560 %.

Table 17 Pushchair instability results for velocities obtained between y=4 m and y=2 m at z=2 m

<b>Percentage pushchair unsteadiness caused by slipstreams</b>			
<b>Distance from COT (m)</b>	<b>No crosswind</b>	<b>10 crosswind</b>	<b>30 crosswind</b>
<b>4.0</b>	0	5	85
<b>3.5</b>	0	5	83
<b>3.0</b>	1	5	85
<b>2.5</b>	0	5	86
<b>2.0</b>	0	8	88

Due to the fact that there are 20 input velocities are used for the models there is a 5 % likelihood of a given velocity being selected. It is hypothesised that the repeat of the 5 %

pushchair instability between  $y=4$  m and  $y=3.5$  m in the  $10^\circ$  case is due to a single velocity which causes an exceedance of the minimum force value required to move all of the pushchairs it is applied to.

At  $y=3$  m, the likelihood of a person becoming unsteadied in the ambient condition is 0% and the first recorded instance of a pushchair moving occurs with a probability of 1 %. These results appear reasonable considering that yellow lines on station platforms are situated at  $y=2.95$  m and there are no reports of a person becoming unsteadied on the UK rail network standing at this position.

The likelihoods of person unsteadiness at  $y=3$  m for the  $10^\circ$  and  $30^\circ$  crosswinds are 64 % and 97 %, respectively. The pushchair movement probability remains the same as at  $y=3.5$  m for the  $10^\circ$  case and increases by 2 % for the  $30^\circ$  case.

Closer to the train side, at  $y=2.5$  m, the likelihood of a person becoming unsteadied in ambient conditions increases to 7.2 % from 0 % at  $y=3$  m. A negligible increase in person unsteadiness is observed for the  $30^\circ$  case and the percentage of people displaced by the slipstream in the  $30^\circ$  case is less than the  $10^\circ$  case, for the first time. The rate of pushchair movement is 16 times greater for the  $30^\circ$  case than for the  $10^\circ$  case.

The probability of person instability at  $y'=1.5$  m caused by a freight train travelling at 30 m/s through a station was found by Jordan (2008) to be 22 %. In the present case, only 7 % instability is observed 0.34 m closer to the train at  $y=2.5$  m. Jordan (2008) based the freight train slipstream model around measurements obtained on a platform at  $y'=1.5$  m from a British Class 92 with 46 partially loaded container wagons in tow. Fully-loaded consists, such as the one used in the present case, have been shown to produce lower slipstream velocities than partially-loaded consists (Soper, 2014). Therefore it is anticipated that the slipstream of

the no-crosswind case is less likely to cause person instability, which explains the discrepancy between the data.

At  $y=2$  m, the probabilities of person unsteadiness caused by the slipstreams are 34, 96 and 97 % for the no-crosswind,  $10^\circ$  and  $30^\circ$  crosswind cases, respectively. An increase in pushchair movement also occurs for the  $10^\circ$  and  $30^\circ$  crosswind cases between  $y=2.5$  m and  $y=2$  m.

The data in Table 16 show that in the presence of either a  $10^\circ$  or a  $30^\circ$  crosswind, it is extremely likely that a person will become unsteadied due to the slipstream velocities on the leeward side of a train. The near-certainty of human instability at  $y < 3$  m is somewhat mitigated by the probability of a person standing closer to a train than the yellow line, especially considering slipstream risk mitigation methods such as audible announcements on station platforms (RSSB, 2012).

Figure 204 collates data from Table 16 and 2 in order to show the effect of distance from train side on the likelihood of a person becoming unsteadied in each crosswind scenario. For the no-crosswind case the risk is shown to be negligible at  $y=3$  m which gives credence to the appropriateness of the position of the yellow safety line on station platforms. The unsteadiness in the  $10^\circ$  crosswind case exhibits a near-linear decrease with distance from COT whereas the  $30^\circ$  case reaches a peak at  $y=3$  m and then decreases at a slightly higher rate.

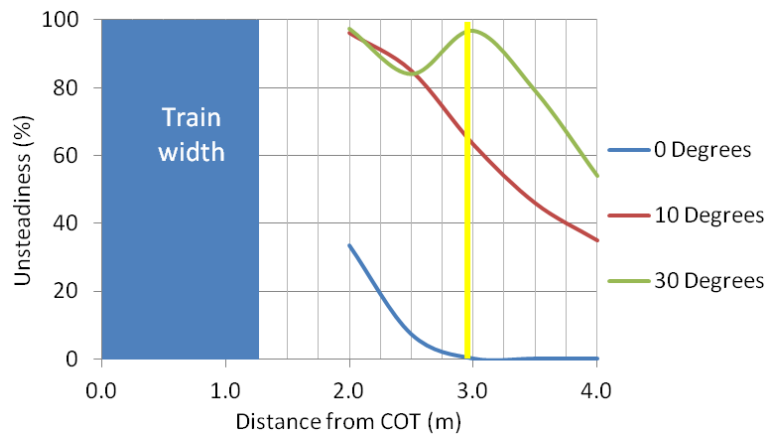


Figure 204 Percentage chance of person instability against distance from train side for the no-crosswind, 10° and 30° crosswind cases, yellow line is positioned at  $y=2.95$  m

If it is assumed that the percentage unsteadiness for the 10° crosswind case decreases at the same rate as in Figure 204, then the position of 0 % person instability will occur at  $y=5.1$  m. Not all station platforms extend up to  $y=5$  m therefore, for the majority of platform scenarios, the occurrence of a 10° crosswind on a Class 66 locomotive-hauled freight train there is a risk to a portion of the population. The effective width of a platform can be reduced when large numbers of passengers are waiting which can cause people to stand closer to train side than would otherwise be the case. Reduced width of station platforms can therefore have the potential to increase the risk of person unsteadiness. However the case presented here is very simplified and other effects will play a part.

## 8.6 Discussion

The data in Table 16 show a general trend of increasing likelihood of person unsteadiness or pushchair movement with increasing yaw angle or decreasing distance from train side. The data are presented from velocities at sampling locations approximately 1 m closer to, and 1 m further from the train than the yellow lines on station platforms which generally reside at  $y=2.95$  m.

In this work it was shown that at  $y=3$  m the likelihood of person unsteadiness is 0 % and at  $y=2.5$  m it is 7 % however Jordan (2008) showed that at  $y'=1.5$  m the likelihood of person unsteadiness was as high as 22 %. Due to the lack of available full-scale slipstream data, the velocities used by Jordan (2008) were at only one position on a platform which is somewhat limited considering the variation in velocities with distance from train side and above TOR. Thus it can be concluded that due to the lack of available data used in Jordan (2008), the results from the current chapter are likely to be more realistic.

The loading configuration of the current freight train is idealistic and has been shown to produce lower slipstream velocities than partially-loaded trains (Soper, 2014). A freight train with a lower loading-efficiency may produce higher instability values due to higher velocities in the boundary layer region.

The velocities obtained from the numerical simulations were sampled from a computational domain which contains only the train and rails. This setup is an idealisation of a real-world scenario where atmospheric wind is seldom so uninhibited. The persons modelled in the mass-spring-damper system are considered to be standing on a station platform which means that the oncoming wind would be blocked or disturbed by adjacent railway infrastructure. Therefore, the instability probabilities presented in the current chapter are likely to be an overestimation of the real world scenario. Due to the vast diversity in station arrangements, an analysis for every station and wind case would be a massive undertaking and therefore not practical. Therefore the values obtained here should be considered indicative of the potential risk but also conservative.

It has been observed that the  $30^\circ$  crosswind case caused the greatest likelihood of unsteadiness for a given distance from train side. In the presence of a 19 m/s mean wind, it is generally regarded that the majority of persons would find it difficult to stand or walk

(Bottema, 1993, BRB, 1971, Durov, 1967, Hunt et al., 1976, Lawson, 1980, Melbourne, 1978, Penwarden et al., 1978, Peters, 1999, Soligo et al., 1998). To this end, the slipstream amplification in the 30° crosswind case would be a secondary concern to the already dangerous wind speeds. Further consequences of such high wind speeds are that the railway network may not be operational due to train overturning risk, or things like trees being blown onto lines (Network Rail, 2013).

It is assumed in this chapter that the spring-mass-damper model has been calibrated to respond correctly to an initial wind. In the presence of a crosswind, a person standing on a platform would experience the wind and, assuming it necessary, would brace or perform some corrective action. The calibration of the model did not consider any such effect, thus the present analysis makes the assumption that the model's reaction to the initial wind is the same as a person's response would be.

## *8.7 Conclusions*

The response of 1000 randomly-generated people and pushchairs was tested when subjected to simulated wind-induced forces. The velocities were obtained from CFD simulations of the slipstream around a fully-loaded Class 66 locomotive hauled container freight train. It was found that the slipstream gusts generated in the presence of no-crosswind, 10° and 30° crosswinds caused varying degrees of person instability and pushchair movement at five evenly-spaced distances from COT. From the results of the model the following conclusions can be drawn:

- Person instability was shown to correlate broadly with increasing yaw angle and decreasing distance from COT
- At  $y=2$  m the rates of person instability for the 10° and 30° crosswinds are 96 and 97 %, respectively

- The theoretical position at which no person instability occurs for the 10° crosswind case is  $y=5.1$  m
- The rate of pushchair movement varies significantly with yaw angle, but less so with distance from COT
- It is assumed that the crosswind preceding the train is accounted for in the model
- The no-crosswind case only produces person unsteadiness at positions less than 3 m from COT

Due to the method of model calibration and the slipstream velocities inputted, the results presented in the current chapter must be considered as indicative only. The additional effect of a crosswind on a slipstream is shown to increase the instability of a person or mobility of a pushchair within 4 m from COT.

The data presented in this chapter show strong justification for an amendment to the CEN and TSI guidelines to ensure that vehicles are not susceptible to large slipstream amplification in the presence of low-speed winds. However, it is not immediately clear how such amendments would best suit passenger safety considering the range of potential crosswind direction, speeds and train station layouts.

# Chapter 9 Conclusions and recommendations for future work

## 9.1 *Conclusions*

The main aim of the present research is to investigate the effect of crosswinds on the slipstream of a model-scale freight train in order to predict possible consequences on persons and pushchairs within close proximity. In this section, conclusions are drawn from the results obtained in this thesis and are presented below each objective set.

Objective 1:

Conduct and validate numerical simulations in which a model-scale Class 66 locomotive-hauled container freight train is subjected to no crosswind,  $10^\circ$  and  $30^\circ$  crosswinds in order to determine their effect on the slipstream of the train.

### **No-Crosswind**

- The time-averaged normalised velocity and pressure coefficients from the numerical simulations were compared to data ensemble-averaged data from previously-conducted moving-model experiments with good agreement shown.
- The no-crosswind case showed that although the velocity was approximately 50% of the TSI limiting value the pressure breached the limit at the majority of the positions tested.
- The highest time-averaged slipstream velocities were observed below  $z=1$  m and a distinguishing divide between velocities was observed from measurements above and below  $z=1$  m.

- The effect of the bogies is visible in the mean pressure signal as roughness whereas higher above TOR, this effect decreases due to the local geometry being the smooth container sides.
- The assumption of the applicability of directly comparing ensemble- and time-averaged velocities was tested using data from the CFD simulations in order to ensure the sources of discrepancies between data acquisition methods was negated. A higher peak velocity occurred at the nose region for the ensemble-averaged data however this was well within the 1 standard deviation bound.
- The magnitude of the nose region velocity and pressure transients was shown to be a result of massive flow separation around the front face of the locomotive.
- The aerodynamic loading on each container is shown to be a function of loading position with some containers experiencing negative pressure drag due to interference effects from adjacent wagons.
- Turbulence length-scales in the slipstream were obtained from autocorrelation and were comparative to full-scale values in the literature for freight trains.

### **30° Crosswind**

- The 30° crosswind simulation was validated against previously-conducted moving-model experiments and the surface pressure coefficients on the third wagon showed good agreement with those from the simulations.
- The slipstream velocity magnitude nose peaks vary very little with distance from COT in comparison to the rate at which the velocities from the other cases decreased.

- The effect of flow separation over the container roofs on the velocities on the windward side of the train is evident above  $z=2$  m for most distances from train side where acceleration is observed.
- Higher than train speed velocities occurred on the leeward side of the freight train as a result of flow separation around the locomotive as well as flow shearing around the leeward corners of the containers.
- Pressure transients on the leeward side of the train exhibit peak-to-peak values of approximately  $\Delta C_p=1.4$  whereas the greatest transient at an inter-wagon spacing is  $\Delta C_p=1.0$ .
- Large-scale recirculation occurs on the leeward side of the train similar to that observed in crosswind simulations of the flow around a passenger train subjected to a  $30^\circ$  crosswind.
- Force and moment coefficients show a general trend of decreasing with loading position, although the relatively large inter-wagon spacing preceding the third container wagon causes it to experience higher forces than adjacent wagons.
- Turbulence intensity on the windward side of the freight train is generally below  $I=20\%$  except for in the near wake region where peak values are observed at  $y=1.59$  m due to flow separation around the windward rear corner of the container wagon.
- Turbulence length-scales obtained from static probes positioned on the leeward side of the train close to inter-wagon spacings have maximum and minimum values of  $L_x=4.79$  m and  $L_x=2.28$  m, respectively; where values decrease with position along the train.

## 10° Crosswind

- Velocity peaks are observed at approximately  $x=0$  m at the closest measurement position to the train on the windward side due to flow separating around the windward front corner of the locomotive.
- On the leeward side of the train velocity magnitudes that are greater than train speed are observed but decrease more rapidly with distance from train side than was seen for the 30° crosswind case but less rapidly than the no-crosswind case.
- Peak-to-peak pressure transients are observed to be greater than those obtained from the no-crosswind case but lower than those from the 30° crosswind case.
- The freight train causes normalised velocities which are four times greater than were seen in the ICE's slipstream on the leeward side. Considering the velocities in terms of full-scale units, the peak velocity in the freight train's slipstream is twice as great as in the slipstream of the passenger train even though the crosswind in the freight train case is half of the speed as in the passenger train case.
- The turbulence length-scales increase in size with position along the train such that at the first inter-wagon spacing  $L_x=1.17$  m and at the last inter-wagon spacing  $L_x=2.87$  m.
- Both pressure and velocity exceed the TSI limits although the analysis is not strictly valid because the crosswind is 2.7 times greater than the maximum allowable value of 2 m/s.

## Comparison chapter

- The means of instantaneous peak slipstream velocities for the three yaw angle cases were shown to increase with yaw angle at  $y=3.34$  m. Closer to train side however the lower yaw angles have the higher mean velocities and the standard deviation of the peak velocities is lowest for the  $30^\circ$  case.
- The frictional contribution to the total force coefficient is lower for greater yaw angles due to the shorter distance that the flow travels over the surface but also due to the dominance of low pressure due to massive flow separation.
- Pressure profiles on the windward side of the train are largely positive for the  $30^\circ$  case whereas for the  $10^\circ$  and no-crosswind cases the pressure coefficient fluctuates about, or close to zero.
- On the leeward side of the train the pressure profiles for the  $30^\circ$  case remain negative for the majority of the train length for nearly all positions from COT, whereas the  $10^\circ$  case shows only comparatively minor negativity.

### Objective 2:

Use instantaneous slipstream velocities obtained from the numerical simulations as inputs to spring-mass-damper model in order to determine effect of slipstream amplification on a range of persons' stability

- At  $y=4$ m, the slipstream velocities from the  $10^\circ$  and  $30^\circ$  crosswind cases were shown to be responsible for causing 35 % and 54 % person unsteadiness.
- It is anticipated that for the majority of cases the design of railway stations will impede crosswinds and therefore affect the relevance of any results obtained here.

- At  $y=3$  m the no-crosswind velocity is shown to cause 0% person unsteadiness which is in accordance with observations on the UK railway network no person has been reported to have been unsteadied by the slipstream of a fully-loaded Class66 locomotive-hauled container freight train whilst standing behind the yellow line.

## 9.2 *Recommendations for future work*

In this thesis it has been shown that the slipstream of a freight train can be significantly affected when subjected to a crosswind and consequently slipstream velocities which are potentially dangerous to persons waiting on a station platform can be produced.

In light of these findings the following points are recommended for future work:

- Previous work has shown that freight trains with lower loading efficiencies produce higher slipstream velocities and pressure transients than freight trains with higher loading efficiencies (Soper et al., 2014). It is hypothesised that the addition of a crosswind may cause significantly higher slipstream velocities than those observed in this work for the fully-loaded case and hence the effect of crosswinds on the slipstream of a partially-loaded train should be investigated.
- Baker et al.(2013b, 2013a) showed that even crosswinds below 2 m/s could affect the velocities measured in the slipstream of a high speed passenger train. Baker (2007) showed that the rate of increase in slipstream velocities with yaw angle was greater for freight trains than for passenger trains. To this end, the effect of a 2 m/s crosswind should be investigated to determine whether future certification for freight trains could be compromised by the 2 m/s ambient wind limit.
- Future work using CFD which investigates the effect of crosswinds on the slipstreams of trains should use LES or DES with strict monitoring of the levels of sub-grid

viscosity in regions of high strain-rate such as wakes in order to ensure that unphysical levels do not occur. Potential methods of reducing unnecessary SGS levels could be testing mesh densities (which could be unfeasibly expensive) or using a dynamic SGS model.

- The wind considered in the present work had a uniform velocity profile that was incident to the train although in reality, atmospheric winds have a power-law or logarithmic profile. Future work should consider the effect of ABL profiles on the slipstream as well as on the force coefficients.
- Nearly all numerical simulations of trains subjected to crosswinds consider the wind to be steady in nature. In reality, no wind is truly steady and in some cases can be very gusty. There is large scope for the effects of gusts to be considered on the train, in terms of slipstream development and forces experienced.
- The current work assumed that the inlet velocity profile was a laminar inlet condition. This was applied due to the relative simplicity with which it could be implemented. The effect of freestream turbulence has been totally neglected in this work even though the literature has shown that surface pressures on ground vehicles are significantly affected at higher yaw angles. Future work should also consider the effect of a turbulent inlet on the slipstream velocities and pressures around the train as well as the force coefficients on the containers.

## References

- ALAM, F. & WATKINS, S. Crosswinds effects on high cube freight trains. The 3rd BSME-ASME thermal engineering conference, 20-22 December 2006 Dhaka, Bangladesh.
- ALAM, F. & WATKINS, S. 2007. Effects of Crosswinds on Double Stacked Container Wagons. *16th Australasian Fluid Mechanics Conference, 2-7 December*. Gold Coast, Australia.
- ANDERSON, J. D. 2001. *Fundamentals of aerodynamics*, McGraw-Hill New York.
- ASHFORD, G. 1996. *An unstructured grid generation and adaptive solution technique for high Reynolds number compressible flows*. PhD Thesis, University of Michigan.
- ATSB 2010. Derailment of train 2PM6 - near Loongana, Western Australia.
- ATSB 2011. Derailment of freight train 4DA2 near Cadney Park, South Australia 25 November 2010.
- AÏTA, S., TABBAL, A., MESTREAU, E., MONTMAYEUR, N., MASBERNAT, F., WOLFHUGEL, Y. & DUMAS, J. 1992. CFD aerodynamics of the French high-speed train. SAE Technical Paper.
- BAKER, C. J. 1991a. Ground vehicles in high cross winds part I: Steady aerodynamic forces. *Journal of Fluids and Structures*, 5, 69-90.
- BAKER, C. J. 1991b. Ground vehicles in high cross winds part II: Unsteady aerodynamic forces. *Journal of Fluids and Structures*, 5, 91-111.
- BAKER, C. J. 2010. The flow around high speed trains. *Journal of Wind Engineering and Industrial Aerodynamics*, 98, 277-298.
- BAKER, C. J., DALLEY, S. J., JOHNSON, T., QUINN, A. D. & WRIGHT, N. G. 2001. The slipstream and wake of a high-speed train. *Proceedings of the Institution of Mechanical Engineers, Part F: Journal of Rail and Rapid Transit*, 215, 83-99.
- BAKER, C. J., HEMIDA, H., IWNICKI, S., XIE, G. & ONGARO, D. 2011. Integration of crosswind forces into train dynamic modelling. *Proceedings of the Institution of Mechanical Engineers, Part F: Journal of Rail and Rapid Transit*, 225, 154-164.
- BAKER, C. J., JORDAN, S. C., GILBERT, T., QUINN, A. D., STERLING, M., JOHNSON, T. & LANE, J. 2012a. Transient aerodynamic pressures and forces on trackside and overhead structures due to passing trains. Part 1 Model scale experiments. *Proceedings of the Institution of Mechanical Engineers, Part F: Journal of Rail and Rapid Transit*, 0954409712464859.
- BAKER, C. J., JORDAN, S. C., GILBERT, T., QUINN, A. D., STERLING, M., JOHNSON, T. & LANE, J. 2012b. Transient aerodynamic pressures and forces on trackside and overhead structures due to passing trains. Part 2 Standards applications. *Proceedings of the Institution of Mechanical Engineers, Part F: Journal of Rail and Rapid Transit*, 0954409712464859.
- BAKER, C. J., QUINN, A., SIMA, M., HOEFENER, L. & LICCIARDELLO, R. 2013a. Full-scale measurement and analysis of train slipstreams and wakes. Part 2 Gust analysis. *Proceedings of the Institution of Mechanical Engineers, Part F: Journal of Rail and Rapid Transit*.
- BAKER, C. J. & QUINN, A. D. 2012. Train slipstream measurements at Uffington on the Western Main Line. Technical report, Birmingham Centre for Railway Research and Education at the University of Birmingham.
- BAKER, C. J., QUINN, A. D., SIMA, M., HOEFENER, L. & LICCIARDELLO, R. 2013b. Full-scale measurement and analysis of train slipstreams and wakes: Part 1 Ensemble averages. *Proceedings of the Institution of Mechanical Engineers, Part F: Journal of Rail and Rapid Transit*.
- BAKER, C. J., STERLING, M., FIGURA-HARDY, G., JOHNSON, T., FREE, P., MUNLEY, G., BOWMAN, I., POPE, C. & GAWTHORPE, R. The effect of train slipstreams on passengers and trackside workers. *Proceedings of the 7 th World Congress on Railway Research*, Montral, 2006.
- BAKER, C. J., STERLING, M., JOHNSON, T., FIGURA-HARDY, G. I. & POPE, C. W. The effect of crosswinds on train slipstreams. *12th International Conference on Wind Engineering*, Cairns, Australia, 2007 Cairns, Australia.
- BEARMAN, P. W. & MOREL, T. 1983. Effect of free stream turbulence on the flow around bluff bodies. *Progress in Aerospace Sciences*, 20, 97-123.

- BELL, C. 1991. Trackside safety tests for trains travelling at speeds up to and including 100 mile/h. *British Rail Research report LR-AER-039*.
- BELL, J. R., BURTON, D., THOMPSON, M., HERBST, A. & SHERIDAN, J. 2014. Wind tunnel analysis of the slipstream and wake of a high-speed train. *Journal of Wind Engineering and Industrial Aerodynamics*, 134, 122-138.
- BELL, J. R., BURTON, D., THOMPSON, M. C., HERBST, A. H. & SHERIDAN, J. 2015. Moving model analysis of the slipstream and wake of a high-speed train. *Journal of Wind Engineering and Industrial Aerodynamics*, 136, 127-137.
- BETTLE, J., HOLLOWAY, A. & VENART, J. 2003. A computational study of the aerodynamic forces acting on a tractor-trailer vehicle on a bridge in cross-wind. *Journal of Wind Engineering and Industrial Aerodynamics*, 91, 573-592.
- BOTTEMA, M. 1993. Wind climate and urban geometry. Technical University, Eindhoven.
- BOUFERROUK, A., HARGREAVES, D. & MORVAN, H. 2012. CFD Simulations of Crosswind Impinging on a High Speed Train Model.
- BOWMAN, I. 2005. Safety of Slipstream Effects Produced by Trains: Pilot CFD Analysis of the Effect of Crosswinds on Train Slipstreams.
- BRB 1971. High speed tests at Cheddington, 1970. British Railways Board.
- CEN 2010. Part 6: Requirements and test procedures for cross wind assessment.
- CEN 2011. Railway applications - Aerodynamics - Part 4: Requirements and test procedures for aerodynamics on open track.
- CHELI, F., RIPAMONTI, F., ROCCHI, D. & TOMASINI, G. 2010. Aerodynamic behaviour investigation of the new EMUV250 train to cross wind. *Journal of Wind Engineering and Industrial Aerodynamics*, 98, 189-201.
- CHIU, T. W. & SQUIRE, L. C. 1992. An experimental study of the flow over a train in a crosswind at large yaw angles up to 90°. *Journal of Wind Engineering and Industrial Aerodynamics*, 45, 47-74.
- CITYNOISE.ORG. 2006. *Train derails on bridge* [Online]. Available: <http://www.citynoise.org/article/3039> [Accessed 2 October 2014].
- COLEMAN, S. A. & BAKER, C. J. 1990. High sided road vehicles in cross winds. *Journal of Wind Engineering and Industrial Aerodynamics*, 36, Part 2, 1383-1392.
- COOPER, R. 1984. Atmospheric turbulence with respect to moving ground vehicles. *Journal of Wind Engineering and Industrial Aerodynamics*, 17, 215-238.
- COPLEY, J. M. 1987. The three-dimensional flow around railway trains. *Journal of Wind Engineering and Industrial Aerodynamics*, 26, 21-52.
- CORIN, R., HE, L. & DOMINY, R. 2008. A CFD investigation into the transient aerodynamic forces on overtaking road vehicle models. *Journal of Wind Engineering and Industrial Aerodynamics*, 96, 1390-1411.
- DAVIDSON, P. A. 2004. *Turbulence: An Introduction for Scientists and Engineers*, Oxford University Press.
- DECK, S. Detached and Large Eddy Simulation of Unsteady Side-Loads Over AN Axisymmetric Afterbody. Fifth European Symposium on Aerothermodynamics for Space Vehicles, 2005. 297.
- DEEG, P., JÖNSSON, M., KALTENBACH, H., SCHÖBER, M. & WEISE, M. 2008. Cross-comparison of measurement techniques for the determination of train induced aerodynamic loads on the track bed. *Proc. BBAA VI*. Milano, Italy.
- DFT 2007. Delivering a sustainable railway. In: TRANSPORT, D. F. (ed.).
- DIEDRICHS, B. 2003. On computational fluid dynamics modelling of crosswind effects for high-speed rolling stock. *Proceedings of the Institution of Mechanical Engineers, Part F: Journal of Rail and Rapid Transit*, 217, 203-226.

- DIEDRICHS, B., SIMA, M., ORELLANO, A. & TENGSTRAND, H. 2007. Crosswind stability of a high-speed train on a high embankment. *Proceedings of the Institution of Mechanical Engineers, Part F: Journal of Rail and Rapid Transit*, 221, 205-225.
- DORIGATTI, F. 2013. *Rail vehicles in crosswinds: analysis of steady and unsteady aerodynamic effects through static and moving model tests*. PhD Thesis, University of Birmingham.
- DU BOIS, D. & DU BOIS, E. F. 1916. A formula to estimate the approximate surface area if height and weight be known. *Nutrition (Burbank, Los Angeles County, Calif.)*, 5, 303.
- DUROV, A. 1967. Questions relating to the aerodynamics of high-speed trains. *Zheleznodorozhni Transport*, 49, 34-36.
- ERCOFTAC. 2014. *European Research Community on Flow, Turbulence and Combustion Database* [Online]. Available: <http://cfd.mace.manchester.ac.uk/ercoftac/index.html> [Accessed 17th July 2014].
- ESKRIDGE, R. E. & HUNT, J. 1979. Highway Modeling. Part I: Prediction of Velocity and Turbulence Fields in the Wake of Vehicles. *Journal of Applied Meteorology*, 18, 387-400.
- FARES, E. 2006. Unsteady flow simulation of the Ahmed reference body using a lattice Boltzmann approach. *Computers & Fluids*, 35, 940-950.
- FIGURA-HARDY, G., I. 2002a. 90 mph freight train slipstream tests – Stage 1. AEA technology rail report AEATR-T&S-2001-214, confidential commercial report.
- FIGURA-HARDY, G., I. 2002b. 90 mph freight train slipstream tests – Stage 2. AEA technology rail report AEATR-T&S-2002-004, confidential commercial report, 2002.
- FIGURA-HARDY, G., I. 2005. RSSB Slipstream Safety - Analysis of Existing Experimental Data on Train Slipstreams Including the Effects on Pushchairs.
- FIGURA, G., I., HARRIS, F. S., HOWLETT, A. B. & SCHOFIELD, R. S. 1993. Trackside safety tests at Northallerton. *British Rail Research report RR-AER-014*.
- FUKUCHI, G. 1961. Field Measurements of Train Drafts. *Permanent Way*, 4.
- GARCÍA, J., CRESPO, A., BERASARTE, A. & GOIKOETXEA, J. 2011. Study of the flow between the train underbody and the ballast track. *Journal of Wind Engineering and Industrial Aerodynamics*, 99, 1089-1098.
- GERMANO, M., PIOMELLI, U., MOIN, P. & CABOT, W. H. 1991. A dynamic subgrid-scale eddy viscosity model. *Physics of Fluids A: Fluid Dynamics*, 3, 1760-1765.
- GIL, N., BAKER, C. J., ROBERTS, C. & QUINN, A. D. 2010. Passenger train slipstream characterization using a rotating rail rig. *Journal of Fluids Engineering*, 132, 061401.
- GILBERT, T., BAKER, C. & QUINN, A. 2013. Aerodynamic pressures around high-speed trains: the transition from unconfined to enclosed spaces. *Proceedings of the Institution of Mechanical Engineers, Part F: Journal of Rail and Rapid Transit*, 227, 609-622.
- GOLOVANEVSKIY, V. A., CHMOVZH, V. V. & GIRKA, Y. V. 2012. On the optimal model configuration for aerodynamic modeling of open cargo railway train. *Journal of Wind Engineering and Industrial Aerodynamics*, 107-108, 131-139.
- GUILMINEAU, E., CHIKHAOUI, O., DENG, G. & VISONNEAU, M. 2013. Cross wind effects on a simplified car model by a DES approach. *Computers & Fluids*, 78, 29-40.
- HEMIDA, H. & BAKER, C. J. 2010. Large-eddy simulation of the flow around a freight wagon subjected to a crosswind. *Computers & Fluids*, 39, 1944-1956.
- HEMIDA, H., BAKER, C. J. & GAO, G. 2012a. The calculation of train slipstreams using Large-Eddy Simulation. *Proceedings of the Institution of Mechanical Engineers, Part F: Journal of Rail and Rapid Transit*, 228, 25-36.
- HEMIDA, H., BAKER, C. J. & GAO, G. 2012b. The calculation of train slipstreams using Large-Eddy Simulation. *Proceedings of the Institution of Mechanical Engineers, Part F: Journal of Rail and Rapid Transit*, 227.

- HEMIDA, H., BAKER, C. J. & GAO, G. 2014. The calculation of train slipstreams using Large-Eddy Simulation. *Proceedings of the Institution of Mechanical Engineers, Part F: Journal of Rail and Rapid Transit*, 228, 25-36.
- HEMIDA, H., GIL, N. & BAKER, C. J. 2010. LES of the slipstream of a rotating train. *Journal of Fluids Engineering*, 132, 1 - 9.
- HEMIDA, H. & KRAJNOVIC, S. 2005. Large-Eddy Simulation of the flow around a simplified high speed train under the influence of a cross-wind. *17th AIAA Computational Fluid Dynamics Conference*. Toronto, Canada.
- HESS, J. L. & SMITH, A. M. O. 1967. Calculation of potential flow about arbitrary bodies. *Progress in Aerospace Sciences*, 8, 1-138.
- HINTERBERGER, C., GARCIA-VILLALBA, M. & RODI, W. 2004. Large eddy simulation of flow around the Ahmed body. *The Aerodynamics of Heavy Vehicles: Trucks, Buses, and Trains*. Springer.
- HOLMES, J. D. 2007. *Wind loading of structures*, Taylor & Francis.
- HU, X.-J., PENG, Q., LEI, L., PENG, G., WANG, J.-Y. & BO, Y. 2014. Numerical simulation of the aerodynamic characteristics of heavy-duty trucks through viaduct in crosswind. *Journal of Hydrodynamics, Ser. B*, 26, 394-399.
- HUANG, S., HEMIDA, H. & YANG, M. 2014. Numerical calculation of the slipstream generated by a CRH2 high-speed train. *Proceedings of the Institution of Mechanical Engineers, Part F: Journal of Rail and Rapid Transit*, 1-14.
- HUNT, J. C. R., POULTON, E. C. & MUMFORD, J. C. 1976. The effects of wind on people; New criteria based on wind tunnel experiments. *Building and Environment*, 11, 15-28.
- IDO, A., SAITOU, S., NAKADE, K. & IKURA, S. 2008. Study on under-floor flow to reduce ballast flying phenomena. *Proc. World Congress on Rail Research*. Seoul.
- ISSA, R. I. 1986. Solution of the implicitly discretised fluid flow equations by operator-splitting. *Journal of Computational Physics*, 62, 40-65.
- JEONG, J. & HUSSAIN, F. 1995. On the identification of a vortex. *Journal of Fluid Mechanics*, 285, 69-94.
- JOHNSON, T. 2012. Investigation of freight vehicle aerodynamic performance in accordance with GM/RT 2142 Resistance of Railway Vehicles to Roll-over in Gales.
- JOHNSON, T. & PREVEZER, T. 2005. Mechanical model of human loss of balance due to wind gusts. *EACWE4 – The Fourth European and African Conference on Wind Engineering*. Prague, Czech Republic.
- JORDAN, S., C. 2008. *An investigation of the slipstreams and wakes of trains and the associated effects on trackside people and objects*. PhD, The University of Birmingham.
- JORDAN, S. C., JOHNSON, T., STERLING, M. & BAKER, C. J. 2008. Evaluating and modelling the response of an individual to a sudden change in wind speed. *Building and Environment*, 43, 1521-1534.
- KAREEM, A., KIJEWski, T. & LU, P.-C. 1998. Investigation of interference effects for a group of finite cylinders. *Journal of Wind Engineering and Industrial Aerodynamics*, 77-78, 503-520.
- KHIER, W., BREUER, M. & DURST, F. 2000. Flow structure around trains under side wind conditions: a numerical study. *Computers & Fluids*, 29, 179-195.
- KRAJNOVIC, S. On Unsteady Simulations in Train Aerodynamics. Railways 2014 The Second International Conference on Railway Technology: Research, Development and Maintenance Ajaccio, Corsica, France 8-11 April 2014, 2014.
- KRAJNOVIĆ, S. 2009a. Large eddy simulation of flows around ground vehicles and other bluff bodies. *Philosophical Transactions of the Royal Society A: Mathematical, Physical and Engineering Sciences*, 367, 2917-2930.
- KRAJNOVIĆ, S. 2009b. Optimization of aerodynamic properties of high-speed trains with CFD and response surface models. *The Aerodynamics of Heavy Vehicles II: Trucks, Buses, and Trains*. Springer.

- KRAJNOVIĆ, S. 2010. LES study of the influence of nose shapes and yaw angles on flow structures around trains. *Journal of Wind Engineering and Industrial Aerodynamics*, 98, 34-46.
- KRÖNKE, I. & SOCKEL, H. 1994. Model tests about cross wind effects on containers and wagons in atmospheric boundary layers. *Journal of Wind Engineering and Industrial Aerodynamics*, 52, 109-119.
- KUMAR, A., NAIR, P. B., KEANE, A. J. & SHAHPAR, S. 2008. Robust design using bayesian monte carlo. *International Journal for Numerical Methods in Engineering*, 73, 1497-1517.
- KUMAR, A., RICKETT, T., VEMULA, A. & HART, J. 2011. Aerodynamic Analysis of Intermodal Freight Trains Using Machine Vision. *9th World Congress on Railway Research*. Lille, France.
- LAM, K. M., H. LEUNG, M. Y. & ZHAO, J. G. 2008. Interference effects on wind loading of a row of closely spaced tall buildings. *Journal of Wind Engineering and Industrial Aerodynamics*, 96, 562-583.
- LAUNDER, B. E. & SPALDING, D. 1974. The numerical computation of turbulent flows. *Computer Methods in Applied Mechanics and Engineering*, 3, 269-289.
- LAWSON, T. V. 1980. *Wind Effects on Buildings: Design Applications*, London, Spon Press.
- LEE, B., E., 1975. The effect of turbulence on the surface pressure field of a square prism. *Journal of Fluid Mechanics*, 69, 263-282.
- LEWIS, R., MOSEDALE, A. & ANNETS, I. Using OpenFOAM and ANSA for road and race car CFD. 3rd ANSA & μETA Int. Conf, September 9-11 2009 Halkidiki, Greece.
- LIU, Y., HEMIDA, H. & LIU, Z. 2013. Large eddy simulation of the flow around a train passing a stationary freight wagon. *Proceedings of the Institution of Mechanical Engineers, Part F: Journal of Rail and Rapid Transit*.
- MACKEY, D. C. & ROBINOVITCH, S. N. 2006. Mechanisms underlying age-related differences in ability to recover balance with the ankle strategy. *Gait & posture*, 23, 59-68.
- MAVRIPLIS, D. & VENKATAKRISHNAN, V. 1995. A 3D agglomeration multigrid solver for the Reynolds-averaged Navier-Stokes equations on unstructured meshes. *33rd Aerospace Sciences Meeting and Exhibit*. American Institute of Aeronautics and Astronautics.
- MELBOURNE, W. H. 1978. Criteria for environmental wind conditions. *Journal of Wind Engineering and Industrial Aerodynamics*, 3, 241-249.
- MENTER, F. & KUNTZ, M. 2004. Adaptation of eddy-viscosity turbulence models to unsteady separated flow behind vehicles. *The aerodynamics of heavy vehicles: trucks, buses, and trains*, 19, 339-352.
- MINGUEZ, M., PASQUETTI, R. & SERRE, E. 2008. High-order large-eddy simulation of flow over the "Ahmed body" car model. *Physics of Fluids*, 20, 095101.
- MULD, T. W., EFRAIMSSON, G. & HENNINGSON, D. S. 2012. Flow structures around a high-speed train extracted using Proper Orthogonal Decomposition and Dynamic Mode Decomposition. *Computers & Fluids*, 57, 87-97.
- MULD, T. W., EFRAIMSSON, G. & HENNINGSON, D. S. 2013. Wake characteristics of high-speed trains with different lengths. *Proceedings of the Institution of Mechanical Engineers, Part F: Journal of Rail and Rapid Transit*.
- MUNSON, B. R., YOUNG, D. F. & OKIISHI, T. H. 1990. *Fundamentals of fluid mechanics*, New York.
- NATIONAL CENTER FOR HEALTH STATISTICS. 2007. *Prevalence of Overweight and Obesity Among Adults: United States, 2003-2004* [Online]. Available: [http://www.cdc.gov/nchs/data/hestat/overweight/overweight\\_adult\\_03.htm](http://www.cdc.gov/nchs/data/hestat/overweight/overweight_adult_03.htm) [Accessed 25 September 2014].
- NATIONAL HIGHWAY TRAFFIC SAFETY ADMINISTRATION. 2002. *Adult crash test dummies, hybrid III 50th percentile male* [Online]. Available: [www-nrd.nhtsa.dot.gov/vrtc/bio/adult/hybIII50dat.htm](http://www-nrd.nhtsa.dot.gov/vrtc/bio/adult/hybIII50dat.htm) [Accessed 27/03/15].
- NETWORK RAIL. 2013. *Our Plans For Winter* [Online]. [Accessed 23/08/13 2013].
- OGAWA, T. & FUJII, K. 1997. Numerical investigation of three-dimensional compressible flows induced by a train moving into a tunnel. *Computers & Fluids*, 26, 565-585.

- OKE, T. R. 1988. Street design and urban canopy layer climate. *Energy and Buildings*, 11, 103-113.
- OPEN FOUNDATION. 2012. *OpenFOAM 2.1.0 User Guide* [Online]. [Accessed 10/09/2013 2013].
- ÖSTH, J. & KRAJNOVIĆ, S. 2014. A study of the aerodynamics of a generic container freight wagon using Large-Eddy Simulation. *Journal of Fluids and Structures*, 44, 31-51.
- PATANKAR, S. V. & SPALDING, D. B. 1972. A calculation procedure for heat, mass and momentum transfer in three-dimensional parabolic flows. *International Journal of Heat and Mass Transfer*, 15, 1787-1806.
- PENWARDEN, A. D. 1973. Acceptable wind speeds in towns. *Building Science*, 8, 259-267.
- PENWARDEN, A. D., GRIGG, P. F. & RAYMENT, R. 1978. Measurements of wind drag on people standing in a wind tunnel. *Building and Environment*, 13, 75-84.
- PETERS, J. W. H. 1999. Air movements and human postural stability.: Arbo Management Groep, Ergonomics 2109-E (AM) Project Organisation High Speed Line South Infrastructure (HSL South Infra), Utrecht, Netherlands.
- PII, L., VANOLI, E., POLIDORO, F., GAUTIER, S. & TABBAL, A. 2014. A full scale simulation of a high speed train for slipstream prediction. *Proceedings of the Transport Reserach Arena, Paris, France*.
- POPE, C. 2006. Safety of Slipstreams Effects Produced by Trains. 2 ed. Mott MacDonald, Croydon.
- POPE, S. B. 2000. *Turbulent flows*, Cambridge university press.
- QUINN, A. & RICHARDS, P. 2002. A 6m cube in an atmospheric boundary layer flow Part 2: Computational solutions. *Wind and Structures*, 5, 177-192.
- QUINN, A. D., BAKER, C. J., STERLING, M., SIMA, M., WEISE, M., HOFENER, L. & EISENLAUER, M. 2011. The Effect of Crosswinds on the Slipstreams of High Speed Trains. In: C GUERTS, T., EDITOR (ed.) *The 13th international conference on wind engineering*. Amstrerdam, The Netherlands.
- QUINN, A. D., HAYWARD, M., BAKER, C. J., SCHMID, F., PRIEST, J. A. & POWRIE, W. 2009. A full scale experiment and modelling study of ballast flight under high speed trains. *Proceedings of the Institution of Mechanical Engineers Part F- Journal of Rail and Rapid Transit*, 224, 61-74.
- QUINN, A. D., STERLING, M., ROBERTSON, A. & BAKER, C. J. 2007. An investigation of the wind-induced rolling moment on a commercial vehicle in the atmospheric boundary layer. *Proc. IMechE Part D: J. Automobile Engineering*, 221, 1367-1379.
- RAIB 2009. Detachment of containers from freight wagons near Cheddington and Hardendale, 1 March 2008.
- RAILWAY GROUP STANDARD 2009. Resistance of Railway Vehicles to Roll-Over in Gales: GM/RT2142.
- REVUZ, J., HARGREAVES, D. & OWEN, J. Numerical Simulation of the Dynamic Wind Loading on and Response of Tall Buildings. EACWE 5, 19th – 23rd July 2009 2009 Florence, Italy.
- RIGBY, P. R. 1982. Slipstream effects of aerodynamically rough trains. British Rail research report.
- ROACHE, P. J. 1998. *Verification and validation in computational science and engineering*, Albuquerque, N.M, Hermosa publishers.
- ROBINSON, C. G. & BAKER, C. J. 1990. The effect of atmospheric turbulence on trains. *Journal of Wind Engineering and Industrial Aerodynamics*, 34, 251-272.
- RSSB 2007. Aerodynamic influences of vehicle design on wheel/rail contamination. Rail safety standards board.
- RSSB 2009. Principles and Practice of CFD-Modelling of the Forces and Moments Acting on Trains in Crosswind.
- RSSB 2012. T749: Guidance on protecting people from the aerodynamic effects of passenger trains.
- SANZ-ANDRÉS, A. & SANTIAGO-PROWALD, J. 2002. Train-induced pressure on pedestrians. *Journal of Wind Engineering and Industrial Aerodynamics*, 90, 1007-1015.
- SAUNDERS, J. W., WATKINS, S. & CASSAR, R. J. 1993. Vortex optimisation of slotted tops and cavities of two different open rail wagons. *Journal of Wind Engineering and Industrial Aerodynamics*, 49, 421-430.

- SAUSSINE, G., ALLAIN, E., VAILLANT, A., RIBOURG, M. & NEEL, O. High speed in extreme conditions: ballast projection phenomenon. International Workshop on Train Aerodynamics, 2013.
- SCHUMANN, U. 1975. Subgrid scale model for finite difference simulations of turbulent flows in plane channels and annuli. *Journal of Computational Physics*, 18, 376-404.
- SIMA, M., GRAPPEIN, E., WEISE, M., PARADOT, N., HIEKE, M., BAKER, C., LICCIARDELLO, R. & COUTURIER, M. Presentation of the EU FP7 AeroTRAIN project and first results. The ninth world congress on railway research, 2011.
- SMAGORINSKY, J. 1963. General Circulation Experiments With The Primitive Equations. *Monthly Weather Review*, 91, 99-164.
- SOLIGO, M. J., IRWIN, P. A., WILLIAMS, C. J. & SCHUYLER, G. D. 1998. A comprehensive assessment of pedestrian comfort including thermal effects. *Journal of Wind Engineering and Industrial Aerodynamics*, 77, 753-766.
- SOPER, D. 2014. *The aerodynamics of a container freight train*. PhD thesis, University of Birmingham.
- SOPER, D., BAKER, C. & STERLING, M. 2014. Experimental investigation of the slipstream development around a container freight train using a moving model facility. *Journal of Wind Engineering and Industrial Aerodynamics*, 135, 105-117.
- SPALART, P. R. & ALLMARAS, S. R. 1992. A one equation turbulence model for aerodynamic flows. *AIAA Journal*, 92-0439.
- SPALART, P. R., DECK, S., SHUR, M., SQUIRES, K., STRELETS, M. K. & TRAVIN, A. 2006. A new version of detached-eddy simulation, resistant to ambiguous grid densities. *Theoretical and Computational Fluid Dynamics*, 20, 181-195.
- STERLING, M., BAKER, C. J., C., J. S. & T., J. 2008. A study of the slipstreams of high-speed passenger trains and freight trains. *Proceedings of the Institution of Mechanical Engineers, Part F: Journal of Rail and Rapid Transit*, 222, 177-193.
- SWEBY, P. K. 1984. High resolution schemes using flux limiters for hyperbolic conservation laws. *SIAM journal on numerical analysis*, 21, 995-1011.
- TAGISHSIMON 2004. Class 66 railway locomotive. [http://upload.wikimedia.org/wikipedia/commons/4/4a/Class\\_66\\_railway\\_locomotive\\_-\\_Freightliner\\_livery\\_-\\_Virginia\\_Water\\_station\\_-\\_England\\_-\\_280404.jpg](http://upload.wikimedia.org/wikipedia/commons/4/4a/Class_66_railway_locomotive_-_Freightliner_livery_-_Virginia_Water_station_-_England_-_280404.jpg).
- TEMPLE, J. & HOWLETT, A. B. 1994. Apsley pushchair tests. An assessment of the effects of train slipstreams on buggy-style pushchairs. *British Rail Research report RR-AER-013*.
- TSBC 1999. Railway Investigation Report R99W0231.
- TSI 2008. Relating to the 'Rolling Stock' Sub-System of the Trans-European High-Speed Rail System, 2008/232/CE. *Official Journal of The European Union*.
- VERSTEEG, H., K., & MALALASEKERA, W. 2007. *An introduction to computational fluid dynamics: The finite volume method*, Pearson publishing.
- WATKINS, S., SAUNDERS, J. & KUMAR, H. 1992. Aerodynamic drag reduction of goods trains. *Journal of Wind Engineering and Industrial Aerodynamics*, 40, 147-178.
- WEIBULL, W. 1951. A statistical distribution function of wide applicability. *Journal of applied mechanics*, 293-297.
- WEXLER, A. S., DING, J. & BINDER-MACLEOD, S. A. 1997. A mathematical model that predicts skeletal muscle force. *Biomedical Engineering, IEEE Transactions on*, 44, 337-348.

## **Appendix A Author's publications**

### *Introduction*

The following section contains a journal paper published in Wind Engineering and Industrial Aerodynamics:

FLYNN, D., HEMIDA, H., SOPER, D. & BAKER, C. 2014. Detached-eddy simulation of the slipstream of an operational freight train. *Journal of Wind Engineering and Industrial Aerodynamics*, 132, 1-12.

The paper investigates the slipstream of the freight train studied where no crosswind is present. The results are essentially a condensed version of those presented in Chapter 4 and provide a deeper insight into the flow around a freight train than has previously been presented.



Contents lists available at ScienceDirect

## Journal of Wind Engineering and Industrial Aerodynamics

journal homepage: [www.elsevier.com/locate/jweia](http://www.elsevier.com/locate/jweia)



### Detached-eddy simulation of the slipstream of an operational freight train



Dominic Flynn\*, Hassan Hemida, David Soper, Chris Baker

Centre for Railway Research and Education, School of Civil Engineering, University of Birmingham, Edgbaston, Birmingham B15 2TT, UK

#### ARTICLE INFO

##### Article history:

Received 17 February 2014

Received in revised form

30 May 2014

Accepted 12 June 2014

##### Keywords:

Freight train

Slipstream

Computational fluid dynamics (CFD)

TSI

Numerical simulation

DEES

#### ABSTRACT

With increasing train speeds the subsequent increase in slipstream velocities can have a detrimental effect on the safety of persons in close proximity to the vehicle. Due to their uneven loading and bluff geometries, freight trains can produce higher slipstream velocities than passenger trains at given measurement locations. The highly turbulent non-stationary slipstream of a model-scale Class 66 locomotive and wagons was investigated using delayed detached-eddy simulation (DDES). The Reynolds number of the flow was 300,000 and results were compared for meshes of 25 and 34 million hexahedral cells. Good agreement was observed between the DDES and model-scale physical experiments. Slipstream velocities along the train side and roof were investigated and the bogie region was seen to produce the highest slipstream velocities. A comparison between time-averaged and ensemble-averaged data from the simulations gave comparable results. The technical standards for interoperability (TSI) analysis showed that the slipstream velocities generated were below half of the maximum permissible value of the standard whereas the pressure was 43% greater than the limiting value. Furthermore the presence of a periodic phenomenon is detected above the roof of the locomotive.

© 2014 Elsevier Ltd. All rights reserved.

